The Static Strength of I-beam to Circular Hollow Section Column Connections

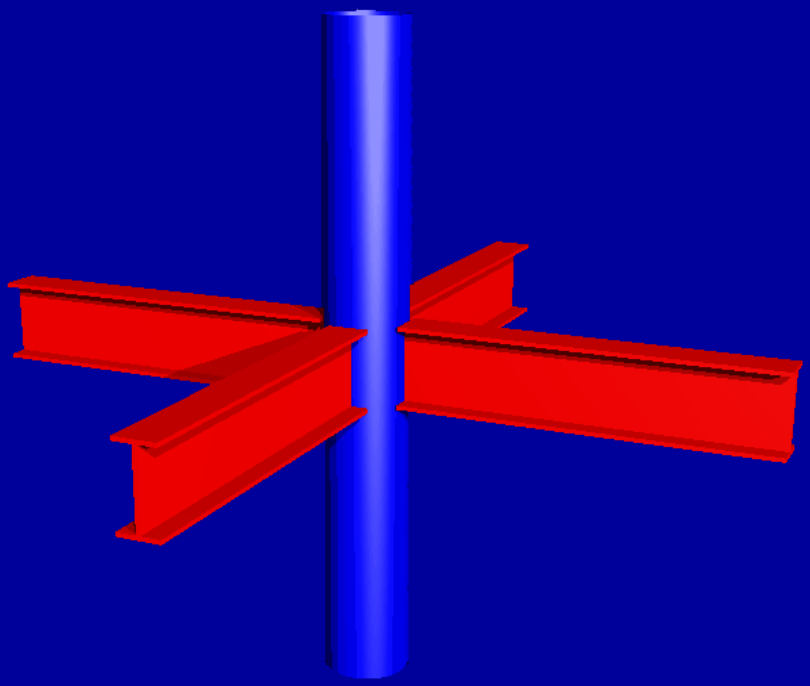

G.D. de Winkel

THE STATIC STRENGTH OF I-BEAM TO CIRCULAR HOLLOW SECTION COLUMN CONNECTIONS

THE STATIC STRENGTH OF I-BEAM TO CIRCULAR HOLLOW SECTION COLUMN CONNECTIONS

PROEFSCHRIFT

ter verkrijging van de graad van doctor
aan de Technische Universiteit Delft,
op gezag van de Rector Magnificus Prof.ir. K.F. Wakker,
in het openbaar te verdedigen ten overstaan van een commissie,
door het College voor Promoties aangewezen,
op dinsdag 22 december 1998 te 13:30 uur.

door

Gerben Dick DE WINKEL

civiel ingenieur

geboren te Loosdrecht

Dit proefschrift is goedgekeurd door de promotor:
Prof.dr.ir. J. Wardenier

Samenstelling promotiecommissie:

Rector Magnificus,	Voorzitter
Prof.dr.ir. J. Wardenier,	Technische Universiteit Delft
Prof.ir. J.W.B. Stark,	Technische Universiteit Delft
Prof.ir. L.A.G. Wagemans,	Technische Universiteit Delft
Prof.ir. H.H. Snijder,	Technische Universiteit Eindhoven
Prof.ir. F. Soetens,	Technische Universiteit Eindhoven
Prof.dr.eur.-ing. R.S. Puthli,	Universiteit van Karlsruhe
Prof.ir. J. de Back,	Emeritus (1989) hoogleraar Technische Universiteit Delft, gast

ISBN 90-76554-01-3
NUGI 833

Copyright © 1998 by G.D. de Winkel, Delft, The Netherlands

All parts reserved.
No part of this material protected by this copyright notice may be reproduced or utilized in any form or by any means, electronic of mechanical, including photocopying, recording or by any information storage and retrieval system, without permission from the publisher.

ACKNOWLEDGMENTS

The research reported in this thesis has been carried out at the Faculty of Civil Engineering and Geosciences of Delft University of Technology.

I like to thank the staff of the Stevin Laboratory for Steel Structures and the staff of the Steel Structures Laboratory of TNO Building and Construction Research for carrying out the experimental tests, with special thanks to Henk Munter, Alex Verheul and Cees de Koning for their input for the design of the test rigs and the instrumentation.
Thanks are also due to my colleagues in the section Steel and Timber Structures for their help, support and encouragements during the work.
I also thank Arno van Wingerde for his help during the last part of this work and for checking the thesis on content and language.
Thanks are expressed to the members of the "Semi-rigid" research team of the ECSC research project, with whom I worked closely together for a long time. Specially, I like to thank Harold Rink for his assistance with the numerical work, George Frater for taking care of the detailed measurements and Ram Puthli for his input on the finite element work.
I want to thank all current and former members of commission TC-10B (Tubular Structures) of the Staalbouw Instituut for their technical support and feedback throughout the research.

Thanks are also expressed to the Stichting Technische Wetenschappen (STW), the European Steel and Coal Community (ECSC), Comité International pour le Développement et l'Etude de la Construction Tubulaire (CIDECT), Nationale Computer Faciliteit (NCF), Rijkswaterstaat and Van Leeuwen Buizen for their financial support of the various parts of the research and finally, IBM Nederland NV for making available an IBM RS/6000 model 350 workstation for a period of two years in the framework of a study contract.

SUMMARY

The Static Strength of I-beam to Circular Hollow Section Column Connections
G.D. de Winkel

Semi-rigid connections between I-section beams and tubular columns can be used economically for buildings and offshore structures. The lack of stiffening plates allows the fabrication of these connections in a cost effective way. Furthermore, by taking into account the connection strength and stiffness, the connections are also economically in terms of material use. By filling the tubular column with reinforced concrete, the connection strength and stiffness are increased. With this concrete filling sufficient fire resistance can be achieved without the need of external fire protection. The strength and stiffness of the connection can be further increased in case of a composite steel-concrete floor.
Current design codes and recommendations lack sufficient information on the strength of I-beam to tubular column connections to design these connections efficiently.
The research consists of an experimental and a numerical investigation on the static strength and behaviour of multiplanar connections between I-section beams or plates and circular hollow section columns. The influence of a reinforced concrete filling of the columns and the effect of a composite floor or a steel floor on the behaviour and strength of the connections is also included in the research.
The results of the experimental work are used to calibrate numerical models. Generally, a good agreement is found between the numerical and experimental results. With the calibrated models an extensive parameter investigation has been carried out. The main geometrical parameters are varied as well as the loading conditions.
Analytical models have been derived based upon Togo's Ring model. These models, in combination with the finite element results form the basis of newly developed strength formulae for the investigated connection types.
The strength formulae derived can form the basis for future design recommendations.

KEYWORDS

Static strength, Welded connections, Bolted connections, I-beam to CHS column connections, Experimental tests, Finite element analyses, Analytical models.

SAMENVATTING

De Statische Sterkte van Verbindingen tussen I-profielen en Buisvormige Kolommen
G.D. de Winkel

Onverstijfde verbindingen tussen I-profielen en buisvormige kolommen kunnen zowel in gebouwen als in offshore constructies economisch worden toegepast. De afwezigheid van verstijvingsplaten houdt de fabricagekosten laag, terwijl het in rekening brengen van de verbindingsstijfheid en -sterkte bijdraagt tot een economischer materiaal gebruik.
Door het vullen van de buiskolom met gewapend beton kan de verbindingsstijfheid en -sterkte worden verhoogd. Tevens kan hierdoor voldoende brandwerendheid worden bereikt, zonder dat externe bescherming nodig is.
In geval van toepassing van een staalplaat-betonvloer kan de stijfheid en sterkte van de verbinding verder worden verhoogd.
In de huidige ontwerpregels en -normen ontbreekt voldoende informatie om dit type gelaste balk-kolom verbindingen op een efficiënte wijze te ontwerpen.
Dit onderzoeksprogramma naar het gedrag en de sterkte van verbindingen tussen platen of I-profielen en buiskolommen bevat zowel een experimenteel als numeriek gedeelte. De invloed van een met gewapend beton gevulde buiskolom en het effect van een stalen vloer of staalplaatbeton vloer op het verbindingsgedrag maakt ook deel van het onderzoek.
De resultaten van de experimenten zijn gebruikt om de eindige elementenmodellen te verifiëren en te kalibreren. In het algemeen is er goede overeenstemming gevonden tussen de experimentele en numerieke resultaten. Met de gekalibreerde eindige elementen modellen is een uitgebreide parameterstudie uitgevoerd. Hierbij zijn de belangrijkste geometrische parameters en de belastingscondities gevarieerd.
Analytische modellen zijn afgeleid aan de hand van Togo's Ring model. Deze modellen vormen samen met de eindige elementen resultaten de basis voor sterkte formules voor de onderzochte verbindingen.
De afgeleide sterkte formules kunnen de basis vormen voor toekomstige ontwerprichtlijnen en -normen.

TREFWOORDEN

Statische sterkte, Gelaste verbindingen, Geboute verbindingen, Balk-kolom verbindingen, Experimenteel onderzoek, Eindige elementen analyse, Analytische modellen.

LIST OF SYMBOLS

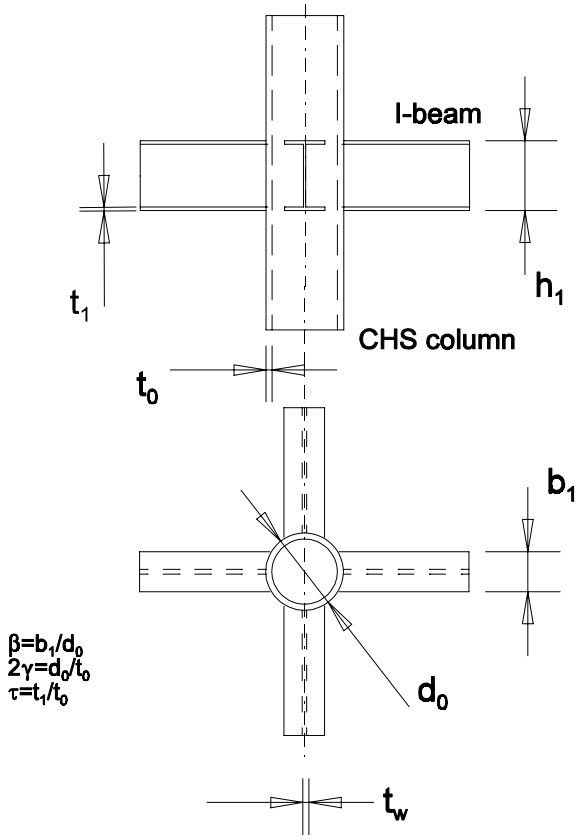

b_1 - Width of the I-beam flange

d_0 - Outer diameter of the CHS column

f(n') - function of the ratio between the total axial load in the column and the squash load

f_c - Concrete cube crushing strength

f_t - Concrete splitting strength

f_u - Ultimate stress

$f_{u,0}$ - Ultimate stress of the column

$f_{u,1}$ - Ultimate stress of the plate or the I-beam flange

$f_{u,w}$ - Ultimate stress of the I-beam web

$f_{y,0}$ - Yield stress of the column

$f_{y,1}$ - Yield stress of the plate or the I-beam flange
$f_{y,w}$ - Yield stress of the I-beam web
h_1 - Height of the I-beam
h_m - Height of the I-beam for the finite element models ($h_m=h_1-t_1$)
k_{bolt} - Stiffness of bolt in axial direction
l_0 - Column length
l_1 - Length of the I-beam
l_{bolt} - Length of the bolt
n' - Ratio between the total axial load in the column and the squash load
r_1 - Corner radius of the beam
r^2 - Coefficient of correlation (regression model)
t_0 - Wall thickness of the column
t_1 - Thickness of plate or I-beam flange
t_w - Beam web thickness
A_{bolt} - Cross-sectional area of the bolt
A_1 - Cross-sectional area of the I-beam or plate
A_0 - Cross-sectional area of the CHS column
A_s - Area of steel reinforcement
A_t - Total area of concrete + steel reinforcement
COV - Coefficient of variation (regression model)
DOF - Number of degrees of freedom of the regression model.
E_c - Modulus of elasticity of concrete
F - F-statistic, to test the significancy of the regression model.
F_1 - Vertical load on in-plane beam
F_2 - Vertical load on out-of-plane beam
M - In-plane bending moment in the I-beam at the column face
M_1 - In-plane bending moment in the in-plane I-beams at the column face due to F_1
M_2 - Bending moment in the out-of-plane I-beams at the column face due to F_2
$M_{Allow.}$ - Allowable in-plane bending moment loading (AIJ Recommendations)
$M_{R.d}$ - Design in-plane bending moment strength
M_u - Ultimate bending moment in the I-beam at the column face
N_1 - Axial force on the in-plane plates or I-beams
N_2 - Axial force on the out-of-plane plates or I-beams
$N_{Allow.}$ - Allowable axial loading (AIJ Recommendations)
$N_{p,0}$ - Squash load of the CHS column (= $A_0.f_{y,0}$)
$N_{p,1}$ - Squash load of the I-beam (= $A_1.f_{y,1}$)

$N_{R.d}$ - Design strength of the axial loading
N_u -Axial force on the plates or I-beams at the ultimate capacity of the connection
$N_{u,1}$ -Axial force on the in-plane plates or I-beams at the ultimate capacity of the connection
$N_{u,2}$ - Axial force on the out-of-plane plates or I-beams at the ultimate capacity of the connection
$R_1..R_8$ - Regression constants
SSE - Total sum of squares (regression model)
α - Two times the column length to column diameter ratio ($2*l_0/d_0$)
β - Plate or I-beam flange width to column diameter ratio (b_1/d_0)
ϵ - Strain or elongation
ϵ_0 - Strain at ultimate stress of the column
$\epsilon_{1,f}$ - Strain at ultimate stress of the I-beam flange
$\epsilon_{1,w}$ - Strain at ultimate stress of the I-beam web
η - beam height to column diameter ratio (h_1/d_0)
ø - Beam rotation at column face
2γ - Column wall thickness to diameter ratio (d_0/t_0)
τ - Plate or I-beam flange thickness to column wall thickness ratio

CHS - Circular Hollow Section
FE - Finite Element
RHS - Rectangular Hollow Section

CIDECT - Comité International pour le Développement et l'Etude de la Construction Tubulaire
ECSC - European Coal and Steel Community
NCF - Stichting Nederlandse Computer Faciliteit
SARA - Stichting Academisch Rekencentrum Amsterdam
STW - Stichting Technische Wetenschappen

TABLE OF CONTENTS

ACKNOWLEDGMENTS V

SUMMARY VII

SAMENVATTING IX

LIST OF SYMBOLS XI

1 INTRODUCTION 1
1.1 General introduction 1
1.2 Scope of work 3
1.3 Definition of various characteristics 6
1.4 Outline of the thesis 7

2 REVIEW OF LITERATURE 9
2.1 Introduction 9
2.2 Test data on plate to CHS column connections 11
2.3 Numerical data on plate to CHS column connections 12
2.4 Test data on web cleat to CHS column connections 13
2.5 Test data on I-beam to CHS column connections 15
2.6 Design recommendations and strength formulae 16
2.6.1 Introduction 16
2.6.2 Strength formulae for plate to CHS column connections 17
2.6.3 Strength formulae for web cleat to CHS column connections 25
2.6.4 Strength formulae for I-beam to CHS column connections 33

3 EXPERIMENTAL TESTS 43
3.1 Introduction 43
3.2 Overview experimental work 43
3.3 Mechanical properties 45
3.3.1 Steel members 45
3.3.2 Weld material 47
3.3.3 Reinforced concrete filling of CHS columns 47
3.3.3.1 Concrete composition for the composite columns 50
3.3.3.2 Concreting operations of the columns 50

3.3.3.3 Properties of cured concrete cubes for the composite columns 51
3.3.4 Composite floor comprising a steel deck (PMF CF46) and a 110 mm deep concrete slab for series 4 tests 51
3.3.4.1 Assembly of the test specimens 53
3.3.4.2 Concrete composition of composite floors 56
3.3.4.3 Concreting operations for the composite floor 59
3.3.4.4 Properties of cured concrete cubes for the composite floors 59
3.4 Measured dimensions 60
3.5 Weld measurements 63
3.6 Test rigs and testing procedures 64
3.6.1 Connections with axially loaded plates and beams and CHS columns (series 1 and 2) 64
3.6.2 Connections with moment loaded beams and CHS columns (series 3 and 4) 66
3.7 Measurements 69
3.7.1 Strains 69
3.7.2 Column indentations for the axially loaded specimens (series 1 and 2) 69
3.7.2.1 Transducer measurements for series 1 70
3.7.2.2 Transducer measurements for series 2 71
3.7.3 Transducer measurements for series 3 72
3.7.4 Transducer measurements for series 4 73
3.7.5 Determination of the beam rotation for series 3 and 4 74
3.8 Results of the experimental tests 75

4 GENERAL DETAILS FOR THE FINITE ELEMENT ANALYSES 79
4.1 Software and hardware used for the finite element modelling and analyses 79
4.2 Method of analyses 79
4.3 Method of modelling 81
4.3.1 Calibration 81
4.3.1.1 General 81
4.3.1.2 Test series 1, axial loading tests 82
4.3.1.3 Test series 2, axial loading interaction tests 83
4.3.1.4 Test series 3, in-plane bending moment tests 84
4.3.1.5 Test series 4, in-plane bending moment tests 84
4.3.2 Parametric investigation 88

5 CALIBRATION OF THE FINITE ELEMENT MODELS 89
5.1 Plate to CHS column connections under axial loading 89
5.1.1 General observations 89
5.1.2 Comparison of experimental and numerical results 92
5.1.3 Concluding remarks 93
5.2 Plate to CHS column connections under axial loading, interaction effects 93
5.2.1 General observations 93
5.2.2 Comparison of experimental and numerical results 95
5.3 I-beam to CHS column connections under in-plane bending moments 96
5.3.1 General observations 96
5.3.2 Comparison of experimental and numerical results 97
5.4 Bolted I-beam to CHS column connections in combination with a steel sheeted concrete floor loaded with in-plane bending moments 99
5.4.1 General observations 99
5.5 General conclusions on the calibration of the finite element models 103

6 PARAMETRIC STUDY 105
6.1 Plate to CHS column connections under axial loading 105
6.1.1 Research programme 105
6.1.2 Results finite element analyses for the uniplanar plate to CHS column connections under axial loading 106
6.1.3 Results of the finite element analyses for the multiplanar plate to CHS column connections under axial loading 113
6.2 Plate to CHS column connections under axial loading, interaction effects 118
6.2.1 Research programme for multiplanar connections 118
6.3 I-beam to CHS column connections under in-plane bending 141
6.3.1 Research programme 141
6.3.2 Uniplanar connections 144
6.3.3 Multiplanar connections 147
6.3.4 Influence of pre-stress of the column 154

7 THE RING MODEL 161
7.1 Introduction 161
7.2 Derivation ring model 162
7.3 Solution ring model for uniplanar connections 166
7.4 Solution ring model for uniplanar loaded multiplanar connections (load ratio J=0) 167
7.5 Solution ring model for multiplanar connections with load case J = 1 168

7.6 Solution ring model for multiplanar connections for $\beta=1/\sqrt{2}$ 169
7.7 Conclusions 170

8 DETERMINATION OF STRENGTH FORMULAE 171
8.1 General 171
8.2 Method used for regression analyses 172
8.3 Plate to CHS column connections under axial loading 174
8.3.1 Uniplanar connections 174
8.3.2 Multiplanar connections 175
8.4 Plate to CHS column connections under axial loading, interaction effects 178
8.4.1 Multiplanar connections, no web influence included 178
8.5 I-beam to CHS column connections under axial loading 180
8.5.1 Influence of the web on the connection strength 180
8.5.2 Multiplanar loading effect 182
8.6 I-beam to CHS column connections under in-plane bending 186
8.6.1 Uniplanar connections 186
8.6.2 Multiplanar connections 186
8.6.3 Influence of pre-stress on the column on the connection strength 190

9 COMPARISON WITH EXISTING EVIDENCE 195
9.1 General 195
9.2 Plate to CHS column connections under axial loading 195
9.3 Uniplanar I-beam to CHS column connections under axial compression load . . . 199
9.4 Uniplanar I-beam to CHS column connections under in-plane bending 200

10 SUMMARY AND CONCLUSIONS 203
10.1 Introduction 203
10.2 General conclusions 203
10.3 Conclusions on the welded plate and I-beam to CHS column connections 204
10.4 Conclusions on the bolted I-beam to CHS column connections with a composite concrete floor 210
10.5 Summary ultimate strength formulae 212
10.6 Recommendations for further research work 217

11 REFERENCES 219

CURRICULUM VITAE 227

LIST OF FIGURES

Figure 1.1 Connection types considered in the experimental research 4
Figure 1.2 Connection types considered in the parametric investigations 5
Figure 2.1 Overview welded plate and I-beam to CHS column connections 10
Figure 2.2 Formulae for TP-1 connections under axial compression load 18
Figure 2.3 Formulae for XP-1 connections under axial compression load 18
Figure 2.4 Comparison formulae for TP-1 connections under axial compression load with existing test data (Table 2.1) 19
Figure 2.5 Comparison formulae for XP-1 connections under axial compression load with existing test data (Table 2.1) 20
Figure 2.6 Formulae for TP-1 connections under axial tension load 22
Figure 2.7 Formulae for XP-1 connections under axial tension load 22
Figure 2.8 Comparison formulae for TP-1 connections under axial tension load with existing test data (Table 2.1) 23
Figure 2.9 Comparison formulae for XP-1 connections under axial tension load with existing test data (Table 2.1) 24
Figure 2.10 Formulae for TP-2 connections under axial compression load 26
Figure 2.11 Formulae for XP-2 connections under axial compression load 26
Figure 2.12 Comparison formulae for TP-2 connections under axial compression load with existing test data (Table 2.3) 27
Figure 2.13 Comparison formulae for XP-2 connections under axial compression load with existing test data (Table 2.3) 28
Figure 2.14 Formulae for TP-2 connections under axial tension load 30
Figure 2.15 Formulae for XP-2 connections under axial tension load 30
Figure 2.16 Comparison formulae for TP-2 connections under axial tension load with existing test data (Table 2.3) 31
Figure 2.17 Comparison formulae for XP-2 connections under axial tension load with existing test data (Table 2.3) 32
Figure 2.18 Formulae for TP-4 connections under axial compression load 34
Figure 2.19 Formulae for XP-4 connections under axial compression load 34
Figure 2.20 Comparison formulae for TP-4 connections under axial compression load with existing test data (Table 2.4) 35
Figure 2.21 Comparison formulae for XP-4 connections under axial compression load with existing test data (Table 2.4) 36
Figure 2.22 Formulae for TP-4 connections under axial tension load 38
Figure 2.23 Formulae for XP-4 connections under axial tension load 38

Figure 2.24 Comparison formulae for XP-4 connections under axial compression load with existing test data (Table 2.4) 39
Figure 2.25 Formulae for TP-4 connections under in-plane bending moments 41
Figure 2.26 Formulae for XP-4 connections under in-plane bending moments 41
Figure 2.27 Comparison formulae for XP-4 connections under in-plane bending moments with existing test data (Table 2.4) 42
Figure 3.1 Welding details 45
Figure 3.2 CHS column with reinforced concrete filling 49
Figure 3.3 Configuration test specimen series 4 52
Figure 3.4 Reinforcement composite floor 52
Figure 3.5 Cross-section composite floor 53
Figure 3.6 Weld measurements for test series 1 and 2 64
Figure 3.7 Test rig for test 3C3 with load ratio -1. 67
Figure 3.8 Locations displacement transducers for test series 1 70
Figure 3.9 Location displacement transducers for test series 2 71
Figure 3.10 Location displacement transducers for series 3 72
Figure 3.11 Location displacement transducers for series 4 73
Figure 3.12 Definition of the connection rotation 74
Figure 4.1 Stress-strain curves 80
Figure 4.2 Weld modelling for test 3C3 81
Figure 4.3 Symmetry planes and boundary conditions for models 1C1 and 1C3 83
Figure 4.4 Symmetry planes and boundary conditions for model 1C2, 1C4-1C8 83
Figure 4.5 Symmetry planes and boundary conditions for model 2C1-2C3 83
Figure 4.6 Symmetry planes and boundary conditions for model 3C1-4C4 83
Figure 4.7 Finite element model of test series 4 84
Figure 4.8 Bolt slip, experimentally determined and the slip for the numerical model . 85
Figure 4.9 Modelling of the composite steel-concrete floor 86
Figure 4.10 Tension softening 87
Figure 5.1 Deformed finite element mesh for model 1C2 89
Figure 5.2 Deformed finite element mesh for model 1C3 89
Figure 5.3 Deformed finite element mesh for model 1C5 89
Figure 5.4 Experimental and numerical load-deformation curves for 1C1 90
Figure 5.5 Experimental and numerical load-deformation curves for 1C2 90
Figure 5.6 Experimental and numerical load-deformation curves for 1C3 90
Figure 5.7 Experimental and numerical load-deformation curves for 1C4 90
Figure 5.8 Experimental and numerical load-deformation curves for 1C5 91
Figure 5.9 Experimental and numerical load-deformation curves for 1C6 91

Figure 5.10 Experimental and numerical load-deformation curves for 1C7 91
Figure 5.11 Experimental and numerical load-deformation curves for 1C8 91
Figure 5.12 Experimental and numerical load-deformation curves for 2C1 94
Figure 5.13 Experimental and numerical load-deformation curves for 2C2 94
Figure 5.14 Experimental and numerical load-deformation curves for 2C3 94
Figure 5.15 Deformed finite element model for test 2C3 94
Figure 5.16 Deformed finite element model for test 3C2 96
Figure 5.17 Deformed finite element model for test 3C3 97
Figure 5.18 Experimental and numerical moment-rotation curves for test 3C3 98
Figure 5.19 Experimental and numerical moment- rotation curves for test 3C1 98
Figure 5.20 Experimental and numerical moment-rotation curves for test 3C4 98
Figure 5.21 Experimental and numerical moment- rotation curves for test 3C2 98
Figure 5.22 Experimental and numerical moment-rotation curves for test 4C1 101
Figure 5.23 Experimental and numerical moment-rotation curves for test 4C2 101
Figure 5.24 Experimental and numerical moment-rotation curves for test 4C3 101
Figure 5.25 Experimental and numerical moment-rotation curves for test 4C4 101
Figure 5.26 Experimental and numerical moment-rotation curves, with numerical lower and upper bound 101
Figure 5.27 Comparison experimental cracking pattern with the numerical cracking strain pattern of test 4C1 102
Figure 5.28 Comparison experimental cracking pattern with the numerical cracking strain pattern of test 4C2 102
Figure 5.29 Comparison experimental cracking pattern with the numerical cracking strain pattern of test 4C3 102
Figure 5.30 Comparison experimental cracking pattern with the numerical cracking strain pattern of test 4C4 102
Figure 6.1 Main dimensions FE model for plate to CHS column connections 105
Figure 6.2 Deformed finite element mesh of model XUP1-58 108
Figure 6.3 Load-displacement curve for model XUP1-02 109
Figure 6.4 Load-displacement curve for model XUP1-08 109
Figure 6.5 Load-displacement curve for model XUP1-04 109
Figure 6.6 Load-displacement curve for model XUP1-10 109
Figure 6.7 Load-displacement curve for model XUP1-06 109
Figure 6.8 Load-displacement curve for model XUP1-12 109
Figure 6.9 Load-displacement curve for model XUP1-38 110
Figure 6.10 Load-displacement curve for model XUP1-50 110
Figure 6.11 Load-displacement curve for model XUP1-40 110

Figure 6.12 Load-displacement curve for model XUP1-52 110
Figure 6.13 Load-displacement curve for model XUP1-42 110
Figure 6.14 Load-displacement curve for model XUP1-54 110
Figure 6.15 Load-displacement curve for model XUP1-14 111
Figure 6.16 Load-displacement curve for model XUP1-56 111
Figure 6.17 Load-displacement curve for model XUP1-34 111
Figure 6.18 Load-displacement curve for model XUP1-58 111
Figure 6.19 Load-displacement curve for model XUP1-36 111
Figure 6.20 Load-displacement curve for model XUP1-60 111
Figure 6.21 Load-displacement curve for model XUP1-62 112
Figure 6.22 Load-displacement curve for model XUP1-64 112
Figure 6.23 Load-displacement curve for model XUP1-66 112
Figure 6.24 Deformed finite element mesh model XXP1-40 with load ratio +1.0 113
Figure 6.25 Load-displacement curves for model XXP1-02 115
Figure 6.26 Load-displacement curves for model XXP1-08 115
Figure 6.27 Load-displacement curves for model XXP1-04 115
Figure 6.28 Load-displacement curves for model XXP1-10 115
Figure 6.29 Load-displacement curves for model XXP1-06 115
Figure 6.30 Load-displacement curves for model XXP1-12 115
Figure 6.31 Load-displacement curves for model XXP1-38 116
Figure 6.32 Load-displacement curves for model XXP1-50 116
Figure 6.33 Load-displacement curves for model XXP1-40 116
Figure 6.34 Load-displacement curves for model XXP1-52 116
Figure 6.35 Load-displacement curves for model XXP1-42 116
Figure 6.36 Load-displacement curves for model XXP1-54 116
Figure 6.37 Load-displacement curves for model XXP1-14 117
Figure 6.38 Load-displacement curves for model XXP1-34 117
Figure 6.39 Load-displacement curves for model XXP1-36 117
Figure 6.40 Main dimensions FE model for axially loaded I-beam to CHS column connections 118
Figure 6.41 Deformed finite element mesh of model XXP2-72 (with web) for load ratio +0.5 119
Figure 6.42 Deformed finite element mesh of model XXP2-72 (without web) for load ratio +1.0 119
Figure 6.43 Load-displacement curves for model XXP2-20 124
Figure 6.44 Load-displacement curves for model XXP2-02 124
Figure 6.45 Load-displacement curves for model XXP2-22 124

Figure 6.46 Load-displacement curves for model XXP2-04 124
Figure 6.47 Load-displacement curves for model XXP2-24 124
Figure 6.48 Load-displacement curves for model XXP2-06 124
Figure 6.49 Load-displacement curves for model XXP2-62 125
Figure 6.50 Load-displacement curves for model XXP2-26 125
Figure 6.51 Load-displacement curves for model XXP2-64 125
Figure 6.52 Load-displacement curves for model XXP2-28 125
Figure 6.53 Load-displacement curves for model XXP2-66 125
Figure 6.54 Load-displacement curves for model XXP2-30 125
Figure 6.55 Load-displacement curves for model XXP2-08 126
Figure 6.56 Load-displacement curves for model XXP2-68 126
Figure 6.57 Load-displacement curves for model XXP2-10 126
Figure 6.58 Load-displacement curves for model XXP2-70 126
Figure 6.59 Load-displacement curves for model XXP2-12 126
Figure 6.60 Load-displacement curves for model XXP2-72 126
Figure 6.61 Load-displacement curves for model XXP2-44 127
Figure 6.62 Load-displacement curves for model XXP2-38 127
Figure 6.63 Load-displacement curves for model XXP2-46 127
Figure 6.64 Load-displacement curves for model XXP2-40 127
Figure 6.65 Load-displacement curves for model XXP2-48 127
Figure 6.66 Load-displacement curves for model XXP2-42 127
Figure 6.67 Load-displacement curves for model XXP2-80 128
Figure 6.68 Load-displacement curves for model XXP2-50 128
Figure 6.69 Load-displacement curves for model XXP2-82 128
Figure 6.70 Load-displacement curves for model XXP2-52 128
Figure 6.71 Load-displacement curves for model XXP2-84 128
Figure 6.72 Load-displacement curves for model XXP2-54 128
Figure 6.73 Load-displacement curves for model XXP2-56 129
Figure 6.74 Load-displacement curves for model XXP2-86 129
Figure 6.75 Load-displacement curves for model XXP2-58 129
Figure 6.76 Load-displacement curves for model XXP2-88 129
Figure 6.77 Load-displacement curves for model XXP2-60 129
Figure 6.78 Load-displacement curves for model XXP2-90 129
Figure 6.79 Load-displacement curves for model XXP2-32 130
Figure 6.80 Load-displacement curves for model XXP2-14 130
Figure 6.81 Load-displacement curves for model XXP2-34 130
Figure 6.82 Load-displacement curves for model XXP2-16 130

Figure 6.83 Load-displacement curves for model XXP2-36 130
Figure 6.84 Load-displacement curves for model XXP2-18 130
Figure 6.85 Load-displacement curves for model XXP2-74 131
Figure 6.86 Load-displacement curves for model XXP2-76 131
Figure 6.87 Load-displacement curves for model XXP2-78 131
Figure 6.88 Load-displacement curves for model XXP2-20 133
Figure 6.89 Load-displacement curves for model XXP2-02 133
Figure 6.90 Load-displacement curves for model XXP2-22 133
Figure 6.91 Load-displacement curves for model XXP2-04 133
Figure 6.92 Load-displacement curves for model XXP2-24 133
Figure 6.93 Load-displacement curves for model XXP2-06 133
Figure 6.94 Load-displacement curves for model XXP2-62 134
Figure 6.95 Load-displacement curves for model XXP2-26 134
Figure 6.96 Load-displacement curves for model XXP2-64 134
Figure 6.97 Load-displacement curves for model XXP2-28 134
Figure 6.98 Load-displacement curves for model XXP2-66 134
Figure 6.99 Load-displacement curves for model XXP2-30 134
Figure 6.100 Load-displacement curves for model XXP2-08 135
Figure 6.101 Load-displacement curves for model XXP2-68 135
Figure 6.102 Load-displacement curves for model XXP2-10 135
Figure 6.103 Load-displacement curves for model XXP2-70 135
Figure 6.104 Load-displacement curves for model XXP2-12 135
Figure 6.105 Load-displacement curves for model XXP2-72 135
Figure 6.106 Load-displacement curves for model XXP2-44 136
Figure 6.107 Load-displacement curves for model XXP2-38 136
Figure 6.108 Load-displacement curves for model XXP2-46 136
Figure 6.109 Load-displacement curves for model XXP2-40 136
Figure 6.110 Load-displacement curves for model XXP2-48 136
Figure 6.111 Load-displacement curves for model XXP2-42 136
Figure 6.112 Load-displacement curves for model XXP2-80 137
Figure 6.113 Load-displacement curves for model XXP2-50 137
Figure 6.114 Load-displacement curves for model XXP2-82 137
Figure 6.115 Load-displacement curves for model XXP2-52 137
Figure 6.116 Load-displacement curves for model XXP2-84 137
Figure 6.117 Load-displacement curves for model XXP2-54 137
Figure 6.118 Load-displacement curves for model XXP2-56 138
Figure 6.119 Load-displacement curves for model XXP2-86 138

Figure 6.120 Load-displacement curves for model XXP2-58 138
Figure 6.121 Load-displacement curves for model XXP2-88 138
Figure 6.122 Load-displacement curves for model XXP2-60 138
Figure 6.123 Load-displacement curves for model XXP2-90 138
Figure 6.124 Load-displacement curves for model XXP2-32 139
Figure 6.125 Load-displacement curves for model XXP2-14 139
Figure 6.126 Load-displacement curves for model XXP2-34 139
Figure 6.127 Load-displacement curves for model XXP2-16 139
Figure 6.128 Load-displacement curves for model XXP2-36 139
Figure 6.129 Load-displacement curves for model XXP2-18 139
Figure 6.130 Load-displacement curves for model XXP2-74 140
Figure 6.131 Load-displacement curves for model XXP2-76 140
Figure 6.132 Load-displacement curves for model XXP2-78 140
Figure 6.133 Main dimensions FE model for I-beam to CHS column connections loaded with in-plane bending moments 141
Figure 6.134 Deformed finite element mesh of model XXP4-342U 144
Figure 6.135 Deformed finite element mesh of model XXP4-38 for load ratio +1.0 147
Figure 6.136 Load-displacement curves for model XXP4-20 150
Figure 6.137 Load-displacement curves for model XXP4-02 150
Figure 6.138 Load-displacement curves for model XXP4-22 150
Figure 6.139 Load-displacement curves for model XXP4-04 150
Figure 6.140 Load-displacement curves for model XXP4-24 150
Figure 6.141 Load-displacement curves for model XXP4-06 150
Figure 6.142 Load-displacement curves for model XXP4-25 151
Figure 6.143 Load-displacement curves for model XXP4-07 151
Figure 6.144 Load-displacement curves for model XXP4-26 151
Figure 6.145 Load-displacement curves for model XXP4-08 151
Figure 6.146 Load-displacement curves for model XXP4-28 151
Figure 6.147 Load-displacement curves for model XXP4-10 151
Figure 6.148 Load-displacement curves for model XXP4-44 152
Figure 6.149 Load-displacement curves for model XXP4-38 152
Figure 6.150 Load-displacement curves for model XXP4-46 152
Figure 6.151 Load-displacement curves for model XXP4-40 152
Figure 6.152 Load-displacement curves for model XXP4-48 152
Figure 6.153 Load-displacement curves for model XXP4-42 152
Figure 6.154 Load-displacement curves for model XXP4-32 153
Figure 6.155 Load-displacement curves for model XXP4-14 153

Figure 6.156 Load-displacement curves for model XXP4-34 153
Figure 6.157 Load-displacement curves for model XXP4-09 153
Figure 6.158 Load-displacement curves for model XXP4-36 153
Figure 6.159 Load-displacement curves for model XXP4-11 153
Figure 6.160 Load-displacement curves for model XUP4-20 156
Figure 6.161 Load-displacement curves for model XUP4-02 156
Figure 6.162 Load-displacement curves for model XUP4-22 156
Figure 6.163 Load-displacement curves for model XUP4-04 156
Figure 6.164 Load-displacement curves for model XUP4-24 156
Figure 6.165 Load-displacement curves for model XUP4-06 156
Figure 6.166 Load-displacement curves for model XUP4-25 157
Figure 6.167 Load-displacement curves for model XUP4-07 157
Figure 6.168 Load-displacement curves for model XUP4-26 157
Figure 6.169 Load-displacement curves for model XUP4-08 157
Figure 6.170 Load-displacement curves for model XUP4-28 157
Figure 6.171 Load-displacement curves for model XUP4-10 157
Figure 6.172 Load-displacement curves for model XUP4-44 158
Figure 6.173 Load-displacement curves for model XUP4-38 158
Figure 6.174 Load-displacement curves for model XUP4-46 158
Figure 6.175 Load-displacement curves for model XUP4-40 158
Figure 6.176 Load-displacement curves for model XUP4-48 158
Figure 6.177 Load-displacement curves for model XUP4-42 158
Figure 6.178 Load-displacement curves for model XUP4-32 159
Figure 6.179 Load-displacement curves for model XUP4-14 159
Figure 6.180 Load-displacement curves for model XUP4-34 159
Figure 6.181 Load-displacement curves for model XUP4-09 159
Figure 6.182 Load-displacement curves for model XUP4-36 159
Figure 6.183 Load-displacement curves for model XUP4-11 159
Figure 7.1 Ring model 161
Figure 7.2 Ring model for $\beta = 0.25$, multiplanar loading influence 164
Figure 7.3 Ring model for $\beta = 0.40$, multiplanar loading influence 165
Figure 7.4 Ring model for $\beta = 0.65$, multiplanar loading influence 165
Figure 7.5 Ring model for the uniplanar connections 166
Figure 7.6 Ring model for load ratio J = 0 167
Figure 7.7 Ring model for load ratio J = 1 168
Figure 7.8 Ring model for $\beta = \frac{1}{2}\sqrt{2}$ 169

Figure 8.1 Results regression analysis uniplanar plate to CHS column connections under axial loading 175
Figure 8.2 Axially loaded multiplanar plate to CHS column connections with load ratio J = 0 176
Figure 8.3 Multiplanar axially loaded plate to CHS column connections, multiplanar loading influence 177
Figure 8.4 Interaction effects of plates to CHS column connections loaded with axial loading, according to Eq. 8.8 179
Figure 8.5 Interaction effects of plate to CHS column connections loaded with axial loading, according to Eq. 8.9 180
Figure 8.6 Results regression analysis, influence of the presence of the web on the connections strength (Eq. 8.10) 181
Figure 8.7 Results regression analysis for the interaction effects of I-beam to CHS column connections loaded with axial loading, enhanced model with web influence included (Eq. 8.11) 182
Figure 8.8 Results regression analysis for the multiplanar loading effects for 2γ=15 (Eq. 8.12) 184
Figure 8.9 Results regression analysis for the multiplanar loading effects for 2γ=30 (Eq. 8.12) 185
Figure 8.10 Results regression analysis for the multiplanar loading effects for 2γ=45 (Eq. 8.12) 185
Figure 8.11 Results regression analysis for uniplanar I-beam to CHS column connections loaded with in-plane bending moments (Eq. 8.16) 186
Figure 8.12 Results regression analysis for multiplanar I-beam to CHS column connections loaded with in-plane bending moments for load ratio J = 0 (Eq. 8.17) 187
Figure 8.13 Results regression analysis for multiplanar I-beam to CHS column connections loaded with in-plane bending moments for 2γ=15, multiplanar loading effects (Eq. 8.18) 188
Figure 8.14 Results regression analysis for multiplanar I-beam to CHS column connections loaded with in-plane bending moments for 2γ=30, multiplanar loading effects (Eq. 8.18) 189
Figure 8.15 Results regression analysis for multiplanar I-beam to CHS column connections loaded with in-plane bending moments for 2γ=45, multiplanar loading effects (Eq. 8.18) 189
Figure 8.16 Results regression analysis, influence pre-stress on the connection strength for 2γ=15 (Eq. 8.19) 192

Figure 8.17 Results regression analysis, influence pre-stress on the connection strength for 2γ=15 (Eq. 8.19) 192
Figure 8.18 Results regression analysis, influence pre-stress on the connection strength for 2γ=30 (Eq. 8.19) 193
Figure 8.19 Results regression analysis, influence pre-stress on the connection strength for 2γ=30 (Eq. 8.19) 193
Figure 8.20 Results regression analysis, influence pre-stress on the connection strength for 2γ=45 (Eq. 8.19) 194
Figure 8.21 Results regression analysis, influence pre-stress on the connection strength for 2γ=45 (Eq. 8.19) 194
Figure 9.1 Comparison strength formulae with test and finite element results for Uniplanar Plate to CHS column connections loaded with axial loading . . . 196
Figure 9.2 Comparison strength formula Eq. 8.5 with test results for Uniplanar plate to CHS column connections under axial loading 197
Figure 9.3 Comparison of the strength formula Eq. 8.5 with existing numerical results (see Table 2.2) for Uniplanar plate to CHS column connections under axial loading 197
Figure 9.4 Comparison of the combined strength formula Eq. 8.6 and 8.7 with the existing numerical results (see Table 2.2) for Multiplanar plate to CHS column connections under axial loading 198
Figure 9.5 Comparison combined strength formula Eq. 8.5, Eq.8.8 and Eq. 8.10. with test results for Uniplanar I-beam to CHS column connections loaded under axial compression loading 199
Figure 9.6 Comparison of the strength formulae with existing test results for Uniplanar I-beam to CHS column connections loaded with in-plane bending moments 201
Figure 9.7 Comparison of the strength formula Eq. 8.16 with existing test results for Uniplanar I-beam to CHS column connections loaded with in-plane bending moments 201

LIST OF TABLES

Table 2.1 Experimental tests on plate to CHS column connections 11
Table 2.2 Numerical data on plate to CHS column connections 12
Table 2.3 Test data on web cleat to CHS column connections 14
Table 2.4 Test data on I-beam to CHS column connections 15
Table 2.5 Strength formulae for plate to CHS column connections under axial compression load 17
Table 2.6 Strength formulae for plate to CHS column connections under axial tension load 21
Table 2.7 Strength formulae for web cleat to CHS column connections under axial compression load 25
Table 2.8 Strength formulae for web cleat to CHS column connections under axial tension load 29
Table 2.9 Strength formulae for I-beam to CHS column connections under axial compression load 33
Table 2.10 Strength formulae for I-beam to CHS column connections under axial tension load 37
Table 2.11 Strength formulae for I-beam to CHS column connections under in-plane bending moments 40
Table 3.1 Overview experimental research programme (1) 44
Table 3.2 Overview experimental research programme (2) 45
Table 3.3 Mechanical properties determined with tensile coupon tests (dp5). 46
Table 3.4 Mechanical properties determined with tensile coupon tests (dp5). 47
Table 3.5 Concrete cube properties for composite columns 48
Table 3.6 Concrete cube properties of batch 1 used for composite floor of specimens 4C1 and 4C2 57
Table 3.7 Concrete cube properties of batch 2 used for composite floor of specimens 4C3 and 4C4 58
Table 3.8 Nominal dimensions test specimen 60
Table 3.9 Averaged measurements for each stock number from CHS columns 61
Table 3.10 Averaged measurements for each stock number from IPE sections 62
Table 3.11 Averaged measurements for each stock number from Plates 120*10, 170*12 and steel floor 63
Table 3.12 Experimental results for test series 1 and 2 76
Table 3.13 Experimental results for test series 3 78
Table 3.14 Experimental results for test series 4 78
Table 5.1 Comparison experimental and numerical results of test series 1 92

Table 5.2 Comparison experimental and numerical results of test series 2 94
Table 5.3 Comparison experimental and numerical results of test series 3 97
Table 5.4 Comparison experimental and numerical results of test series 4 100
Table 6.1 Overview of the research programme uniplanar plate to CHS column connections 106
Table 6.2 Overview of the research programme multiplanar plate to CHS column connections 106
Table 6.3 Geometrical and material characteristics of the plate to CHS column connections 107
Table 6.4 Finite element results of the uniplanar plate to CHS column connections . 108
Table 6.5 Results finite element analyses multiplanar plate to CHS column connections 114
Table 6.6 Overview of the research programme on multiplanar I-beam to CHS column connections loaded with axial loading 120
Table 6.7 Geometrical and material characteristics of the I-beam to CHS column connections loaded with axial loading 121
Table 6.8 Finite element results of I-beam to CHS under axial loading, influence presence of web 123
Table 6.9 Results of the finite element analyses on multiplanar I-beam to CHS column connections under axial loading 132
Table 6.10 Overview of the research programme on uniplanar and multiplanar XXP4 connections 142
Table 6.11 Overview research programme uniplanar and multiplanar I-beam to CHS column connections loaded with in-plane bending moments 143
Table 6.12 Results finite element analyses uniplanar I-beam to CHS column connections loaded with in-plane bending moments 146
Table 6.13 Results of the finite element analyses on multiplanar I-beam to CHS column connections loaded with in-plane bending moments 149
Table 6.14 Results finite element analyses uniplanar I-beam to CHS column connections loaded with in-plane bending moments and a pre-stress on the column. 155
Table 8.1 Results of the regression analyses for uniplanar plate to CHS column connections loaded with axial loading 174
Table 8.2 Results of the regression analyses for multiplanar plate to CHS column connections under axial loading with load ratio J=0 175
Table 8.3 Results of the regression analyses for multiplanar axial loading 177
Table 8.4 Results of the regression analyses for interaction effects, simple model . . . 178

Table 8.5 Results of the regression analyses for interaction effects, enhanced model 180
Table 8.6 Results of the regression analyses, influence presence of the web 181
Table 8.7 Results of the regression analysis for interaction effects, enhanced model . 182
Table 8.8 Results of the regression analysis for multiplanar loading influence 184
Table 8.9 Results of the regression analyses for in-plane bending 186
Table 8.10 Results of the regression analyses for in-plane bending with load ratio J=0 187
Table 8.11 Results of the regression analyses for in-plane bending, multiplanar loading effects 188
Table 8.12 Results of the regression analyses for pre-stress effects 190
Table 8.13 Results of the regression analyses for pre-stress effects, based upon the total axial load in the column 191
Table 10.1 Main results and conclusions for axially loaded plate to CHS column connections 206
Table 10.2 Main results and conclusions for axially loaded I-beam to CHS column connections 207
Table 10.3 Main results and conclusions for I-beam to CHS column connections loaded with in-plane bending moments 208
Table 10.4 Main results and conclusions for I-beam to CHS column connections loaded with in-plane bending moments and a pre-loading on the column . 209
Table 10.5 Main results and conclusions for bolted I-beam to CHS column connections with a composite concrete floor and loaded with in-plane bending moments 211
Table 10.6 The ultimate strength formula for axially loaded plate to CHS column connections 213
Table 10.7 The ultimate strength formula for axially loaded I-beam (or plates at two levels) to CHS column connections 214
Table 10.8 The ultimate strength formula for I-beam to CHS column connections loaded by in-plane bending moments 215
Table 10.9 The ultimate strength formula for bolted I-beam to CHS column connections with a composite concrete floor loaded by in-plane bending moments 216

1 INTRODUCTION

1.1 General introduction

This research investigates the static strength and the static behaviour of multiplanar connections between I-section beams and circular hollow section columns.
Semi-rigid connections between I-section beams and tubular columns can be used economically for buildings and offshore structures. The lack of stiffening plates allows the fabrication of these connections in a cost-effective way. By filling the tubular column with reinforced concrete the fire resistance can be increased and the composite column thus obtained also provides an increased joint strength.
For designers, design guidance is necessary to use this kind of connection in practice. Currently, design guidance for multiplanar I-beam to tubular column connections is non-existent, while design guidance for uniplanar I-beam to tubular column connections is limited.
If on top of the I-beams steel or composite floors are used, these can be used to increase the strength and stiffness of the connection.
In the design of steel structures up to now, the I-beam to tubular column connections are either regarded as pinned or rigid. Pinned connections are in general fabrication-friendly, but not economical in terms of material use. Rigid full strength connections result in material savings at the expense of careful detailing of stiffeners to develop the full moment capacity of the members.
Semi-rigid connections can provide optimal material use in combination with economical fabrication.
Within the framework of the ECSC research programme 7210/SA-611 "Semi-rigid connections between I-beams and tubular columns" experiments, including detail tests, interaction tests and overall tests have been carried out at the laboratories of Delft University of Technology and TNO Building and Construction Research.
The aim of the experimental work is to provide detailed test data to be used for calibrating numerical models.
The numerical work with finite element simulations has been carried out in the framework of the Stichting Technische Wetenschappen (Dutch Technology Foundation) research programme DCT 99.1904 "Semi-rigid beam-column connections".
In addition, the work was financially supported by Comité International pour le Développement et l'Etude de la Construction Tubulaire (CIDECT) within the framework of project 5AX.
The main objective of this research is to provide evidence and strength functions for the static strength of multiplanar I-beam to CHS column connections that can form the basis for future

design codes, like EUROCODE 3. In the recent past, similar research programmes have been carried out by Van der Vegte [16] on the static strength of CHS to CHS connections, by Yu [18] on RHS to RHS connections and by Lu [14] on I-beam to RHS connections.

1.2 Scope of work

The scope of work is as follows:

- A review of literature, to consider existing test data and design rules for the investigated connections.
- Simple detail testing on axially loaded multiplanar plate to CHS (Circular Hollow Section) column connections, to simulate the behaviour of I-beam flanges. (See Figure 1.1 a).
- Interaction tests on axially loaded multiplanar I-beam to CHS column connections to investigate the influence of the beam height on the connection strength (see Figure 1.1 b).
- Overall tests on welded multiplanar I-beam to CHS column connections loaded with bending moments (see Figure 1.1 c). The influence on the static behaviour of the presents of a steel floor welded on top of the I-beams is also investigated (Figure 1.1 d).
- Overall tests on bolted multiplanar I-beam to CHS column connections in combination with a composite steel-concrete floor, loaded with in-plane bending moments (see Figure 1.1 e).
- The influence of a concrete filling of the column on the structural behaviour.
- The influence of a steel floor on the structural connection behaviour of welded I-beam to CHS column connections.
- The calibration of finite element (FE) models for all experimental tests.
- Parametric (FE) study on axially loaded plate to CHS column connections, both for uniplanar and multiplanar connections (see Figures 1.2 a and b).
- Parametric (FE) study on axially loaded multiplanar I-beam to CHS column connections, where the influence of the web is investigated separately (see Figures 1.2 c and d).
- Parametric study on uniplanar and multiplanar connections between I-beam to CHS columns loaded with in-plane bending moments (see Figures 2.1 e and f). For the uniplanar connections the influence of a prestress on the column is also investigated.
- The derivation of analytical strength formulae using the ring model approach.
- The determination of strength formulae for the investigated connections on the basis of the analytically derived strength formulae and the finite element results, using non-linear regression analyses.

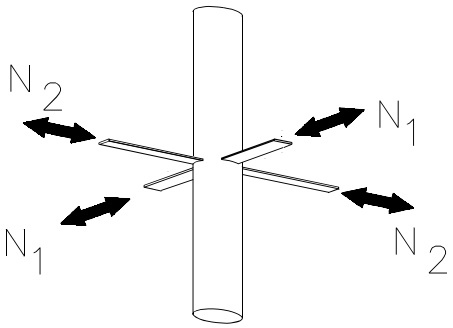

a. Multiplanar plate to CHS column connections loaded with axial loading

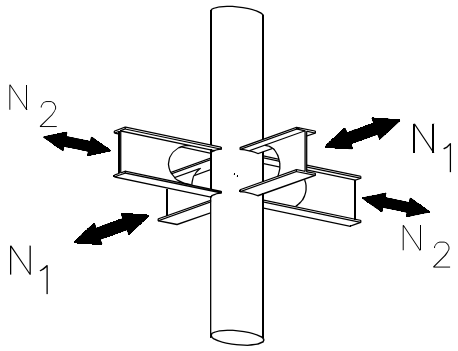

b. Multiplanar I-beam (no web) to CHS column connections loaded with axial loading

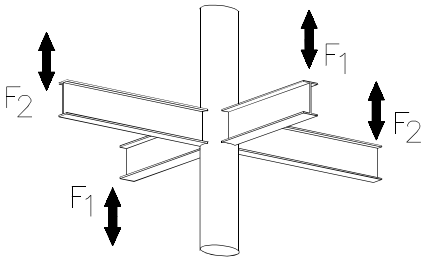

c. Multiplanar I-beam to CHS column connections loaded with in-plane bending

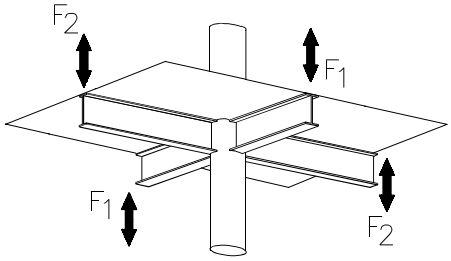

d. Multiplanar I-beam to CHS column connections with steel-floor loaded with in-plane bending

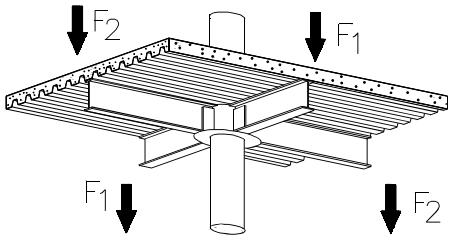

e. Bolted multiplanar I-beam to CHS column connections in combination with a composite steel-concrete floor loaded with in-plane bending

Figure 1.1 Connection types considered in the experimental research

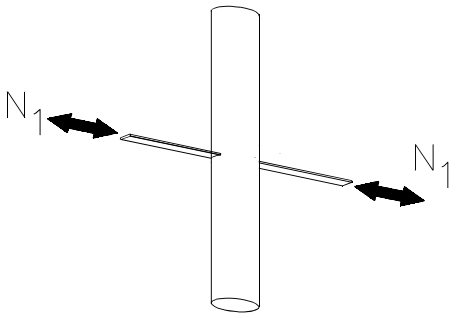

a. Uniplanar plate to CHS column connections loaded with axial loading

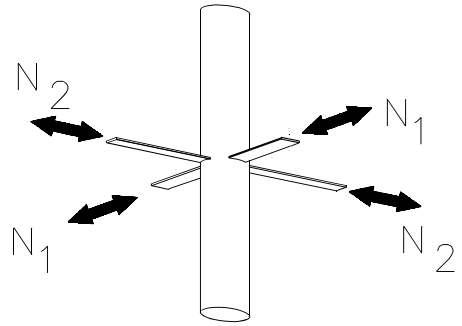

b. Multiplanar plate to CHS column connections loaded with axial loading

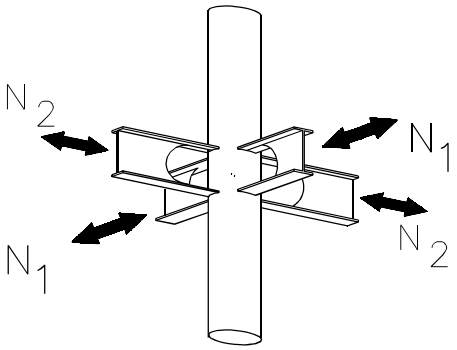

c. Multiplanar I-beam (no web) to CHS column connections loaded with axial loading

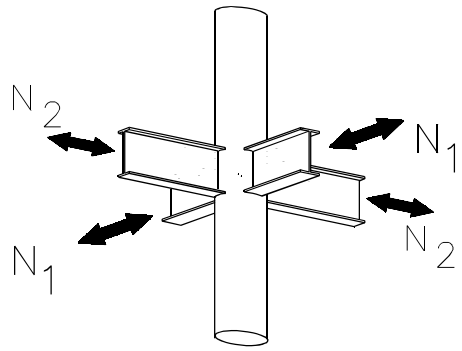

d. Multiplanar I-beam to CHS column connections loaded with axial loading

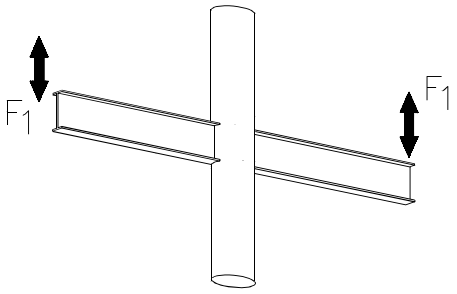

e. Uniplanar I-beam to CHS column connections loaded with in-plane bending moments

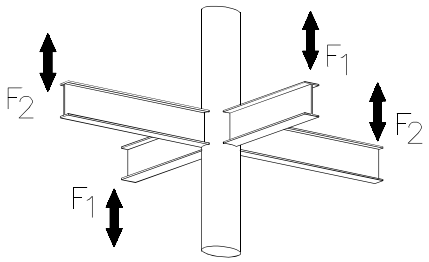

f. Multiplanar I-beam to CHS column connections loaded with in-plane bending moments

Figure 1.2 Connection types considered in the parametric investigations

1.3 Definition of various characteristics

Throughout the text, several characteristics are mentioned that need to be clearly defined. These are listed below:

Indentation

Indentation is defined as the average displacement of a beam or plate into the column face under axial load.

Average indentation

Average indentation is defined as the mean value of the indentations of the two plates or beams in the same plane (on either side of a column).

Moment at the column face

The moment at the column face is defined as the reaction at a beam support multiplied by the distance between the support and the column face, for moment loaded connections.

M_1 is the moment on the in-plane I-beams, M_2 is the moment on the out-of-plane I-beams, in case of multiplanar loading.

Average moment at the column face

The average moment at the column face is defined as the mean value of the moments (at the column face) for the two beams in the same plane (on either side of a column) for moment loaded connections.

Beam rotation

The beam rotation is defined as the in-plane rotation of the beam from its original axis for moment loaded connections. The method of measurement is described in section 3.7.5.

Average beam rotation

The average beam rotation is defined as the mean value of the beam rotations of the beams in the same plane (on either side of the column)

Ultimate load

As ultimate load is taken the first maximum in the load-displacement or moment rotation curve. In case without a maximum, the load is taken at an average indentation equal to 3% of d_0 [13]. For in-plane bending, this deformation limit is equal to $0.06*\eta$ with a maximum of 0.1 rad.

1.4 Outline of the thesis

In Chapter 2, a brief overview is given of the existing evidence on the static strength of plate and I-beam to CHS column connections.
The experimental tests and the test results are presented and discussed in Chapter 3.
The method for the finite element modelling as used for the calibration of the finite element models with the experiments and as used for the parametric investigations is described in Chapter 4.
Chapter 5 presents the calibration of the finite element models with the experiments.
The numerically and experimentally obtained results are compared and discussed.
In Chapter 6, the results of the parametric investigations are presented in tables with the ultimate strengths and in figures with the load-displacement and the moment-rotation curves.
In Chapter 7, the analytical ring model is described. With the obtained general solution, the solutions are derived for uniplanar connections, uniplanar loaded multiplanar connections and multiplanar loaded connections. These solutions are presented in formulae as well as in graphs.
In Chapter 8, the strength formulae are developed for the investigated connections on the basis of the formulae of the ring model and the finite element results. In several cases, both simple and more complex, but more accurate, formula are given.
The derived strength formulae are compared with existing evidence in Chapter 9.
All obtained results are summarized in Chapter 10.

2 REVIEW OF LITERATURE

2.1 Introduction

This review of literature describes the information available on the static strength of unstiffened I-beam to hollow section column connections. The list of references can be found in Chapter 11. The main topics covered in this survey are plate to CHS column connections and I-beam to CHS column connections. The welded connection types included in this survey of literature are shown in Figure 2.1.

In general, the available amount of evidence on unstiffened multiplanar I-beam to circular hollow section columns is very limited. More literature is available on the static strength of uniplanar connections, especially from Japan.
Although, there is no generally accepted type coding for plate or I-beam to CHS column connections, the coding used in this chapter is the same as used in many Japanese publications.
The coding is TP-1, XP-1 and XXP-1 for uniplanar T- and X-joints respectively multiplanar X-joints consisting of plate to CHS column connections as shown in Figure 2.1.
The coding is TP-2, XP-2 and XXP-2 for uniplanar T- and X-joints respectively multiplanar X-joints consisting of web cleat to CHS column connections, and the coding is TP-4, XP-4 and XXP-4 for uniplanar T- and X-joints respectively multiplanar X-joints consisting of I-beam to CHS column connections, as also shown in Figure 2.1.
In the sections hereafter, experimental test and numerical finite element results of these types of connections are given, as well as strength and design formula.
The strength of the connections as listed in the tables of this chapter is the ultimate strength as obtained from the tests.

The load cases of the tests are marked in the tables as follows:

comp: axial compression loading on the plate or I-beams
tens: axial tension loading on the plate or I-beams
bend: in-plane bending moments on the I-beams

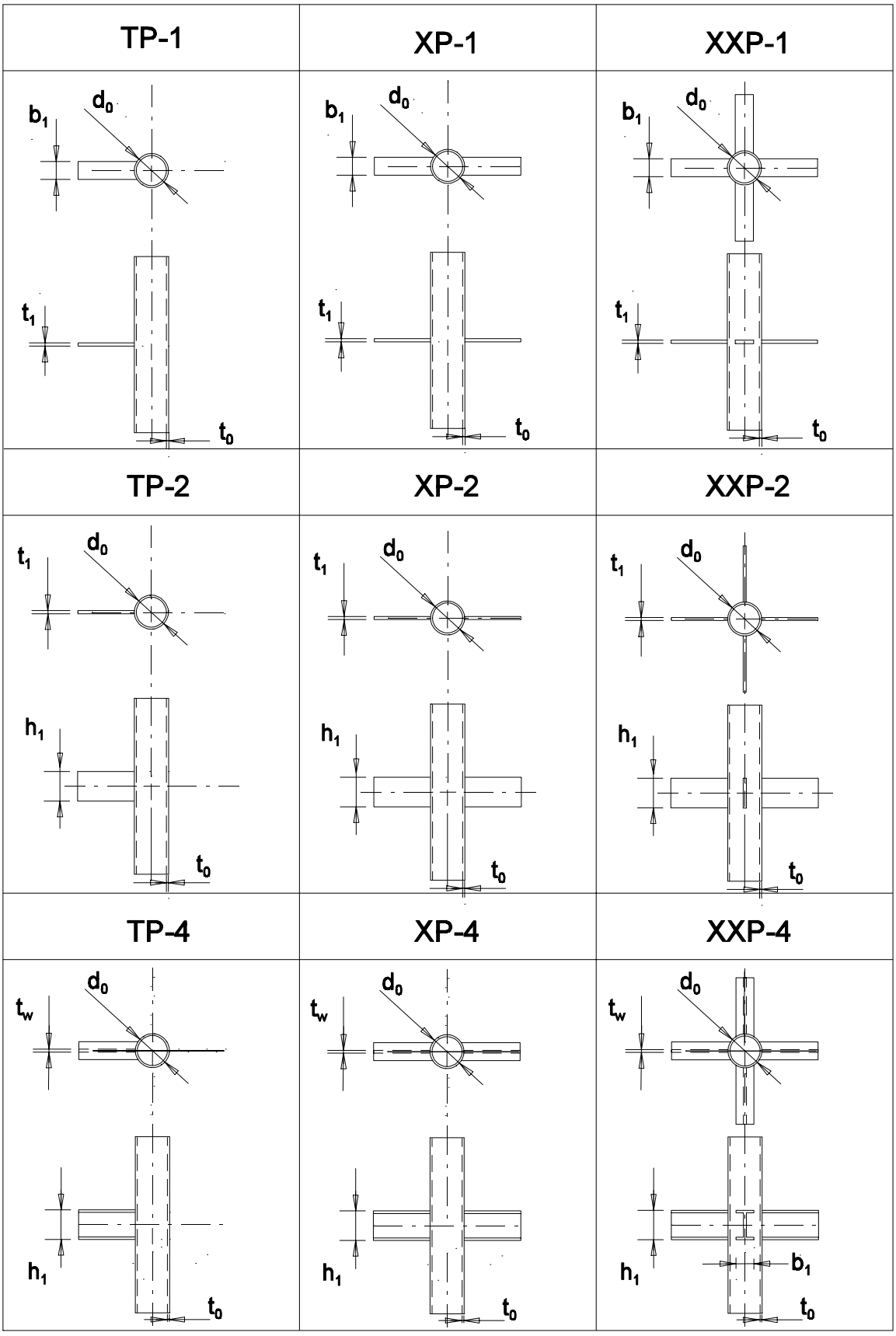

Figure 2.1 Overview welded plate and I-beam to CHS column connections

2.2 Test data on plate to CHS column connections

In Japan, several tests were carried out on axially loaded T-joint plate to CHS column connections (TP1), see Figure 2.1. Compression tests were reported by Akiyama et al. [30] and Kurobane et al. [40]. Tensile tests were reported by Akiyama et al. [30].
Compression tests on uniplanar X-joint plate to CHS column connections (XP1) were carried out by Kurobane et al. [40] and Makino et al [46]. Tension tests on XP1 joints were reported by Kanatani et al. [37] and Naka et al. [47].
One tensile test on a multiplanar plate to CHS column connection (XXP1) has been carried out by Van der Broek et al. [12].
The experimental results are listed in Table 2.1.

Table 2.1 Experimental tests on plate to CHS column connections

TYPE	load	Reference	β	2γ	load ratio	$f_{y,0}$	$N_{u,exp.}$	$N_u/(t_0^2*f_{y,0})$
						[MPa]	[kN]	
TP1	comp	[40]	0.500	31.769		314.0	124.0	14.604
TP1	comp	[40]	0.700	31.769		314.0	174.0	20.552
TP1	comp	[40]	0.900	31.769		314.0	256.0	30.257
TP1	comp	[40]	0.696	41.856		350.0	107.0	27.533
TP1	comp	[40]	0.895	41.856		350.0	188.0	48.150
TP1	comp	[40]	0.259	71.896		438.0	60.0	7.050
TP1	comp	[40]	0.500	71.896		438.0	107.0	12.448
TP1	comp	[40]	0.707	71.896		438.0	154.0	17.916
TP1	comp	[40]	0.259	90.535		450.0	68.2	5.943
TP1	comp	[40]	0.276	93.116		420.0	75.0	7.407
TP1	comp	[40]	0.500	90.535		450.0	116.0	10.108
TP1	comp	[40]	0.501	91.440		420.0	130.0	12.381
TP1	comp	[40]	0.707	90.535		450.0	186.1	16.216
TP1	comp	[40]	0.707	93.689		430.0	225.0	21.972
TP1	comp	[30]	0.260	91.000		440.0	68.2	6.200
TP1	comp	[30]	0.502	91.000		440.0	116.0	10.545
TP1	comp	[30]	0.711	91.000		440.0	186.0	16.909
TP1	comp	[30]	0.260	72.000		440.0	60.6	7.114
TP1	comp	[30]	0.503	72.000		440.0	107.0	12.561
TP1	comp	[30]	0.796	72.000	-	440.0	154.0	18.079
TP1	tens	[30]	0.260	91.000	-	440.0	184.0	16.727
TP1	tens	[30]	0.502	91.000	-	440.0	256.0	23.273
TP1	tens	[30]	0.711	91.000	-	440.0	317.0	28.818
TP1	tens	[30]	0.260	72.000	-	440.0	158.0	18.548
TP1	tens	[30]	0.503	72.000	-	440.0	190.0	22.305
TP1	tens	[30]	0.796	72.000	-	440.0	394.0	46.253
XP1	comp	[40]	0.500	31.769	-	314.0	94.8	11.165
XP1	comp	[40]	0.700	31.769	-	314.0	126.3	14.875
XP1	comp	[40]	0.900	31.769	-	314.0	191.0	22.496
XP1	comp	[46]	0.520	29.661	-	488.0	409.2	10.306
XP1	tens	[37]	0.460	36.050	-	353.0	165.0	12.984
XP1	tens	[37]	0.460	27.038	-	355.0	265.0	11.664
XP1	tens	[37]	0.460	21.630	-	357.0	328.0	9.188

TYPE	load	Reference	β	2γ	load ratio	$f_{y,0}$	$N_{u,exp.}$	$N_u/(t_0^2*f_{y,0})$
						[MPa]	[kN]	
XP1	tens	[37]	0.460	18.025	-	349.0	448.0	8.914
XP1	tens	[47]	0.800	31.769	-	314.0	260.0	30.622
XP1	tens	[47]	0.800	31.769	-	314.0	296.0	34.862
XP1	tens	[47]	0.800	31.769	-	314.0	284.0	33.449
XXP1	tens	[12]	0.367	40.640	1.00	268.0	400.0	14.925

2.3 Numerical data on plate to CHS column connections

A limited numerical parameter study on uniplanar and multiplanar plate to CHS column connections (XP1 and XXP1) has been carried out by Van der Broek et al. [12]. The results of this parameter study are listed in Table 2.2. The finite element programme DIANA was used for the calculations.

Table 2.2 Numerical data on plate to CHS column connections

TYPE	load	Reference	β	2γ	τ	load ratio	$f_{,y0}$	$N_{u.}$	$N_u/(t_0^2*f_{y,0})$
							[MPa]	[kN]	
XP1	comp	[12]	0.369	25.40	1.00	-	355.0	542.10	5.97
XP1	comp	[12]	0.369	32.50	0.96	-	355.0	352.50	6.35
XP1	comp	[12]	0.369	40.60	1.00	-	355.0	237.80	6.70
XP1	comp	[12]	0.615	40.60	1.00	-	355.0	393.70	11.09
XXP1	mpl	[12]	0.369	25.40	0.94	1.00	355.0	596.90	6.37
XXP1	mpl	[12]	0.369	25.40	0.94	0.50	355.0	583.20	6.42
XXP1	comp	[12]	0.369	25.40	0.94	0.00	355.0	542.40	5.97
XXP1	mpl	[12]	0.369	25.40	0.94	-0.50	355.0	492.60	5.42
XXP1	mpl	[12]	0.369	25.40	0.94	1.00	355.0	429.90	4.73
XXP1	mpl	[12]	0.369	32.50	0.96	1.00	355.0	397.60	7.17
XXP1	mpl	[12]	0.369	32.50	0.96	0.50	355.0	381.30	6.87
XXP1	comp	[12]	0.369	32.50	0.96	0.00	355.0	350.70	6.32
XXP1	mpl	[12]	0.369	32.50	0.96	-0.50	355.0	317.80	5.73
XXP1	mpl	[12]	0.369	32.50	0.96	-1.00	355.0	280.10	5.05
XXP1	mpl	[12]	0.369	40.60	1.00	1.00	355.0	275.00	7.76
XXP1	mpl	[12]	0.369	40.60	1.00	0.50	355.0	260.30	7.33
XXP1	comp	[12]	0.369	40.60	1.00	0.00	355.0	237.50	6.69
XXP1	mpl	[12]	0.369	40.60	1.00	-0.50	355.0	214.30	6.04
XXP1	mpl	[12]	0.369	40.60	1.00	-1.00	355.0	189.90	5.35
XXP1	tens	[12]	0.369	40.60	1.00	0.00	355.0	478.30	13.47

2.4 Test data on web cleat to CHS column connections

Experimental tests on web cleat to CHS column connections (TP2 and XP2, see Figure 2.1) were reported by Kurobane et al [40], Akiyama et al [30] and Makino et al [46]. In these test programmes both T-joints and X-joints are included, loaded with axial loading on the web cleats. Kurobane's tests also include some tests with in-plane bending moments. See Table 2.3.

Table 2.3 Test data on web cleat to CHS column connections

TYPE	load	Reference	η	2γ	$f_{y,0}$	$N_{u.}$	$N_u/(t_0^2*f_{y,0})$
					[MPa]	[kN]	
TP2	comp	[40]	1.000	31.77	314.0	111.50	13.13
TP2	comp	[40]	1.998	31.77	314.0	135.00	15.90
TP2	comp	[40]	0.314	71.41	436.0	56.60	6.53
TP2	comp	[40]	0.628	71.09	433.0	67.10	7.72
TP2	comp	[40]	0.942	71.90	418.0	80.10	9.76
TP2	comp	[40]	0.328	93.12	445.0	62.80	5.85
TP2	comp	[40]	0.984	93.12	445.0	92.80	8.65
TP2	comp	[40]	0.547	93.12	445.0	72.00	6.71
TP2	comp	[46]	0.521	29.61	488.0	294.50	7.42
TP2	comp	[30]	0.329	93.00	450.0	145.00	13.42
TP2	comp	[30]	0.549	93.00	450.0	126.00	11.66
TP2	comp	[30]	0.988	93.00	450.0	170.00	15.73
TP2	comp	[30]	0.316	72.00	440.0	114.00	13.38
TP2	comp	[30]	0.626	71.00	430.0	120.00	13.78
TP2	comp	[30]	0.947	72.00	420.0	135.00	16.60
TP2	tens	[30]	0.329	97.00	450.0	183.00	18.41
TP2	tens	[30]	0.548	97.00	450.0	223.00	22.43
TP2	tens	[30]	0.987	97.00	450.0	223.00	22.43
TP2	tens	[30]	0.316	72.00	440.0	183.00	21.48
TP2	tens	[30]	0.631	72.00	440.0	153.00	17.96
TP2	tens	[30]	0.947	72.00	440.0	203.00	23.83
XP2	comp	[40]	1.000	33.42	386.0	34.00	9.53
XP2	comp	[40]	1.500	33.42	386.0	38.10	10.68
XP2	comp	[40]	2.000	33.42	386.0	42.00	11.77
XP2	comp	[40]	1.000	24.72	447.0	67.40	8.93
XP2	comp	[40]	1.500	24.72	447.0	77.40	10.25
XP2	comp	[40]	2.000	24.72	447.0	85.50	11.32
XP2	comp	[40]	1.000	17.82	360.0	95.00	8.12
XP2	comp	[40]	1.500	17.82	360.0	120.50	10.30
XP2	comp	[40]	2.000	17.82	360.0	138.00	11.80
XP2	comp	[40]	1.000	28.50	376.0	56.50	9.35
XP2	comp	[40]	2.000	28.22	376.0	68.00	11.03
XP2	tens	[40]	1.000	32.77	370.0	88.00	24.75
XP2	tens	[40]	1.500	32.77	370.0	100.00	28.12
XP2	tens	[40]	2.000	32.77	370.0	161.00	45.28
XP2	tens	[40]	1.000	24.72	370.0	167.00	26.72
XP2	tens	[40]	1.500	24.72	370.0	155.00	24.80
XP2	tens	[40]	2.000	24.72	370.0	178.00	28.48
XP2	tens	[40]	1.000	17.82	370.0	177.00	14.72
XP2	tens	[40]	1.500	17.82	370.0	232.00	19.30
XP2	tens	[40]	2.000	17.82	370.0	310.00	25.79
XP2	tens	[30]	0.329	93.00	440.0	130.00	12.31
XP2	tens	[30]	0.549	93.00	440.0	160.00	15.15
XP2	tens	[30]	0.988	93.00	440.0	180.00	17.04
XP2	tens	[30]	0.313	71.00	430.0	150.00	17.23
XP2	tens	[30]	0.626	71.00	430.0	160.00	18.38
XP2	tens	[30]	0.939	71.00	430.0	160.00	18.38

TYPE	load	Reference	η	2γ	$f_{y,0}$	$M_{u.}$	$M_u/(t_0^2*f_{y,0}*h_1)$
						[kNm]	
XP2	bend	[40]	1.000	31.77	314.0	9.874	7.04
XP2	bend	[40]	2.000	31.77	314.0	21.92	7.81
XP2	bend	[40]	1.000	49.46	350.0	4.80	7.44
XP2	bend	[40]	2.000	49.46	350.0	10.09	7.82

2.5 Test data on I-beam to CHS column connections

Experimental tests on axially loaded I-beam to CHS column connections were reported by Kurobane et al [40] and Makino et al [45]. Tests on this type of connections loaded with in-plane bending were reported by Kamba et al [35], Makino [46] and Naka et al [47]. The experimental tests are listed in Table 2.4.

Table 2.4 Test data on I-beam to CHS column connections

TYPE	load	Reference	β	2γ	η	τ	$f_{y,0}$	$N_{u.}$	$N_u/(t_0^2*f_{y,0})$
							[MPa]	[kN]	
TP4	comp	[40]	0.700	31.77	2.000		314.0	265.50	31.27
TP4	comp	[40]	0.800	31.77	1.000		314.0	290.50	34.21
XP4	comp	[40]	0.700	31.77	1.500		314.0	182.50	21.49
XP4	comp	[40]	0.900	31.77	1.500		314.0	270.00	31.80
XP4	comp	[40]	0.800	31.77	1.000		314.0	215.50	25.38
XP4	comp	[40]	0.800	31.77	1.000		314.0	200.50	23.61
XP4	comp	[40]	0.867	26.71	1.000		376.0	180.00	26.13
XP4	comp	[40]	0.867	28.22	2.000		376.0	195.00	31.62
XP4	tens	[45]	0.867	27.74	1.000		376.0	248.00	38.86
XP4	tens	[45]	0.867	28.58	2.000		376.0	300.60	49.97
XP4	tens	[45]	0.870	23.84	2.000		367.0	226.00	60.13
TYPE	load	Reference	β	2γ	η	τ	$f_{y,0}$	$M_{u.}$	$M_u/(t_0^2*f_{y,0}*h_1)$
							[MPa]	[kNm]	
XP4	bend	[47]	0.700	31.77	1.000		314.0	28.49	20.31
XP4	bend	[47]	0.700	31.77	2.000		314.0	44.88	16.00
XP4	bend	[47]	0.832	41.62	2.377		350.0	21.89	16.97
XP4	bend	[47]	0.900	31.77	1.000		314.0	33.19	23.66
XP4	bend	[47]	0.900	31.77	2.000		314.0	63.98	22.81
XP4	bend	[35]	0.694	27.04	1.387		386.0	106.54	14.38
XP4	bend	[35]	0.694	37.29	1.387		355.0	71.27	19.89
XP4	bend	[46]	0.450	50.82	0.930		403.0	19.50	13.24
XP4	bend	[46]	0.460	50.82	1.850		403.0	35.50	12.11

2.6 Design recommendations and strength formulae

2.6.1 Introduction

Currently, a limited amount of design formulae exists for plate or I-beam to CHS column connections. All these design formulae are based upon the Japanese tests as described in the previous sections. The most complete set of design formulae can be found in the "Recommendations for the design and fabrication of tubular structures in steel" of AIJ in Japan [1]. Other sets of design formulae can be found in the CIDECT " Design guide for circular hollow section (CHS) joints under predominantly static loading" [11] and in Wardenier's "Hollow Section Joints"[19]. Strength formulae for the ultimate strength based on the Japanese tests are published by Makino et al [45].
In the sections hereafter, an overview is given of the currently available design and strength formulae for the connection types as shown in Figure 2.1.
For each connection type and loading a separate table is given where the corresponding T-, and X-joints are combined in the same table. Each table is followed by a page with figures showing the formulae graphically. To reduce the number of lines in the figures, only lines are shown for a fixed $2\gamma=30$, $\alpha=12$ and $\beta=\eta/2$. The last constraint defines an I-beam with a height of two times the beam width.
The formulae are also graphically compared with the available test data. No test data for comparison is available for T-joint connections between I-beams and CHS columns (TP-4), loaded with axial tension load or loaded with in-plane bending moments.

A few remarks have to be made for the comparisons. The AIJ recommendations allow for the given formulae for cold formed sections an approximately 1.375 higher yield stress than for hot formed sections with a comparable steel grade. This gives some problems for the comparison of the test data with the strength formulae, since the measured yield stress is used as input for the formulae. Since most of the Japanese tests were done using cold formed sections, in the figures separate reference lines are given for cold and hot formed sections. The AIJ formulae give values for the maximum connection strength, so the test data should be equal or higher than the AIJ formulae.
The formulae of Makino are based upon the mean values of the test result and does not give a lower bound for the connection strength. Therefore, these formulae can be non-conservative.
The formulae of Wardenier and CIDECT give design values and should give values that are approximately 20% lower than the test results. In cases the connection deformation is governing, these formulae may give lower values.

2.6.2 Strength formulae for plate to CHS column connections

Table 2.5 Strength formulae for plate to CHS column connections under axial compression load

TP1-compression	Ref.	Strength formula
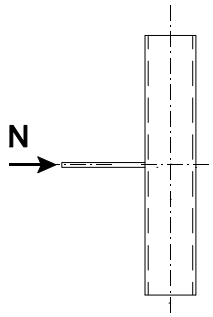	[1]	$N_{Allow.}=0.75\cdot(1+4.9\cdot\beta^2)\cdot\gamma^{0.2}\cdot f_{y,0}\cdot t_0^2$ (2.1)
	[45]	$N_u=4.83\cdot(1+4.94\cdot\beta^2)\cdot(2\gamma)^{0.233}\cdot(\frac{\alpha}{2})^{-0.45}\cdot f_{y,0}\cdot t_0^2$ (2.2)
	[19]	$N_{R.d}=(4.2+21.3\cdot\beta^2)\cdot f_{y,0}\cdot t_0^2\cdot f(n')$ (2.3)
	[11]	$N_{R.d}=\frac{5}{1-0.81\cdot\beta}\cdot f_{y,0}\cdot t_0^2\cdot f(n')$ (2.4)
XP1-compression		
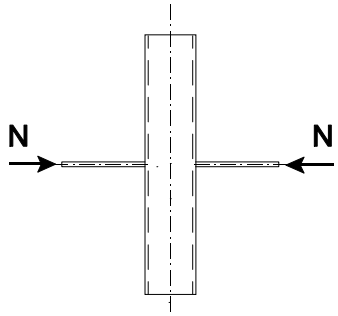	[1]	$N_{Allow.}=2.8\cdot\frac{1}{1-0.81\cdot\beta}\cdot\gamma^{-0.1}\cdot f_{y,0}\cdot t_0^2$ (2.5)
	[45]	$N_u=\frac{7.23}{1-0.813\cdot\beta}\cdot(2\gamma)^{-0.032}\cdot f_{y,0}\cdot t_0^2$ (2.6)
	[19]	$N_{R.d}=\frac{5.2}{1-0.81\cdot\beta}\cdot f_{y,0}\cdot t_0^2\cdot f(n')$ (2.7)
	[11]	$N_{Allow.}=\frac{5}{1-0.81\cdot\beta}\cdot f_{y,0}\cdot t_0^2\cdot f(n')$ (2.8)

Notes:

Eq. 2.1 and 2.5: According to [1], the ultimate load can be obtained with: $N_u = 2.14*N_{Allow}$.

Eq. 2.2 : α= two times the column length to column diameter ratio.

The CIDECT design guide uses the same formulae for both the TP-1 and XP-1 joints.

The function f(n) in the formulae of [19] and [11] defines the reduction of the connection strength due to a pre-loading on the column. Wardenier [19] proposes to use Togo's formula for this function :

f(n') = 1.2 - 0.5 |n| for n<-0.4 and

f(n') = 1.0 for n>-0.4, where n is the ratio between the total axial load in the column and the squash load of the column.

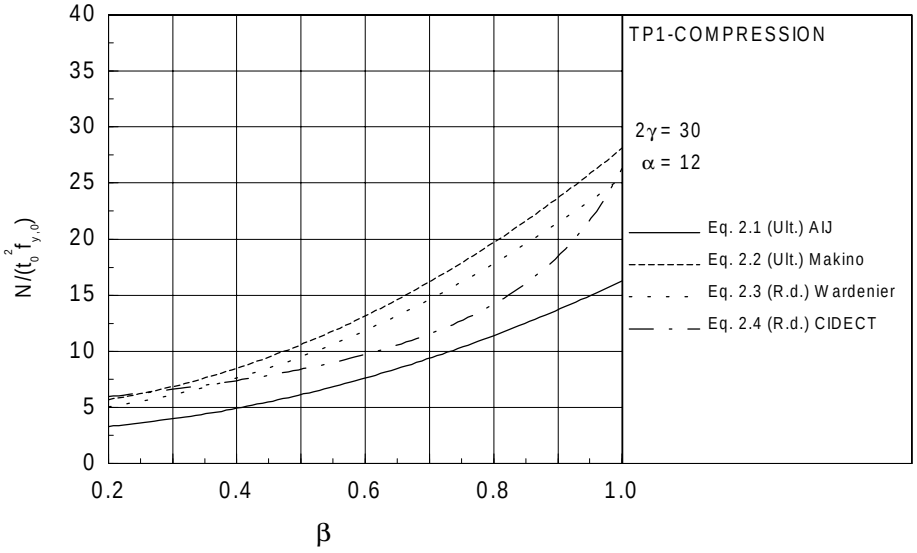

Figure 2.2 Formulae for TP-1 connections under axial compression load

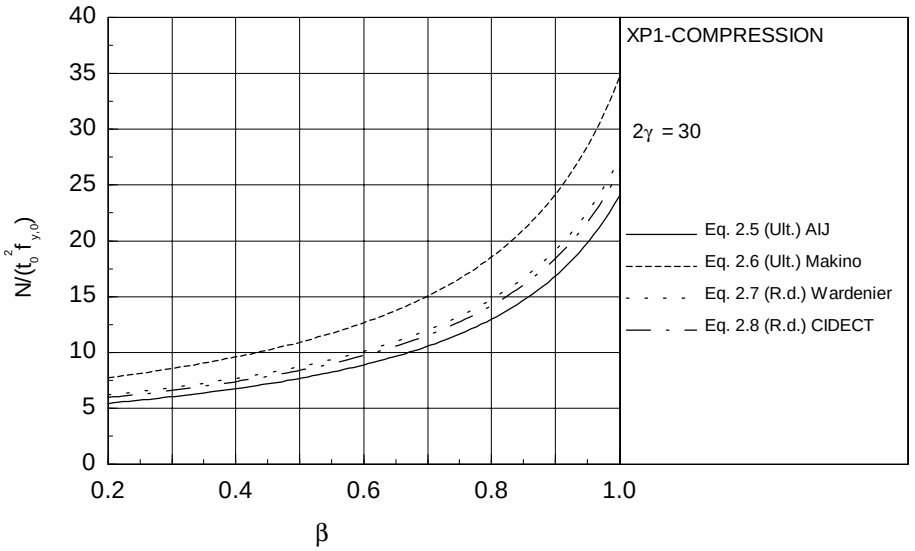

Figure 2.3 Formulae for XP-1 connections under axial compression load

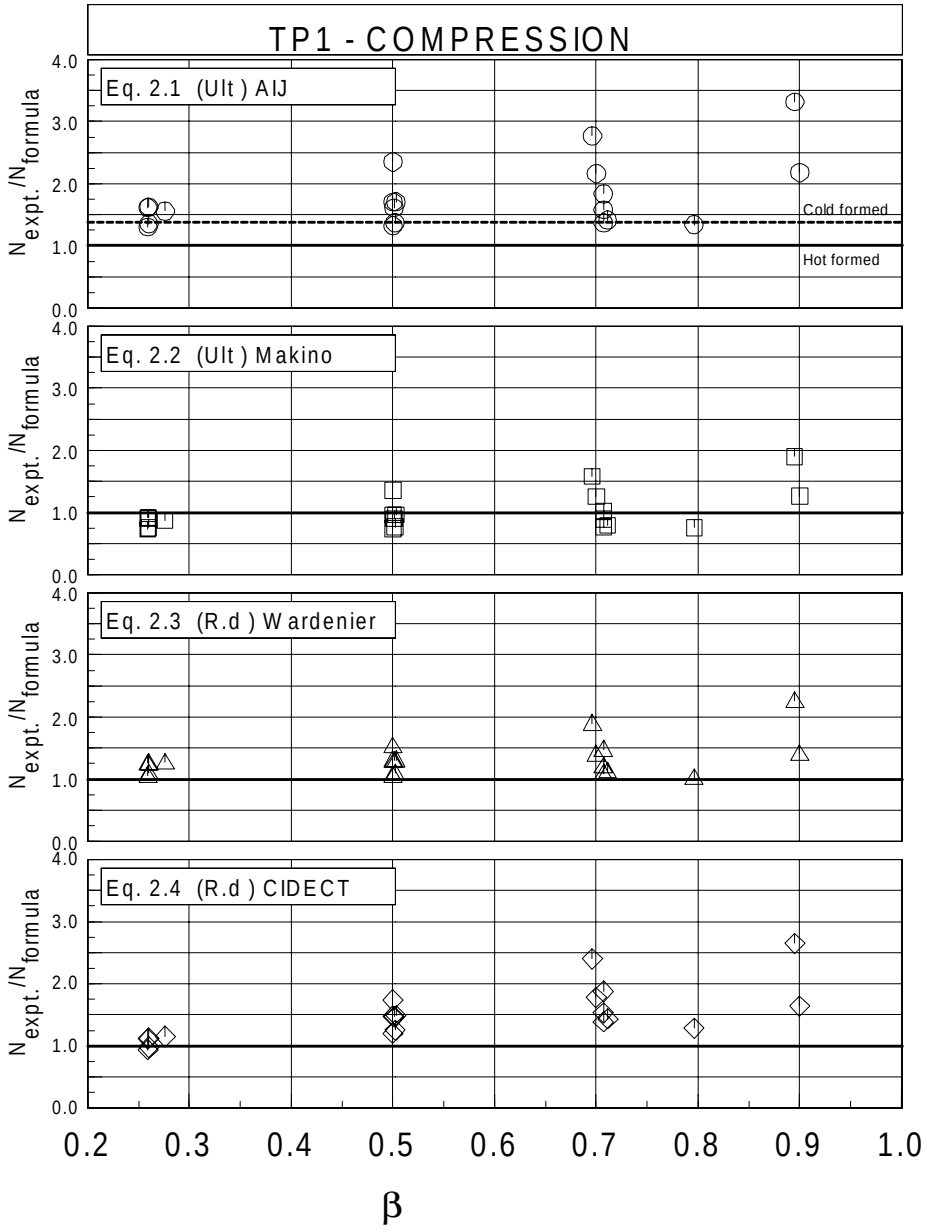

Figure 2.4 Comparison formulae for TP-1 connections under axial compression load with existing test data (Table 2.1)

Remarks:

As shown in Figure 2.4, all formulae have a comparable agreement with the test results. The formulae are conservative for data points with a large β -ration in combination with a large 2γ-ratio.

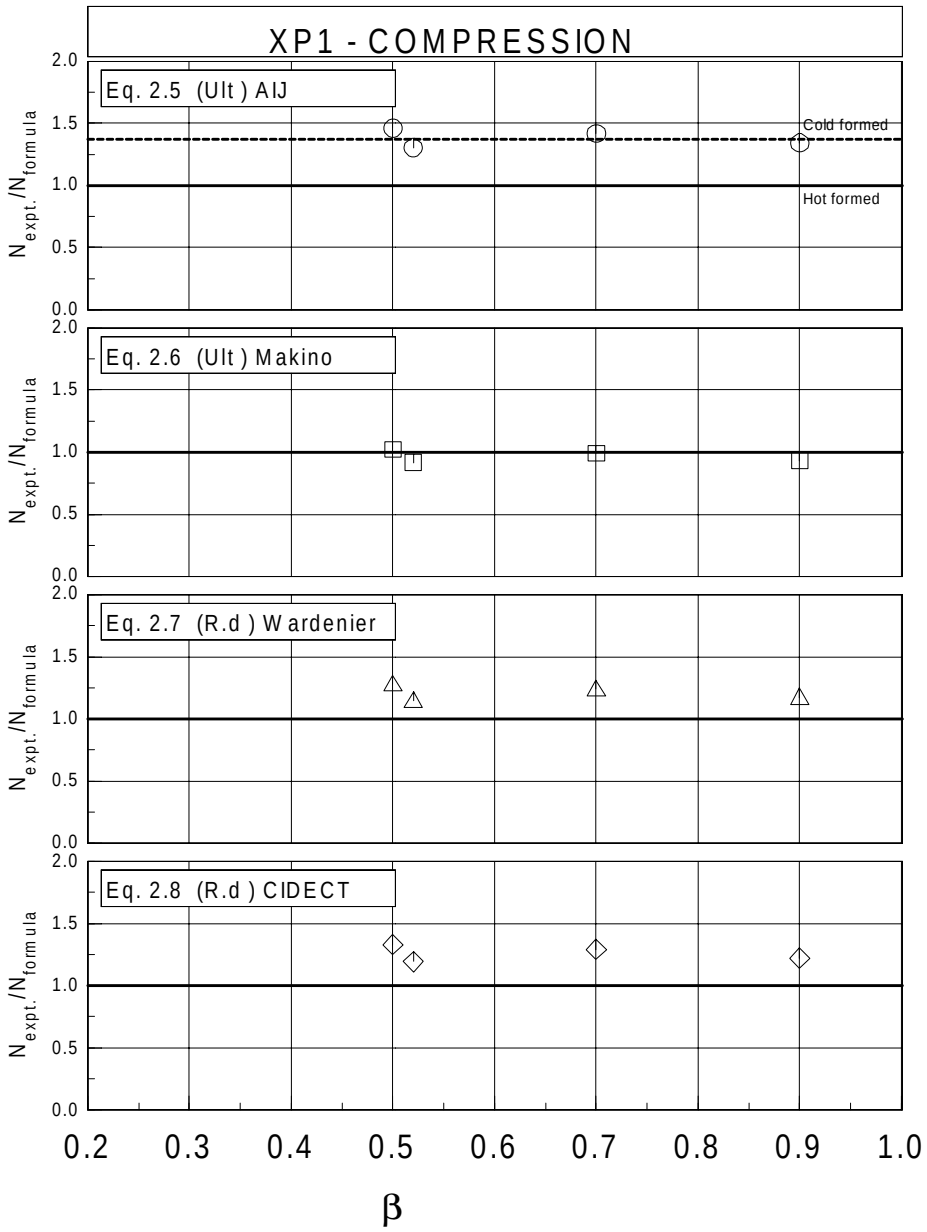

Figure 2.5 Comparison formulae for XP-1 connections under axial compression load with existing test data (Table 2.1)

Remarks:

As shown in Figure 2.5, all formulae show a good agreement with the test results, however the amount of test results and the geometrical parameter ranges covered are very limited.

Table 2.6 Strength formulae for plate to CHS column connections under axial tension load

TP1-tension	Ref.	Strength formula
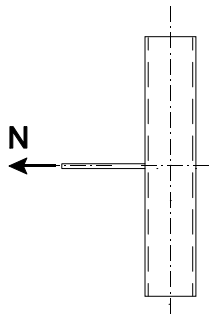	[1]	$N_{Allow.} = 0.15 \cdot (1 + 4.9 \cdot \beta^2) \cdot \gamma^{0.8} \cdot f_{y,0} \cdot t_0^2$ (2.9)
XP1-tension		
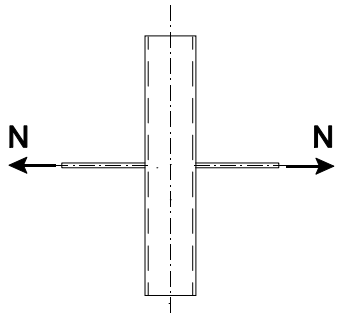	[1]	$N_{Allow.} = 1.9 \cdot \frac{1}{1 - 0.81 \cdot \beta} \cdot \gamma^{0.1} \cdot f_{y,0} \cdot t_0^2$ (2.10)
	[35]	$N_u = 2.87 \cdot (\beta + 0.42) \cdot \gamma^{0.61} \cdot f_{y,0} \cdot t_0^2$ (2.11)

Notes:

Eq. 2.9: According to [1] the ultimate load can be obtained with: $N_u = 4.13 * \gamma^{-0.1} * N_{Allow.}$

Eq. 2.10: According to [1] the ultimate load can be obtained with: $N_u = 1.87 * \gamma^{0.1} * N_{Allow.}$

In [45] , Makino proposes also formulae for TP1 and XP1 connections under axial tension load. These formulae give much higher values (up to 100 % for the TP1 connections) than the available test results (see also Table 9 in [45]). Since these formulae are clearly unsafe, they are not given here in this thesis.

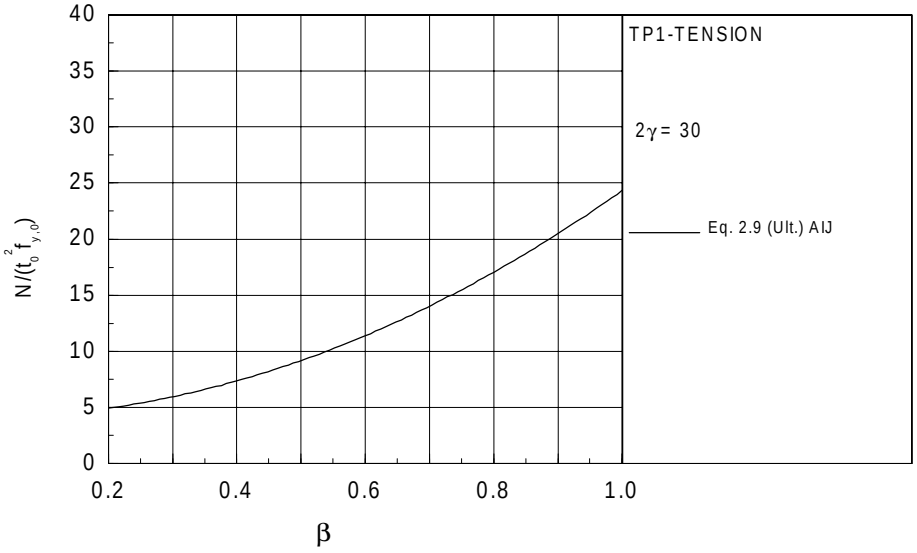

Figure 2.6 Formulae for TP-1 connections under axial tension load

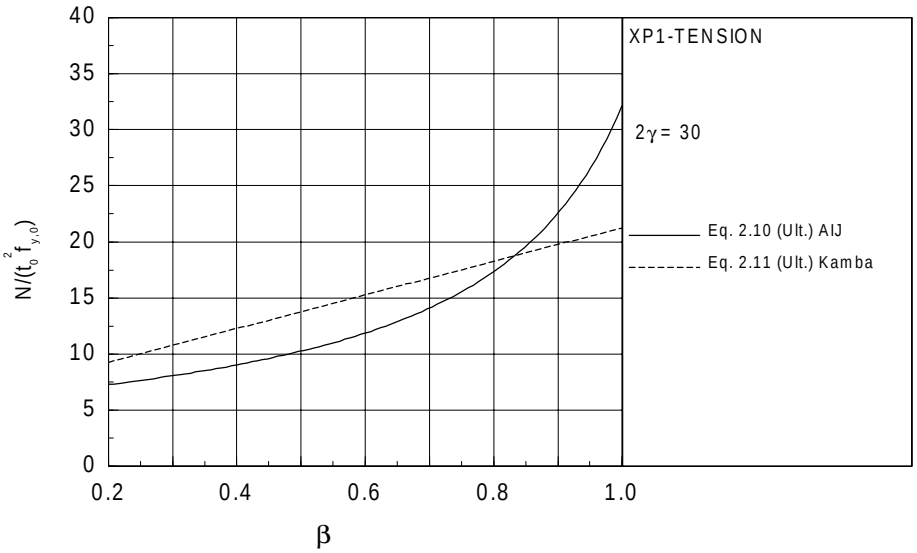

Figure 2.7 Formulae for XP-1 connections under axial tension load

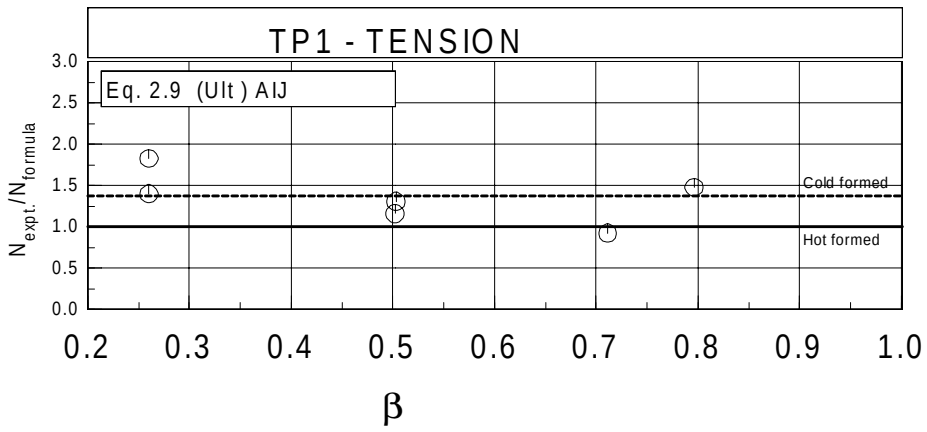

Figure 2.8 Comparison formulae for TP-1 connections under axial tension load with existing test data (Table 2.1)

Remarks:

As shown in Figure 2.8, the AIJ formula shows a poor agreement with the test results.

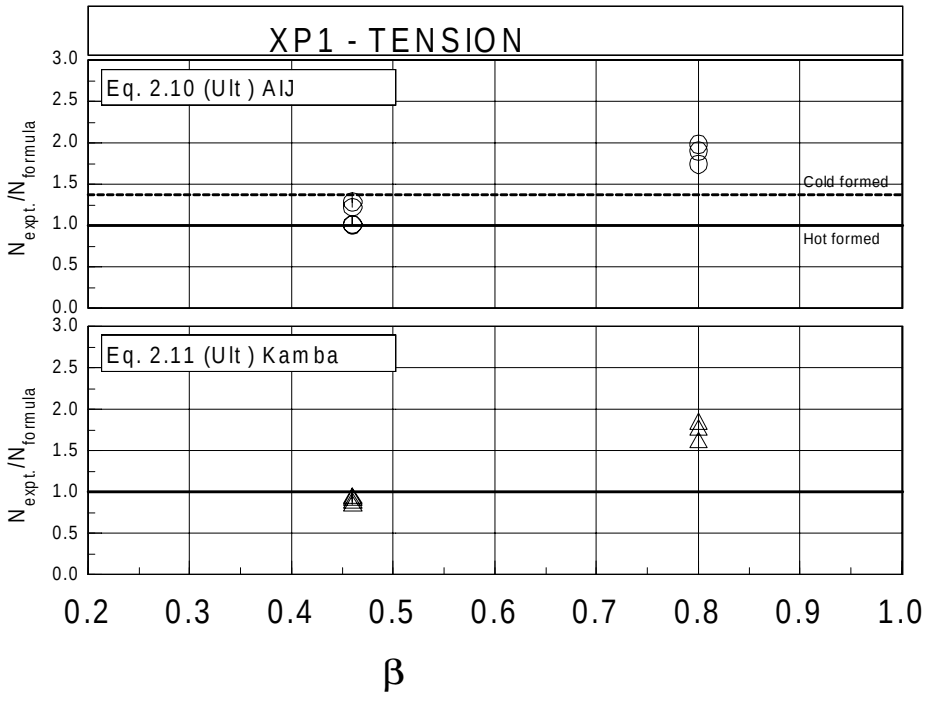

Figure 2.9 Comparison formulae for XP-1 connections under axial tension load with existing test data (Table 2.1)

Remarks:

As shown in Figure 2.9, all formulae show a poor agreement with the test results. The β-ratio influence of the test results is not covered by these formulae. The amount of test data is limited.

2.6.3 Strength formulae for web cleat to CHS column connections

Table 2.7 Strength formulae for web cleat to CHS column connections under axial compression load

TP2-compression	Ref.	Strength formula
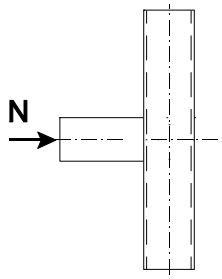	[1]	$N_{Allow.}=0.75\cdot(\gamma^{0.2}+1.5\cdot\eta\cdot\gamma^{-0.1})\cdot f_y\cdot t_0^2$ (2.12)
	[45]	$N_u=4.83\cdot\left((2\gamma)^{0.233}\cdot(\frac{\alpha}{2})^{-0.45}+\frac{\eta}{1.4}\right)\cdot f_y\cdot t_0^2$ (2.13)
	[19]	$N_{R.d}=(4.2+3\cdot\eta)\cdot f_{y,0}\cdot t_0^2\cdot f(n')$ (2.14)
	[11]	$N_{R.d}=5\cdot(1+0.25\cdot\eta)\cdot f_{y,0}\cdot t_0^2\cdot f(n')$ (2.15)
XP2 compression		
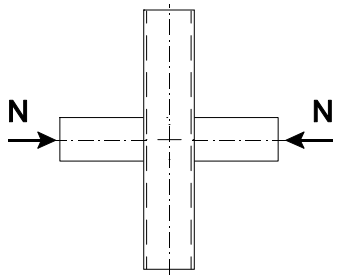	[1]	$N_{Allow.}=2.8\cdot\left((1+0.25\cdot\eta)\cdot\gamma^{-0.1}+0.55\cdot\eta\cdot\gamma^{-0.3}\right)\cdot f_{y,0}\cdot t_0^2$ (2.16)
	[45]	$N_u=\left(7.23\cdot(2\gamma)^{-0.032}+4.49\cdot\eta\cdot(2\gamma)^{-0.201}\right)\cdot f_{y,0}\cdot t_0^2$ (2.17)
	[19]	$N_{R.d}=(5.2+2\cdot\eta)\cdot f_{y,0}\cdot t_0^2\cdot f(n')$ (2.18)
	[11]	$N_{R.d}=5\cdot(1+0.25\cdot\eta)\cdot f_{y,0}\cdot t_0^2\cdot f(n')$ (2.19)

Notes:

Eq. 2.12 and 2.16: According to [1] the ultimate load can be obtained with: $N_u = 2.14^* N_{Allow.}$

For a note on f(n') see section 2.6.2.

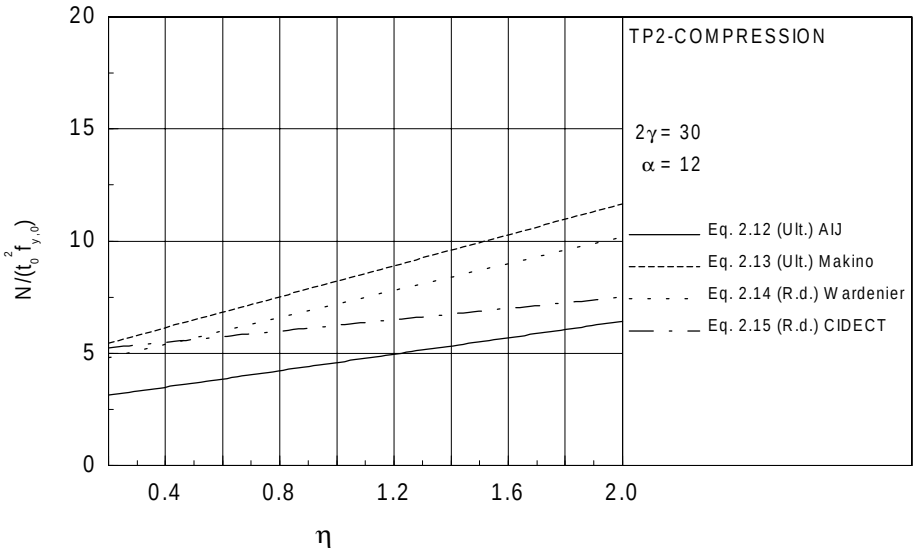

Figure 2.10 Formulae for TP-2 connections under axial compression load

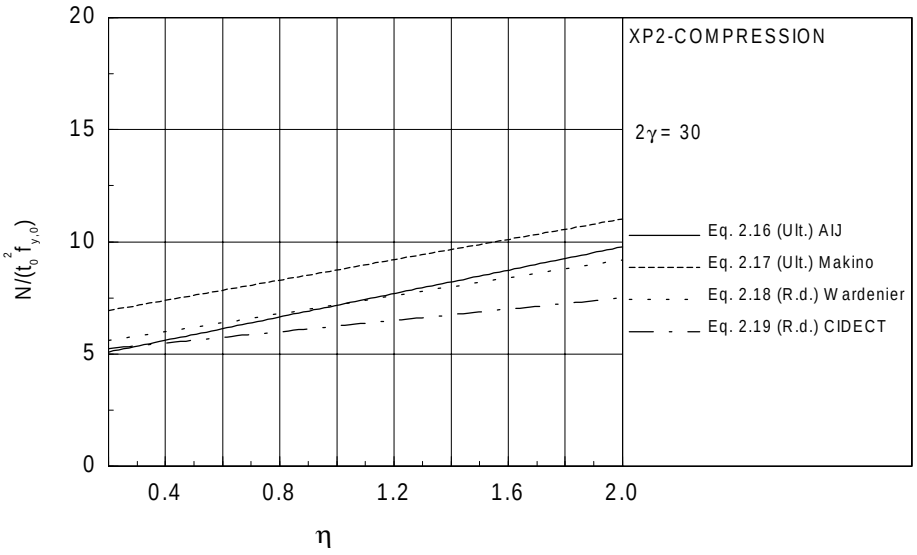

Figure 2.11 Formulae for XP-2 connections under axial compression load

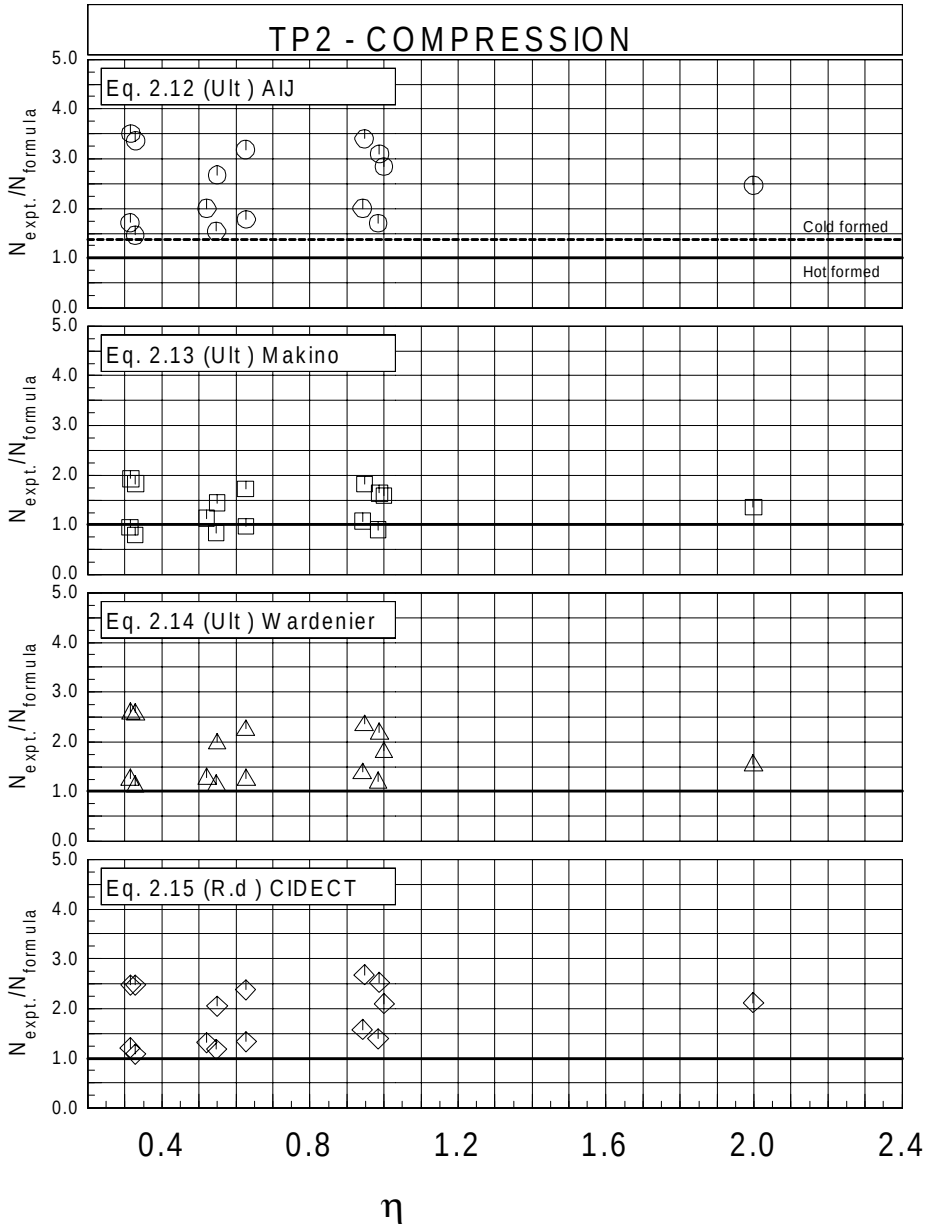

Figure 2.12 Comparison formulae for TP-2 connections under axial compression load with existing test data (Table 2.3)

Remarks:

As shown in Figure 2.12, all formulae give conservative results. The test data show a significant 2γ influence.

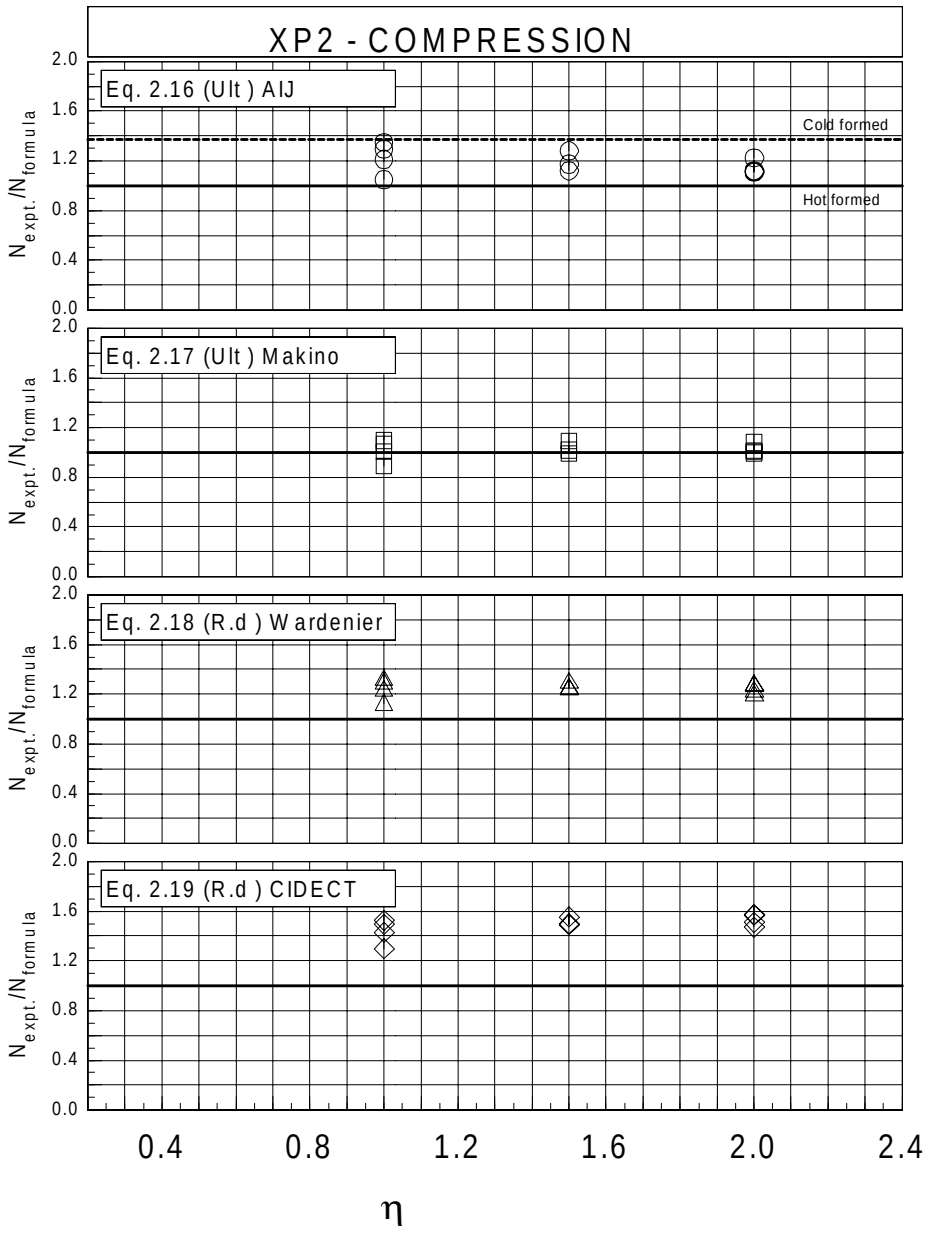

Figure 2.13 Comparison formulae for XP-2 connections under axial compression load with existing test data (Table 2.3)

Remarks:

As shown in Figure 2.13, all formulae, except AIJ give conservative results. However, it is unknown whether for these tests hot or cold formed sections were used.

Table 2.8 Strength formulae for web cleat to CHS column connections under axial tension load

TP2-tension	Ref.	Strength formula
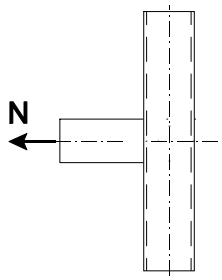	[1]	$N_{Allow.}=0.15\cdot(\gamma^{0.8}+3.2\cdot\eta)\cdot f_y\cdot t_0^2$ (2.20)
	[45]	$N_u=1.61\cdot\left((2\gamma)^{0.765}\cdot\alpha^{-0.45}+\frac{\eta}{0.45}\right)\cdot f_y\cdot t_0^2$ (2.21)
XP2-tension		
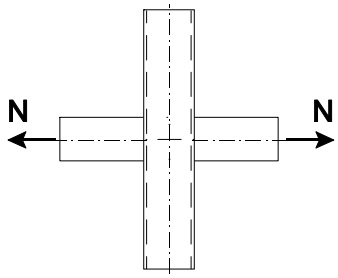	[1]	$N_{Allow.}=2.8\cdot\left((1+0.25\cdot\eta)\cdot\gamma^{-0.1}+0.55\cdot\eta\cdot\gamma^{-0.3}\right)\cdot f_{y,0}\cdot t_0^2$ (2.22)
	[45]	$N_u=\left(2.42\cdot(2\gamma)^{0.322}\cdot\alpha^{0.24}+3.42\cdot\eta\cdot(2\gamma)^{-0.034}\right)\cdot f_{y,0}\cdot t_0^2$ (2.23)

Notes:

Eq. 2.20: According to [1] the ultimate load can be obtained with: $N_u = 4.13*\gamma^{-0.1}* N_{Allow}$.

Eq. 2.22: According to [1] the ultimate load can be obtained with: $N_u = 1.87*\gamma^{0.1}* N_{Allow.}$

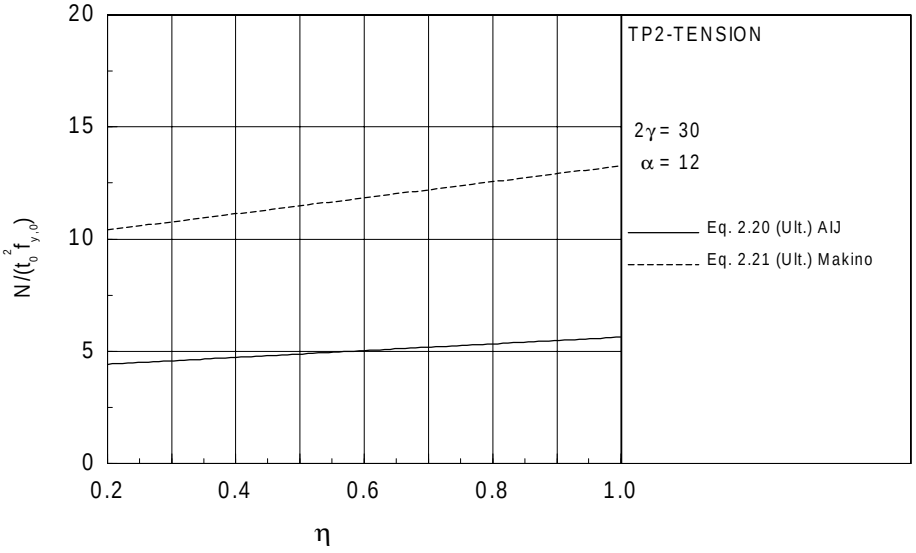

Figure 2.14 Formulae for TP-2 connections under axial tension load

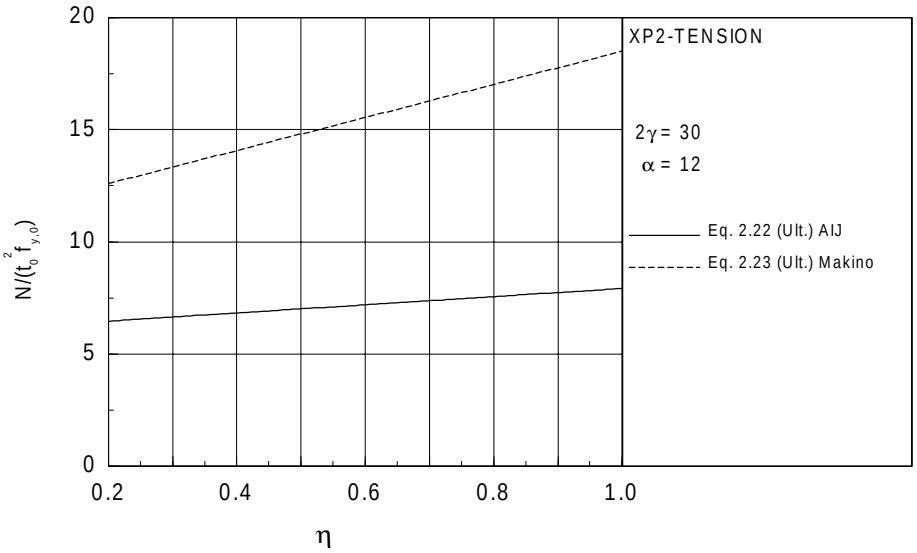

Figure 2.15 Formulae for XP-2 connections under axial tension load

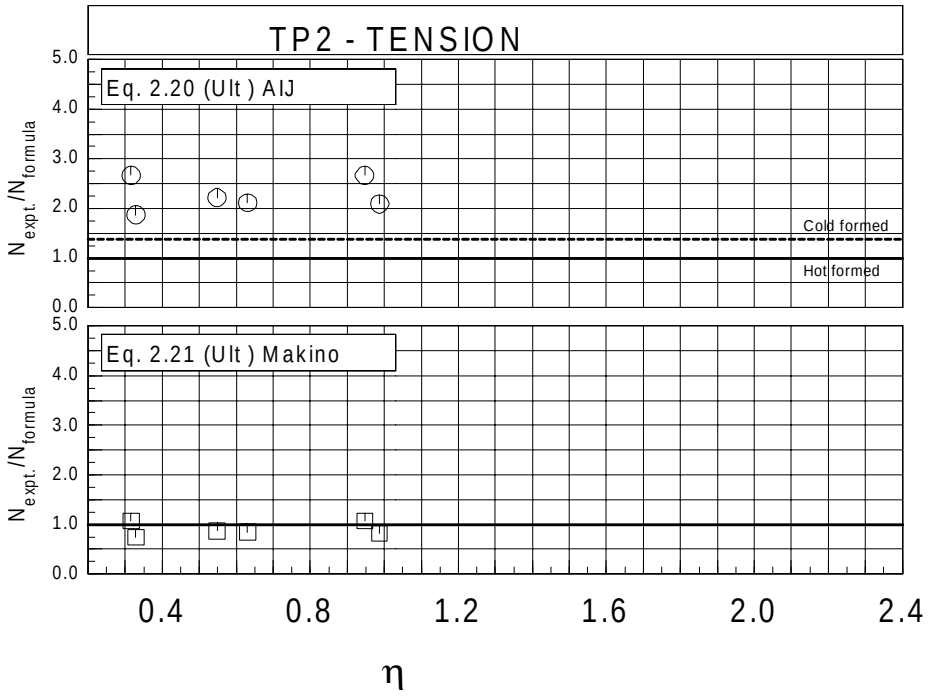

Figure 2.16 Comparison formulae for TP-2 connections under axial tension load with existing test data (Table 2.3)

Remarks:

As shown in Figure 2.16, the AIJ formula gives conservative results. Makino's formula shows a good agreement with the test results.

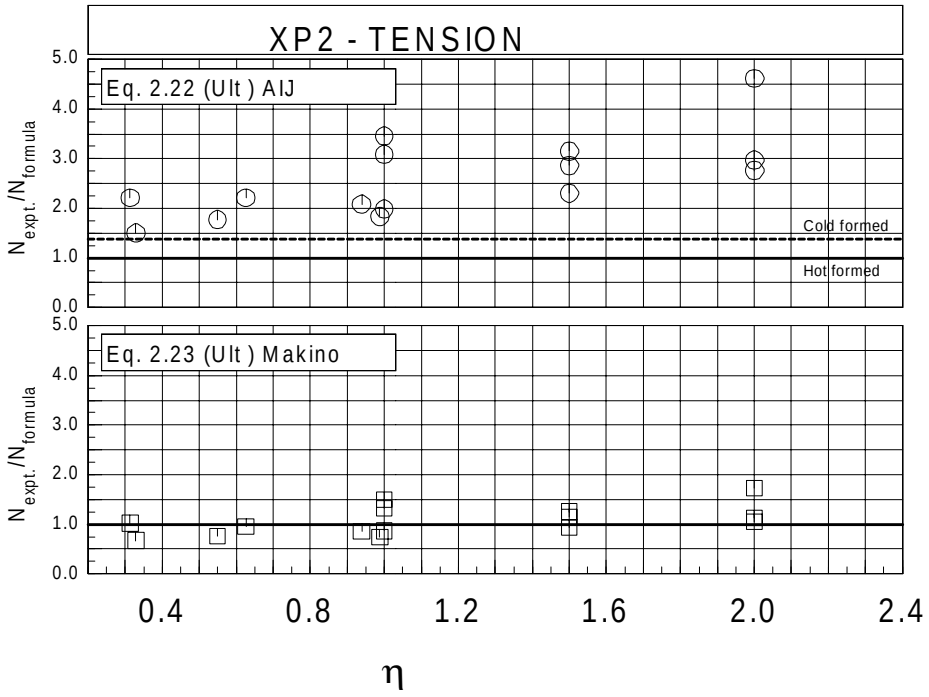

Figure 2.17 Comparison formulae for XP-2 connections under axial tension load with existing test data (Table 2.3)

Remarks:

As shown in Figure 2.17, the AIJ formula gives conservative results. Makino's formula shows a reasonable agreement with the test results.

2.6.4 Strength formulae for I-beam to CHS column connections

Table 2.9 Strength formulae for I-beam to CHS column connections under axial compression load

TP4-compression	Ref.	Strength formula
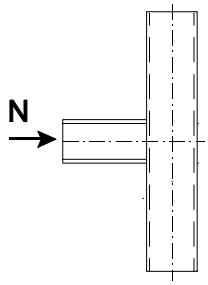	[1]	$N_{Allow.}=0.75\cdot(1+0.25\cdot\eta)\cdot(1+4.9\cdot\beta^2)\cdot\gamma^{0.2}\cdot f_{y,0}\cdot t_0^2$ (2.24)
	[45]	$N_u=4.83\cdot(1+0.25\cdot\eta)\cdot(1+4.94\cdot\beta^2)\cdot(2\gamma)^{0.233}\cdot\alpha^{-0.45}\cdot f_{y,0}\cdot t_0^2$ (2.25)
	[19]	$N_{R.d}=(1+0.25\cdot\eta)\cdot(4.2+21.3\cdot\beta^2)\cdot f_{y,0}\cdot t_0^2\cdot f(n')$ (2.26)
	[11]	$N_{R.d}=5.0\cdot\left(\frac{1+0.25\cdot\eta}{1-0.81\cdot\beta}\right)\cdot f_{y,0}\cdot t_0^2\cdot f(n')$ (2.27)
XP4 compression		
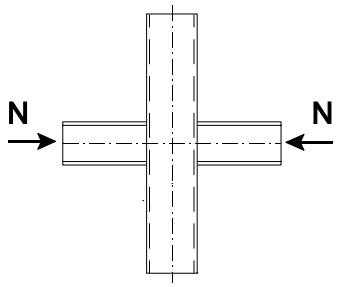	[1]	$N_{Allow.}=2.8\cdot\left(\frac{1+0.25\cdot\eta}{1-0.81\cdot\beta}\cdot\gamma^{-0.1}\right)\cdot f_{y,0}\cdot t_0^2$ (2.28)
	[45]	$N_u=7.23\cdot\left(\frac{1+0.25\cdot\eta}{1-0.812\cdot\beta}\right)\cdot(2\gamma)^{-0.032}\cdot f_{y,0}\cdot t_0^2$ (2.29)
	[19]	$N_{R.d}=5.2\cdot\left(\frac{1+0.25\cdot\eta}{1-0.81\cdot\beta}\right)\cdot f_{y,0}\cdot t_0^2\cdot f(n')$ (2.30)
	[11]	$N_{R.d}=5.0\cdot\left(\frac{1+0.25\cdot\eta}{1-0.81\cdot\beta}\right)\cdot f_{y,0}\cdot t_0^2\cdot f(n')$ (2.31)

Eq. 2.24 and 2.28: According to [1] the ultimate load can be obtained with: $N_u = 2.14^* N_{Allow.}$

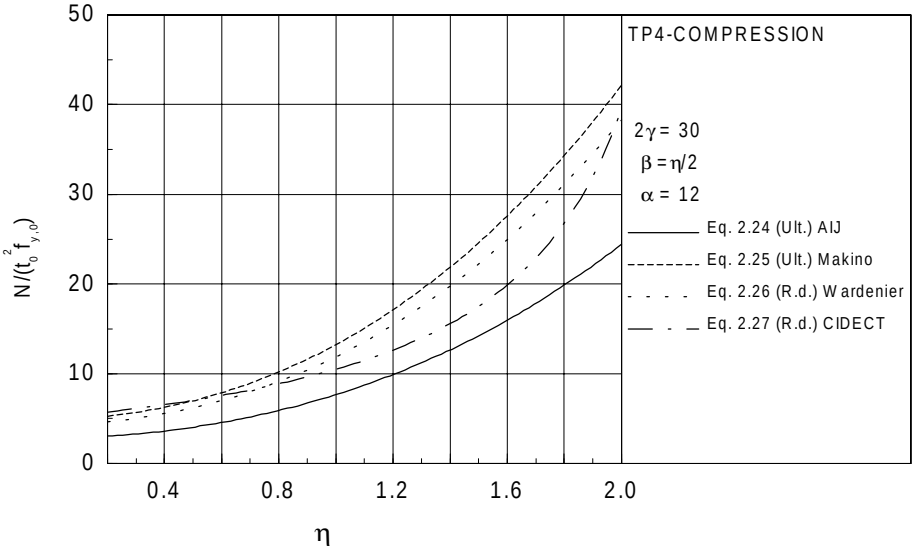

Figure 2.18 Formulae for TP-4 connections under axial compression load

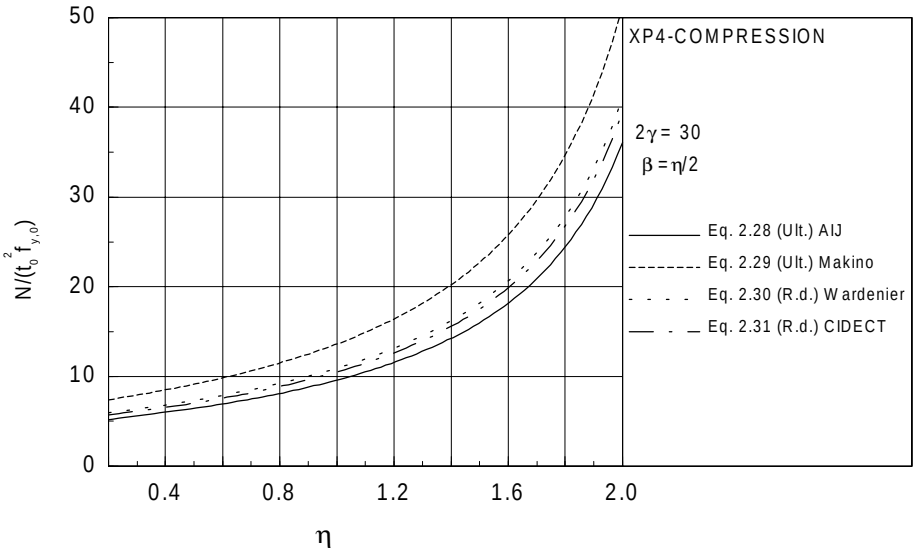

Figure 2.19 Formulae for XP-4 connections under axial compression load

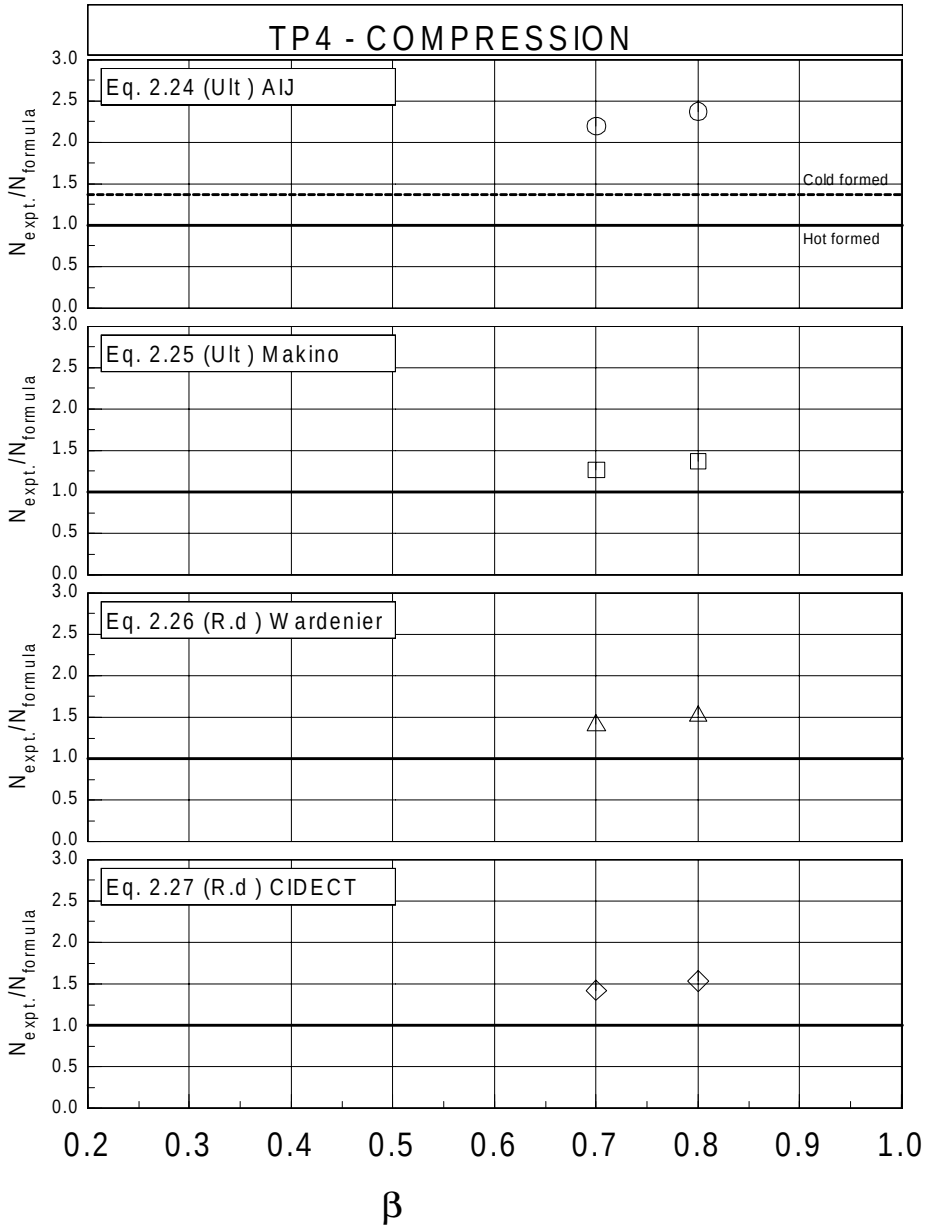

Figure 2.20 Comparison formulae for TP-4 connections under axial compression load with existing test data (Table 2.4)

Remarks:

As shown in Figure 2.20, all formulae give conservative results. However, only two tests are available for comparison.

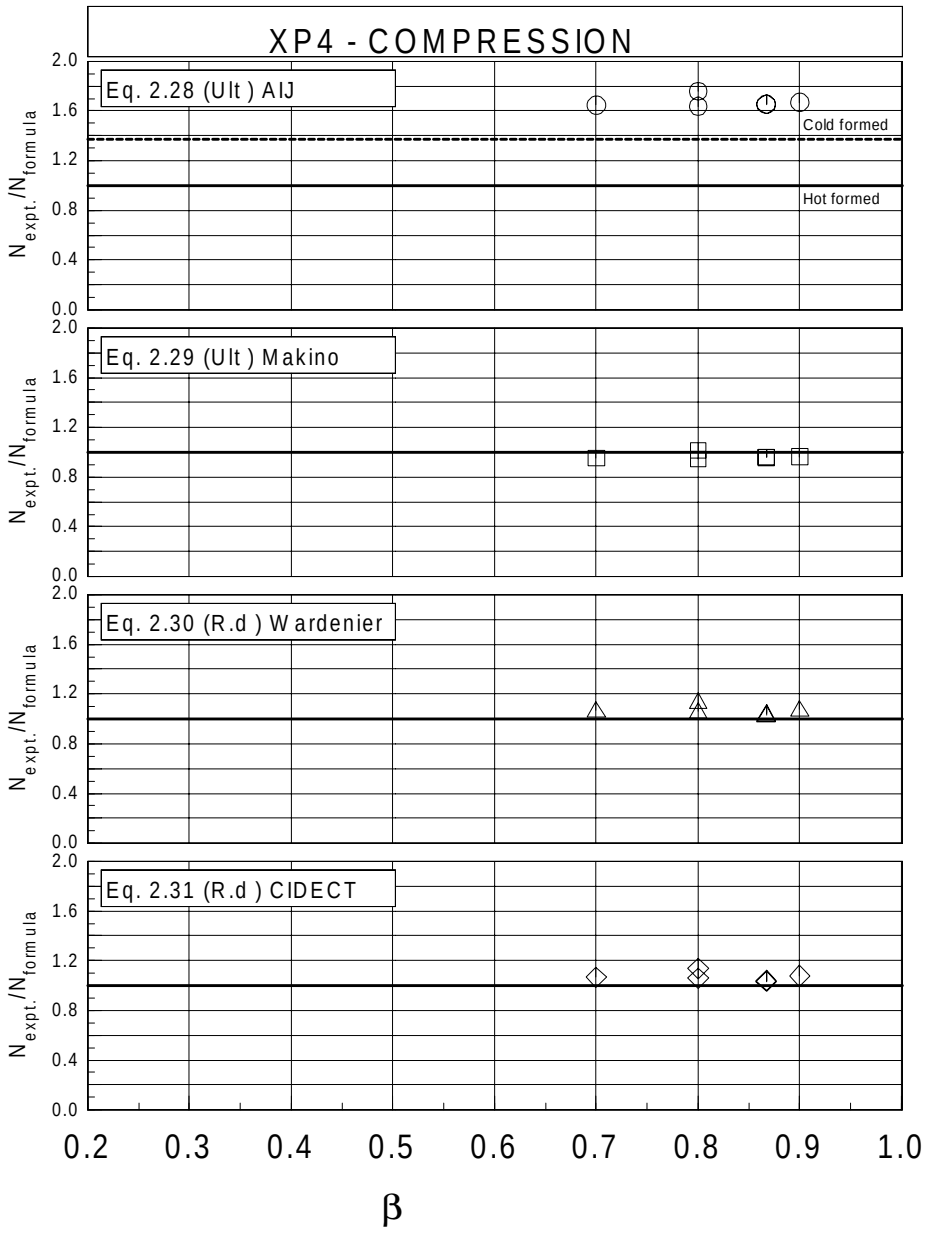

Figure 2.21 Comparison formulae for XP-4 connections under axial compression load with existing test data (Table 2.4)

Remarks:

As shown in Figure 2.21, all formulae show a good agreement with the test results. However, only a very limited amount of test results are available for comparison.

Table 2.10 Strength formulae for I-beam to CHS column connections under axial tension load

TP4-tension	Ref.	Strength formula
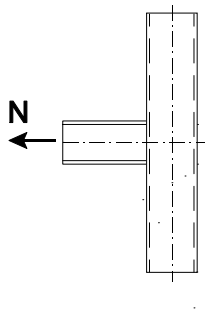	[1]	$N_{Allow.}=0.15\cdot(1+0.25\eta)\cdot(1+4.9\cdot\beta^2)\cdot\gamma^{0.8}\cdot f_{y,0}\cdot t_0^2$ (2.32)
XP4 tension		
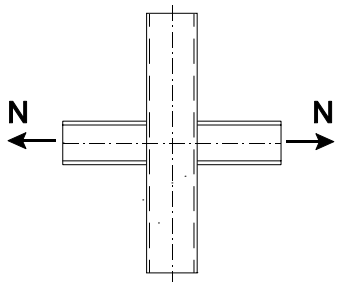	[1]	$N_{Allow.}=1.9\cdot\left(\frac{1+0.25\cdot\eta}{1-0.81\cdot\beta}\cdot\gamma^{0.1}\right)\cdot f_{y,0}\cdot t_0^2$ (2.33)
	[45]	$N_u=2.42\cdot\left(\frac{1+0.25\cdot\eta}{1-0.813\cdot\beta}\right)\cdot(2\gamma)^{0.322}\cdot\alpha^{0.24}\cdot f_{y,0}\cdot t_0^2$ (2.34)

Notes:

Eq. 2.32: According to [1] the ultimate load can be obtained with: $N_u = 4.13*\gamma^{-0.1}* N_{Allow.}$

Eq. 2.33: According to [1] the ultimate load can be obtained with: $N_u = 1.87*\gamma^{0.1}* N_{Allow.}$

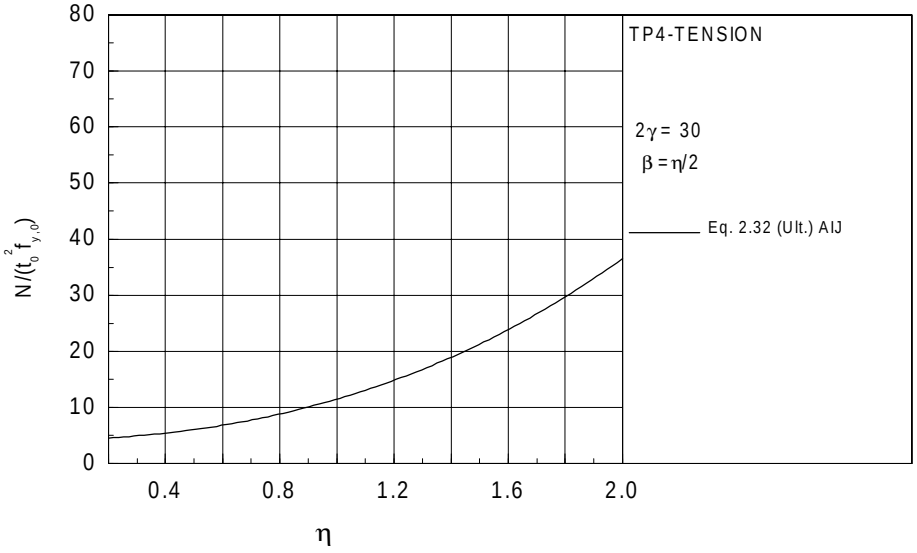

Figure 2.22 Formulae for TP-4 connections under axial tension load

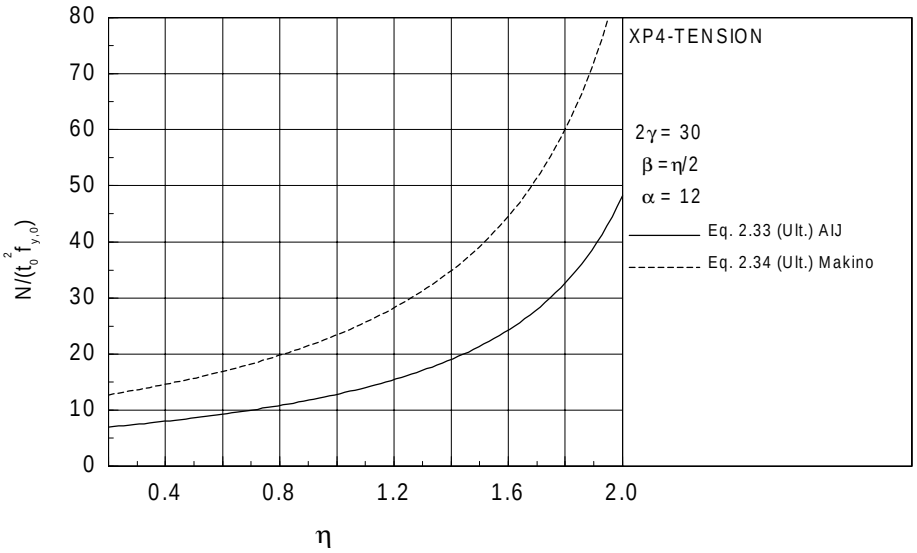

Figure 2.23 Formulae for XP-4 connections under axial tension load

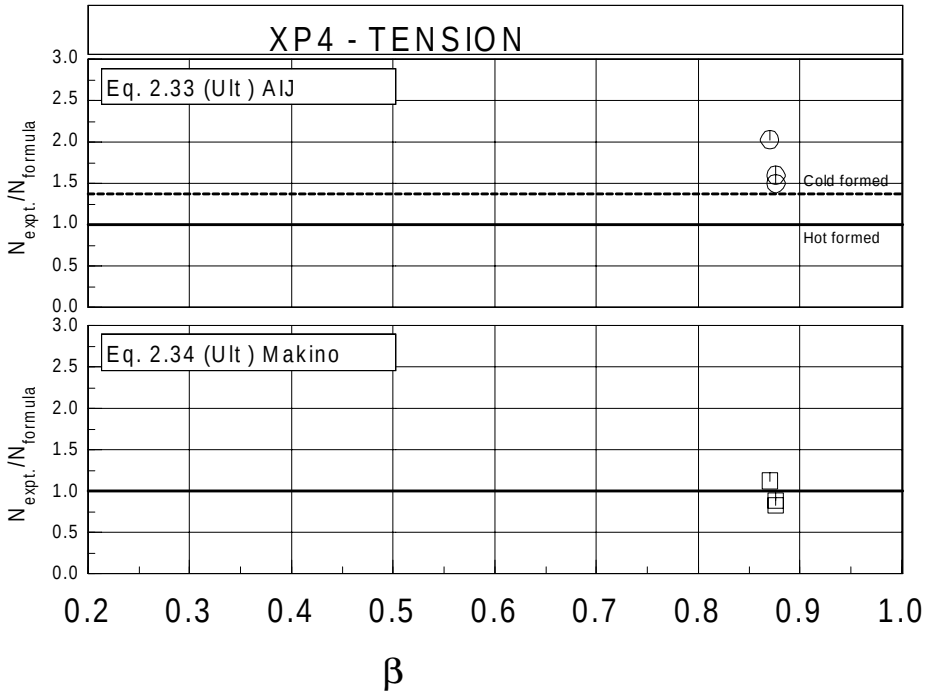

Figure 2.24 Comparison formulae for XP-4 connections under axial compression load with existing test data (Table 2.4)

Remarks:

As shown in Figure 2.24, the AIJ formula gives conservative results while Makino's formula gives a good agreement with the test results. However, only a very limited amount of test results are available for comparison.

Table 2.11 Strength formulae for I-beam to CHS column connections under in-plane bending moments

TP4-bending	Ref.	Strength formula
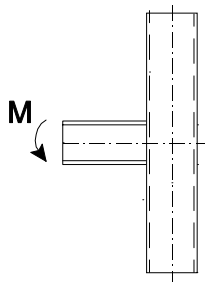	[1]	$M_{Allow.}=0.75\cdot(1+4.9\cdot\beta^2)\cdot\gamma^{0.2}\cdot h_1\cdot f_{y,0}\cdot t_0^2$ (2.35)
	[11]	$M_{R.d}=5\cdot\frac{h_1}{1-0.81\cdot\beta}\cdot f_{y,0}\cdot t_0^2\cdot f(n')$ (2.36)
XP4 bending		
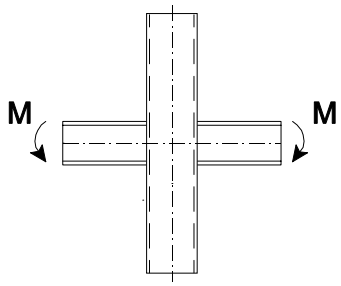	[1]	$M_{Allow.}=\frac{2.8}{1-0.81\cdot\beta}\cdot\gamma^{-0.1}\cdot h_1\cdot f_{y,0}\cdot t_0^2$ (2.37)
	[19]	$M_{R.d}=5.2\cdot\frac{h_1}{1-0.81\cdot\beta}\cdot f_{y,0}\cdot t_0^2\cdot f(n')$ (2.38)
	[11]	$M_{R.d}=5\cdot\frac{h_1}{1-0.81\cdot\beta}\cdot f_{y,0}\cdot t_0^2\cdot f(n')$ (2.39)

Notes:

Eq. 2.35 and 2.37: According to [1] the ultimate load can be obtained with:
$M_u = 2.14^* M_{Allow.}$

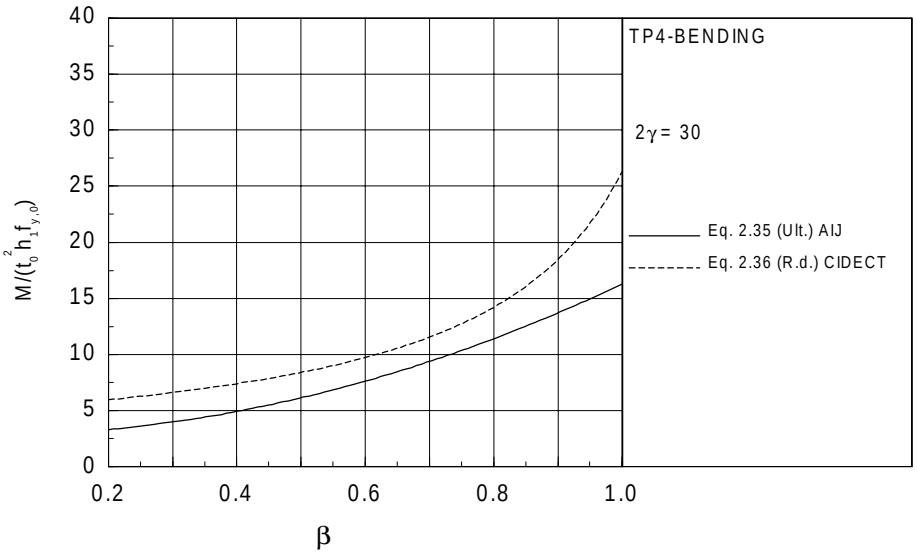

Figure 2.25 Formulae for TP-4 connections under in-plane bending moments

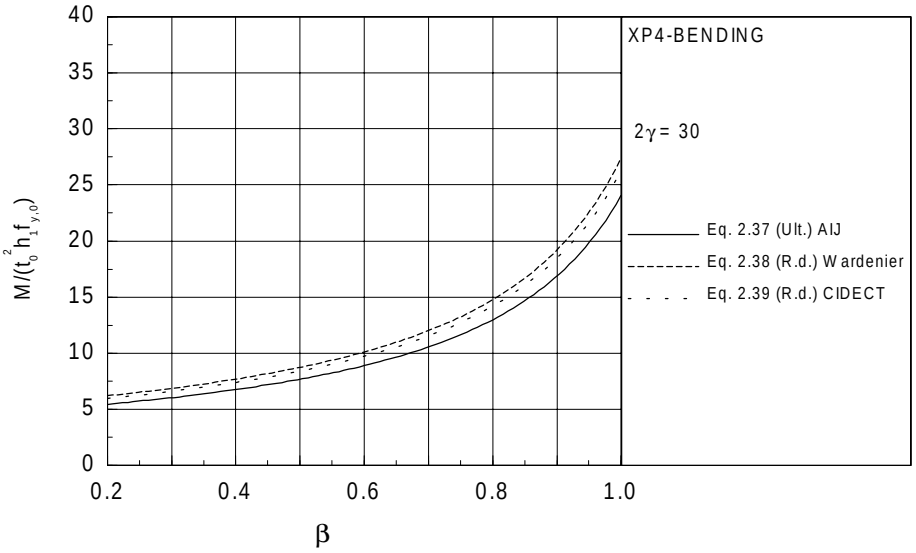

Figure 2.26 Formulae for XP-4 connections under in-plane bending moments

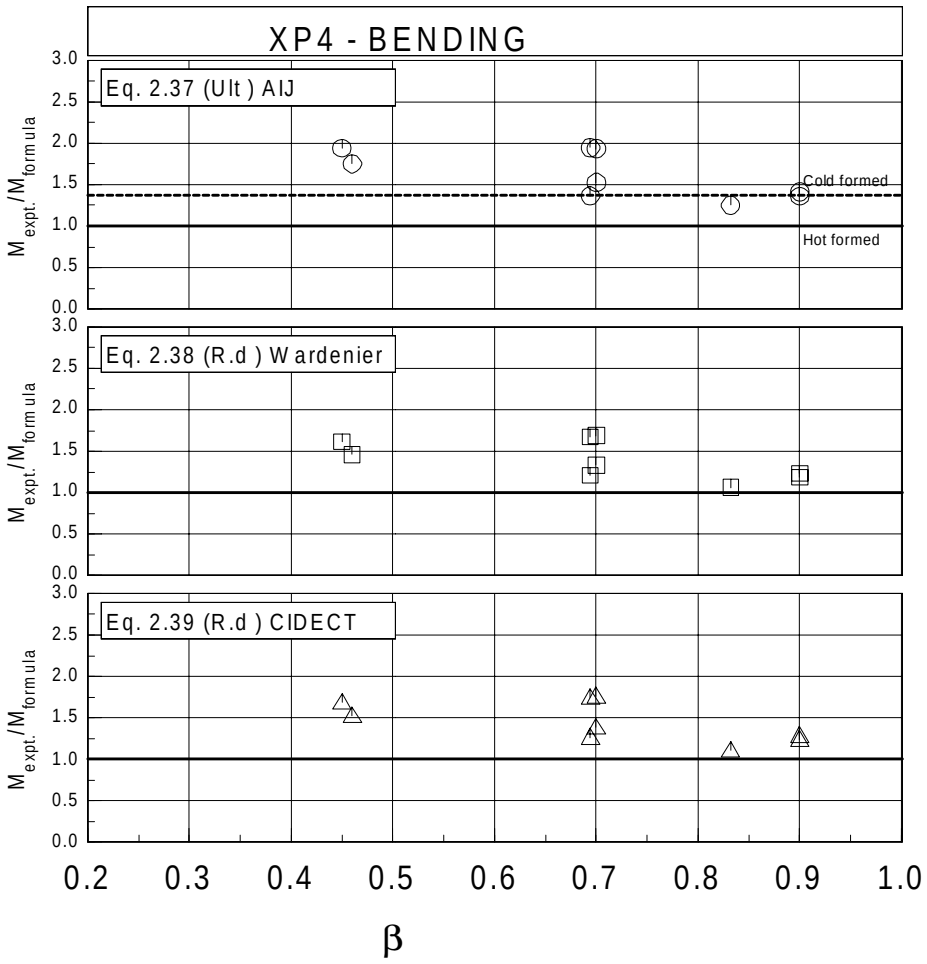

Figure 2.27 Comparison formulae for XP-4 connections under in-plane bending moments with existing test data (Table 2.4)

Remarks:

As shown in Figure 2.27, all formulae give conservative results.

3 EXPERIMENTAL TESTS

3.1 Introduction

The experimental work was done in the framework of the ECSC research programme 7210-SA-611 "Semi Rigid Connections Between I-Beams and Tubular Columns" [17]. The experimental tests, including detail and interaction tests, were carried at the TNO Building and Construction Research Laboratory, Rijswijk. The overall connection tests were carried out at the Stevin Laboratory for Steel Structures of the Delft University of Technology.
The aim of the experimental work was to provide detailed test data to be used for calibrating numerical models. The most important test data are the measured geometrical and material properties, the load-deflection or moment-rotation curves and the observed failure modes. Also, additional deformation and strain gauge measurements were carried out.

3.2 Overview experimental work

Tables 3.1 and 3.2 give an overview of the experimental work. Table 3.1 shows the experimental programme of test series 1 to 3, with various loading combinations carried out on multiplanar joints using I-beams (IPE 240 or IPE 360), or plates representing individual flanges of I-beams (120 x 10 or 170 x 12) and circular hollow section (CHS) columns (ø 324 x 9.5). In some cases the columns are composite (with reinforced concrete infill). Table 3.2 shows the experimental programme of test series 4, the tests of bolted connections between I-beams and tubular columns in combination with composite steel-concrete floors.
The experimental tests are grouped into four test series. Test series 1 consist of axial loading tests on multiplanar plate to CHS column connections loaded with an axial load on the plates. In total, 8 tests were carried out in this test series, two of the test specimens have a composite column. See Table 3.1 for the details.
Test series 2 consist of three tests on I-beam to CHS column connections loaded with axial loading. At the intersection of the I-beam with the column, the web of the I-beam has been removed in order to be able to investigate the influence of the flanges separately.
Test series 3 consist of four tests on I-beam to CHS column connections loaded with in-plane bending moments. In one of the tests, the influence of a steel floor is also investigated. In comparison with offshore applications, the tests were carried out as scale models. The scale is approximately equal to 1/3. However, the thickness of the steel floor was kept on a minimum of 5 mm.
The plates and beam flanges were welded to the CHS columns with butt welds. All weld design was to full capacity, as used for offshore work, as shown in Figure 3.1. The webs of beams were welded to the column on both sides of the web with fillet welds. There were no starts or stops of the welding process at the flange corners and there was a smooth

transformation of the fillet welds in the web to the back welds at the inner face of the flanges. The steel plate of specimen 3C2 was welded to the I-beam flanges with fillet welds.

Table 3.1 Overview experimental research programme (1)

Series	Test spec.	Configuration	β	2γ	τ	N_2/N_1 or F_2/F_1	Concrete filled column	Type of loading	N_1	Steel floor
1	1C1	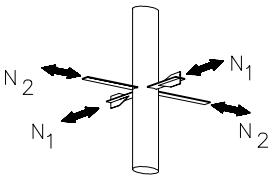	0.37	34	1.05	0		Axial	C[1]	
	1C2		0.37	34	1.05	0	yes	Axial	T[1]	
	1C3		0.52	34	1.26	0		Axial	C	
	1C4		0.52	34	1.26	0	yes	Axial	C	
	1C5		0.37	34	1.05	-1		Axial	C	
	1C7		0.52	34	1.26	-1		Axial	C	
	1C6		0.37	34	1.05	1		Axial	C	
	1C8		0.52	34	1.26	1		Axial	C	
2	2C1	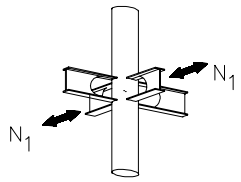	0.37	34	1.03	0		Axial	C	
	2C2		0.37	34	1.03	0	yes	Axial	T	
	2C3		0.52	34	1.34	0		Axial	C	
3	3C1	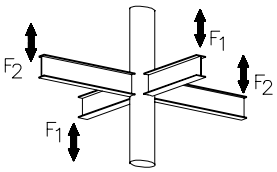	0.37	34	1.03	0		Bending		
	3C2		0.37	34	1.03	0		Bending		yes
	3C3		0.37	34	1.03	-1		Bending		
	3C4		0.37	34	1.03	1		Bending		

Notes:

[1](C = N_1 in compression

T = N_1 in tension

Test series 4 (Table 3.2) consists of four tests on bolted I-beam to CHS column connections in combination with a composite steel-concrete floor. The tubular column is either filled or not filled with concrete and two load cases were investigated, namely uniplanar and multiplanar in-plane bending.

Table 3.2 Overview experimental research programme (2)

Series	Test spec.	Configuration	β	2γ	τ	F_2/F_1	Concrete filled column	Type of loading	Composite floor
4	4C1	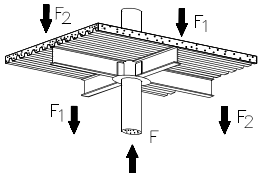	0.37	34	1.05	0		Bending	yes
	4C2		0.37	34	1.05	0	yes	Bending	yes
	4C3		0.37	34	1.05	1		Bending	yes
	4C4		0.37	34	1.05	1	yes	Bending	yes

3.3 Mechanical properties

3.3.1 Steel members

The ø 323.9 x 9.5 circular hollow section columns are seamless steel tubes in accordance with API-5L Gr. X52N . The IPE 240 and IPE 360 beams are Fritenar M 355 offshore steels. The plates and steel floor are grade St52-3 according to DIN 17100 and tolerances in accordance with DIN 1543. These steel grades are equivalent to S355 according to EN10210-1.
The actual mechanical properties f_y (yield stress), f_u (ultimate stress), ϵ (permanent elongation) of the above-mentioned steel sections were determined with tensile tests (dp 5) and carried out in accordance with Euronorm 2-80 "Tensile tests for steel". The measured mechanical properties are summarized in Tables 3.3 and 3.4.

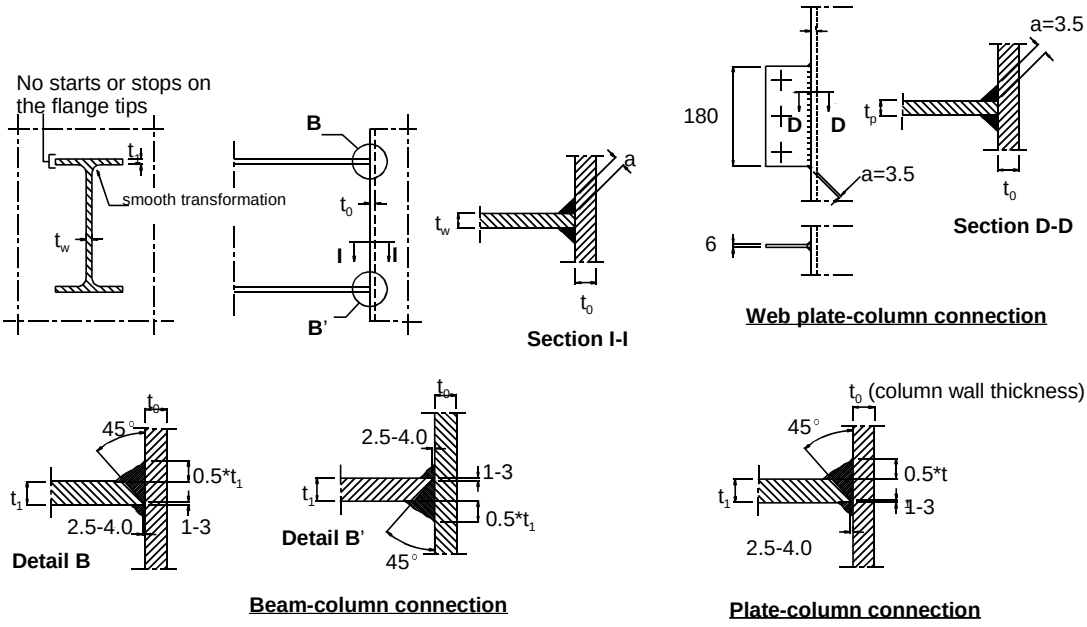

Figure 3.1 Welding details

Table 3.3 Mechanical properties determined with tensile coupon tests (dp5).

Section	Stock no	Coupon no	From:	f_y [MPa]	f_y (average) [MPa]	f_u [MPa]	f_u (average) [MPa]	ϵ [%]	ϵ (aver.) [%]
CHS 323.9*9.5	1	1	Circum.	387	392	510	512	26	27
		2	Circum.	397		513		28	
	2	1	Circum.	386	387	513	510	31	30
		2	Circum.	387		507		28	
	3	1	Circum.	384	391	512	513	29	31
		2	Circum.	398		513		33	
IPE-240	1	1	Flange	417	421	514	516	32	33
		2	Flange	425		517		33	
		3	Web	487	-	565	-	27	-
	2	1	Flange	429	433	525	526	32	33
		2	Flange	436		526		33	
		3	Web	502	-	573	-	27	-
	6	1	Flange	440	440	527	525	31	31
		2	Flange	440		523		30	
		3	Web	518	-	564	-	29	-
	7	1	Flange	436	436	526	528	32	32
		2	Flange	435		529		31	
		3	Web	483	-	556	-	29	-
		2	Flange	414		526		31	
IPE-360	1	1	Flange	401	399	499	497	31	32
		2	Flange	396		494		33	
		3	Web	442	-	532	-	27	-
	2	1	Flange	404	404	497	496	33	34
		2	Flange	404		495		34	
		3	Web	442	-	540	-	28	-

Table 3.4 Mechanical properties determined with tensile coupon tests (dp5).

Section [mm]	Stock no	Coupon no	From:	f_y [MPa]	f_u [MPa]	ϵ [%]
Plate:	1	1		396	521	29
10*120	2	1	Longitudinal	389	514	31
Plate: 12*170	1	1	Longitudinal direction	392	516	31
Steel floor (5 mm)	1	1	Longitudinal direction	427	516	29
		2	Transverse direction	436	531	30
Ring stiffener *)	-	1	-	355	510	22
Web plate *)	-	1	-	355	510	22

*) Nominal values

3.3.2 Weld material

All test specimens were welded with basic electrodes, trade name Kryo 1, electrode size ø 3.2 (nominal mechanical properties being f_y = 470 N/mm^2, f_u = 520 N/mm^2, ϵ = 31%) for the butt welds; and with basic electrodes, trade name Safdry 52, electrode size ø 5.0 (nominal mechanical properties being f_y = 408 N/mm^2, f_u = 511 N/mm^2, ϵ = 34%) for the fillet welds.

3.3.3 Reinforced concrete filling of CHS columns

The concrete strength class for the concrete filling of the columns is C 35/45 according to Eurocode 2 and the corresponding 20 mm ø steel reinforcement is Grade B500H (measured f_y = 565 N/mm^2, f_u = 644 N/mm^2, ϵ_u = 9%) according to Eurocode 2. The 8 mm ø stirrups are also grade B500H (measured f_y = 589 N/mm^2, f_u = 658 N/mm^2, ϵ_u = 5.3%).
Table 3.5 summarizes the mechanical properties of the concrete of the filling in the column at the time of testing. Figure 3.2 and Photo 3.1 show the configuration of the reinforcement.

Table 3.5 Concrete cube properties for composite columns

Cube No.	Specimen No.	Age [days]	Control cube strength in climate chamber [MPa]	Hardened cube strength at test site [MPa]	Hardened splitting tensile strength at test site [MPa]	Density [kg/m^3]	Modulus of elasticity [MPa]
1	-	7	37.5	-	-	2354	-
13	-	7	35.9	-	-	2349	-
5	-	14	42.4	-	-	2362	-
17	-	14	42.2	-	-	2361	-
9	-	28	51.0	-	-	2362	-
20	-	28	50.5	-	-	2353	-
2	1C4	24	-	-	-	-	27000
3		24	-	49.5	-	2340	-
4		24	-	-	4.15	2335	-
6	4C4	326	-	-	-	-	28100
7		326	-	57.7	-	2318	-
8		326	-	-	5.12	2315	-
10	2C2	67	-	-	-	-	27200
11		67	-	54.7	-	2321	-
12		67	-	-	3.88	2321	-
14	1C2	54	-	-	-	-	25100
15		54	-	56.6	-	2351	-
16		54	-	-	4.82	2348	-
18	4C2	196	-	60.3	-	2312	-
19		196	-	-	4.00	2315	-

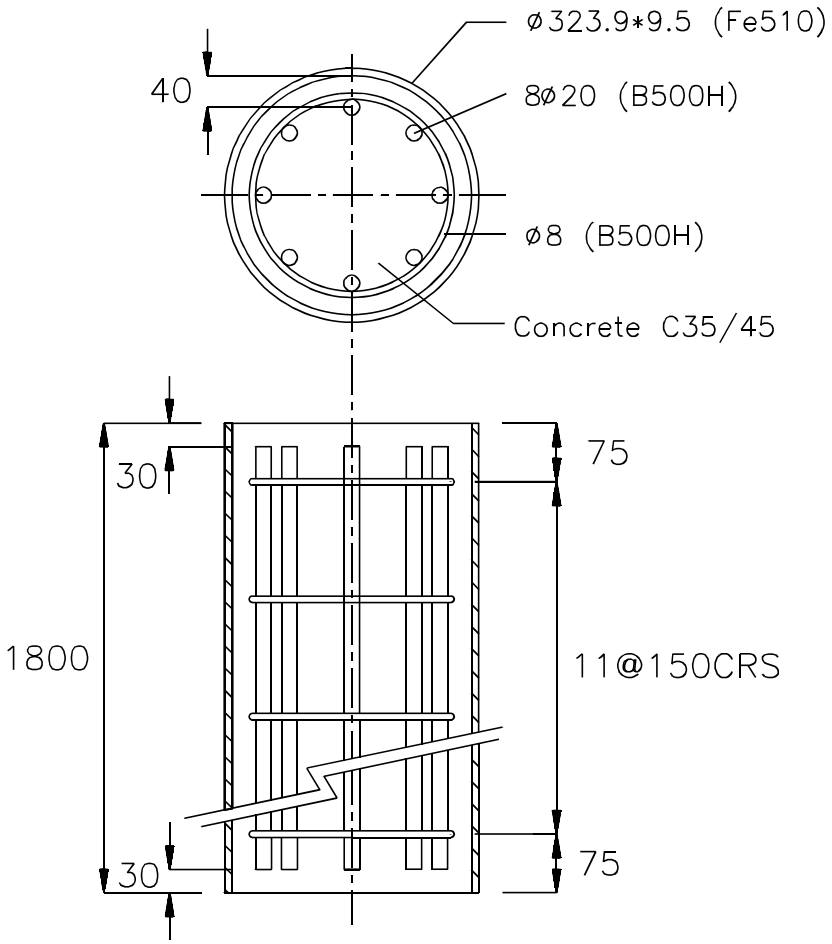

Figure 3.2 CHS column with reinforced concrete filling

Photo 3.1 Reinforcement composite column

3.3.3.1 Concrete composition for the composite columns

The CHS columns were filled with a ready mixed concrete as given below:

- quality C35/45
- maximum particle size = 32 mm
- cement content = 360 kg/m^3 (180 kg HC-A and 180 kg PC-C)
- consistency = between 3 and 4 according to NEN 5950 (ISO 4103 (1979) class S3-S4), where necessary achieved with a superplastifier
- water cement (w/c) ratio = 0.47.

Note:

HC = Hoogovens cement
PC = Portland cement

On arrival of the truck mixer, the concrete consistency was 1, so that just as much water is added as reasonably sufficient to give good compaction with a needle vibrator. To achieve a consistency of 3, 13.3 litres/m^3 is added.

The following properties of the concrete were determined:

- slump according to NEN 5956 (ISO 4109 (1980)[1]) = 113 mm
- flow according to NEN 5957 (ISO 9812[2]) = 430 mm
- density of fresh concrete according to NEN 5959 (ISO 6276, 1982) = 2362 kg/m^3
- air content of fresh concrete according to NEN 5962 (ISO 4848, 1980) = 0.9% v/v
- water-cement ratio due to extra water increased from 0.47 to 0.51.

On the basis of the standard cement strength and a w/c ratio of 0.47, a cube strength of 54 N/mm^2 at 28 days is expected. However, the addition of extra water gives an expected cube strength of 50 N/mm^2 at 28 days. Based upon NEN 5950 the corrected strength is: 45 + 8 = 53 N/mm2, thus the requirements for class C 35/45 are fulfilled.

3.3.3.2 Concreting operations of the columns

The 1800 mm high columns prepared with the reinforcement cages were filled in 4 layers of approximately 450 mm with a concreting skip and each layer was compacted with a heavy needle vibrator. Twenty 150 mm cubes, were cast according to NEN 5956 (ISO 2736/2

[1] The required compaction for NEN 5956 is less intensive than for ISO 4109

[2] The required cone capacity for NEN 5957 is larger than for ISO 9812

(1986)). Six of these were cured in the controlled environment of a humidity chamber for strength development control tests and fourteen for hardening tests. Of the 14 cubes for hardening tests, 5 were reserved for cube compression tests and 5 for splitting tensile strength tests, both sets placed in plastic foil adjacent to the test specimens, at approximately 20°C. The remaining 4 cubes were cured at 20°C and 50% relative humidity and used for determining the modulus of elasticity. For this purpose, the 4 test cubes were sawn into 75 x 75 x 150 mm prisms.

3.3.3.3 Properties of cured concrete cubes for the composite columns

The following properties were determined:

- The control and hardened cube compression strength according to NEN 5968 (ISO 4012 (1978)).
- The splitting tensile strength according to NEN 5969 (ISO 4108 (1980)). The density according to NEN 5967 (ISO 6275 (1982)).
- The modulus of elasticity according to NEN 3880, Part G, clause 609.2.1, page 463, using the 75 x 75 x 150 mm specimens sawn out from the centre of the cubes.

The results of the cube and prism tests are given in Table 3.5. The following observations are made:

- The expected control cube strength of 50 N/mm^2 at 28 days was achieved.
- The hardened cube strength was increased to 60.3 N/mm^2, at the period of testing test series 4.
- The average hardened splitting tensile strength during the testing period of series 4 is 4.39 N/mm^2.

3.3.4 Composite floor comprising a steel deck (PMF CF46) and a 110 mm deep concrete slab for series 4 tests

The concrete strength class for the concrete floor is C 20/25 in accordance with Eurocode 2. The hot rolled ribbed ø 8 mm steel reinforcement bars (steel grade B500H) for the main reinforcement in the floor are in accordance with EN 10080.
The reinforcement bars with steel grade B500H should have a ductility ϵ_u larger than 5% and a characteristic value of f_u/f_y >1.08. The reinforcement bars should be weldable and should have projected rib factors of not less than 0.045 for 8 mm ø bars.
The measured values for the ø 8 mm reinforcement are f_y=570 MPa, f_u= 645 MPa and ϵ_u=24%, so the requirements are fulfilled.
The ø 6 mm reinforcing net (steel grade B500N) is made of cold formed normal ductility plain bars, see also Figures 3.4 and 3.5.
The measured values for the ø 6 mm reinforcement are f_y=615 MPa, f_u= 627 MPa and

ϵ_u=17%. At time of the fabrication of the test specimens, nets of ø 6 mm reinforcement bars with steel grade B500H could not be delivered within a reasonable period of time, therefore steel grade B500N with lower ductility was used.

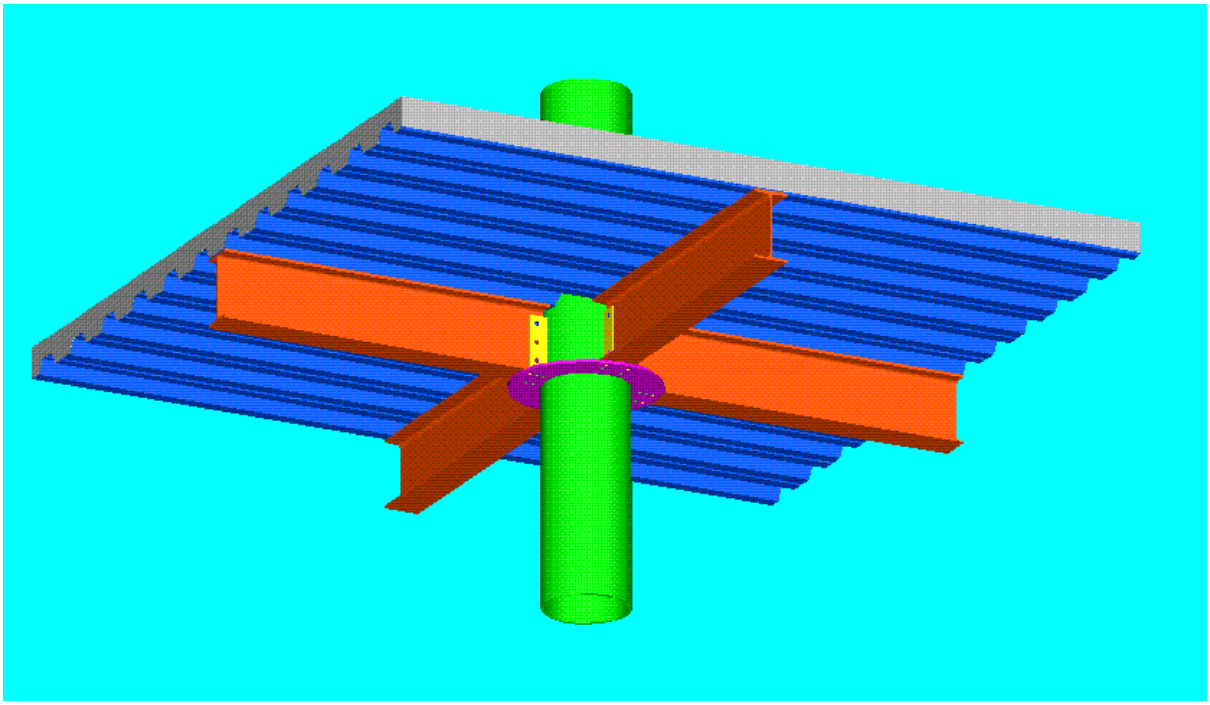

Figure 3.3 Configuration test specimen series 4

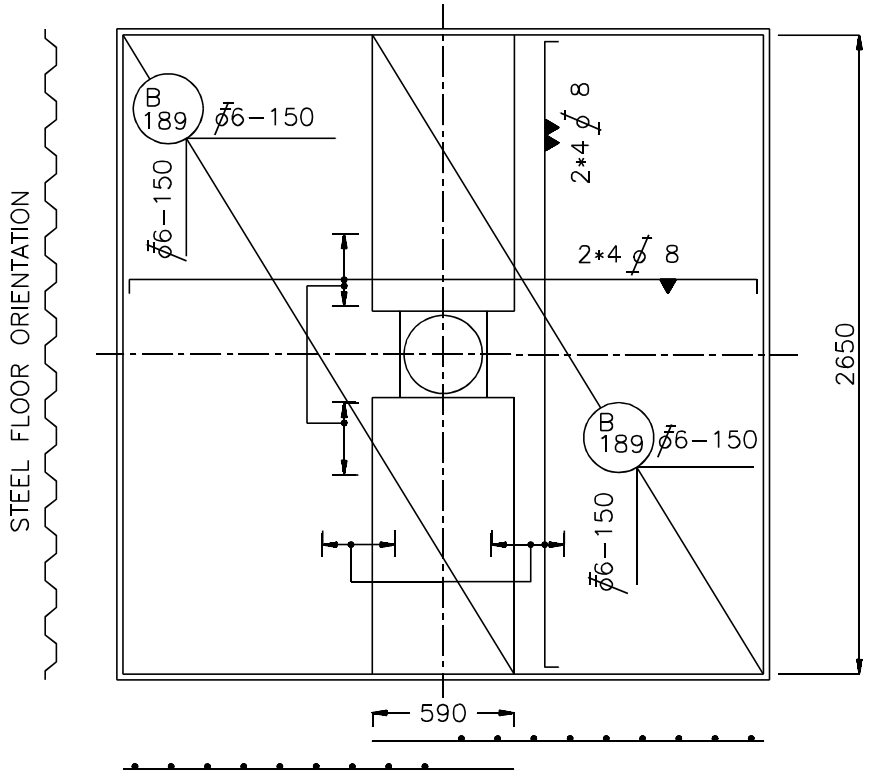

Figure 3.4 Reinforcement composite floor

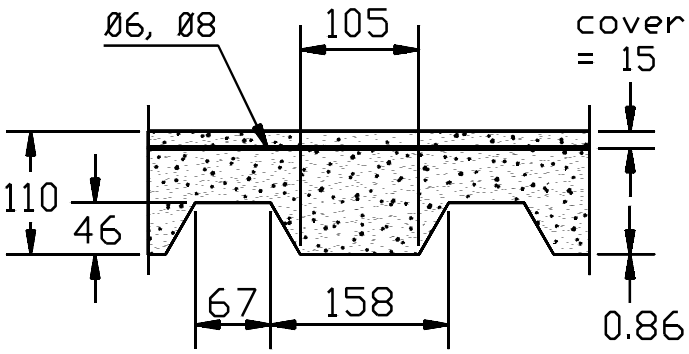

Figure 3.5 Cross-section composite floor

3.3.4.1 Assembly of the test specimens

The beams were firstly bolted to the columns, as shown in Photo 3.2, for specimens 4C1 to 4C4 at the concreting site for the composite floor. The steel deck plates (PMF CF46) with a 0.9 mm wall thickness were then placed over the beams as shown in Photo 3.3. Since the standard widths were 900 mm, they were placed next to each other with an overlap of one upper flange of the steel decks.
One overlap is immediately next to the beam and the two other overlaps were about on a distance of 900 mm from the centerline of the I-beam at both sides. The overlapping sections were connected together with pop rivets.

The ends of the beams as well as the PMF CF46 steel deck are then supported before further operations. The shear studs are then welded to the steel beams through the PMF CF46 steel decks. The formwork is then erected around the edges of the deep steel deck. Photo 3.4 shows the reinforcement meshes placed into position, using spacers to provide the required cover of 15 mm from the upper surface of the concrete floor.
The ready mixed concrete was poured with a skip and was then compacted with needle and surface vibrators. Finally, the surface was trowelled flat.

The composite floors are erected and constructed in two different batches on different dates. Specimens 4C1 and 4C2 were constructed first, followed by 4C3 and 4C4.

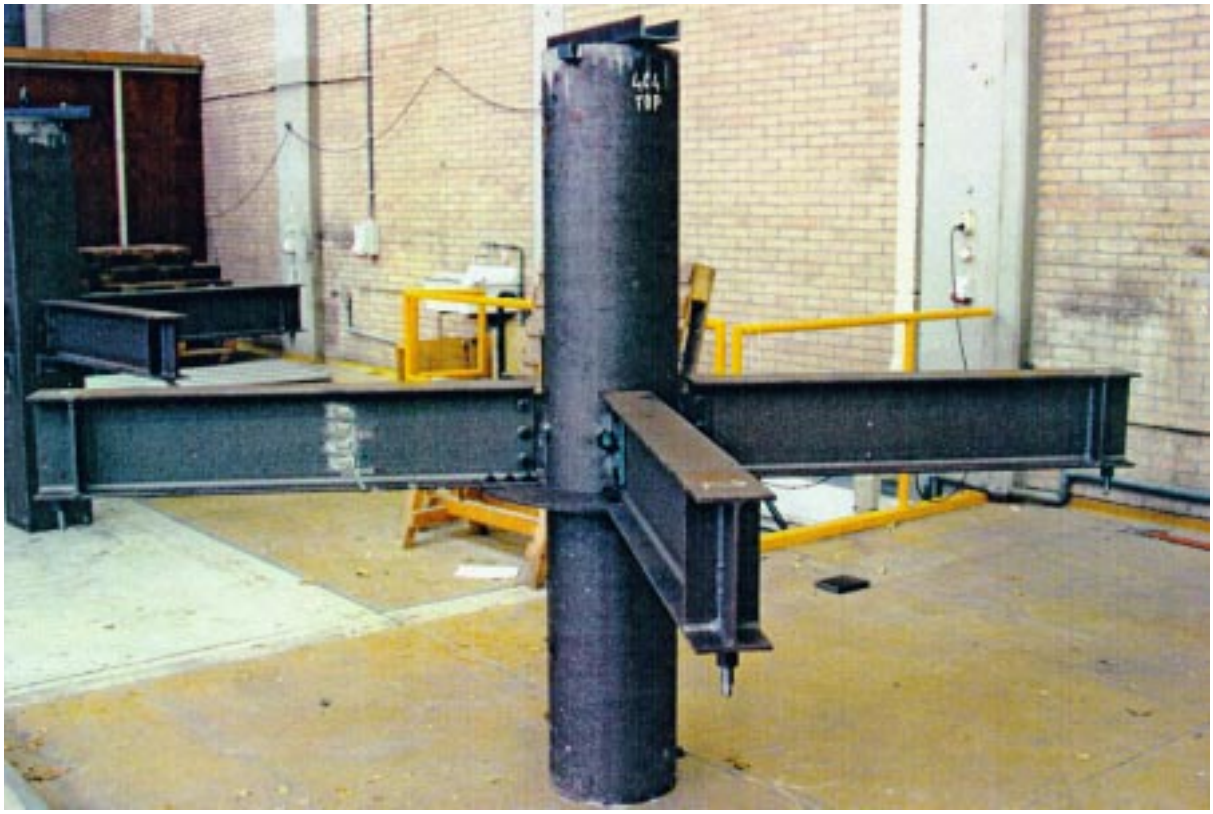

Photo 3.2 Assembly test series 4: I-beams bolted to the column and to the ring.

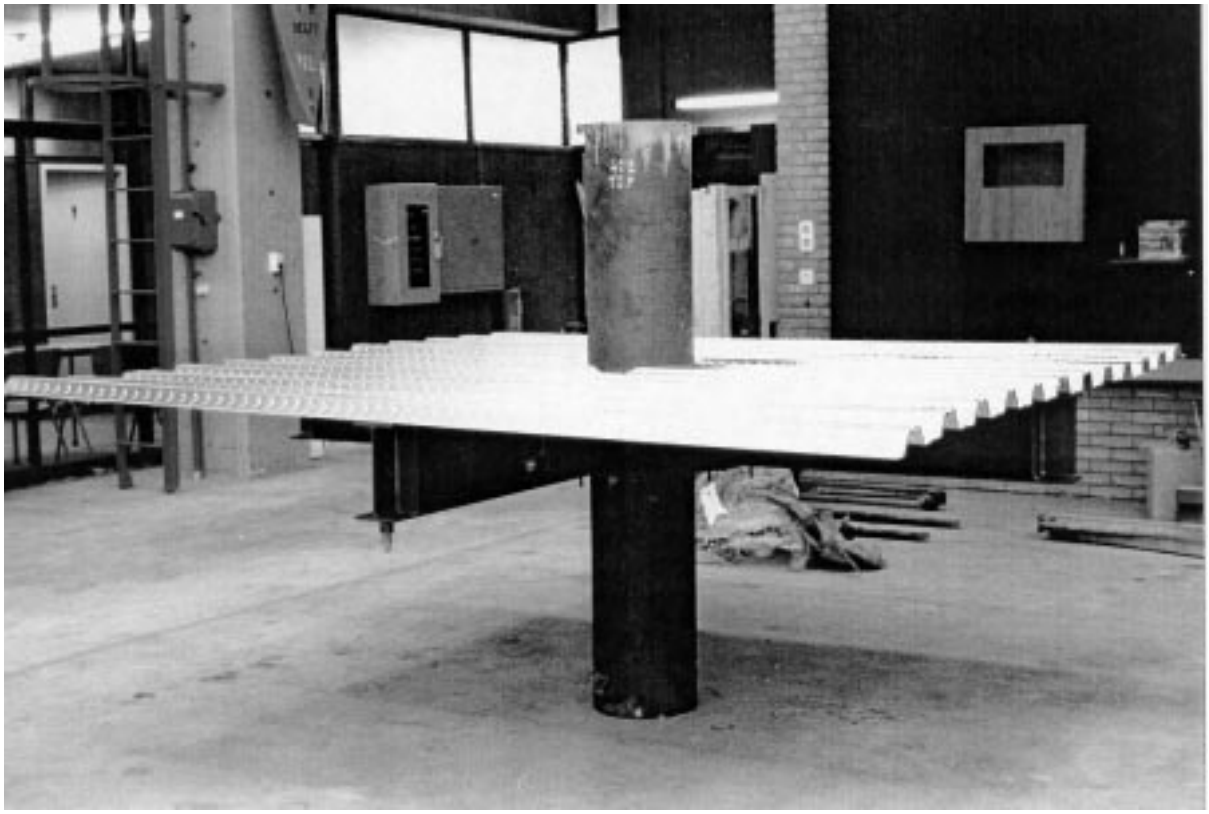

Photo 3.3 Assembly test series 4: steel deck plates placed in position

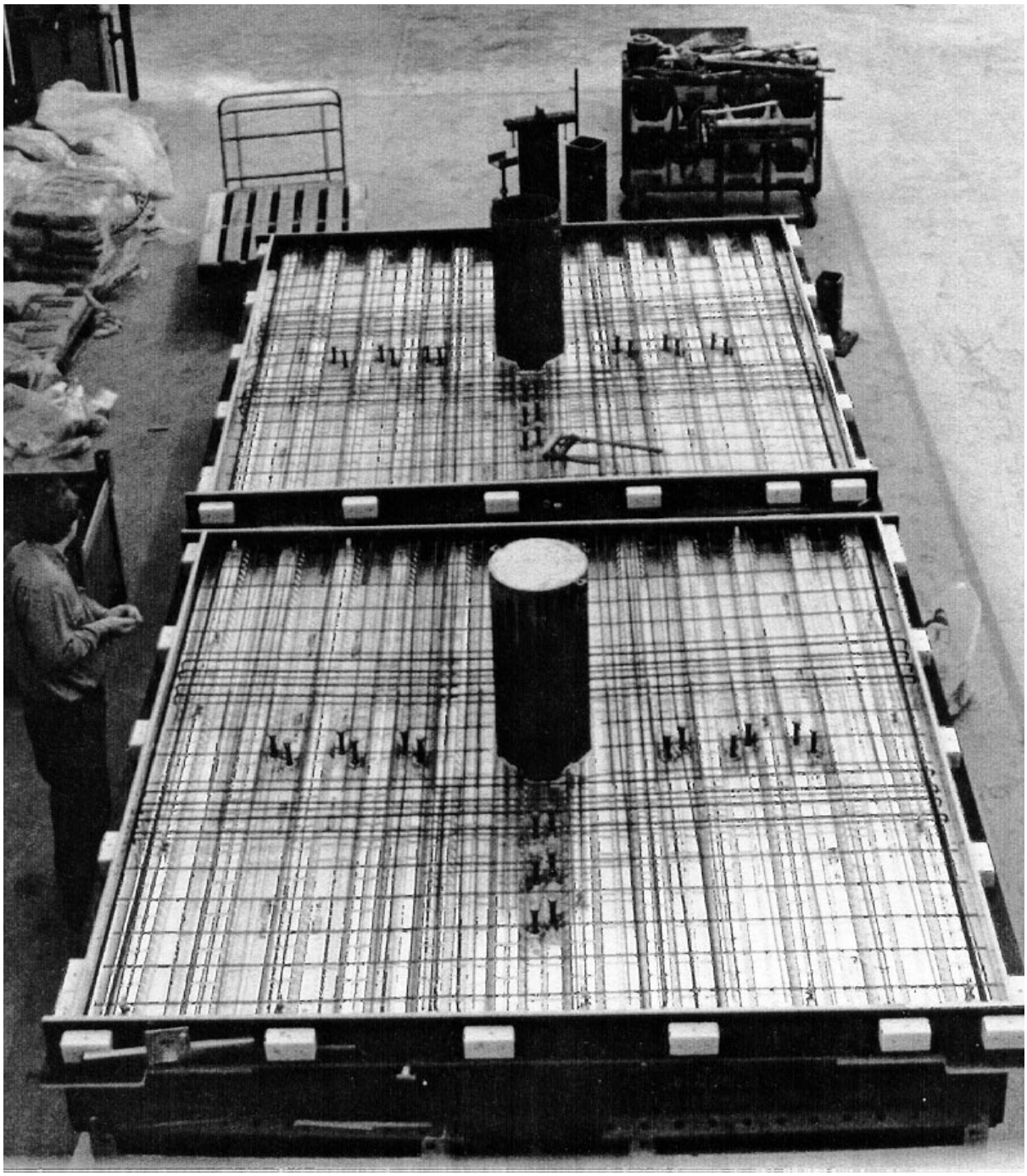

Photo 3.4 Assembly test specimens test series 4: specimens before pouring the concrete

3.3.4.2 Concrete composition of composite floors

Ready mixed concrete of quality C20/25 was used for pouring into the formwork for the floors of the specimens for series 4. Two mixes of concrete were used for pouring the concrete floors for two series of specimens. The first mix was for specimens 4C1 and 4C2 and the second mix for the specimens 4C3 and 4C4.

Concrete composition for the first mix:

- maximum particle size = 16 mm
- cement content = 320 kg/m^3 HC-A , consistency = 3 according to NEN 5950 (ISO 4103 (1979) class S3-S4), where necessary achieved with a superplastifier
- water content = 130 litres
  water cement (w/c) ratio = 0.41

The following properties of the concrete were determined:

- slump according to NEN 5956 (ISO 4109 (1980)[3]) = 210 mm
- flow according to NEN 5957 (ISO 9812[4]) = 490 mm
- density of fresh concrete according to NEN 5959 (ISO 6276, 1982) = 2374 kg/m^3
- air content of fresh concrete according to NEN 5962 (ISO 4848, 1980) = 0.4 % v/v

Concrete composition for the second mix

- maximum particle size = 16 mm
- cement content = 320 kg/m^3 HC-A consistency = 3 according to NEN 5950 (ISO 4103 (1979) class S3-S4), where necessary achieved with a superplastifier
- water content = 130 litres
  water cement (w/c) ratio = 0.41

The following properties of the concrete were determined:

- slump according to NEN 5956 (ISO 4109 (1980)[5]) = 180 mm
- flow according to NEN 5957 (ISO 9812[6]) = 470 mm
- density of fresh concrete according to NEN 5959 (ISO 6276, 1982) = 23471 kg/m^3
- air content of fresh concrete according to NEN 5962 (ISO 4848, 1980) = 1.6 % v/v

---

[3] The compaction required for NEN 5956 is less than for ISO 4109

[4] The cone capacity required for NEN 5957 is larger than for ISO 9812

[5] The compaction required for NEN 5956 is less intensive than for ISO 4109

[6] The cone capacity required for NEN 5957 is larger than for ISO 9812

Table 3.6 Concrete cube properties of batch 1 used for composite floor of specimens 4C1 and 4C2

Cube No.	Age	150*150*150 Cube strength of specimens in 95% R.H. climate chamber		150*150*150 Cube splitting tensile strength of specimens in 95% R.H climate chamber		Modules of Elasticity of 100*100*400 Prism	
	[days]	[N/mm^2]	[N/mm^2] Averaged	[N/mm^2]	[N/mm^2] Averaged	[N/mm^2]	[N/mm^2] Averaged
7210	28	35.88					
7211	28	36.01	35.84				
7212	28	35.62					
7213	28			3.71			
7214	28			3.46	3.49		
7215	28			3.30			
7228	28					36380	
7229	28					34180	36500
7230	28					38940	
7216	41	37.90					
7217	41	38.36	37.64				
7218	41	36.66					
7219	41			3.38			
7220	41			3.48	3.58		
7221	41			3.89			
7222	73	42.11					
7223	73	39.38	40.64				
7224	73	40.42					
7225	73			3.75			
7226	73			3.85	3.79		
7227	73			3.77			

Table 3.7 Concrete cube properties of batch 2 used for composite floor of specimens 4C3 and 4C4

Cube No.	Age	150*150*150 Cube strength of specimens in 95% R.H. climate chamber		150*150*150 Cube splitting tensile strength of specimens in 95% R.H climate chamber		Modules of Elasticity of 100*100*400 Prism	
	[days]	[N/mm^2]	[N/mm^2] Averaged	[N/mm^2]	[N/mm^2] Averaged	[N/mm^2]	[N/mm^2] Averaged
7312	28	36.59					
7313	28	33.54	34.59				
7314	28	34.71					
7316	28			3.77			
7317	28			2.90	3.34		
7330	28					35650	
7331	28					37330	36447
7332	28					36360	
7318	67	41.91					
7319	67	39.10	40.18				
7320	67	39.45					
7321	67			3.71			
7322	67			3.96	3.84		
7323	67			3.85			
7324	106	41.59					
7325	106	41.07	40.72				
7326	106	39.51					
7327	106			3.63			
7328	106			3.57	3.60		
7329	106			3.60			

3.3.4.3 Concreting operations for the composite floor

The formwork for the floors is prepared with reinforcement bars and meshes (see Photo 3.5), the ready mixed concrete is then poured by a skip. After pouring, the concrete is then compacted by a needle and surface vibrators and the surface is trowelled flat.
The formwork and reinforcement bars and meshes are positioned in such a way that the thickness of the floor, after trowelling the concrete surface smooth, is 110 mm, and the cover to the reinforcement bars is 15 mm.
From each mix twenty 150*150*150 cubes and one 75*75*150 prism are cast according to NEN 5956 (ISO 2736/2 (1986)). All the cubes and the prism are cured in a humidity chamber at 20^0 and 95% relative humidity. These cubes are used for or determination of the cube strength and the cube splitting tensile strength, whereas for the determination of the E modulus the prism is used.

3.3.4.4 Properties of cured concrete cubes for the composite floors

At the start of testing each series of four specimens, the following properties are determined: The cube compression strength according to NEN 5968 (ISO 4102 (1978)) (3 cubes); the splitting tensile strength according to NEN 5969 (ISO 4108 (1980))
(3 cubes); the modulus of elasticity according to NEN 3880, Part G, Clause 609.2.1, page 463, using the 75 x 75 x 150 mm prism (one prism). At the same day of testing the third specimen, the compression strength of 3 cubes and the splitting tensile strength of 3 cubes are determined. When the last specimen is tested, the compression strength of 3 cubes and the splitting tensile strength of 3 cubes are again repeated.
The results of the cube and prism tests are given in Table 3.6 for the specimens 4C1 and 4C2, whereas for specimens 4C3 and 4C4 they are given in Table 3.7. The following observations are made:

- The expected control cube strength of 25 N/mm^2 at 28 days is achieved.
- The hardened cube strength in the period of testing increased to 41 N/mm^2.
- The average hardened splitting tensile strength over the testing period is 3.61 N/mm^2.

Table 3.8 Nominal dimensions test specimen

Series	Test spec.	Configuration	Sizes and Lengths of Plates or Beams	β	2γ	τ	N_2/N_1 or F_2/F_1	Concrete filled column	Stock No. Column	Stock No. Plates or Beams
1	1C1	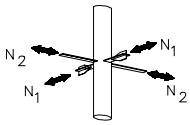	10*120*615	0.37	34	1.05	0		1	1
	1C2		10*120*615	0.37	34	1.05	0	yes	1	1
	1C3		12*170*780	0.52	34	1.26	0		1	1
	1C4		12*170*780	0.52	34	1.26	0	yes	1	1
	1C5		10*120*615	0.37	34	1.05	-1		1	2
	1C7		12*170*780	0.52	34	1.26	-1		1	1
	1C6		10*120*615	0.37	34	1.05	1		1	2
	1C8		12*170*780	0.52	34	1.26	1		2	1
2	2C1	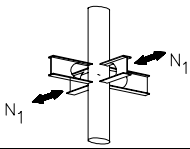	IPE 240-600	0.37	34	1.03	0		2	3
	2C2		IPE 240-600	0.37	34	1.03	0	yes	2	3
	2C3		IPE 360-800	0.52	34	1.34	0		3	1
3	3C1	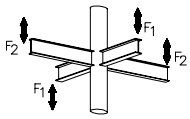	IPE 240-1200	0.37	34	1.03	0		2	1
	3C2		IPE 240-1200	0.37	34	1.03	0		2	1
	3C3		IPE 240-1200	0.37	34	1.03	-1		2	2
	3C4		IPE 240-1200	0.37	34	1.03	1		2	2
4	4C1	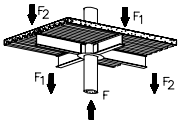	IPE 240-1200	0.37	34	1.03	0		3	6
	4C2		IPE 240-1200	0.37	34	1.03	1	yes	3	6
	4C3		IPE 240-1200	0.37	34	1.03	0		3	7
	4C4		IPE 240-1200	0.37	34	1.03	1	yes	3	7

3.4 Measured dimensions

Table 3.8 gives all the relevant details, including the nominal sizes and lengths of members used in test specimens.

The actual dimensional measurements were taken from stubs, which were also used for the determination of the mechanical properties, with the exception of the CHS columns, where additional measurements of thickness around the circumference have also been made on individual specimens, mainly for series 1 and 2, where imperfection sensitivity was observed. The stock numbers for the members of each test specimen are also identified in Table 3.8. Tables 3.9 to 3.11give the average actual measurements for the stubs from each stock number, for the CHS, IPE and plate (including floor) sections, respectively. The cross-sectional areas of the specimens were based upon weights of the stubs from each stock length

(approximately 700 mm long), measured up to an accuracy of 0.01 kg. A density of 7850 kg/m^3 was used whereas the stock lengths was accurately measured to calculate the cross-sectional areas.

For each of the stubs from the different stock lengths, a number of measurements were taken of the different components to obtain the average thickness. Table 3.9 shows the averaged measured values for the diameter of CHS sections and the CHS wall thicknesses. For the I-sections, Table 3.10 shows that 4 locations are taken in each flange and 3 locations in the web for the thickness measurements. The I-beam heights were measured at three locations and the widths of both flanges were also measured. All 4 fillet radii were also measured to an accuracy of 0.5 mm with gauges. Table 3.11 shows 3 measurements of plate thicknesses and 4 measurements of steel floor thickness from the stubs, used to determine the average thickness.

Table 3.9 Averaged measurements for each stock number from CHS columns

Stock No.	d_0 [mm]	t_0 avg. from 16 measurements [mm]	Cross-sectional area [mm^2]
1	324.4	9.48	9521
2	324.3	9.44	9393
3	324.2	9.30	9320

Table 3.10 Averaged measurements for each stock number from IPE sections

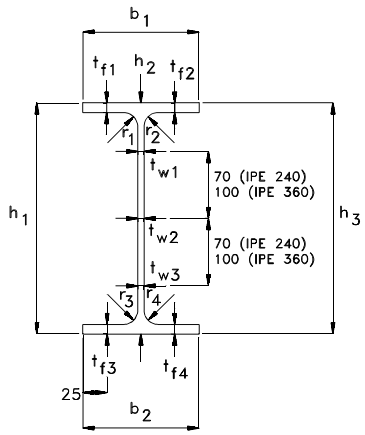

Type of beam	Stock No.	t_f [mm]	t_w [mm]	b [mm]	h [mm]	r [mm]	Cross-sectional area [mm^2]
	1	9.82	6.59	120.02	242.13	15.13	3969
	2	9.80	6.58	120.41	242.02	15.25	3988
IPE 240	3	9.74	6.42	120.00	242.08	15.25	3934
	6	9.87	6.83	119.90	242.33	15.63	3996
	7	9.83	6.64	119.80	242.33	15.88	3928
IPE 360	1	12.84	8.15	169.69	363.79	15.75	7282

Table 3.11 Averaged measurements for each stock number from Plates 120*10, 170*12 and steel floor

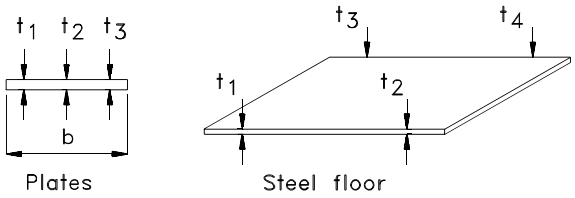

Plate width	Stock No.	Thickness [mm]	Width (b) [mm]	cross-sectional area [mm^2]
120	1	9.90	119.9	1187
	2	9.97	119.7	1193
170	1	11.53	170.0	1960
Steel floor	1	4.93	-	-

3.5 Weld measurements

The weld measurements are also given as average values, but in contrast to the dimensional measurements of the member sizes, the welds were measured individually for each specimen. The measurements made are "horizontal" and "vertical" leg lengths, representing leg lengths on beams (or plates) and the columns, respectively.

For series 1 using CHS with axially loaded plates, measurements of the leg lengths were made for the butt welds on one side of the plate and the back weld run on the other side at 3 positions of the plate width (see also Figure 3.6). The weld sizes at the two plate corners were also measured. For series 2 using CHS columns with axially loaded beams, the same measurements were made as for series 1, but for both the flange plates which were welded to the columns. For series 3 using CHS columns with beams in bending, 20 measurements were made for the leg lengths around each I-beam (the 2 corners, 3 positions on the outer face and 2 positions on the inner face of each flange, and 3 positions on each side of the web). The results of the weld measurements are given in detail by Verheul [17].

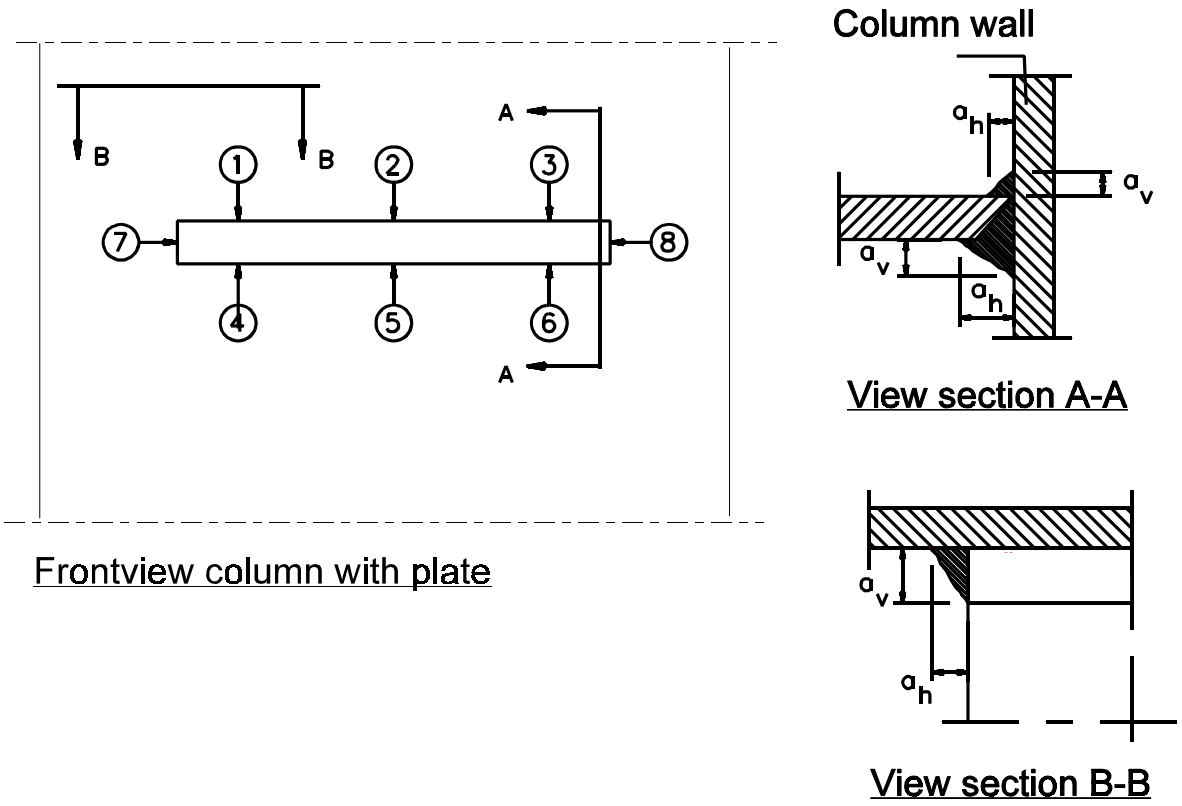

Figure 3.6 Weld measurements for test series 1 and 2

3.6 Test rigs and testing procedures

3.6.1 Connections with axially loaded plates and beams and CHS columns (series 1 and 2)

For the axial load tests two different test rigs were used, namely one for the tests with uniplanar tension load and another for all other tests. The tests with an uniplanar tension load were tested in a tensile machine, since no special precautions had to be made for stability. The test specimens with the in-plane plates in compression were placed in the test rig with the CHS columns in a horizontal position (see Photo 3.5). The ends of the vertically positioned in-plane members (plates or beams) were pin-ended. During the test, the column was maintained horizontal by using a servo controlled hydraulic jack to displace the column vertically at one end of the column. The vertical displacement was measured at both ends of the column with displacement transducers, so that if a difference was noticed, the CHS column was automatically balanced into a horizontal position. The out-of-plane displacement

of the loaded plates and beams was prevented at one-third and two-third positions of the member (plate or beam) lengths by using lateral supports that allow longitudinal displacements.

This prevents buckling of these members under compression loading. The axial load in the vertical direction was applied vertically on the lower member using a servo controlled

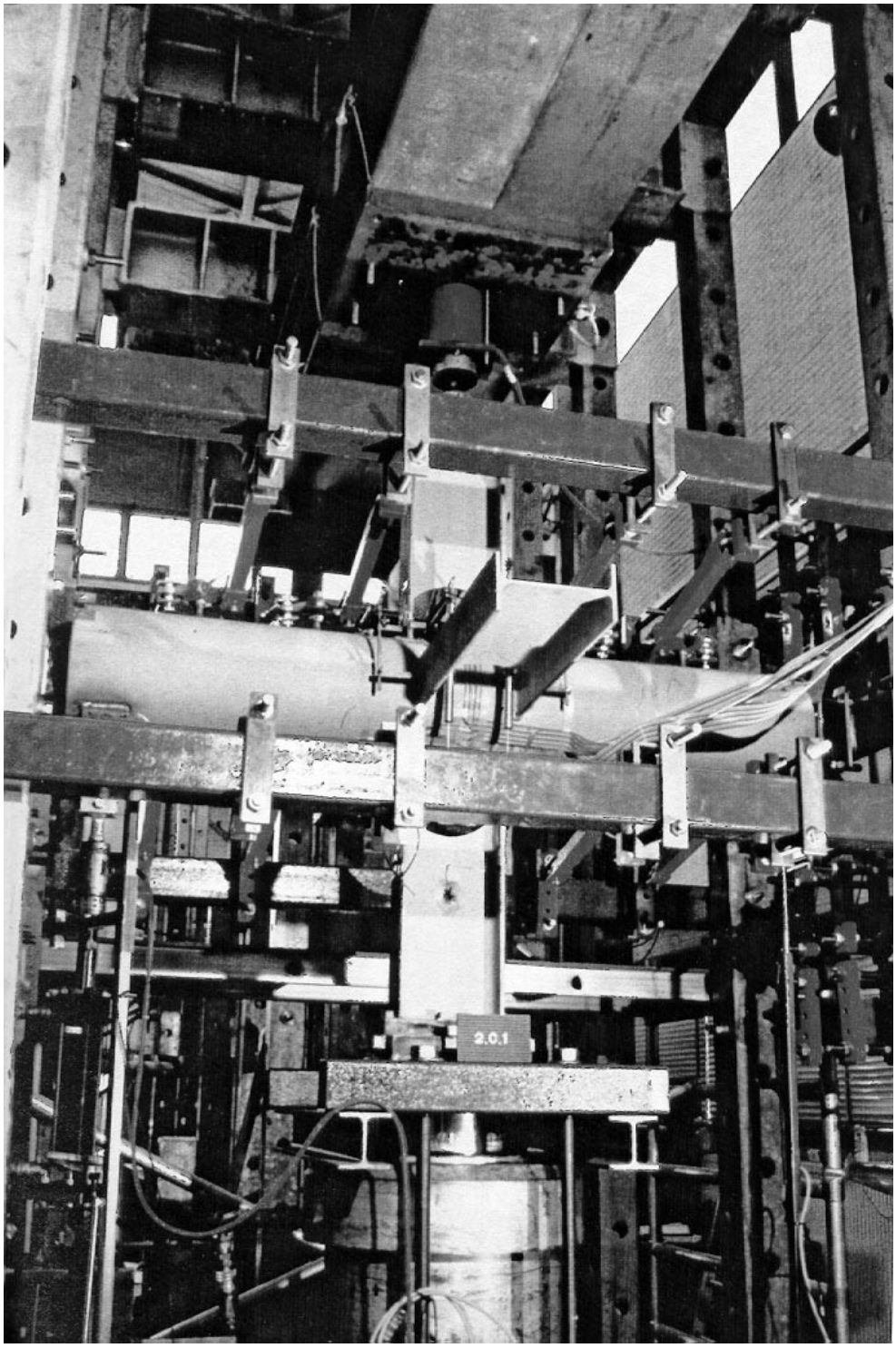

Photo 3.5 Test rig for series 1 and 2

hydraulic jack, while the upper member was pin-supported to the reaction frame through a dynamometer, which measures the axial load. The load was applied by force control until the first occurrence of non-linearity, after which displacement control was applied for the uniplanar load situations. For multiplanar load cases, the ratio of horizontal to vertical load was always maintained constant.
The horizontal (multiplanar) load was applied by means of a hydraulic jack mounted in an independent frame in the horizontal direction along the horizontal members.
The horizontal load was measured with a dynamometer fitted in the end of the frame opposite to the jack end. The ends of the horizontal members, when loaded, were adjustable supported in such a way that during the test, eccentric loading was prevented. This was controlled by means of displacement transducers measuring the indentations into the columns. The column indentations in the two directions was measured through displacement measurements at three locations of each of the 4 members. These locations are in the middle and the two edges of the members, at a distance of 25 mm from the column face. In addition, strain gauge measurements were made on the members.

3.6.2 Connections with moment loaded beams and CHS columns (series 3 and 4)

The test specimens were placed in the test rig with the column always in a vertical position. The configuration of the test rig is shown in Figure 3.7 for test specimen 3C3, where the beams in the two orthogonal planes were loaded in an opposite direction to each other. For specimen 3C3 (Figure 3.9), the in-plane beams were pulled downwards at their ends by a servo controlled hydraulic jack and spreader beam system as shown in the right half of Figure 3.7. The reaction was taken by tension bars to the top of the test rig frame, through the out-of-plane beams which were orthogonal to the in-plane beams, as shown on the left side of Figure 3.7. The forces and reactions on the in-plane and out-of-plane beams were transmitted through roller bearings to ensure only vertical loads. Hinges were provided at the ends of all the tension bars. Also, load cells were provided at the ends of all tension bars to record loads on each of the four individual beams.
A load cell was also provided at the location of the hydraulic jack to record the total applied load. The jack stroke was also recorded. The jack load was applied in small steps using displacement control.

For the other tests in series 3 and 4 another test configuration was used (see Photo 3.6). The load was applied in compression to the lower end of the column through the servo controlled hydraulic jack and the test specimen was supported at the ends of the I-beams. Roller bearings were provided between the I-beams and the reaction frame at the top of the test rig.

For test specimens 3C1, 3C2, 4C1 and 4C2, where uniplanar loading was applied to the in-plane beams, only the in-plane beams were supported.
For test specimen 3C4, 4C3 and 4C4, where all beams were equally loaded downwards, to give a moment with tension on the top flange, all four beams were supported at equal distances away from the face of the column, to give the same moments at the column face. The bending moment in the connection throughout this report was taken at the chord wall face.

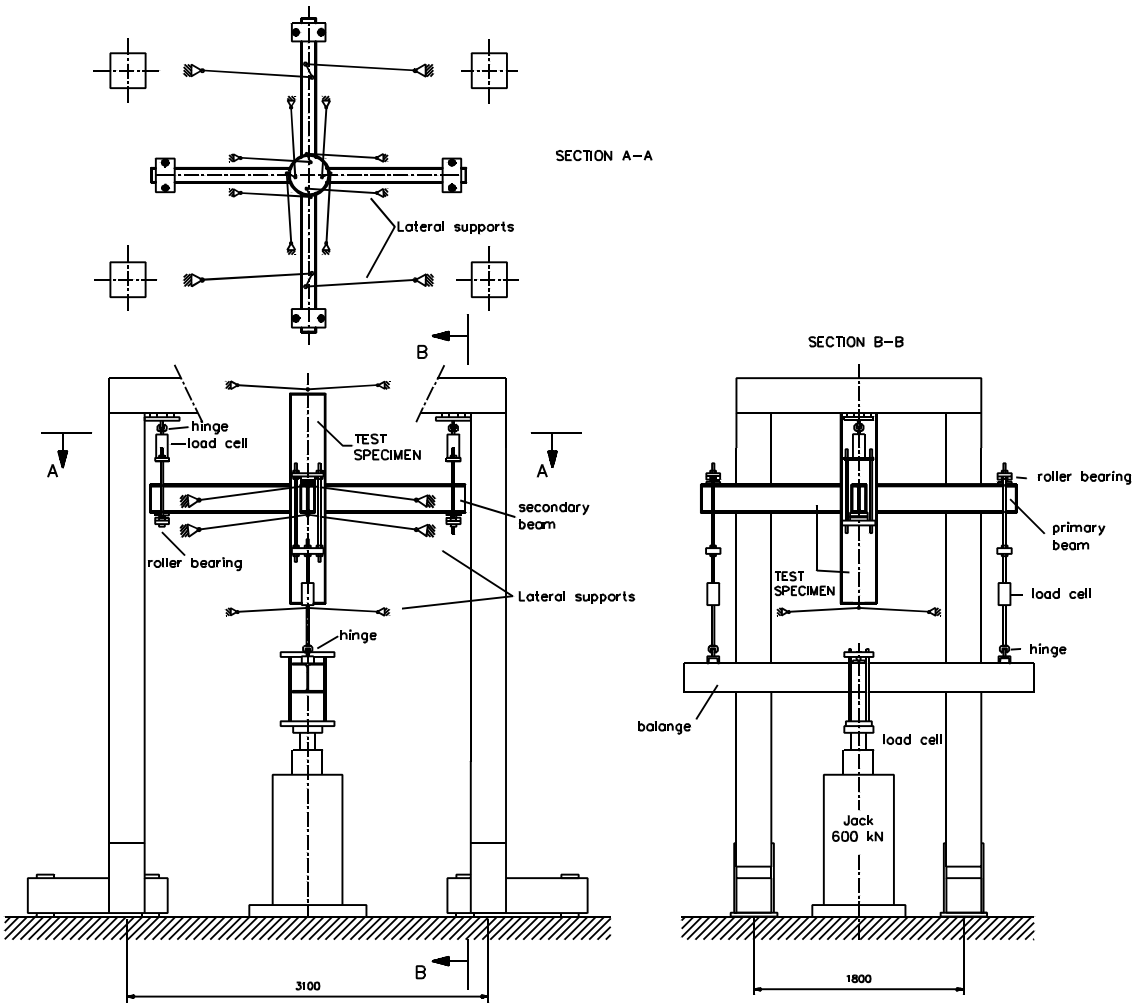

Figure 3.7 Test rig for test 3C3 with load ratio -1.

The used method of loading and supporting the specimens (3C4, 4C3 and 4C4) for multiplanar loading, induces equal deformations of the in-plane and out-of-plane beams, and does not guarantee equal loading on the in-plane and out-of-plane beams. For 4C4 it can be expected that in-plane and out-of-plane loadings will be the same, because of the symmetry of the specimen. However, due to the orthotropic behaviour of the composite floor, differences could be expected for test 4C3 and 4C4.

Load cells were provided at the supports to measure reaction forces at the beam ends and one load cell was placed between the jack and the test specimen. The jack stroke was also recorded.

Photo 3.6 Test rig for test series 4

For all test specimens, the column was supported in the two directions by lateral supports to prevent lateral displacements in any direction. For beams, lateral displacement was also prevented by lateral supports at the unrestrained flanges of the loaded beam ends, see also Figure 3.7.

3.7 Measurements

3.7.1 Strains

Strain gauges were provided at a number of cross-sections of members, so that the forces and moments in the member may be determined in order to control the applied jack loads measured by the dynamometers. Any lack of symmetry in the loading was also controlled by the strain gauges during the loading process. The details of the strain gauge measurements are given by Verheul et al [17].

3.7.2 Column indentations for the axially loaded specimens (series 1 and 2)

During the tests, the column indentations were measured and recorded for all the specimens in series 1 and 2, using electrical transducers. Also, problems of stability were encountered with the detail and interaction tests comprising series 1 and 2, where the specimens were always tested with the column in a horizontal position. Therefore, electrical transducers were provided at the ends of the column to ensure that the vertical displacements at the column ends were the same. Any difference was adjusted by a jack at one end that applies small compressive or tensile forces to bring the column back to the horizontal position. For those tests, where multiplanar loading was applied, so that the out-of-plane members were also subjected to load, the same problem could occur due to bending moments created by the ends of the out-of-plane beams not being in line with the direction of force. Therefore, for cases with the out-of-plane members under load (1C5 to 1C8), transducers were also used at the ends of these members to measure their displacements and correct them with a jack at the ends of the two out-of-plane members.

3.7.2.1 Transducer measurements for series 1

Figure 3.8 give schematic details of the transducers used in series 1. For the in-plane members which were placed vertically in the test rig, transducers 1 and 2 (Figure 3.8) measured the vertical displacements of the column ends so that any variation from the horizontal could be corrected by tensile or compressive forces with the jack at one end.

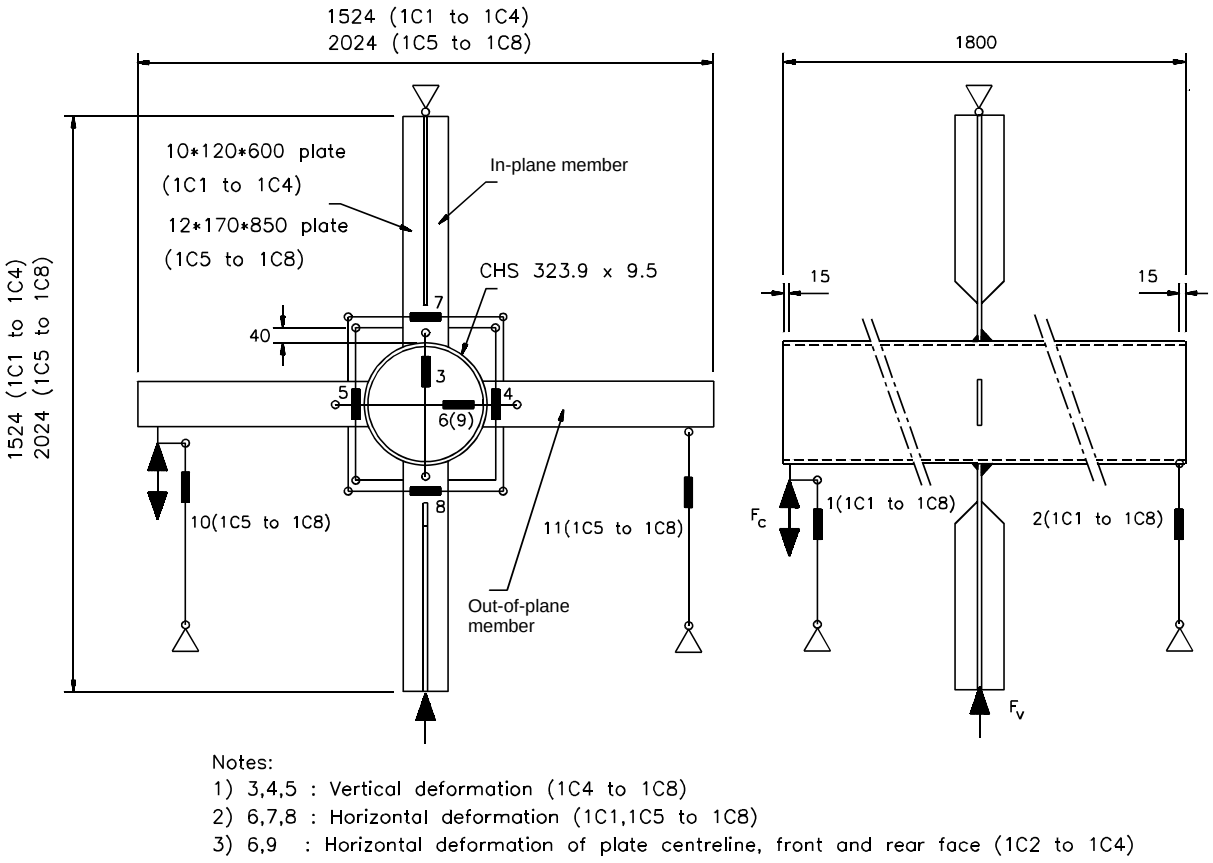

Figure 3.8 Locations displacement transducers for test series 1

For the specimens where both in-plane and out-of-plane members were loaded (1C5 to 1C8), the transducers 10 and 11 also help in maintaining the ends of the out-of-plane members at one level so as not to introduce bending moments in them.

Transducers 3, 4 and 5 measured the central and two edge displacements of the two in-plane members at positions 40 mm from the column face. This effectively measured the sum of the indentations due to the two in-plane members into the column. Transducers 6, 7 and 8 for specimens 1C1 and 1C5 to 1C8 made similar measurements as transducers 3, 4 and 5, but in the horizontal direction between the out-of-plane members. However, for specimens 1C2 to 1C4, where the out-of-plane members were unloaded, transducer measurements were only made along the centre line, on both sides of the out-of-plane members (plates).

3.7.2.2 Transducer measurements for series 2

Figure 3.9 gives the schematic details for the transducers used in series 2. Transducers 1 and 2 measured the vertical displacements of the ends of the column. These measurements were used to keep the column in horizontal position. Transducers 3, 4 and 5 measured the central and two edge displacements between positions at 40 mm from the column face of the flanges which are on one side of the neutral axis of the two in-plane members. Transducers 7, 8 and

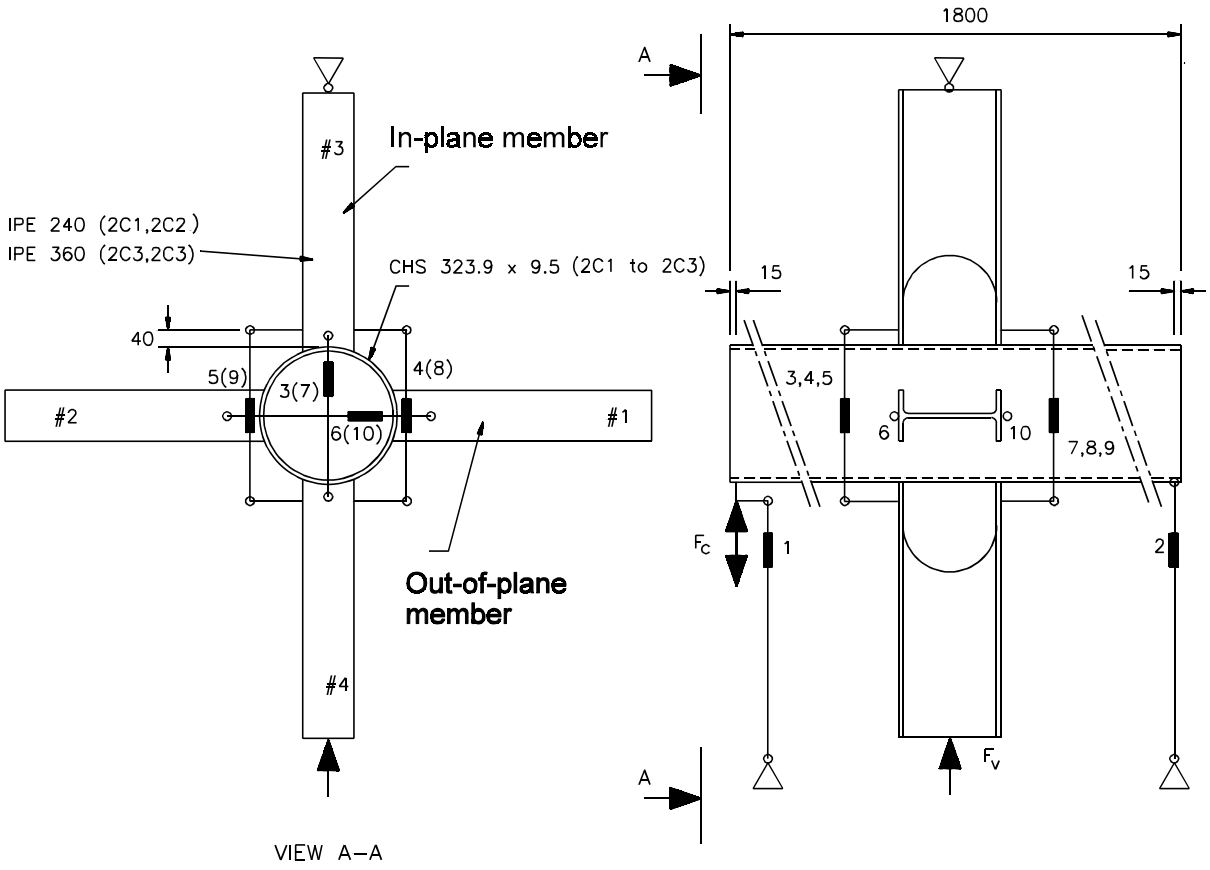

Figure 3.9 Location displacement transducers for test series 2

9 did the same on the flanges which are on the other side of the neutral axis of the two in-plane members. Transducer 6 measures the flange centre line displacement between the out-of-plane members at 40 mm distance from the column face on one flange, while transducer 10 does so for the other flange. These two measurements were adequate for series 2, where all of the out-of-plane beams were unloaded.

3.7.3 Transducer measurements for series 3

Four electrical transducers (identified by numbers 9 to 12 in Figure 3.10) were used to measure and record column indentations for all the specimens in series 3.
The indentation measurements were the same as for series 1 and 2. These measurements were taken by measuring the change in distance between the two opposite flanges in one plane. This movement was recorded on the top and bottom flanges, at a distance of 40 mm from the column face along the centre line of the beam flange. This measurement therefore gives the sum of the indentations due to the two beams in one place. The average indentation was therefore obtained by dividing this value by two.
At approximately one-third and two-third positions of each beam length on both the in-plane and the out-of-plane beams, displacements during load application were measured with 8 electrical transducers, identified by numbers 1 to 8 in Figure 3.10.

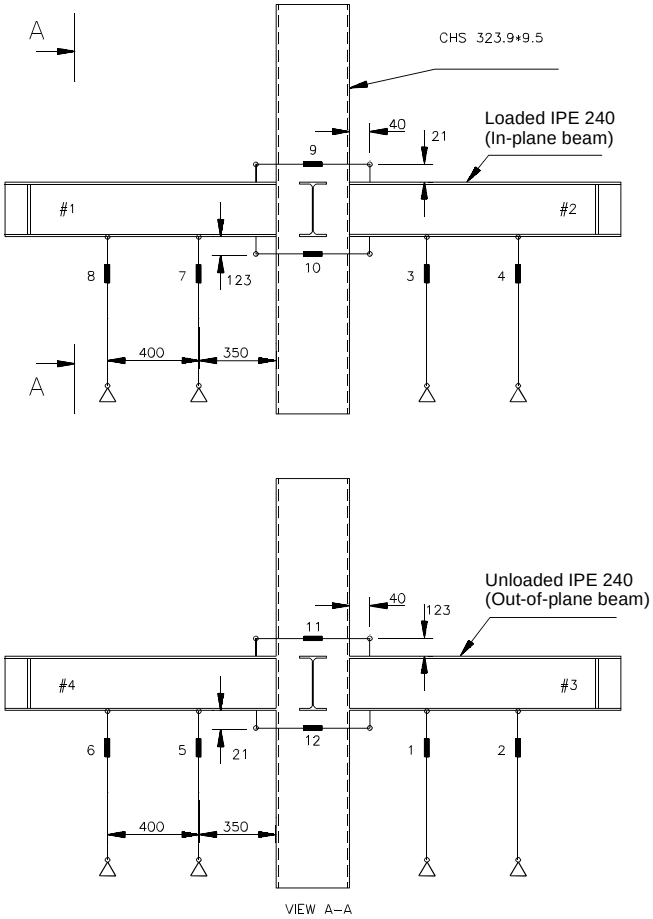

Notes:
1) All transducer measurements are along beam centre–lines
2) Deflection of loaded beams at locations 3, 4, 7 and 8
2) Deflection of unloaded beams at locations 1, 2, 5 and 6
3) Deformation of column at locations 9, 10, 11 and 12

Figure 3.10 Location displacement transducers for series 3

3.7.4 Transducer measurements for series 4

For measuring the horizontal displacements of the concrete floor adjacent to the column wall, the concrete floor has been provided with two transducers (79, 95) in the two main directions (see Figure 3.11). For measuring and recording the column indentations, four transducers were used. The positions of the transducers (80, 403, 96 and 404) is also shown in Figure 3.11). The slip between the stiffener ring and the bottom flange of the in-plane beams was determined by the transducers 80 and 403. For the out-of-plane beams, the slip is determined by the transducers 96 and 404. For measuring the horizontal displacements between I-beams and the column wall, the specimens were provided with transducers 405, 406, 407 and 408. At approximately one-third and two-third positions of each beam length on both in-plane and out-of-plane beams, displacements during load application were also measured by 8 electrical transducers, identified by numbers 48, 47, 63, 64, 32, 31, 143 and 144, in Figure 3.11.

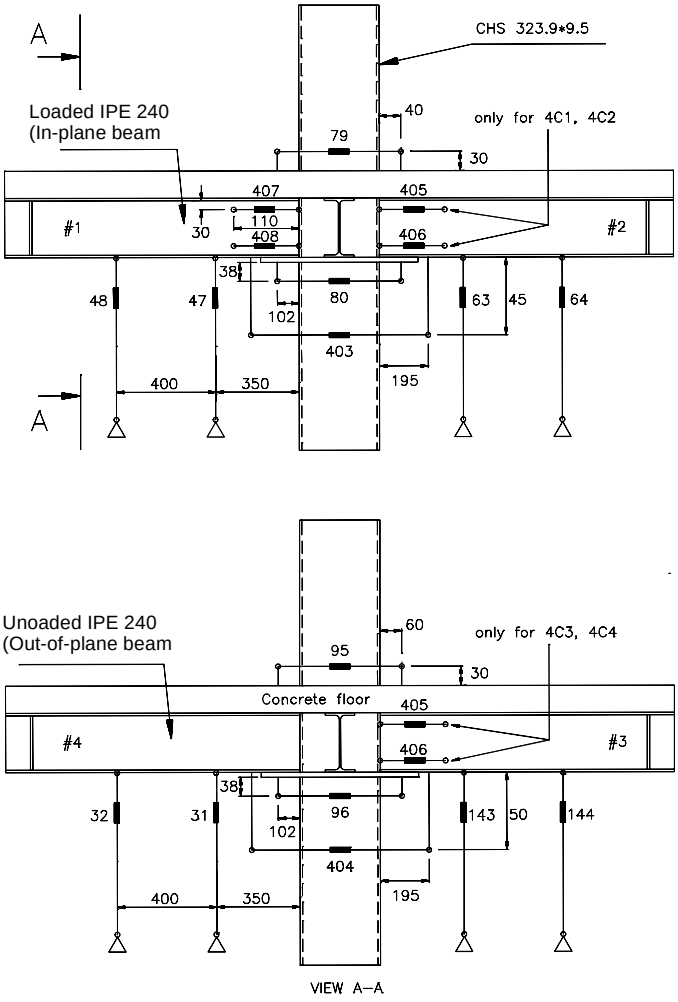

Figure 3.11 Location displacement transducers for series 4

3.7.5 Determination of the beam rotation for series 3 and 4

The first method of calculating the beam rotations is by using the two recorded displacements at their one-third and two-third positions, corrected by the elastic deformations of the beam, and dividing by the distance between the displacement transducers, as shown in Figure 3.12. The rotation is also calculated in a second manner, by adding the transducer measurements used in calculating the column indentation at the upper and lower flange locations, and dividing by the distance between the measurement points of the upper and lower flanges. Both methods give approximately the same results for the investigated type of connections, since the elastic deformations in the beams are small.
Therefore, all the moment-rotation diagrams, the first method, without correction for the elastic beam deformation, is employed.
For test series 4, the beam displacements at the two-third locations (the locations closest to the column) were measured using potentiometers instead of LVDT's (Linear velocity displacement transducers). The measurements of these potentiometers appeared to be not accurate enough in the first part of the tests for the determination of the linear part of the moment-rotation curves. The displacements of the hydraulic jack were used to calculate the beam rotations instead of the measurement results of the potentiometers.

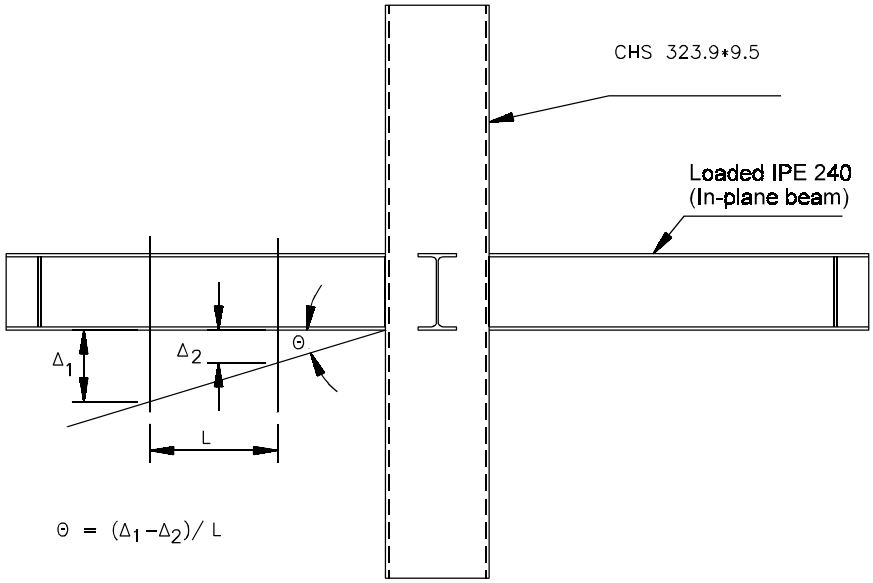

Figure 3.12 Definition of the connection rotation

3.8 Results of the experimental tests

For axially loaded plates and beams (series 1 and 2), the average column indentation represents the average of the indentations into the column due to the two members (plates or beams) in the same plane. For beams under in-plane bending moment, the rotations plotted are the average rotation of the two beams in the same plane.
The moments given in the plots are at the column face at the crown position.
For the axially loaded connections, the testing was stopped when the average indentation is approximately 10% of the column diameter, even if the maximum load was already detected. Thus, the information on the deformation capacity and the possible failure modes were obtained. For beams subjected to bending moments, the testing was stopped when the average beam rotation was approximately 0.15 radians.
For the series 1 tests (1C1 to 1C8), all the connections without a concrete filled column (1C1, 1C3, 1C5 to 1C8) failed by column plastification (see Photo 3.8). Specimen 1C2, with a composite column, in-plane plate members in tension and out-of-plane members unloaded, failed by plate yielding followed by punching shear in the column wall, at the weld toes of the in-plane plate member corners (see Photo 3.7). Specimen 1C4, also with a concrete filled column, but with in-plane plate members in compression and unloaded out-of-plane

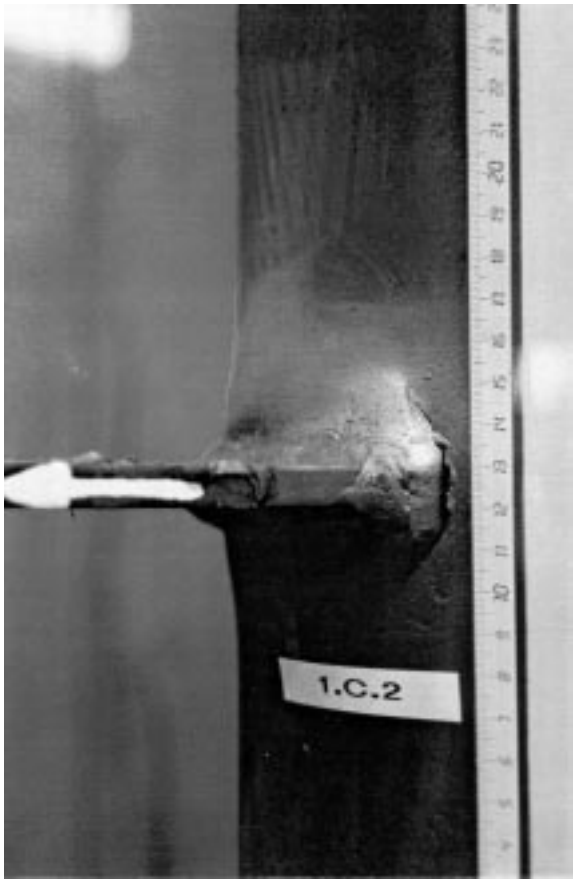

Photo 3.7 Test specimen 1C2 after testing

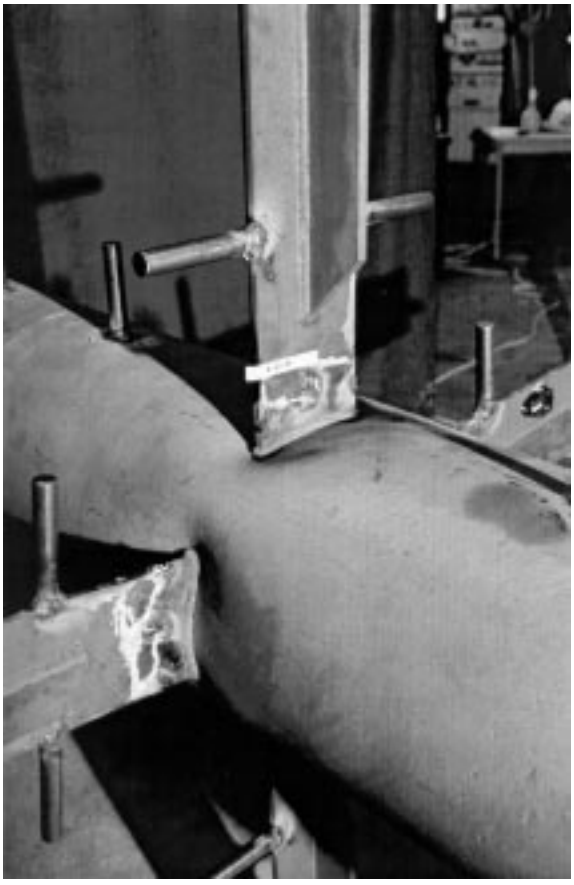
Photo 3.8 Test specimen 1C6 after testing

members, failed by buckling of the in-plane plate members under compression. The maximum load for this test is 15% below the squash load of the in-plane plate member, which could be due to a combination of bending and axial force. Theoretically it can be shown that an eccentricity of 3.4 mm is required to give a 15% lower ultimate load than the squash load. The strain gauge measurements also show a considerable amount of plate bending, which is unavoidable because of the one-sided single V butt welds between the plate members and the column. The main results of test series 1 are given in Table 3.12. The load-deformation curves are shown later on in Figures 5.4 to 5.11.
For the series 2 tests (2C1 to 2C3), the connections 2C1 and 2C3 without a concrete filled column failed by column plastification.

Table 3.12 Experimental results for test series 1 and 2

	TEST	β	Concrete infill in column	$\frac{N_2}{N_1}$	N_1 in Compr. or Tens.	N_u [kN]
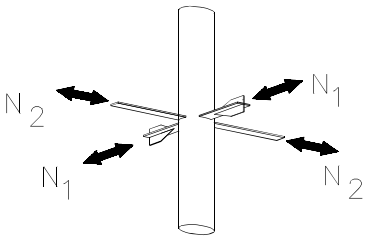	1C1	0.37	no	0	C	245.3
	1C2	0.37	yes	0	T	510.8
	1C3	0.52	no	0	C	325.0
	1C4	0.52	yes	0	C	670.8
	1C5	0.37	no	-1	C	175.6
	1C6	0.37	no	+1	C	300.8
	1C7	0.52	no	-1	C	220.1
	1C8	0.52	no	+1	C	499.9
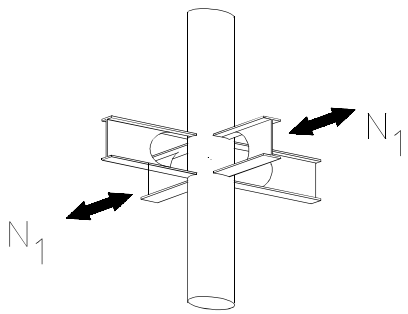	2C1	0.37	no	0	C	350.6
	2C2	0.37	yes	0	T	971.8
	2C3	0.52	no	0	C	456.0

Specimen 2C2, with a composite column, in-plane beams in tension and out-of-plane beams unloaded, failed by punching shear in the column wall, at the weld toes of the flange corners of the in-plane beams. The main experimental results of test series 2 are given in Table 3.12, the load-deformation curves are shown in Figures 5.12 to 5.14. For series 3 (specimens 3C1 to 3C4), all test specimens failed by column plastification (see Photo 3.9). For some specimens, cracks were observed at the weld toes of the tension flanges. These small cracks occur in the plastic region of the moment-rotation curves. There is no drop in the moment capacity after the visual observation of the cracks.

For the connection with the steel floor (3C2), a larger stiffness and slightly larger ultimate strength was observed than for the identical specimen 3C1 without a steel floor and subjected to an identical loading condition. The main experimental results are listed in Table 3.13, the moment-rotation curves are given in Figures 5.18 to 5.21.

For series 4, the test specimens failed by progressive failure of the reinforcement bars in the composite floor. During the tests cracks in the composite floor started to grow from the column to the edges of the floor. The reinforcement bars started to fail one by one at one side of the floor, from the outside to the inside (see Photo 3.10). The main experimental results are listed in Table 3.14 and Figures 5.22 to 5.29. The Figures 5.26 to 5.29 show the cracking patterns in the concrete floor after testing.

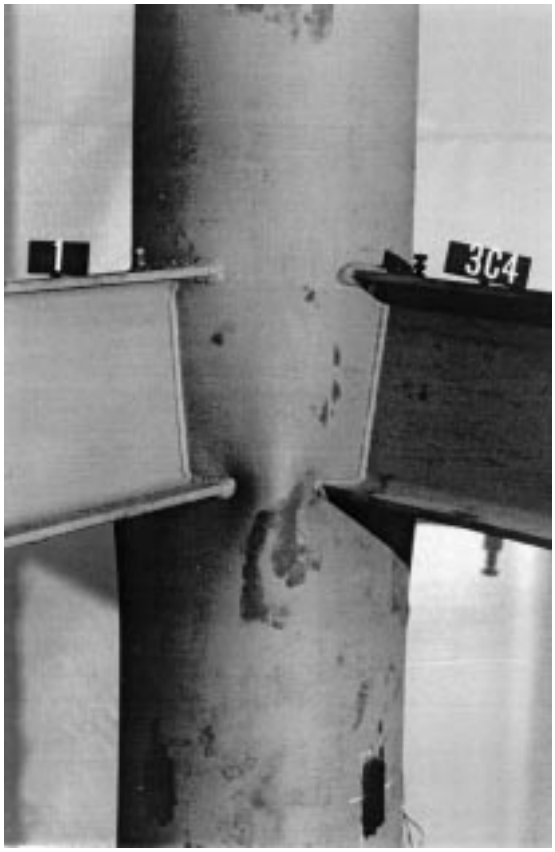

Photo 3.9 Test specimen 3C4 after testing

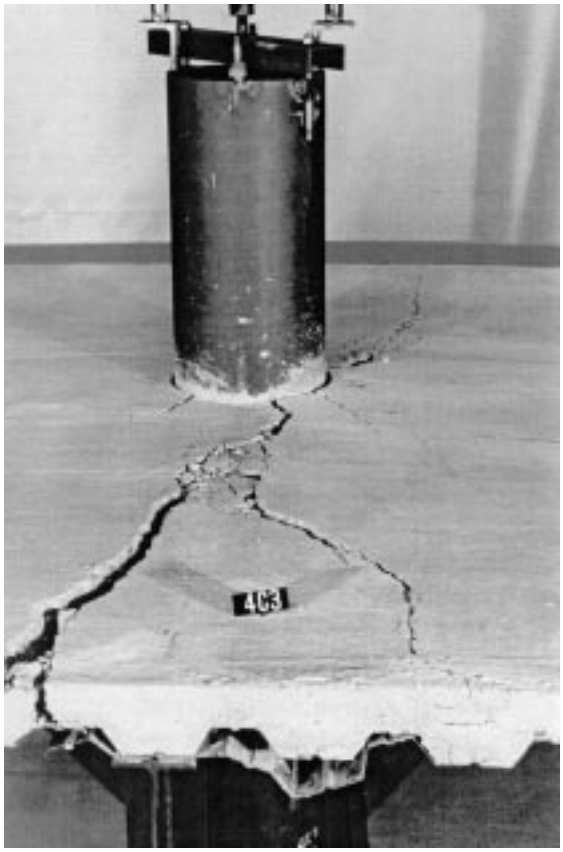

Photo 3.10 Test specimen 4C3 after testing

Table 3.13 Experimental results for test series 3

	TEST	β	Concrete infill in column	$\frac{F_2}{F_1}$	Steel Floor	M_u [kNm]
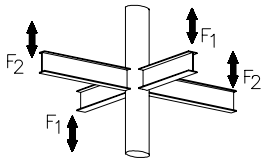	3C1	0.37	no	0		82.5
	3C2	0.37	no	0	yes	87.6
	3C3	0.37	no	-1		54.1
	3C4	0.37	no	+1		79.0

Table 3.14 Experimental results for test series 4

	TEST	β	Concrete infill in column	$\frac{F_2}{F_1}$	M_u [kNm] in-plane	M_u [kNm] out-of-plane
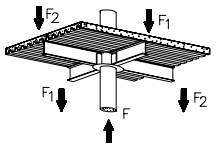	4C1	0.37	no	0	152.99	-
	4C2	0.37	yes	0	177.00	-
	4C3	0.37	no	+1*	128.44	118.41
	4C4	0.37	yes	+1*	121.56	133.93

Note:

)*

For test series 4, the displacements in the in-plane and out-of-plane directions were kept the same and not the loading. At ultimate load, the measured difference between in-plane and out-of-plane loading was approximately 10%.

4 GENERAL DETAILS FOR THE FINITE ELEMENT ANALYSES

4.1 Software and hardware used for the finite element modelling and analyses

For the pre- and postprocessing for the finite element models, the general purpose CAD/CAE program SDRC-IDEAS Level V was used. Apart from the mesh generation tools, the program offers mesh verification options to ensure high quality finite element meshes. Also, this program was used to analyse the results.

The actual finite element analyses were performed with the general purpose finite element package MARC, versions K5.2 and K6.2. No differences were observed between the results of these two different versions. The program Mentat 5.4.3 was used for file conversion between SDRC-IDEAS and MARC.
All finite element pre- and postprocessing was carried out on SUN Sparcstations. The finite element analyses were performed on supercomputers (CRAY YMP4 en Convex 3840) and fast workstations (IBM RS/6000 model 350 and model 3AT).
The calculation time for a typical analyses varied between 2 and 24 hours on the IBM and the Convex, depending on the number of degrees of freedom of the model and the loading type.

4.2 Method of analyses

For the finite element (FE) models, eight node thick shell elements were used with four integration points at Gauss locations, seven layers across the thickness and using Simpson integration (element type 22 in MARC [59]).
The experimentally determined engineering stress-strain curves, obtained with tensile coupon tests, were translated to the true-stress - true-strain relationships, using the Ramberg-Osgood relationship [8]. Figure 4.1 shows typical stress-strain curves for the steel used for a CHS column and an IPE 240 flange.
The load was applied using either displacement or load control, similar to the experimental procedure. Displacement control was used for uniplanar loading conditions and symmetrical multiplanar loading conditions. For the other multiplanar loading conditions load control was used to be able to preserve a fixed ratio between the in-plane and the out-of-plane loadings. For the simulations of test 4C3 and 4C4 the ratio between the vertical displacement of the I-beams was kept constant, similarly to the experiments.
The updated Lagrange method, which allows large curvatures during deformations (see also the MARC manuals [59]) was used for the finite element solution procedure.
During the tests on specimens with composite columns, the column wall near the plate under

tension load was observed to pull away from the concrete filling. The concrete filling was therefore modelled as a rigid contact surface. The characteristics of the rigid contact surface are to provide full resistance against compression and none to tension. The linear elastic deformations of the concrete filling and the adhesive bonding between the concrete filling and the column are neglected with this approach. However, in reality, these influences are small in comparison to the total ovalization for the tensile load cases (1C2 and 2C2). For the test specimen under compression (1C4) the deformations and indentations in the composite columns were observed to be negligible in comparison to the plastic deformation of the plates. Therefore, the numerical modelling assumes a rigid concrete filling in the composite column also for test 1C4, with plates under compression.

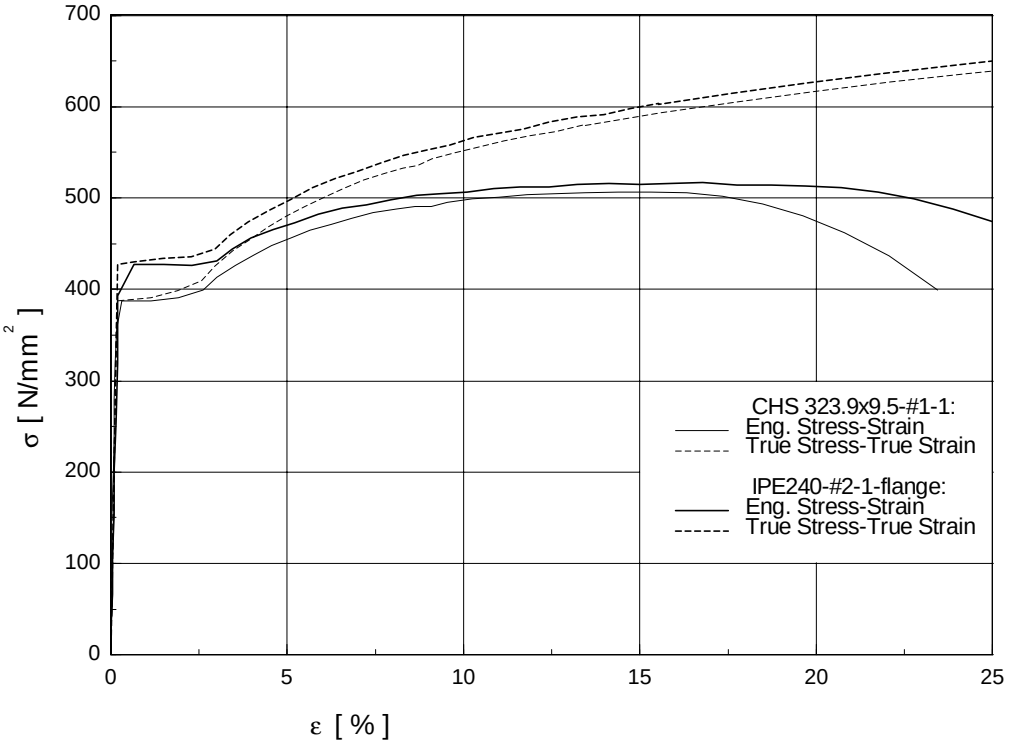

Figure 4.1 Stress-strain curves

4.3 Method of modelling

4.3.1 Calibration

4.3.1.1 General

For the calibration, the finite element modelling uses the averaged values of the measured dimensions for each component of a test specimen. Due to the fabrication method of the columns (seamless circular hollow sections), relative large variations of the column wall thickness along the circumference were found. The nominal thickness is 9.5 mm, but the actual thicknesses varied between 9.0 mm and 10.3 mm.
The nodes were placed on the mid-surfaces of the column wall, the beam flanges and the beam webs. Wherever possible symmetry planes were used in order to reduce computer time.
The influence of the welds was simulated using shell elements. Figure 4.2 shows how the magnitude of the dimensional measurements and thicknesses of the shell elements, modelling the welds, were obtained for model 3C3. The welds of all other models were modelled using the same method.

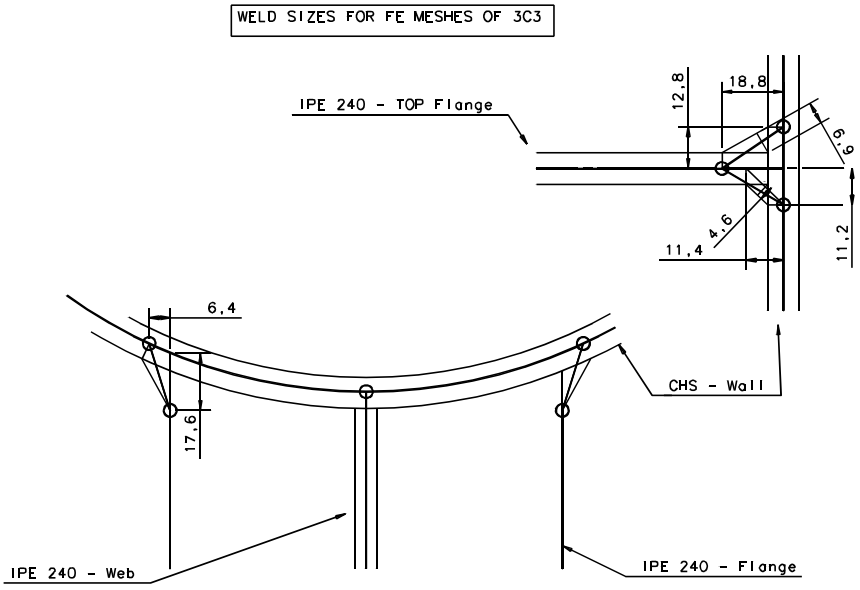

Figure 4.2 Weld modelling for test 3C3

A more accurate method to model the welds is using solid elements. However, a FE model with solid elements leads to an unacceptable amount of computer time for this type of non-linear FE calculations.
The used method provides a realistic method to model the influence of the welds on the strength and stiffness of the connections. However, the method does not give accurate

predictions of the stresses and strains near the welds, therefore this modelling method cannot be used for FE analyses to obtain stress concentration factors. The same method was also used successfully by other researchers (Lu [14], Van der Vegte [16] and Yu [18]).
For the modelling, symmetry planes were used where possible. Two different stress-strain curves were used for the FE analysis of each connection, one for the column and one for the I-section beam or plate. It should be noted that the yield stress of the beam web is higher than the yield stress of the beam flanges. However, since there is no significant plastification in the beam web, so the material properties of the flanges were also used for the web.

4.3.1.2 Test series 1, axial loading tests

For the calibration of the models for test series 1, the boundary conditions chosen for the FE models are similar to those of the experimental tests, to get a realistic simulation of the tests. In the experiments plates under compression were supported in the in-plane direction to prevent local buckling of the plates. The locations of these lateral supports were at one third and at two third of the plate lengths. Also, the columns were restrained at four locations at both sides of the column to prevent global rotation of the column.
For the FE modelling, symmetry planes were used (see Figures 4.3 and 4.4). For all models, except for 1C1 and 1C3, one fourth of the specimens is modelled.
After testing, the deformed shapes of the specimens 1C1 and 1C3 were rather asymmetric. A significant difference in indentation at both sides of the column was observed. Additional measurements along the circumference of the thicknesses of the column wall showed a variation in thickness from 9.2 to 9.56 mm for specimen 1C1 and from 9.32 to 9.65 mm for specimen 1C3. These thickness variations were taken into account for models 1C1 and 1C3, therefore for these models half of the specimen was modelled.
For the FE analyses displacement control was used, except for models 1C5 and 1C7. For these analyses load control was used to preserve a fixed ratio of -1 between the axial loads on the in-plane and out-of-plane plates. For models 1C6 and 1C8 loaded with a fixed load ratio of +1, the fixed load ratio could also be achieved using displacement control, since the deformations are equal the in-plane and in the out-of-plane direction.

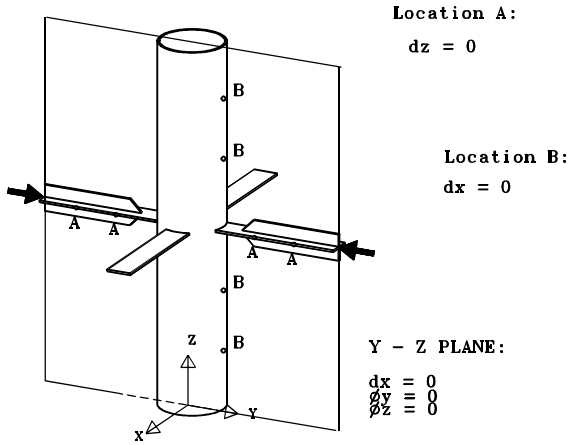

Figure 4.3 Symmetry planes and boundary conditions for models 1C1 and 1C3

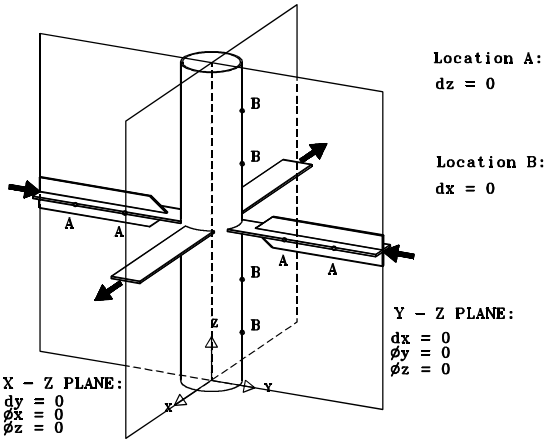

Figure 4.4 Symmetry planes and boundary conditions for model 1C2, 1C4-1C8

4.3.1.3 Test series 2, axial loading interaction tests

The modelling of test series 2 is comparable with the modelling of test series 1. Since the I-beams are symmetrical, an extra symmetry plane could be used (see figure 4.5). All three specimens in this test series were loaded with a uniplanar axial compression loading, therefore only displacement control was used for the FE analyses.

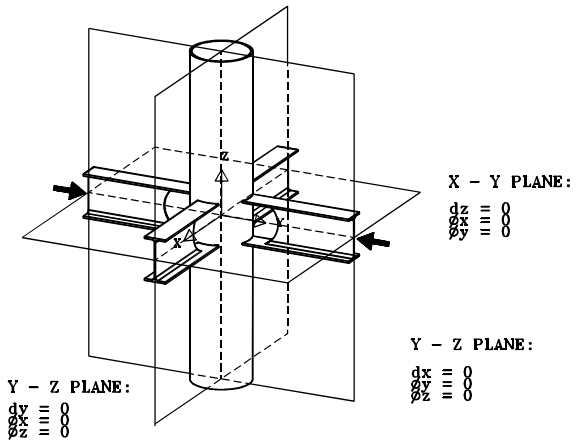

Figure 4.5 Symmetry planes and boundary conditions for model 2C1-2C3

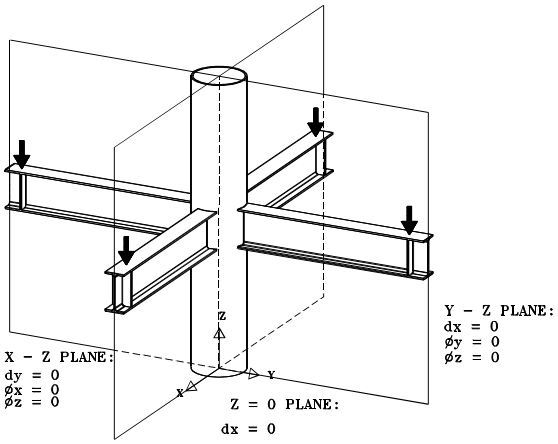

Figure 4.6 Symmetry planes and boundary conditions for model 3C1-4C4

4.3.1.4 Test series 3, in-plane bending moment tests

For all simulations of test series 3 two symmetry planes could be used (see figure 4.6). For the FE analyses for model 3C1, 3C2 and 3C4, the column was restrained at the bottom of the column in vertical direction. For the FE analyses of model 3C3, the column was not restrained at the bottom, similar to the test. The load was applied on the in-plane beams, while the out-of-plane beams were supported in vertical direction.

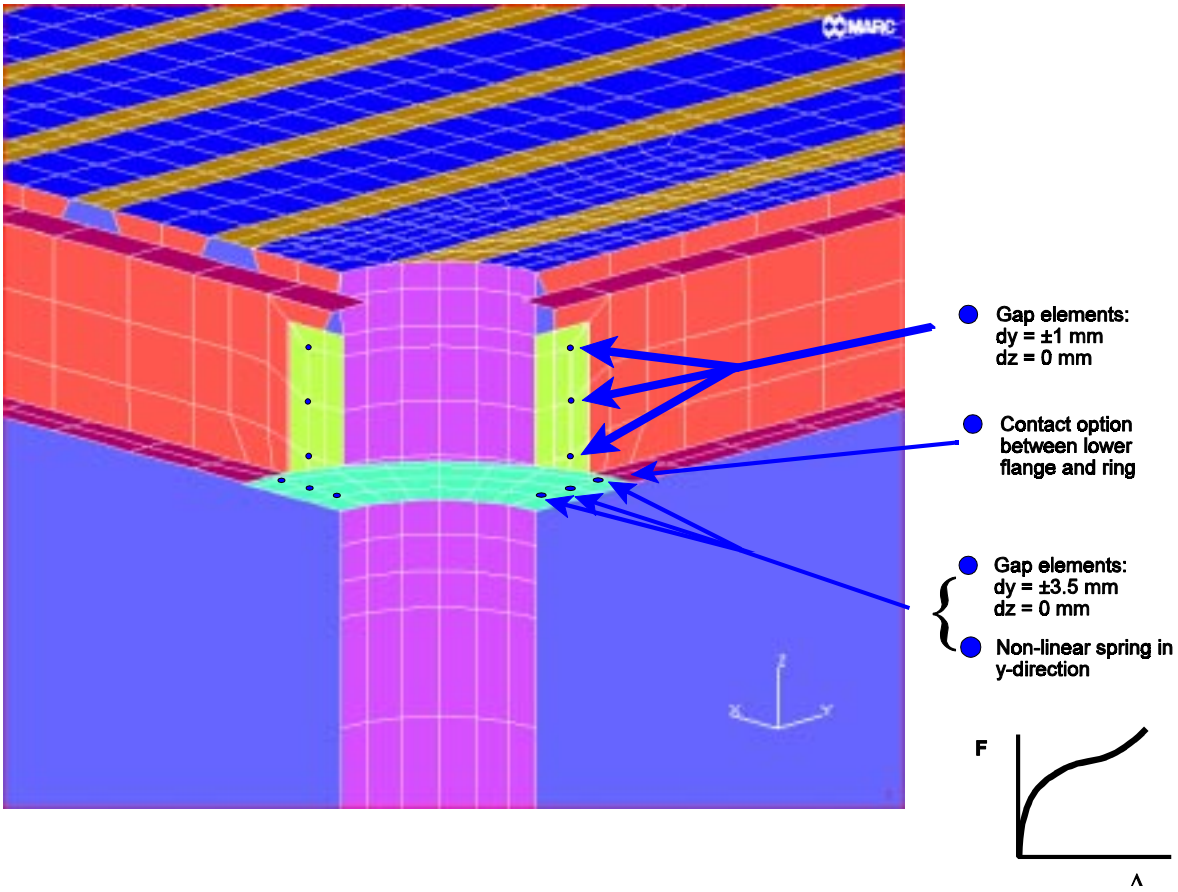

Figure 4.7 Finite element model of test series 4

4.3.1.5 Test series 4, in-plane bending moment tests

The finite element modelling of test series 4 differs significantly from the other test series. The specimens of test series 4 include bolted connections as well as a composite steel-concrete floor. There are two different bolted connections in the specimens.
The first type is the connection between the I-beam web and the vertical plate that is welded to the column. This connection with three bolts was modelled using a relatively simple approach. At the three bolt locations the nodes of the I-beam web and the vertical plate were

tied in vertical direction. Horizontally, the nodes at the bolt locations were tied with gap elements, allowing a small horizontal displacement of 1 mm in either direction in the plane of the I-beam web. Thus, the I-beam can rotate slightly without introducing bending moments. This was also the case for the test specimens since the actual tolerance between the bolt and the bolt hole is 2 mm. Friction in this bolt connection was not modelled.

The second type is the bolted connection between the lower flange and the ring plate. In the numerical model, the parts of the ring and the parts of the lower flanges that touch each other were defined as contact surfaces, thus allowing movement between the parts in plane of the lower flange. At the bolt locations, the lower flange and ring were connected vertically with stiff springs.

The stiffness of these springs is equal to the bolt stiffness:

$k_{bolt} = \frac{E * A_{bolt}}{l_{bolt}}$, where A_{bolt} is the cross-sectional area of the bolt and l_{bolt} is the length of the bolt.

Horizontally, the nodes at bolt locations were tied with both gap elements as well as spring elements. The gap width is 3.5 mm, equal to the maximum measured slip displacement at testing. The spring properties are non-linear and obtained from measurement data (see Figure 4.8). The spring elements thus modelled can simulate friction and slip behaviour of the bolted connection.

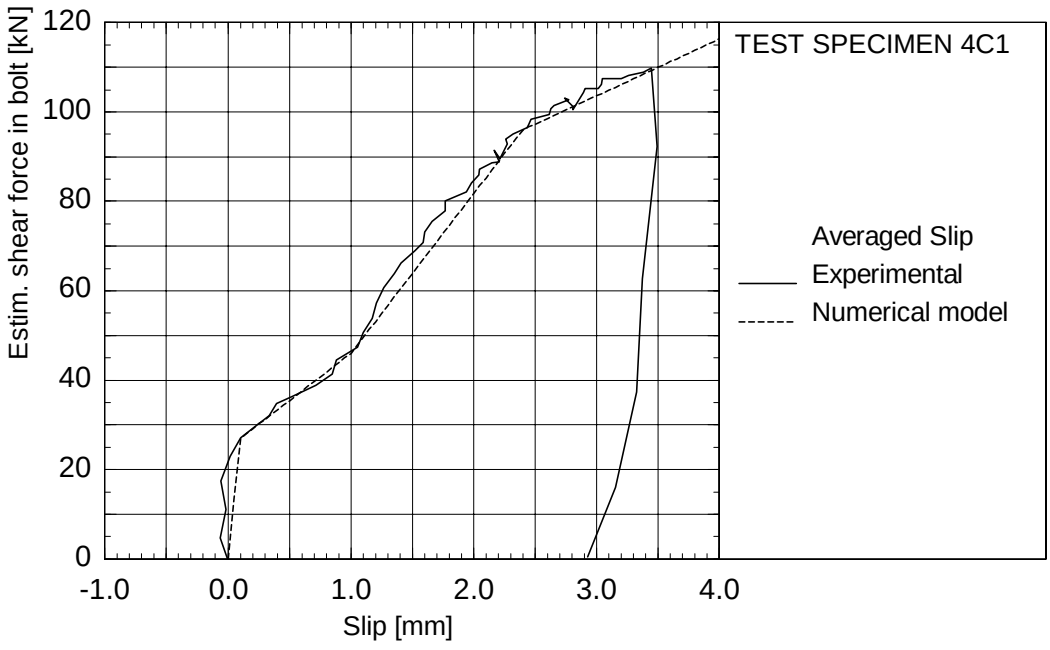

Figure 4.8 Bolt slip, experimentally determined and the slip for the numerical model

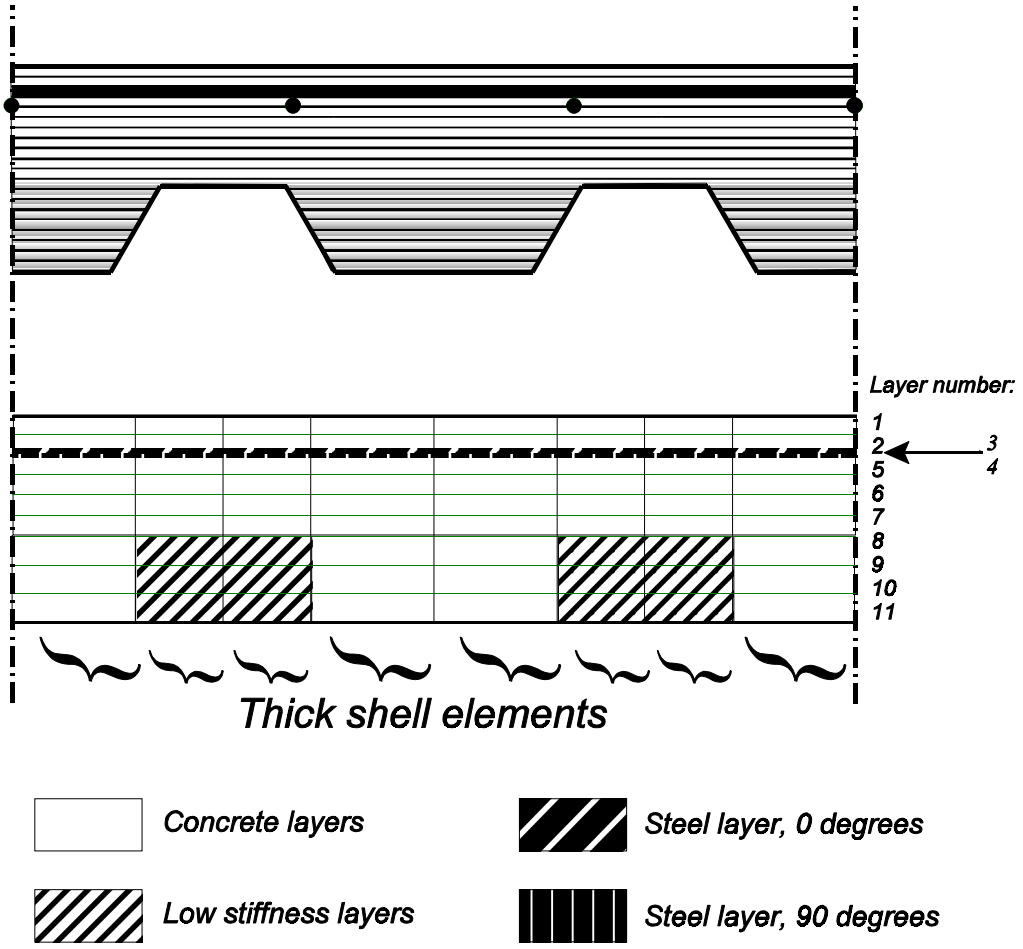

Figure 4.9 Modelling of the composite steel-concrete floor

The concrete floor was modelled using laminated thick shell elements (see Figure 4.9). The reinforcement bars are not modelled individually, but two layers in the thick shell elements were given the averaged properties of the reinforcement. For the two directions of the reinforcement bars separate layers were used. The thickness of the reinforcement layers corresponds with the reinforcement percentage. The reinforcement layers were given orthotropic material properties with isotropic work hardening. Only orthotropic properties were defined in the direction of the reinforcement bars. Thus, no load can be transferred through a reinforcement layer perpendicular to the reinforcement direction. The steel sheet was neglected in the finite element model because at testing the steel sheet became separated from the concrete in the critical parts of the floor during the test. When the steel sheet is separated from the floor, the load-bearing capacity of the steel sheet is almost completely lost. See also Photo 3.10 in Chapter 3.

The concrete properties included in the model were cracking, tension softening and a shear retention factor. No crushing of the concrete was included in the model, since the concrete

floor was predominantly loaded under tension. Also, no crushing was observed during the experimental tests.
The maximum cracking strain (f_{cr}) (=hardened splitting tensile strength as listed in Tables 3.6 and 3.7) of the concrete was obtained from coupon tests. The Young's modulus of the reinforcement bars ($f_{y,reinf.bars}$) was also experimentally obtained (see Section 3.3.4).
The ultimate cracking strain and the tension softening modulus were calculated with the following formulae (see also Figure 4.10):

Ultimate cracking strain (see also the DIANA manuals [54]):

$$\epsilon_u = \frac{f_{y,reinf.bars}}{E_{reinf.bars}} \tag{4.1}$$

Softening modulus (see also the MARC manuals [59]):

$$E_s = \frac{f_{cr}}{\epsilon_u} \tag{4.2}$$

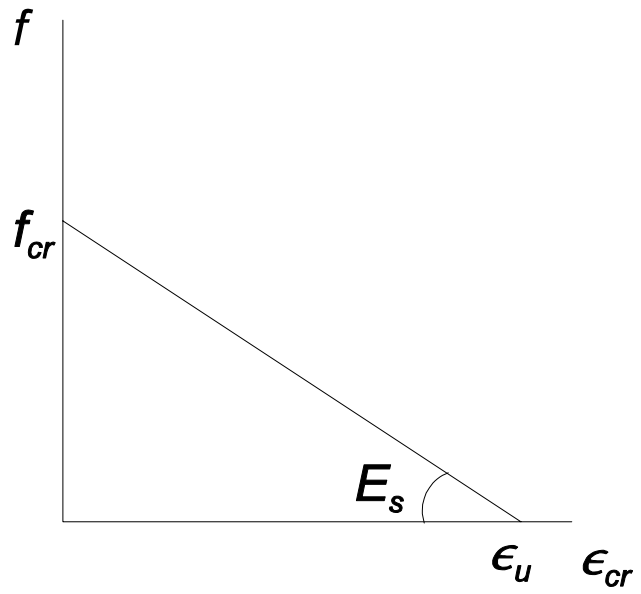

Figure 4.10 Tension softening

The shear retention factor (S.R.F.) defines the amount of shear force that is transferred through a crack. This factor was mainly included in the analyses to get a more stable numerical solution. A S.R.F. equal to 0.05 is widely used. This factor cannot be derived experimentally.
The symmetry planes used for test series 4 were the same as for test series 3.

4.3.2 Parametric investigation

The finite element meshes as used for the parametric investigation are similar to those of the calibration. For the parametric study the welds were not modelled, because the minimum required size of the V butt welds between the beam flanges and the column is equal to the flange thickness.
The steel grade of the column and beams is S355. For some of the connections, if the I-beam could fail, due to full plastification of the flanges or plastic buckling of the compressive flange, steel grade S690 is used for the I-beam to enforce connection failure instead of beam or plate failure. If despite of the higher yield strength the plate or I-beam is still critical an artificial elastic-plastic material is used for the I-beams, with a yield strength of 3550 N/mm^2.

5 CALIBRATION OF THE FINITE ELEMENT MODELS

5.1 Plate to CHS column connections under axial loading

5.1.1 General observations

The connection behaviour is presented in load-deformation diagrams. For the experiments, the axial load was measured with the load cells. The deformation (averaged indentation) was obtained from the displacement transducer measurements. After reaching the maximum load, the testing has been continued to obtain information about the deformation capacity and failure modes. Figures 5.1 to 5.3 show the deformed finite element models simulating test 1C2, 1C3 and 1C5.
The load-deformation diagrams, showing both the experimental and numerical curves, are shown in Figures 5.4 to 5.11. The comparison between the experimental and numerical results are summarized in Table 5.1.

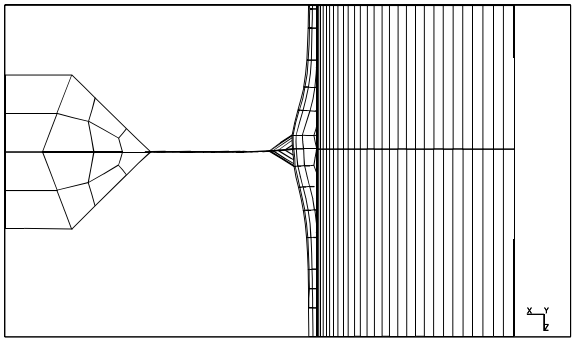

Figure 5.1 Deformed finite element mesh for model 1C2

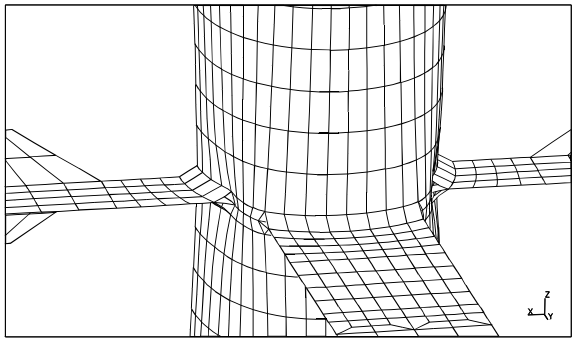

Figure 5.2 Deformed finite element mesh for model 1C3

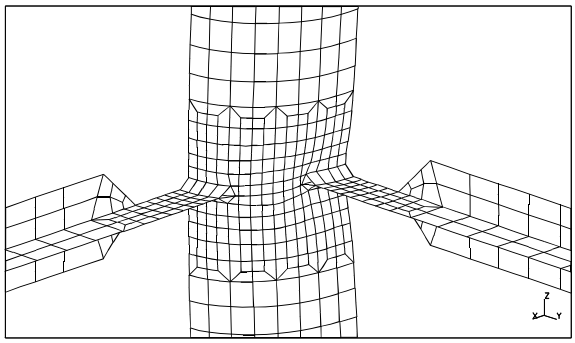

Figure 5.3 Deformed finite element mesh for model 1C5

All the connections without a concrete filling failed by plastification of the column wall. The connection 1C2, with a concrete filling and a tensile uniplanar load, failed by punching shear of the column wall. In this case, cracks were observed in the column wall, at the weld toes of the tension plates, parallel to the column axis. Connection 1C4 failed by yielding of the plates under compression. The maximum load of this test was 15% lower than the squash load of the plates. This could be due a combination of bending and axial force. Theoretically, the relationship between normal force and bending moment for a rectangular cross-section is $(M/M_p) + (N/N_p)^2 = 1$. With substituting $M_p = 0.25*f_{y,1}*b_1*t_1^2$, $N_p = f_{y,1}*b_1*t_1$, and $M = e*N$,

where e is the eccentricity of the axial force in thickness direction a formula for the eccentricity can be obtained: $e = (t_1/4)*(N_p/N)$.
Thus, for t_1=11.53 mm and N_p/N = 1/.85 the eccentricity is equal to 3.4 mm.
So, an eccentricity of 3.4 mm gives a 15% lower ultimate load than the squash load. The strain gauge measurements show also a considerable amount of bending in the plates, which is unavoidable because of the one sided single V butt welds between plate and column.

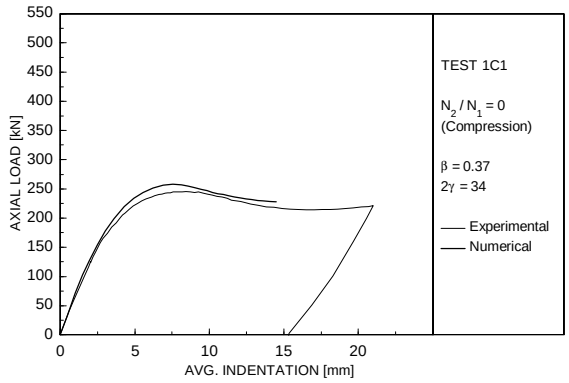

Figure 5.4 Experimental and numerical load-deformation curves for 1C1

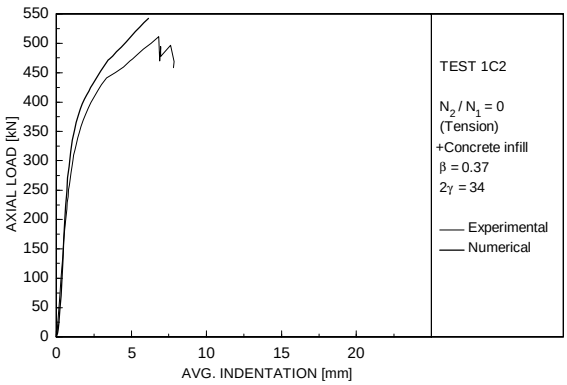

Figure 5.5 Experimental and numerical load-deformation curves for 1C2

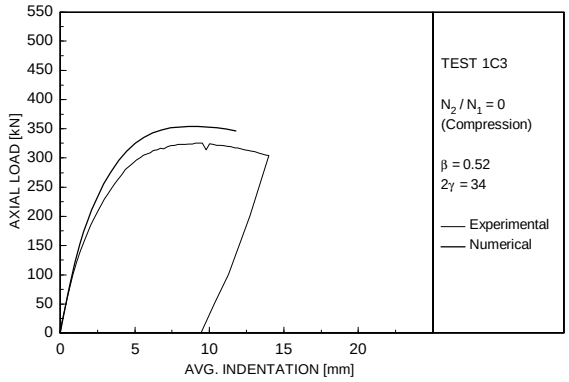

Figure 5.6 Experimental and numerical load-deformation curves for 1C3

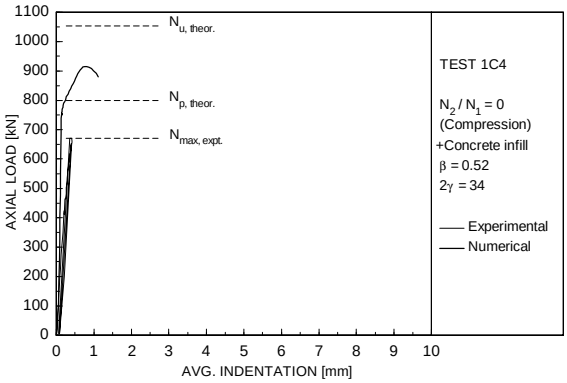

Figure 5.7 Experimental and numerical load-deformation curves for 1C4

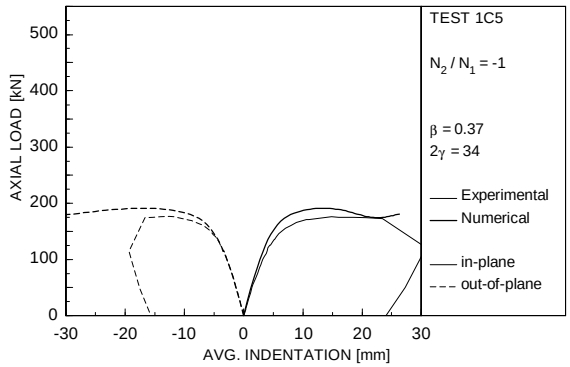

Figure 5.8 Experimental and numerical load-deformation curves for 1C5

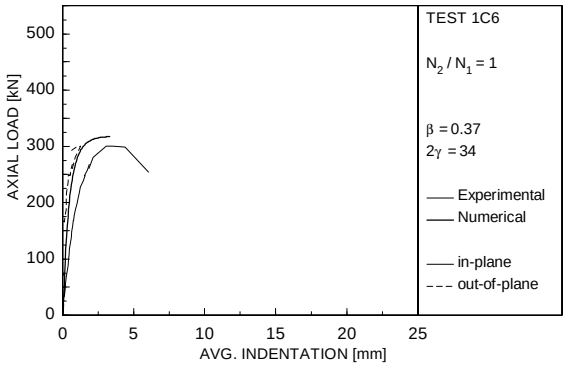

Figure 5.9 Experimental and numerical load-deformation curves for 1C6

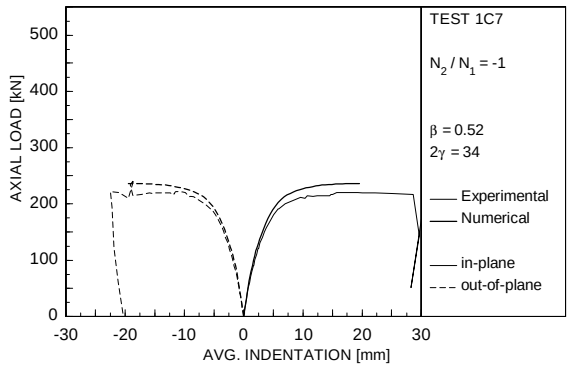

Figure 5.10 Experimental and numerical load-deformation curves for 1C7

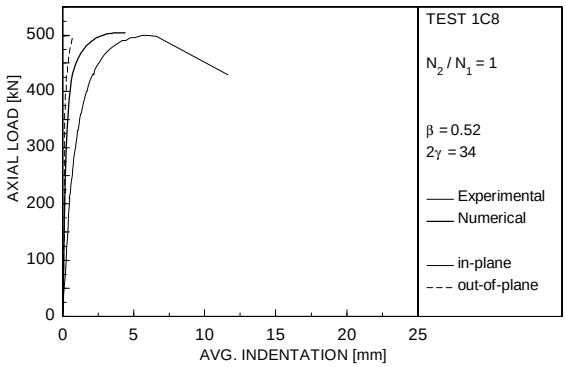

Figure 5.11 Experimental and numerical load-deformation curves for 1C8

5.1.2 Comparison of experimental and numerical results

In general, there is an acceptable to a good agreement between the experimental and numerical results (see Figures 5.4 to 5.11). The deformed shapes of the test specimens and the finite element models agree well. The differences between the results of the numerical models and the experimental tests are quantified in Table 5.1. The finite element model for test 1C2 does not show a maximum in the load displacement curve, because cracking is not included in the finite element model.
The largest difference between the experimental and numerical results is found for test 1C4. The ultimate load of the test specimen is 0.85*Np, while the FE model even exceeds N_p, with continuing loading on the FE model, due to the strain hardening behaviour of the steel. The maximum load of this test cannot accurately be obtained with a finite element analysis, because the failure mode of the test is (plastic) buckling. The outcome of the finite element analysis is sensitive to initial imperfections, like column cross-section shape, weld shapes, misalignments of the plates, etc.
The numerical results are up to 8% higher than the experimental results for the specimens without a concrete filling in the column. These differences are acceptable.

Table 5.1 Comparison experimental and numerical results of test series 1

Nr.	N_2/N_1	concrete filling of column	β	experim. N_u [kN]	numeric N_u [kN]	numeric/ experim.
1C1	0		0.37	245.3	257.9	1.05
1C2	0	yes	0.37	510.8	542.6*	1.06
1C3	0		0.52	325.0	354.0	1.08
1C4	0	yes	0.52	670.8	756.0*	1.12
1C5	-1		0.37	175.6	191.0	1.08
1C6	1		0.37	300.8	317.0	1.05
1C7	-1		0.52	220.1	236.0	1.07
1C8	1		0.52	499.9	504.2	1.00

* Numerical maximum taken at the same displacement as at the maximum of the experiment.

5.1.3 Concluding remarks

The static behaviour of connections between plates and CHS columns under multiplanar axial loadings on the plates can be simulated by means of geometrical and material non-linear finite element analyses. There is an acceptable agreement between experimental and numerical results.
The behaviour of this type of connections, where the column is filled with concrete can be simulated with the use of a rigid contact surface, although the elastic deformations of the concrete are neglected. For small wall thicknesses of the column, the failure of the concrete, due to crushing of the concrete could become critical, in which cases the modelling of the concrete filling should also be modelled.

5.2 Plate to CHS column connections under axial loading, interaction effects

5.2.1 General observations

The load-deformation diagrams, showing both the experimental and numerical curves, are given in Figures 5.12 to 5.14. The deformed finite element mesh of model 2C3 is shown in Figure 5.15. The comparison of the experimental with the numerical results is summarized in Table 5.2.
The two connections without a concrete filling failed by plastification of the column wall. Specimen 2C2, with a concrete filling and a tensile uniplanar load, failed by punching shear of the column wall. In this case, cracks were observed in the column wall, at the weld toes of the tension plates, parallel to the column axis. This failure mode can be described as an initial punching shear failure in the column at the edges of the flanges, continued by a tearing failure mode parallel to the column axis.
The observed punching shear failure mode is different from the theoretical punching shear failure mode. Theoretically it is expected that the cracks are following the circumference of the welds, which connect the flanges to the CHS column.

Table 5.2 Comparison experimental and numerical results of test series 2

Nr.	N_2/N_1	concrete filling of column	β	experim. N_u [kN]	numeric N_u [kN]	numeric/ experim.
2C1	0		0.37	245.3	350.6	1.16
2C2	0	yes	0.37	510.8	971.8	1.07
2C3	0		0.52	325.0	456.0	1.12

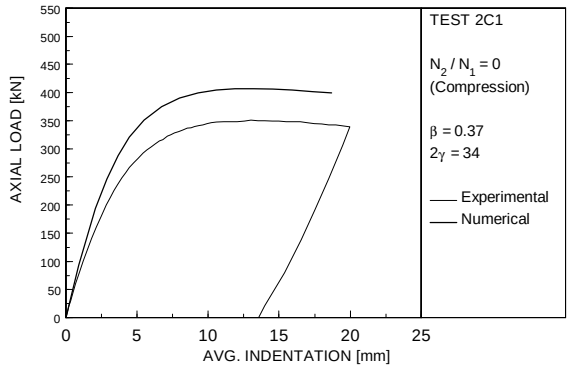

Figure 5.12 Experimental and numerical load-deformation curves for 2C1

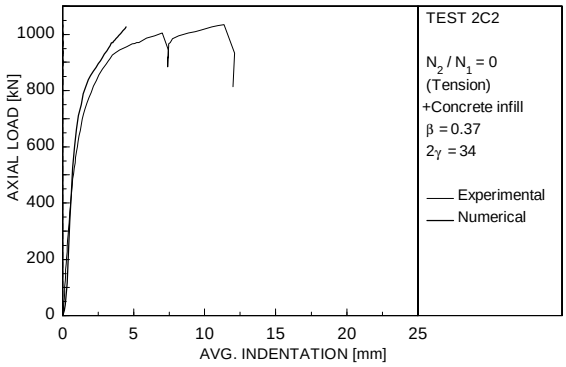

Figure 5.13 Experimental and numerical load-deformation curves for 2C2

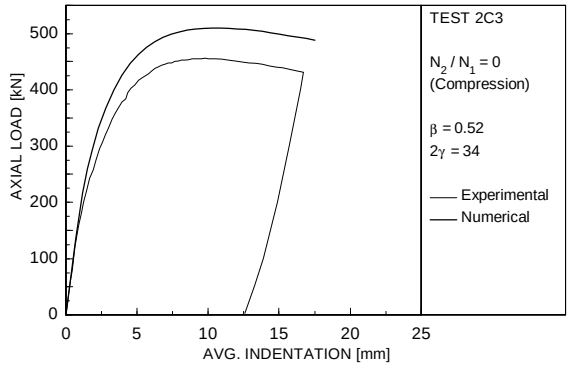

Figure 5.14 Experimental and numerical load-deformation curves for 2C3

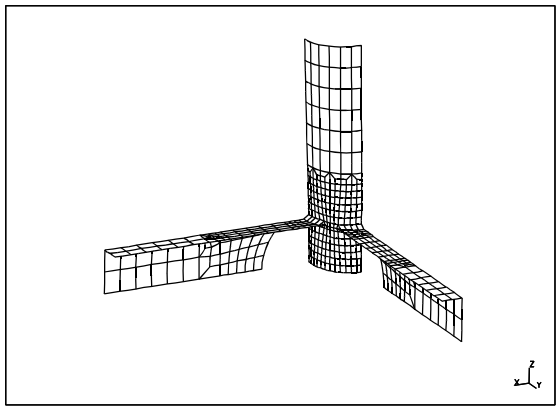

Figure 5.15 Deformed finite element model for test 2C3

5.2.2 Comparison of experimental and numerical results

There is reasonable agreement between the experimental and numerical results (see Figures 5.12 to 5.14). The deformed shapes of the test specimens and the corresponding finite element models agree well. The differences between the results of the numerical models and the experimental tests are quantified in Table 5.2. The largest difference between the experimental and numerical results is found for test 2C1.

For test 2C2, only a comparison between the experimental and numerical results can be made up to an averaged indentation of approximately 4 mm. At a larger deformation, the strength is significantly reduced by the cracks in the column wall. The cracking failure mode is not included in the numerical model.

The numerical results are up to 16% higher than the experimental results, which is larger than generally is acceptable. Additional finite element analyses were carried out to determine the influencing factors of the difference between the experimental and numerical results. The only significant influencing factor found was a misaligned loading (2 mm was used) in combination with a non-rigid support of the column, which prevents the movement of the column in axial direction. If this support was completely removed, the load dropped with 25%. If some movement of the column of test specimen 2C1 in axial direction occurred during the test, this could lead to a significant lower maximum load. However, this displacement was not recorded during the test and thus could not be reconstructed with the finite element analyses.

Therefore, no final conclusion could be drawn to explain the relatively large difference between experimental and numerical results.

5.3 I-beam to CHS column connections under in-plane bending moments

5.3.1 General observations

The connection behaviour is presented in moment-rotation diagrams. For the experiments, the axial load was measured with the load cells. The moments in the beams are calculated at the column face. The beam rotation is calculated from the displacement transducer measurements. After reaching the maximum load, the testing has been continued to obtain information about the deformation capacity and the failure modes. The experimental tests show a peak load. After reaching the peak load the load drops slightly. After this load drop the load increases again, due to membrane action in the column wall. This behaviour is typical for I-beam to CHS column connections under in-plane bending moments. Figure 5.16 shows the deformed geometry of the finite element model of test 3C2, Figure 5.17 shows the deformed geometry of the finite element model of 3C3.
The moment-rotation diagrams, showing both the experimental and numerical curves, can be seen in Figures 5.18 to 5.21. The results are summarized in Table 5.3.

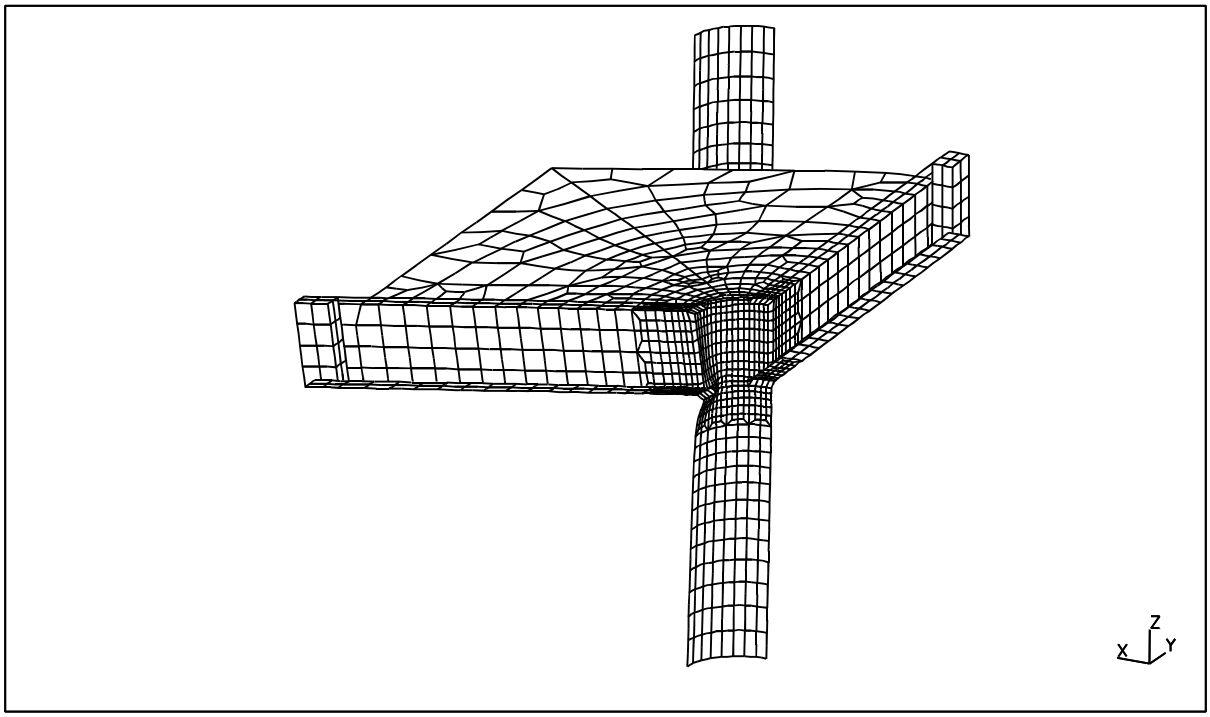

Figure 5.16 Deformed finite element model for test 3C2

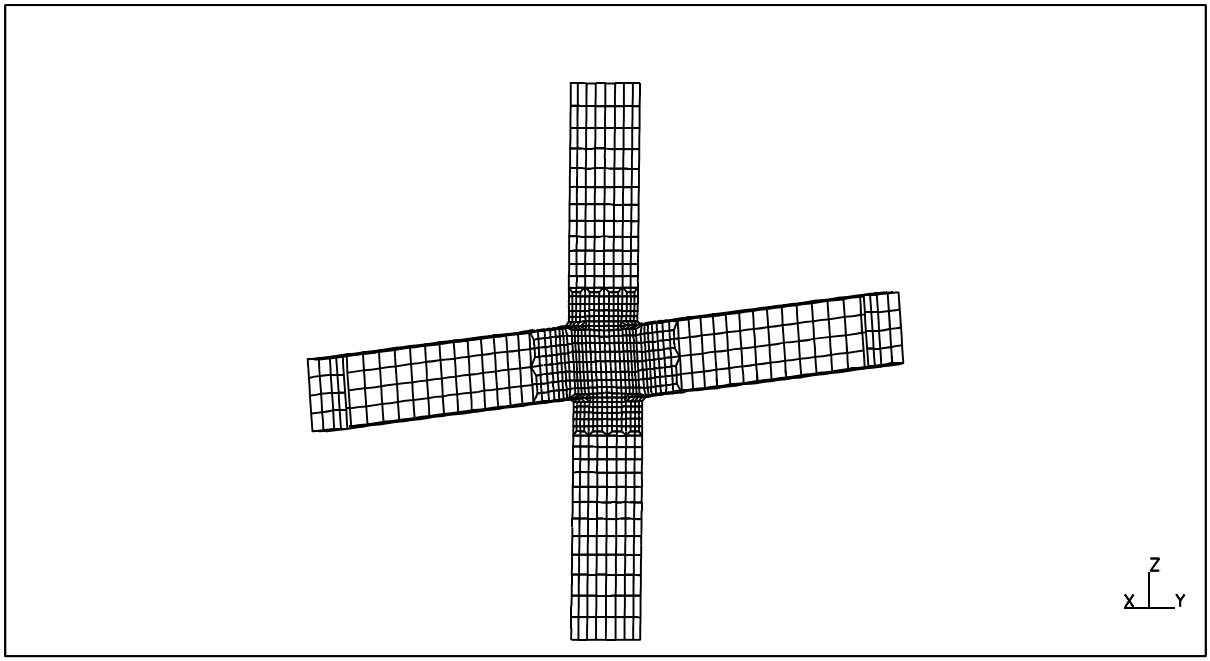

Figure 5.17 Deformed finite element model for test 3C3

Table 5.3 Comparison experimental and numerical results of test series 3

Test	$\frac{M_2}{M_1}$	M_u in [kNm]			
		Expt	Num	Num/Expt	comment
3C1	0	82.5	82.1	0.99	
3C2	0	87.6*	86.1	0.98	+steel floor
3C3	-1	54.1	60.5	1.12	
3C4	+1	79.0	79.7	1.01	

* = No maximum

5.3.2 Comparison of experimental and numerical results

In general, there is good agreement between the experimental and numerical results (see Figures 5.18 to 5.21). Also, the deformed shapes of the test specimens and the corresponding finite element models agree well. The differences between the results of the numerical models and the experimental tests are shown in Table 5.3. For one test, namely 3C3, the numerical ultimate moment is about 12% higher than the experimentally obtained ultimate value. This difference could be caused due to the fact that two of the I-section beams were not properly

aligned when welded to the column, but slightly rotated about the beam axes and not totally perpendicular to the column face.

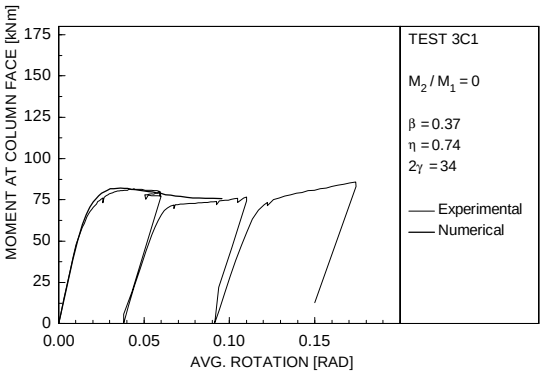

Figure 5.19 Experimental and numerical moment- rotation curves for test 3C1

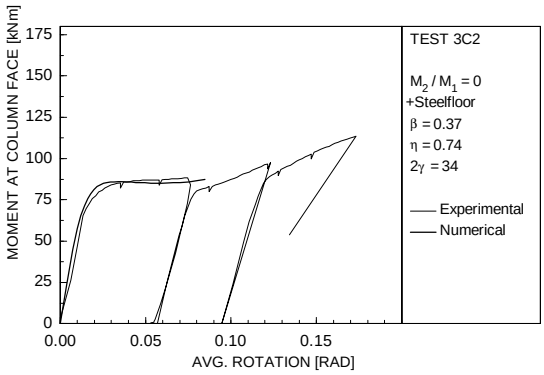

Figure 5.21 Experimental and numerical moment- rotation curves for test 3C2

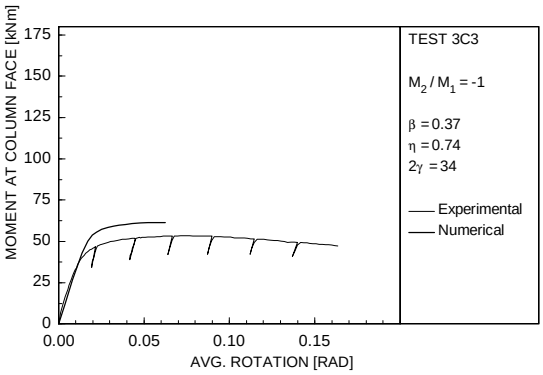

Figure 5.18 Experimental and numerical moment-rotation curves for test 3C3

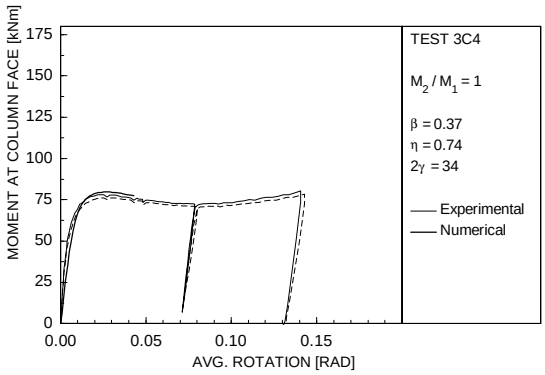

Figure 5.20 Experimental and numerical moment-rotation curves for test 3C4

5.4 Bolted I-beam to CHS column connections in combination with a steel sheeted concrete floor loaded with in-plane bending moments

5.4.1 General observations

The global connection behaviour is presented in moment-rotation diagrams as shown in Figures 5.22 to 5.25. For an accurate comparison of the finite element models with the test results some serious problems appeared. The potentiometers used to measure the vertical displacement of the I-beams appeared to be insufficient accurate to measure the small displacements at the beginning of the test, which are necessary to calculate the initial stiffness.

From the measured data it could also be concluded that the stiffness of the vertical supports of the concrete floor were less rigid than expected. During testing the supports have been moved several millimetres in vertical direction. The impact is small for the uniplanar loading tests, but could have a larger impact for the multiplanar tests, because the stiffness of the supports could have been different in in-plane and out-of-plane directions.

Figures 5.27 to 5.30 show the comparison between the cracking pattern of the composite steel-concrete floor after testing with the pattern of the cracking strain of the corresponding numerical models. Although the finite element analyses were performed on a quarter model, the figures show the complete floor. These pictures were obtained by mirroring the numerical results in two directions. The experimental results are represented by the solid lines, the numerical results by the dots. As can be seen in Figures 5.27 and 5.28, the cracking pattern is almost symmetrical (in the two directions) for the uniplanar loaded test specimens (4C1 and 4C2). The cracking patterns of the multiplanar loaded test specimens (4C3 and 4C4) are less symmetrical. As can be seen in Figure 5.29, the (experimental) cracks are significant larger in the lower-right part of the figure, then in the upper-left part of the figure. This could be caused by differences in spring stiffness of the four supports at the test rig.

As can be concluded from Figures 5.22 to 5.25, there is a reasonable agreement between the experimental and numerical results. The shape of the numerical moment-rotation diagram is strongly dependent on the properties of the non-linear springs used to simulate the slip in the bolted connection between the lower flanges of the I-beams and the ring. Test runs with the finite element models showed that if a lower spring stiffness is used (75% of the stiffness as used for the analyses in Figures 5.22 and 5.25) the shape of the moment-rotation diagrams became close to those of the experiments. However, the exact properties for the non-linear springs to simulate the behaviour of the bolted connections could not be determined accurately, due to insufficient measured data from the experiments.

Figure 5.26 shows again the experimental and numerical results for test 4C1, but also the

results of two extra finite element analyses. The first of these analyses was done with the non-linear springs completely rigid (line labelled with "rigid") and the second with the non-linear springs with a very low spring stiffness (line labelled with "soft"), thus obtaining a lower and a upper bound. As can be concluded from Figure 5.26, the influence of the spring stiffness on the connection behaviour is large.

There is also a reasonable agreement between the cracking patterns of the experiment and the numerically obtained cracking strains. However, since smeared cracking is used for the finite element models, only a qualitative comparison can be made.

Table 5.4 shows the comparisons between the experimental results and the numerical results. Furthermore, the theoretical values for the connection strengths are shown. The theoretical strength is calculated with Eq. 5.1, both for f_y and f_u for the reinforcement bars.

$$M_u(J=0) = h_z \cdot \sum_{i=1}^{n} A_i \cdot f_{y,i} \qquad \textbf{(5.1)}$$

where h_z is the distance between the reinforcement bars and the bottom of the lower flange,
A_i is the cross sectional area of reinforcement bar i,
$f_{y,i}$ is the yield strength of reinforcement bar i.

There is reasonable agreement between the experimental and numerical results. The numerical results are higher than the experimental results, because the numerical model failed symmetrically, whereas the experiment failed rather asymmetrically. Also, the experiments failed below the theoretical capacity of the connections, because some of the reinforcement bars failed before all reinforcement bars reached full plastification, due to the limited deformation capacity of the reinforcement.

The multiplanar loading cases have on average 76% of the uniplanar loading case strength for the experiments and 70% for the numerical analyses.

Table 5.4 Comparison experimental and numerical results of test series 4

Test	M_2/M_1	M_u in [kNm]						
		Expt	Num	Theor (f_y)	Theor (f_u)	Num/ Expt	Theor (f_y)/ Expt	Theor (f_u)/ Expt
4C1	0	152.99	179.53	181.55	193.69	1.17	1.19	1.27
4C2	0	177.00	179.53	181.55	193.69	1.01	1.03	1.09
4C3	+1	128.44	125.01	181.55	193.69	0.97	1.27	1.51
4C4	+1	121.56	125.01	181.55	193.69	1.03	1.49	1.59

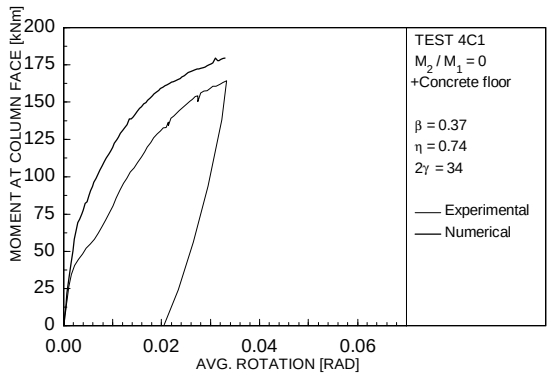

Figure 5.22 Experimental and numerical moment-rotation curves for test 4C1

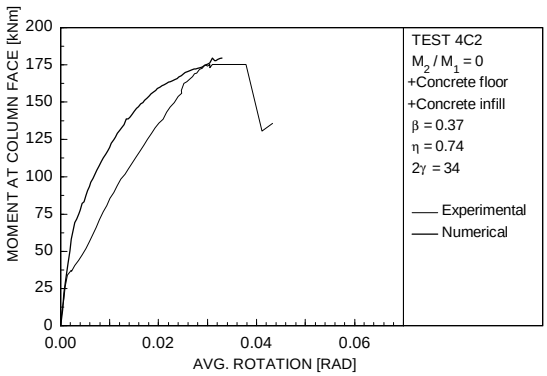

Figure 5.23 Experimental and numerical moment-rotation curves for test 4C2

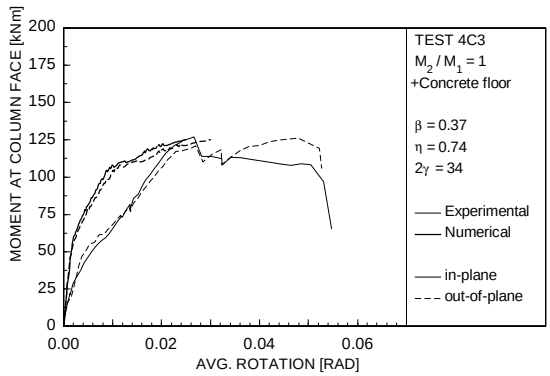

Figure 5.24 Experimental and numerical moment-rotation curves for test 4C3

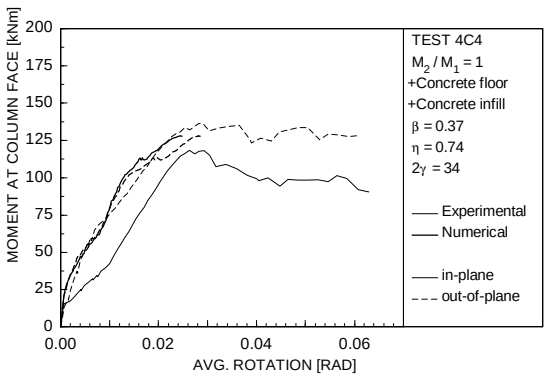

Figure 5.25 Experimental and numerical moment-rotation curves for test 4C4

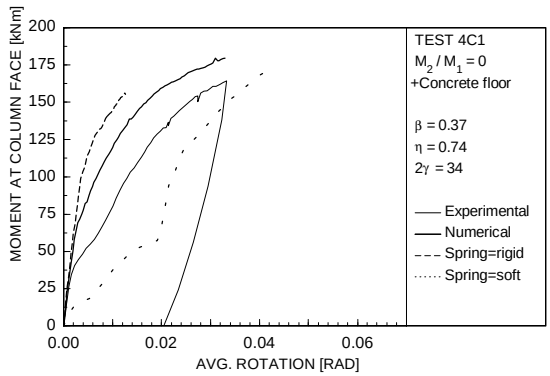

Figure 5.26 Experimental and numerical moment-rotation curves, with numerical lower and upper bound

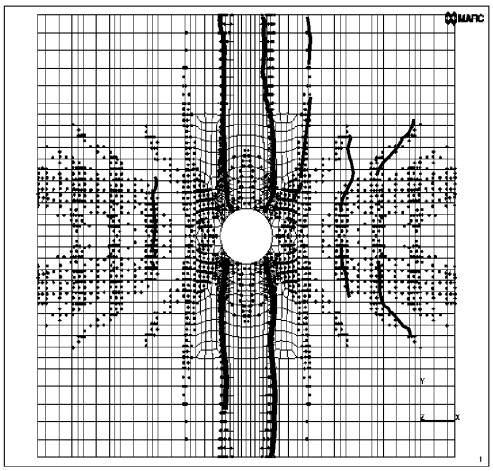

Figure 5.27 Comparison experimental cracking pattern with the numerical cracking strain pattern of test 4C1

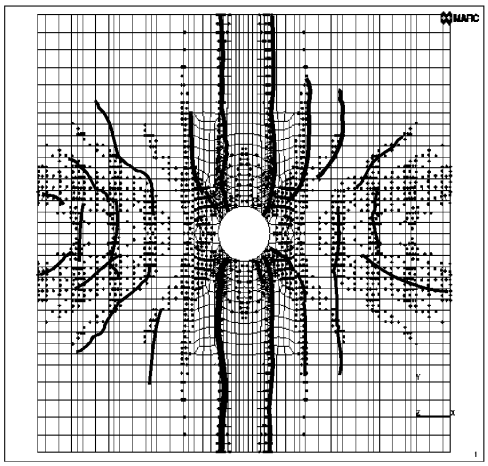

Figure 5.28 Comparison experimental cracking pattern with the numerical cracking strain pattern of test 4C2

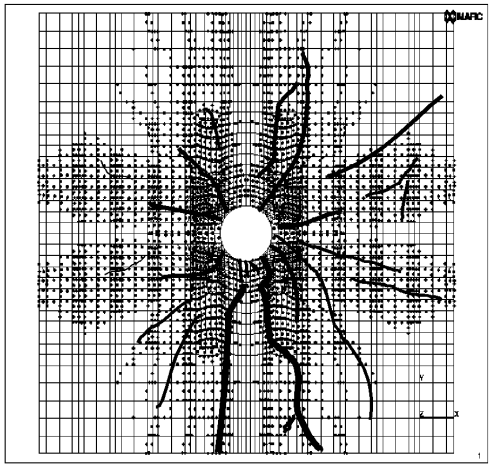

Figure 5.29 Comparison experimental cracking pattern with the numerical cracking strain pattern of test 4C3

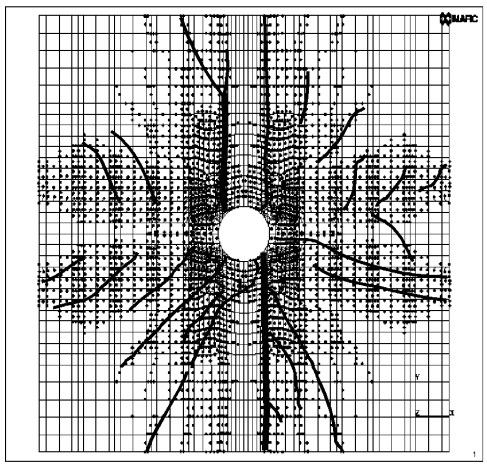

Figure 5.30 Comparison experimental cracking pattern with the numerical cracking strain pattern of test 4C4

5.5 General conclusions on the calibration of the finite element models

As shown in the previous paragraphs, an acceptable agreement is obtained between the experimentally obtained data and the finite element results. Both the ultimate loads as well as the post-critical behaviour of the investigated connections can be simulated by means of the used finite element models.
The used method for the finite element analyses is limited to the cases where no significant cracks in the steel columns occur in the experiments. Cracking in the columns can be expected for specimens with a concrete filled column in combination with tension loading on the plates or flanges. In such cases, the used finite element method can only be used to simulate the first stage of the load-deformation curves.
The behaviour of the composite floor can be simulated by thick shell elements, using the composite option. The behaviour of the bolted connections can be simulated, using gap and (non-linear) spring elements in combination with contact options.

6 PARAMETRIC STUDY

6.1 Plate to CHS column connections under axial loading

6.1.1 Research programme

For the parametric study on plate to CHS column connections, 21 uniplanar and 15 multiplanar connections were analysed with seven different β ratios for the uniplanar connections and seven (five) different β ratios for the uniplanar (multiplanar) connections, three 2γ ratios and one τ ratio. The geometrical parameters of the models are listed in Tables 6.1, 6.2 and 6.3. The column length was taken as six times the column diameter d_0. The plate length is five times the plate width. These lengths are sufficient to minimize boundary and load introduction effects.

The multiplanar models were loaded with five different load cases, namely N_2/N_1 = -1.0, -0.5, 0.0, +0.5 and +1.0. For the finite element analyses, displacement control was used for N_2/N_1 = 0.0 and +1.0, and load control for the other load cases. Displacement control reduces the computer time for the analyses significantly. However, to preserve a fixed ratio between the axial loading on the in-plane and on the out-of-plane plates, only load control can be used. The column diameter d_0 for all models is 300 mm.

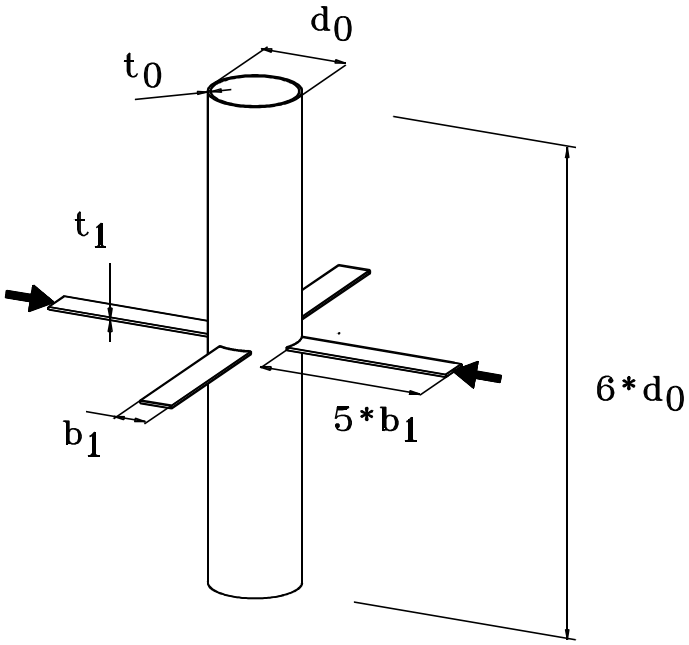

Figure 6.1 Main dimensions FE model for plate to CHS column connections

Table 6.1 Overview of the research programme uniplanar plate to CHS column connections

	2γ		
β	15	30	45
0.25	xup1-02	xup1-04	xup1-06
0.40	xup1-08	xup1-10	xup1-12
0.55	xup1-38	xup1-40	xup1-42
0.60	xup1-50	xup1-52	xup1-54
0.65	xup1-14	xup1-34	xup1-36
0.80	xup1-56	xup1-58	xup1-60
0.90	xup1-62	xup1-64	xup1-66

Table 6.2 Overview of the research programme multiplanar plate to CHS column connections

	2γ		
β	15	30	45
0.25	xxp1-02	xxp1-04	xxp1-06
0.40	xxp1-08	xxp1-10	xxp1-12
0.55	xxp1-38	xxp1-40	xxp1-42
0.60	xxp1-50	xxp1-52	xxp1-54
0.65	xxp1-14	xxp1-34	xxp1-36

6.1.2 Results finite element analyses for the uniplanar plate to CHS column connections under axial loading

In Table 6.4, the main results of the finite element analyses on uniplanar plate to CHS column connections under axial loading are given in an non-dimensional way. Figure 6.2 shows a typical finite element mesh for one of the investigated models. Figures 6.3 to 6.23 show the load-deformation curves. The maxima in the load-displacement curves are clearly marked. In cases, without a peak load, the connection strength is defined at a deformation limit equal to 3% d_0. The deformation limit is plotted in the figures as a dashed vertical line. As can be observed in the figures, larger β-ratios give a larger non- dimensional strength. Larger 2γ-ratios result also in a larger non-dimensional strengths, this effect becomes stronger for larger β-ratios. However, the actual strength decreases with increasing 2γ-ratios.

Table 6.3 Geometrical and material characteristics of the plate to CHS column connections

model	β	2γ	τ	$f_{y,1}^{*}$ [MPa]
xup1/xxp1-02	0.25	15	0.3375	3550
xup1/xxp1-04	0.25	30	0.6750	690
xup1/xxp1-06	0.25	45	1.0125	690
xup1/xxp1-08	0.40	15	0.5400	3550
xup1/xxp1-10	0.40	30	1.0800	690
xup1/xxp1-12	0.40	45	1.5200	690
xup1/xxp1-14	0.65	15	0.8775	690
xup1/xxp1-34	0.65	30	1.7550	690
xup1/xxp1-36	0.65	45	2.6325	690
xup1/xxp1-38	0.55	15	0.7425	690
xup1/xxp1-40	0.55	30	1.4850	690
xup1/xxp1-42	0.55	45	2.2275	690
xup1/xxp1-50	0.60	15	0.8100	690
xup1/xxp1-52	0.60	30	1.6100	690
xup1/xxp1-54	0.60	45	2.4300	690
xup1-56	0.80	15	1.0000	690
xup1-58	0.80	30	1.0000	690
xup1-60	0.80	45	1.0000	690
xup1-62	0.90	15	1.0000	690
xup1-64	0.90	30	1.0000	690
xup1-66	0.90	45	1.0000	690

Note:

*: In cases where plate failure would be critical, a higher steel grade for the plates was used, to avoid local buckling in the compression plates. The plates have a steel grade with $f_{y,1}$=690 N/mm^2 or an artificial elasto-plastic steel grade with $f_{y,1}$=3550 N/mm^2. The column diameter d_0 for all models is 300 mm and the steel grade for the columns is S355 ($f_{y,0}$ = 355 N/mm^2).

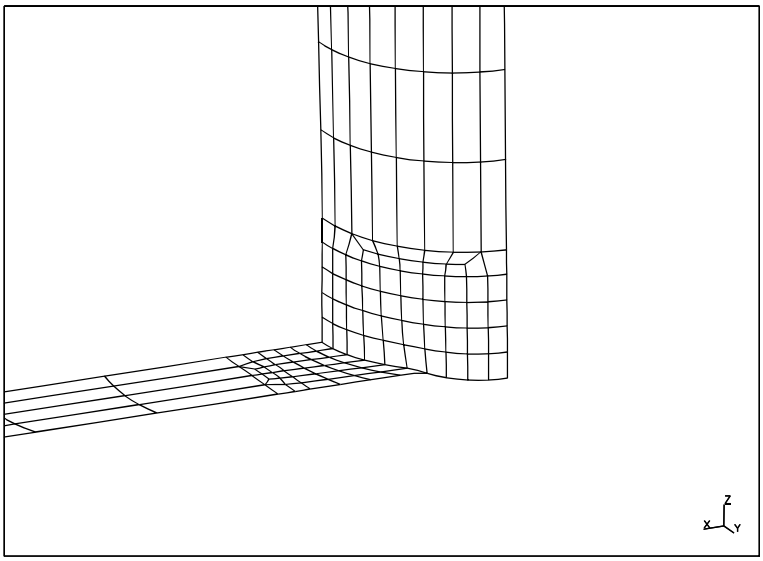

Figure 6.2 Deformed finite element mesh of model XUP1-58

Table 6.4 Finite element results of the uniplanar plate to CHS column connections

name	β	2γ	τ	$N_u/(t_0^2 f_{y,0})$
xup1-02	0.25	15.	0.3375	4.45
xup1-04	0.25	30.	0.6750	5.15
xup1-06	0.25	45.	1.0125	5.39
xup1-08	0.40	15.	0.5400	5.87
xup1-10	0.40	30.	1.0800	7.30
xup1-12	0.40	45.	1.6200	7.92
xup1-14	0.65	15.	0.8775	9.04
xup1-34	0.65	30.	1.7550	11.50
xup1-36	0.65	45.	2.6325	12.55
xup1-38	0.55	15.	0.7425	7.69
xup1-40	0.55	30.	1.4850	9.98
xup1-42	0.55	45.	2.2275	11.01
xup1-50	0.60	15.	0.8100	8.25
xup1-52	0.60	30.	1.6100	10.60
xup1-54	0.60	45.	2.4300	11.62
xup1-56	0.80	15.	1.0000	11.52
xup1-58	0.80	30.	1.0000	14.12
xup1-60	0.80	45.	1.0000	15.42
xup1-62	0.90	15.	1.0000	13.86
xup1-64	0.90	30.	1.0000	17.01
xup1-66	0.90	45.	1.0000	18.43

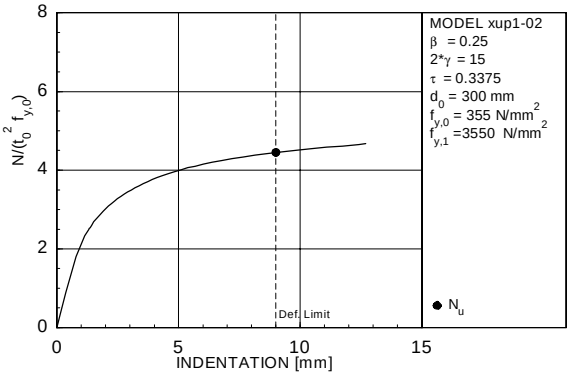

Figure 6.3 Load-displacement curve for model XUP1-02

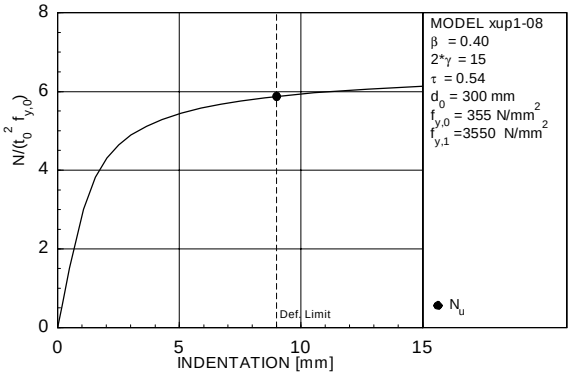

Figure 6.4 Load-displacement curve for model XUP1-08

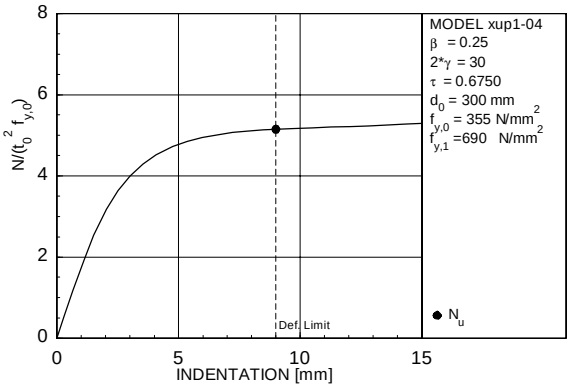

Figure 6.5 Load-displacement curve for model XUP1-04

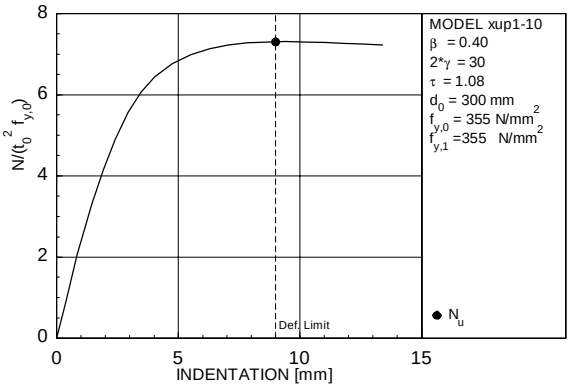

Figure 6.6 Load-displacement curve for model XUP1-10

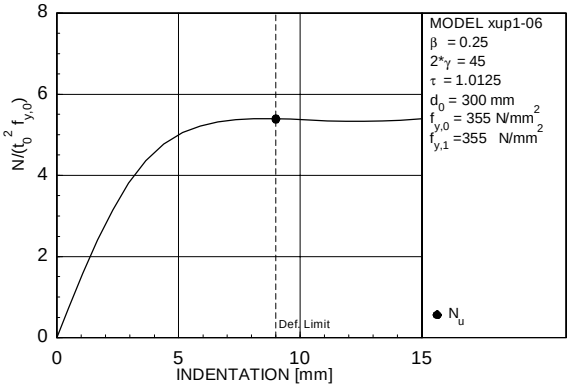

Figure 6.7 Load-displacement curve for model XUP1-06

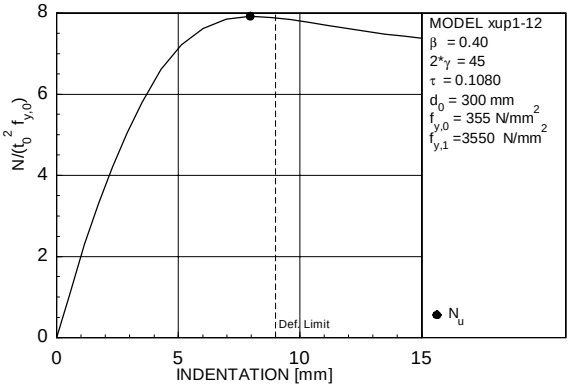

Figure 6.8 Load-displacement curve for model XUP1-12

Note: The figures are organised on this and next pages: top to bottom an increasing 2γ, left to right an increasing β.

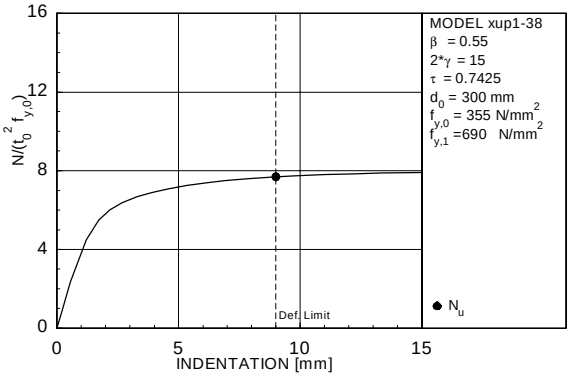

Figure 6.9 Load-displacement curve for model XUP1-38

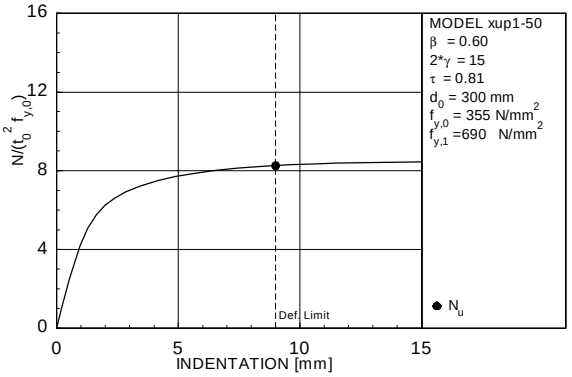

Figure 6.10 Load-displacement curve for model XUP1-50

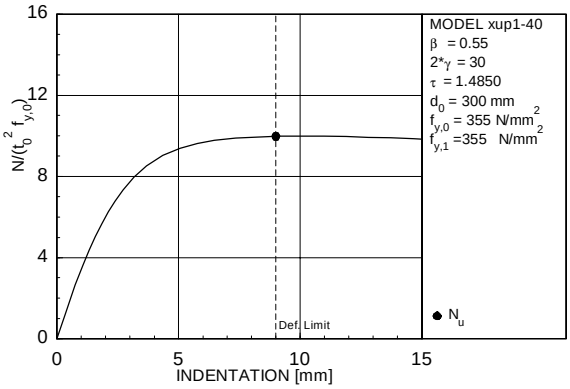

Figure 6.11 Load-displacement curve for model XUP1-40

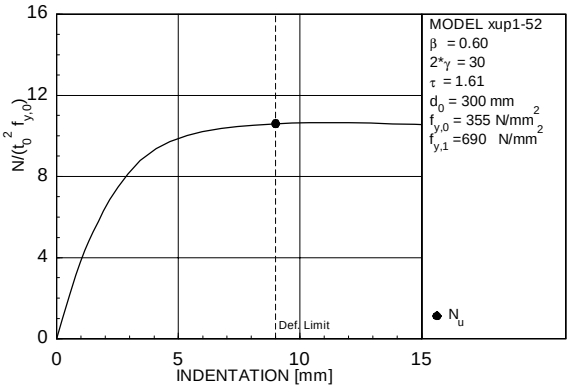

Figure 6.12 Load-displacement curve for model XUP1-52

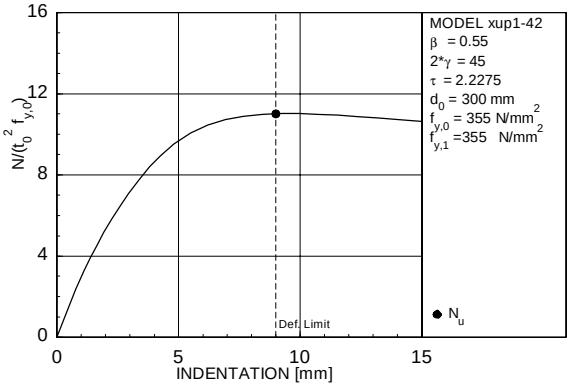

Figure 6.13 Load-displacement curve for model XUP1-42

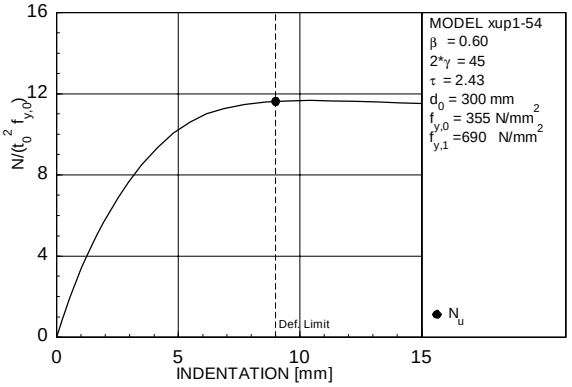

Figure 6.14 Load-displacement curve for model XUP1-54

Note: The figures are organised on this and next pages: from top to bottom an increasing 2γ, from left to right an increasing β.

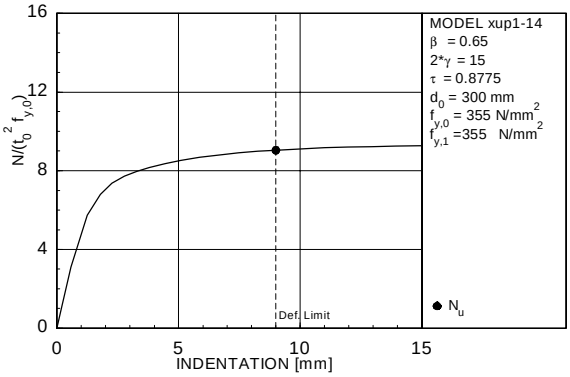

Figure 6.15 Load-displacement curve for model XUP1-14

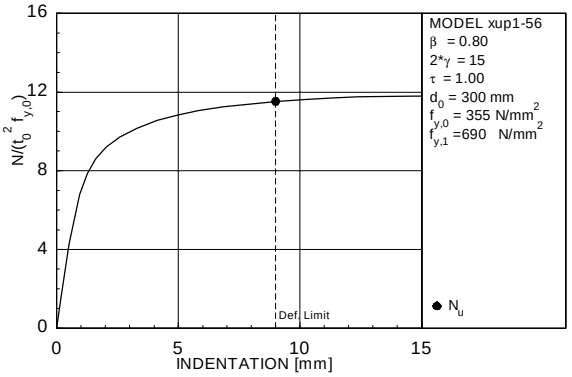

Figure 6.16 Load-displacement curve for model XUP1-56

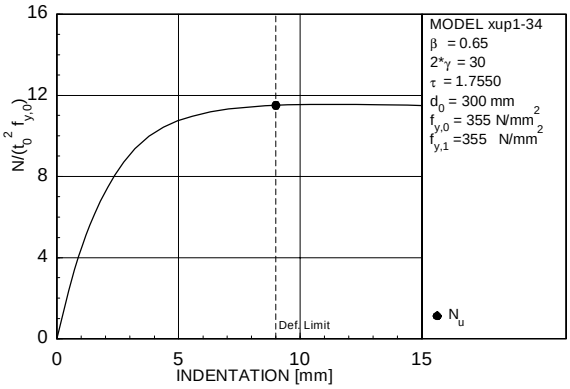

Figure 6.17 Load-displacement curve for model XUP1-34

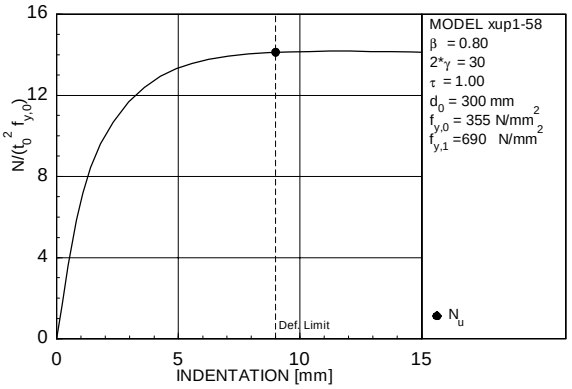

Figure 6.18 Load-displacement curve for model XUP1-58

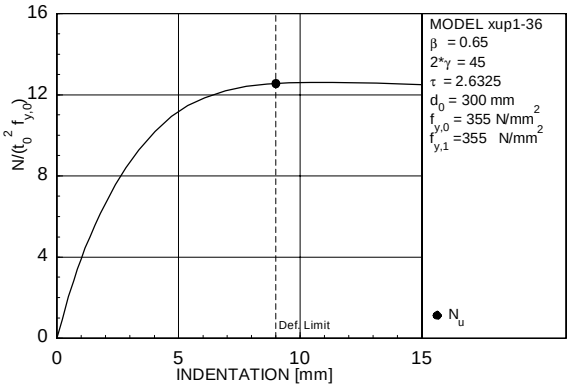

Figure 6.19 Load-displacement curve for model XUP1-36

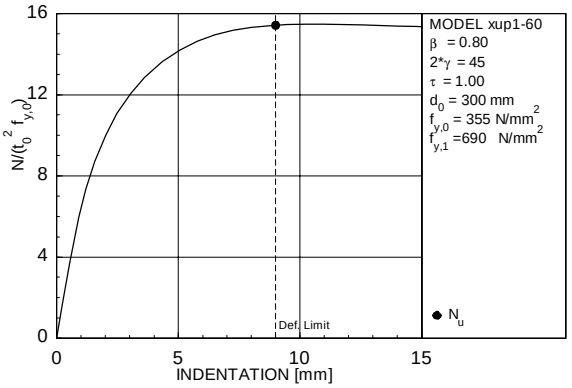

Figure 6.20 Load-displacement curve for model XUP1-60

Note: The figures are organised on this and next pages: from top to bottom an increasing 2γ, from left to right an increasing β.

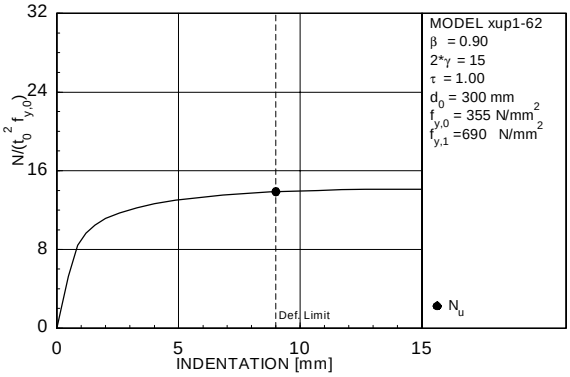

Figure 6.21 Load-displacement curve for model XUP1-62

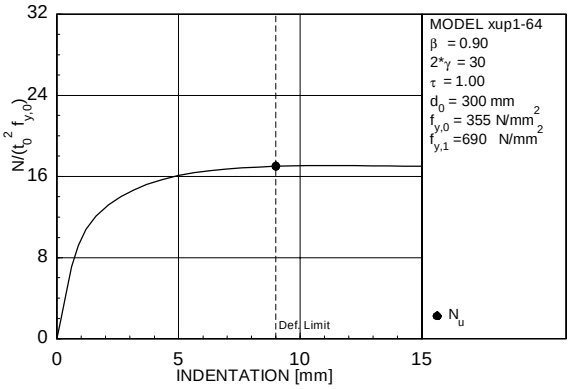

Figure 6.22 Load-displacement curve for model XUP1-64

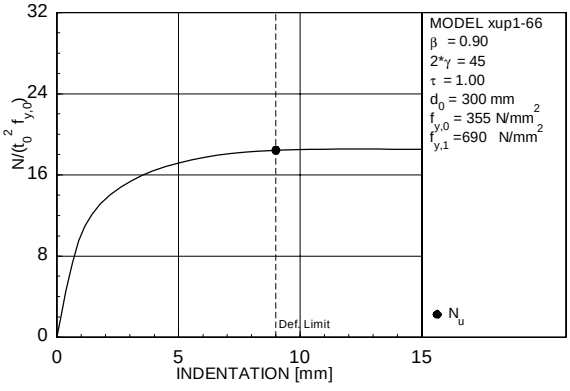

Figure 6.23 Load-displacement curve for model XUP1-66

6.1.3 Results of the finite element analyses for the multiplanar plate to CHS column connections under axial loading

In Table 6.5, the main results of the finite element analyses for the multiplanar plate to CHS column loaded with axial loading are given. Figure 6.24 shows a typical finite element mesh for multiplanar plate to CHS column connections. Figures 6.25 to 6.39. show the load-deformation curves.

The figures show that larger β-ratios give a larger non-dimensional connection strength. Larger 2γ-ratios result in a larger non-dimensional strengths, this effect becomes stronger for larger β-ratios. These results correspond with the results of the uniplanar connections. Negative load ratios reduce the connection strength, while positive load ratios increase the connection strength. The multiplanar loading effect becomes stronger for larger β-ratios and larger 2γ-ratios. Only for a load ratio of +1, a stronger 2γ-ratio effect is found, which can also theoretically be explained, as also discussed in section 7.5.

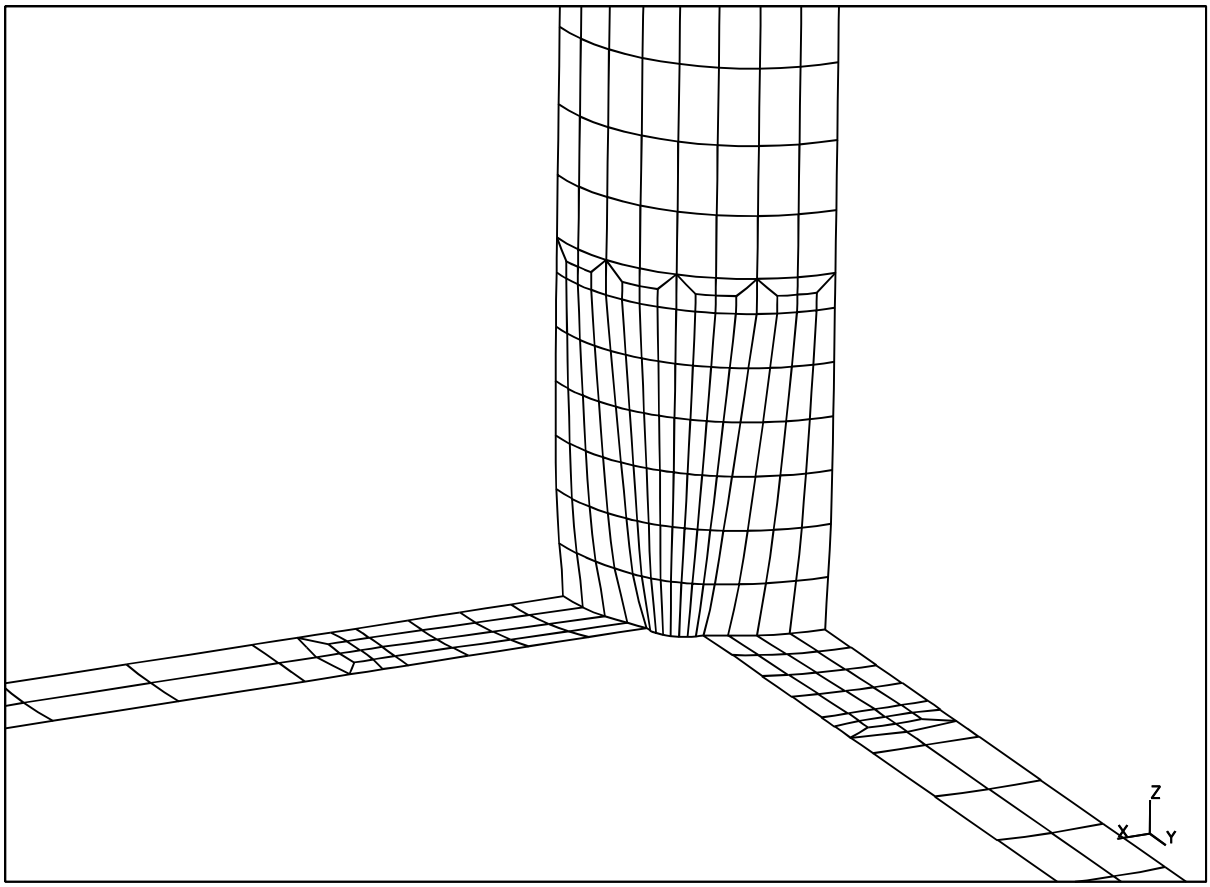

Figure 6.24 Deformed finite element mesh model XXP1-40 with load ratio +1.0

Table 6.5 Results finite element analyses multiplanar plate to CHS column connections

name	β	2γ	τ	$N_u/(t_0^2 f_{y,0})$ for load ratio J =				
				-1.0	-0.5	0.0	+0.5	+1.0
xxp1-02	0.25	15	0.3375	3.53	4.21	4.72	4.95	5.10
xxp1-04	0.25	30	0.6750	4.16	4.75	5.15	5.47	5.62
xxp1-06	0.25	45	1.0125	4.44	4.98	5.39	5.78	6.06
xxp1-08	0.40	15	0.5400	4.22	5.20	6.32	7.01	7.50
xxp1-10	0.40	30	1.0800	5.10	6.23	7.29	8.13	8.41
xxp1-12	0.40	45	1.6200	5.57	6.80	7.90	8.87	9.37
xxp1-14	0.65	15	0.8775	6.22	7.77	9.85	11.87	12.82
xxp1-34	0.65	30	1.7550	8.32	10.24	12.90	16.14	21.49
xxp1-36	0.65	45	2.6325	9.51	11.58	14.46	18.22	28.51
xxp1-38	0.55	15	0.7425	4.98	6.19	7.77	9.08	10.03
xxp1-40	0.55	30	1.4850	6.35	7.86	9.93	12.20	14.20
xxp1-42	0.55	45	2.2275	6.88	8.54	10.92	13.64	15.85
xxp1-50	0.60	15	0.8100	5.45	6.76	8.50	10.03	11.11
xxp1-52	0.60	30	1.6100	6.94	8.55	10.80	13.50	16.75
xxp1-54	0.60	45	2.4300	7.55	9.29	11.77	15.00	19.43

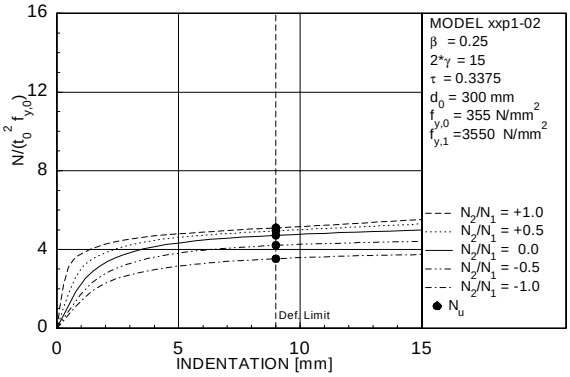

Figure 6.25 Load-displacement curves for model XXP1-02

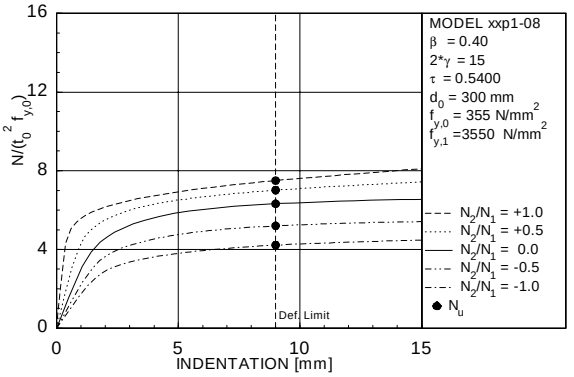

Figure 6.26 Load-displacement curves for model XXP1-08

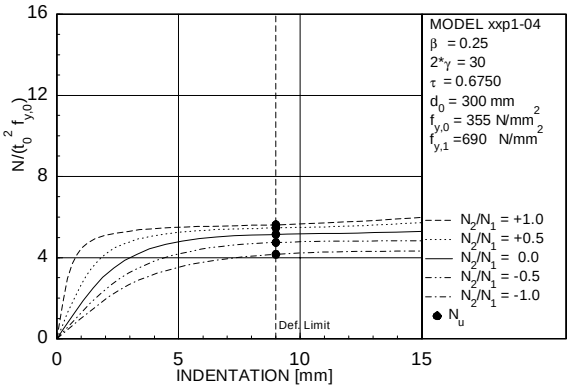

Figure 6.27 Load-displacement curves for model XXP1-04

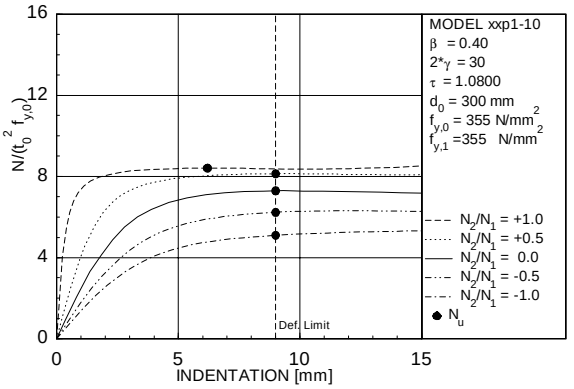

Figure 6.28 Load-displacement curves for model XXP1-10

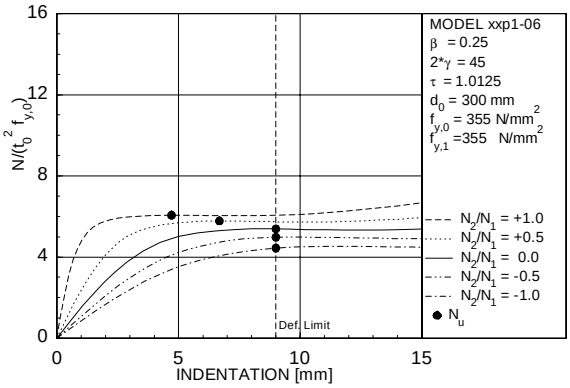

Figure 6.29 Load-displacement curves for model XXP1-06

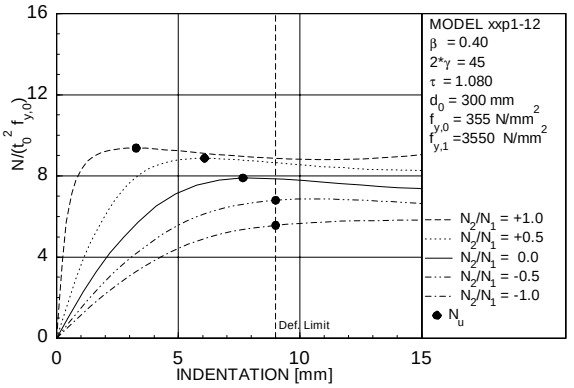

Figure 6.30 Load-displacement curves for model XXP1-12

Note: The figures are organised on this and next pages: top to bottom an increasing 2γ, left to right an increasing β.

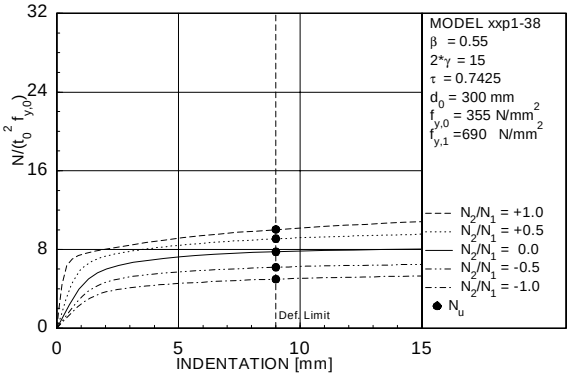

Figure 6.31 Load-displacement curves for model XXP1-38

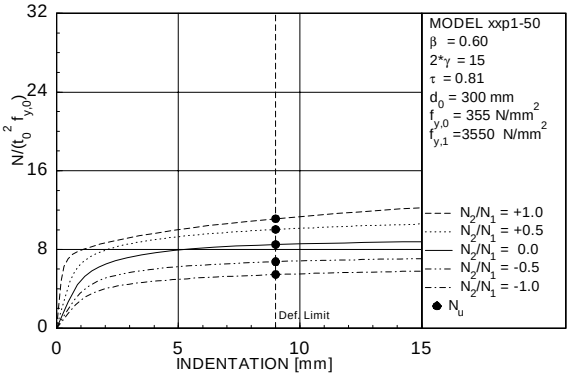

Figure 6.32 Load-displacement curves for model XXP1-50

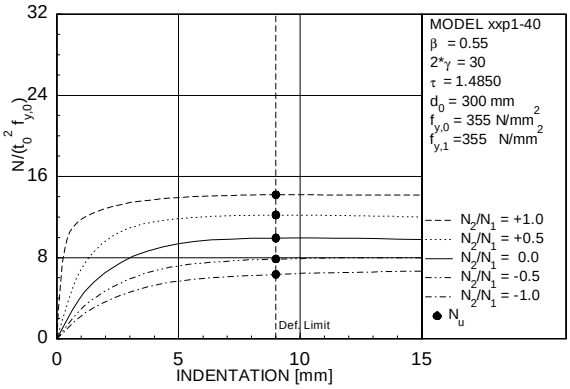

Figure 6.33 Load-displacement curves for model XXP1-40

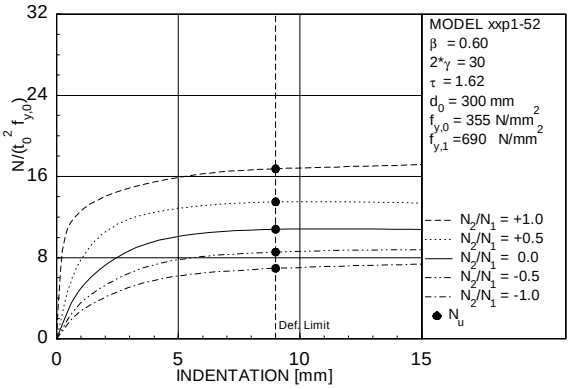

Figure 6.34 Load-displacement curves for model XXP1-52

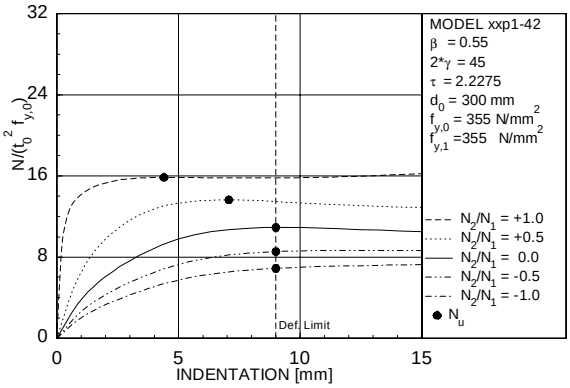

Figure 6.35 Load-displacement curves for model XXP1-42

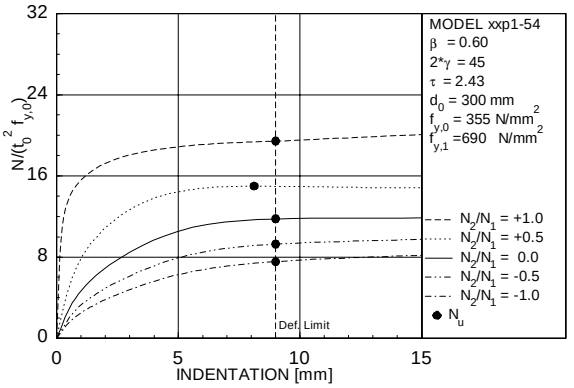

Figure 6.36 Load-displacement curves for model XXP1-54

Note: The figures are organised on this and next pages: from top to bottom an increasing 2γ, from left to right an increasing β.

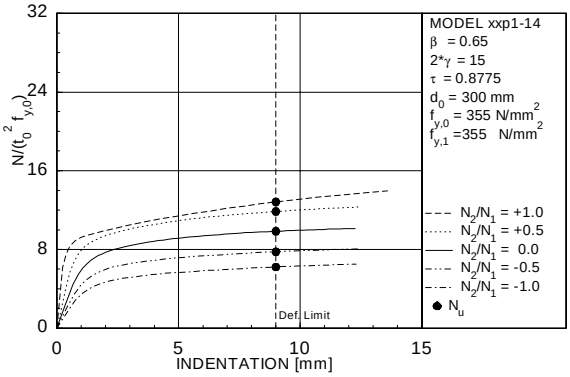

Figure 6.37 Load-displacement curves for model XXP1-14

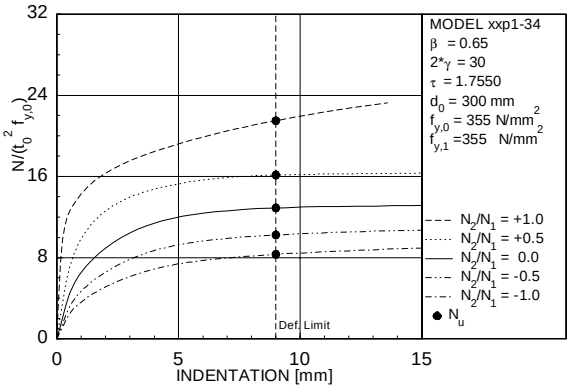

Figure 6.38 Load-displacement curves for model XXP1-34

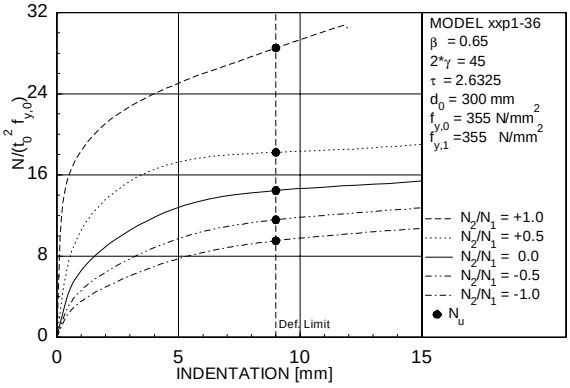

Figure 6.39 Load-displacement curves for model XXP1-36

6.2 Plate to CHS column connections under axial loading, interaction effects

6.2.1 Research programme for multiplanar connections

For the parametric study on connections with plates at two levels or I-beams welded to a CHS column connections, 45 connections were analysed with five different β ratios, for each β ratio three η ratios, three 2γ ratios and one τ ratio. The geometrical parameters of the models are listed in Table 6.6. The column length was taken as six times the column diameter d_0 plus the I-beam height or the distance between the plates in two layers. The I-beam length was taken five times the I-beam width. These lengths are sufficient to minimize boundary and load introduction effects. The flange thickness was taken as 9% of the flange or plate width; the web thickness was taken as 60% of the flange thickness, which agrees approximately with the ratio between the web thickness to flange thickness ratio of IPE sections. The combination of the parameters gives 45 finite element models, as listed in Tables 6.6 and 6.7.

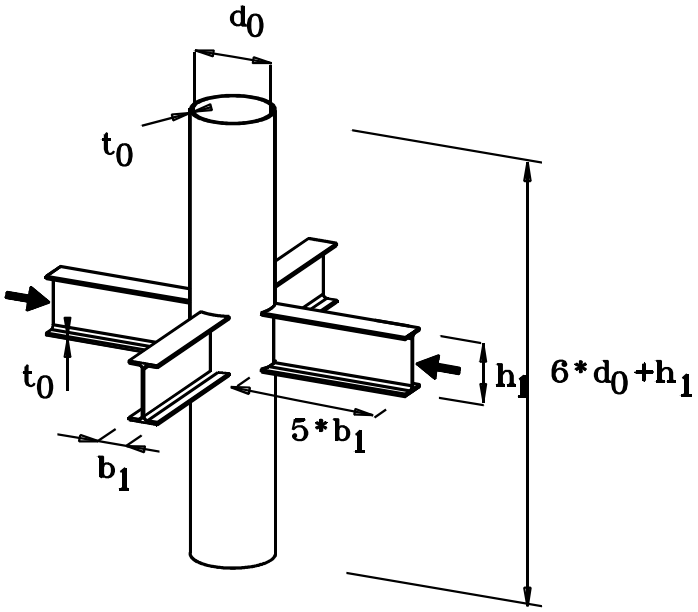

Figure 6.40 Main dimensions FE model for axially loaded I-beam to CHS column connections

The FE models with plates at two levels and the FE models with the I-beams are exactly the same, except that for the models with plates at two levels a part of the web of the I-beam was removed at the intersection of the I-beam with the column (see Figures 6.41 and 6.42). To prevent local buckling of the plates under compression, the other part of the web has been left intact.

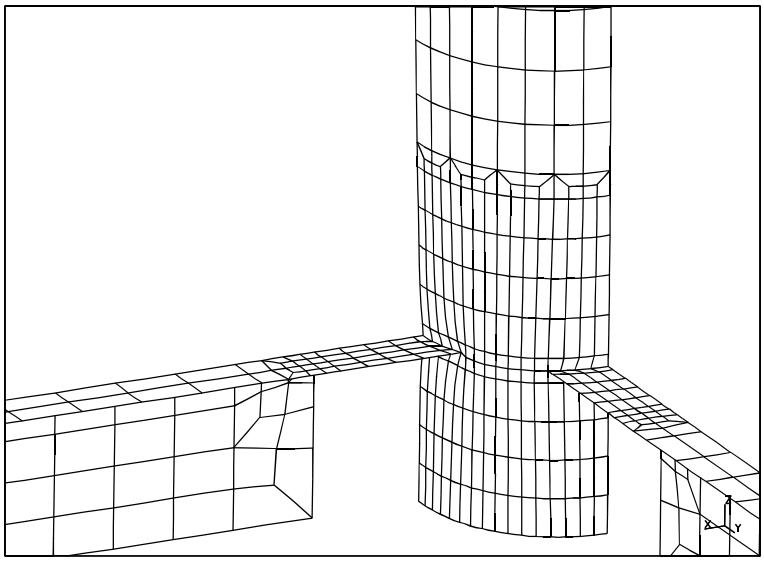

Figure 6.42 Deformed finite element mesh of model XXP2-72 (without web) for load ratio +1.0

The FE analyses without and with web were only carried out for the uniplanar loaded multiplanar connections. The finite element analyses with multiplanar axial loading were only done for the I-beam to CHS column connections.

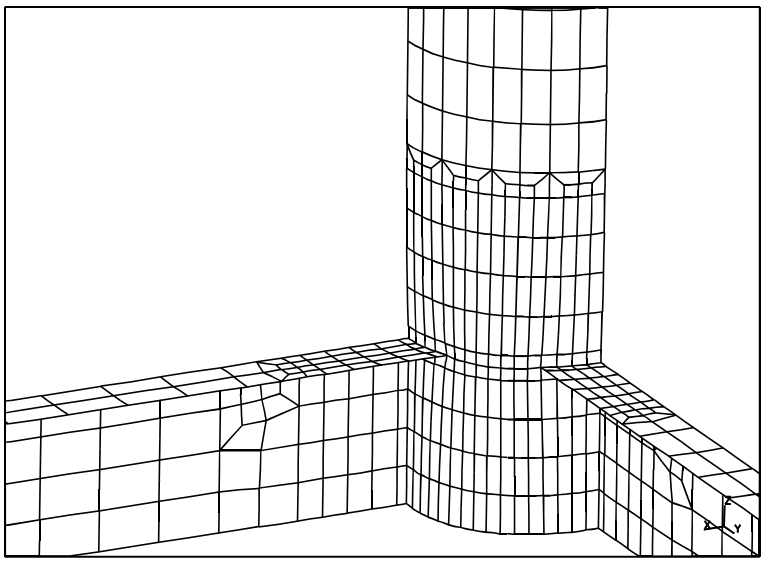

Figure 6.41 Deformed finite element mesh of model XXP2-72 (with web) for load ratio +0.5

The research programme for the multiplanar I-beam to CHS column connections loaded with axial loading is listed in Tables 6.6 and 6.7. For the connection types, with and without web the same geometrical parameters are used.

Table 6.6 Overview of the research programme on multiplanar I-beam to CHS column connections loaded with axial loading

β	η	2γ		
		15	30	45
0.25	0.25	xxp2-20	xxp2-22	xxp2-24
	0.50	xxp2-02	xxp2-04	xxp2-06
	0.75	xxp2-62	xxp2-64	xxp2-66
0.40	0.40	xxp2-26	xxp2-28	xxp2-30
	0.80	xxp2-08	xxp2-10	xxp2-12
	1.20	xxp2-68	xxp2-70	xxp2-72
0.55	0.55	xxp2-44	xxp2-46	xxp2-48
	1.10	xxp2-38	xxp2-40	xxp2-42
	1.65	xxp2-80	xxp2-82	xxp2-84
0.60	0.60	xxp2-50	xxp2-52	xxp2-54
	1.20	xxp2-56	xxp2-58	xxp2-60
	1.80	xxp2-86	xxp2-88	xxp2-90
0.65	0.65	xxp2-32	xxp2-34	xxp2-36
	1.30	xxp2-14	xxp2-16	xxp2-18
	1.95	xxp2-74	xxp2-76	xxp2-87

Table 6.7 Geometrical and material characteristics of the I-beam to CHS column connections loaded with axial loading

name	β	2γ	η	τ	$f_{y,1}$ [MPa]
xxp2-02	0.25	15	0.50	0.3375	3550.0
xxp2-04	0.25	30	0.50	0.6750	690.0
xxp2-06	0.25	45	0.50	1.0125	690.0
xxp2-08	0.40	15	0.80	0.5400	690.0
xxp2-10	0.40	30	0.80	1.0800	690.0
xxp2-12	0.40	45	0.80	1.6200	690.0
xxp2-14	0.65	15	1.30	0.8775	690.0
xxp2-16	0.65	30	1.30	1.7550	690.0
xxp2-18	0.65	45	1.30	2.6325	690.0
xxp2-20	0.25	15	0.25	0.3375	3550.0
xxp2-22	0.25	30	0.25	0.6750	690.0
xxp2-24	0.25	45	0.25	1.0125	690.0
xxp2-26	0.40	15	0.40	0.5400	690.0
xxp2-28	0.40	30	0.40	1.0800	690.0
xxp2-30	0.40	45	0.40	1.6200	690.0
xxp2-32	0.65	15	0.65	0.8775	690.0
xxp2-34	0.65	30	0.65	1.7550	690.0
xxp2-36	0.65	45	0.65	2.6325	690.0
xxp2-38	0.55	15	1.10	0.7425	690.0
xxp2-40	0.55	30	1.10	1.4850	690.0
xxp2-42	0.55	45	1.10	2.2275	690.0
xxp2-44	0.55	15	0.55	0.7425	690.0
xxp2-46	0.55	30	0.55	1.4850	690.0
xxp2-48	0.55	45	0.55	2.2275	690.0
xxp2-50	0.60	15	0.60	0.8100	690.0
xxp2-52	0.60	30	0.60	1.6100	690.0
xxp2-54	0.60	45	0.60	2.4300	690.0
xxp2-56	0.60	15	1.20	0.8100	690.0
xxp2-58	0.60	30	1.20	1.6200	690.0
xxp2-60	0.60	45	1.20	2.4300	690.0
xxp2-62	0.25	15	0.75	0.3375	3550.0
xxp2-64	0.25	30	0.75	0.6750	690.0
xxp2-66	0.25	45	0.75	1.0125	690.0
xxp2-68	0.40	15	1.20	0.5400	690.0
xxp2-70	0.40	30	1.20	1.0800	690.0
xxp2-72	0.40	45	1.20	1.6200	690.0
xxp2-74	0.65	15	1.95	0.8775	690.0
xxp2-76	0.65	30	1.95	1.7550	690.0
xxp2-78	0.65	45	1.95	1.0000	690.0
xxp2-80	0.55	15	1.65	0.7425	690.0
xxp2-82	0.55	30	1.65	1.485	690.0
xxp2-84	0.55	45	1.65	2.2275	690.0
xxp2-86	0.60	15	1.80	0.8100	690.0
xxp2-88	0.60	30	1.80	1.6200	690.0
xxp2-90	0.60	45	1.80	2.4300	690.0

The results of the finite element analyses for the uniplanar loaded connections with and without the web are shown in Table 6.8 and Figures 6.43 to 6.87. The results of the finite element analyses with the complete web included and loaded with multiplanar axial loading are listed in Table 6.9 and shown in Figures 6.88 to 6.132.

From the figures, the following observations can be made:

β Influence:

The non-dimensional strength increases with an increasing β ratio.

2γ Influence:

The non-dimensional strength of the connections is increasing for larger 2γ ratios. This effect becomes stronger for larger β ratios.

η Influence:

The non-dimensional strength increases for larger η-ratios. This effect becomes stronger for larger β ratios.

Presence of the web influence:

The presence of the web has only a small influence on the connection strength.

Multiplanar load effect:

Positive load ratios increase the connection strength, while negative load ratios decrease the connection strength. For a load ratio +1, there is a strong interaction between β and 2γ. This effect can be theoretically explained as shown in section 7.5.

Table 6.8 Finite element results of I-beam to CHS under axial loading, influence presence of web

name	β	2γ	η	τ	$N_u/(t_0^2 f_{y,0})$ no web	$N_u/(t_0^2 f_{y,0})$ with web	web/no web
xxp2-02	0.25	15	0.50	0.3375	7.34	7.49	1.020
xxp2-04	0.25	30	0.50	0.6750	8.06	8.22	1.020
xxp2-06	0.25	45	0.50	1.0125	8.22	8.39	1.021
xxp2-08	0.40	15	0.80	0.5400	9.84	10.18	1.035
xxp2-10	0.40	30	0.80	1.0800	11.02	11.29	1.025
xxp2-12	0.40	45	0.80	1.6200	11.39	11.64	1.022
xxp2-14	0.65	15	1.30	0.8775	17.32	17.91	1.034
xxp2-16	0.65	30	1.30	1.7550	21.97	23.07	1.050
xxp2-18	0.65	45	1.30	2.6325	24.76	26.17	1.057
xxp2-20	0.25	15	0.25	0.3375	6.43	6.48	1.008
xxp2-22	0.25	30	0.25	0.6750	7.23	7.25	1.003
xxp2-24	0.25	45	0.25	1.0125	7.63	7.66	1.004
xxp2-26	0.40	15	0.40	0.5400	8.75	8.86	1.013
xxp2-28	0.40	30	0.40	1.0800	10.04	10.13	1.009
xxp2-30	0.40	45	0.40	1.6200	10.59	10.71	1.011
xxp2-32	0.65	15	0.65	0.8775	15.57	15.80	1.015
xxp2-34	0.65	30	0.65	1.7550	20.15	20.92	1.038
xxp2-36	0.65	45	0.65	2.6325	22.80	23.81	1.044
xxp2-38	0.55	15	1.10	0.7425	13.04	13.49	1.035
xxp2-40	0.55	30	1.10	1.4850	15.26	15.85	1.039
xxp2-42	0.55	45	1.10	2.2275	15.92	16.61	1.043
xxp2-44	0.55	15	0.55	0.7425	11.51	11.68	1.015
xxp2-46	0.55	30	0.55	1.4850	13.71	13.97	1.019
xxp2-48	0.55	45	0.55	2.2275	14.44	14.68	1.017
xxp2-50	0.60	15	0.60	0.8100	13.21	13.41	1.015
xxp2-52	0.60	30	0.60	1.6100	15.98	16.40	1.026
xxp2-54	0.60	45	0.60	2.4300	16.96	17.34	1.022
xxp2-56	0.60	15	1.20	0.8100	14.86	15.37	1.034
xxp2-58	0.60	30	1.20	1.6200	17.67	18.44	1.044
xxp2-60	0.60	45	1.20	2.4300	18.67	19.49	1.044
xxp2-62	0.25	15	0.75	0.3375	7.82	8.24	1.054
xxp2-64	0.25	30	0.75	0.6750	8.53	8.84	1.036
xxp2-66	0.25	45	0.75	1.0125	8.70	8.91	1.024
xxp2-68	0.40	15	1.20	0.5400	10.24	10.85	1.060
xxp2-70	0.40	30	1.20	1.0800	11.88	12.39	1.043
xxp2-72	0.40	45	1.20	1.6200	12.31	12.87	1.045
xxp2-74	0.65	15	1.95	0.8775	18.66	19.81	1.062
xxp2-76	0.65	30	1.95	1.7550	23.40	24.83	1.061
xxp2-78	0.65	45	1.95	1.0000	26.15	27.99	1.070
xxp2-80	0.55	15	1.65	0.7425	14.24	15.09	1.060
xxp2-82	0.55	30	1.65	1.4850	16.55	17.40	1.051
xxp2-84	0.55	45	1.65	2.2275	17.18	18.29	1.065
xxp2-86	0.60	15	1.80	0.8100	16.13	17.11	1.061
xxp2-88	0.60	30	1.80	1.6200	19.06	20.09	1.054
xxp2-90	0.60	45	1.80	2.4300	20.02	21.26	1.062

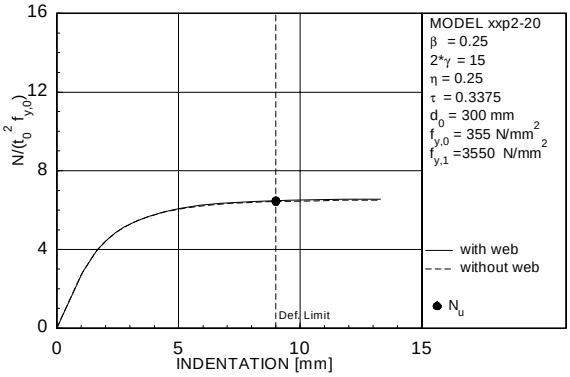

Figure 6.43 Load-displacement curves for model XXP2-20

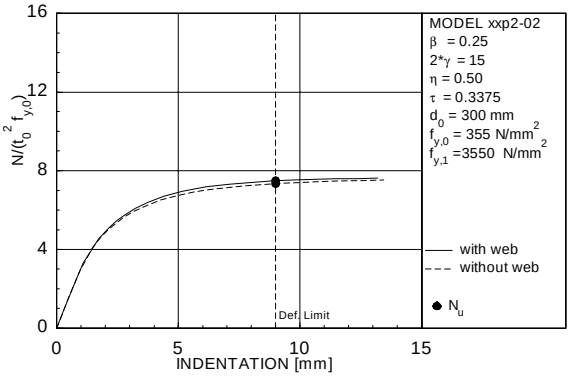

Figure 6.44 Load-displacement curves for model XXP2-02

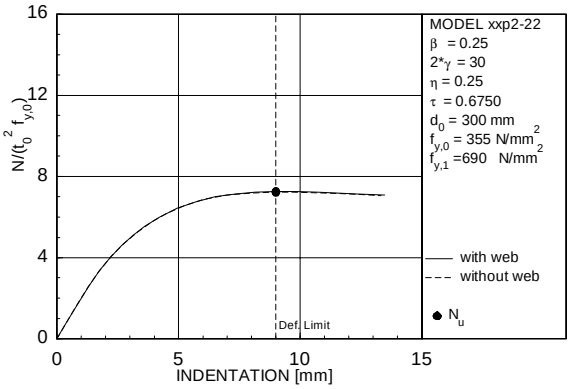

Figure 6.45 Load-displacement curves for model XXP2-22

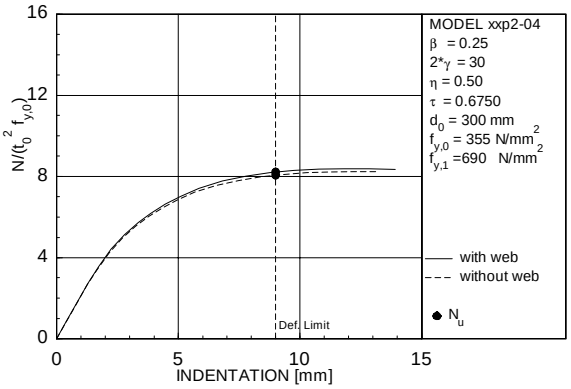

Figure 6.46 Load-displacement curves for model XXP2-04

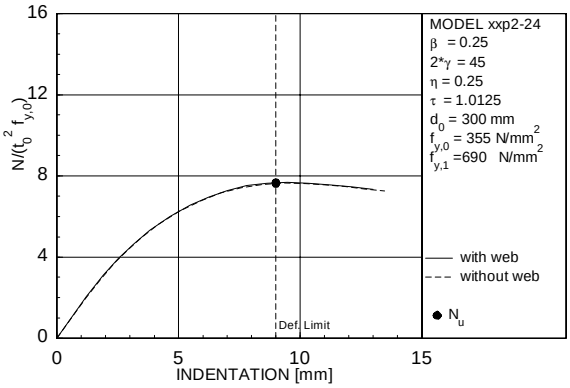

Figure 6.47 Load-displacement curves for model XXP2-24

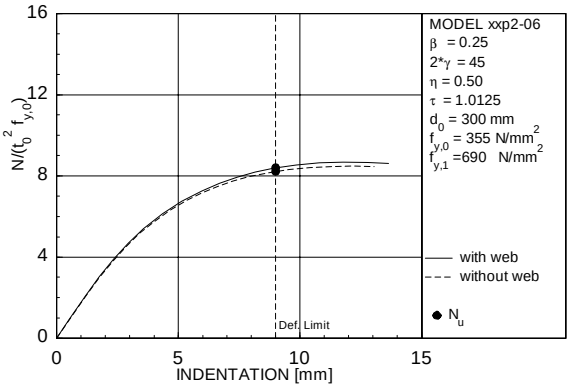

Figure 6.48 Load-displacement curves for model XXP2-06

Note: The figures are organised on this and next pages: from top to bottom an increasing 2γ, from left to right an increasing η and β.

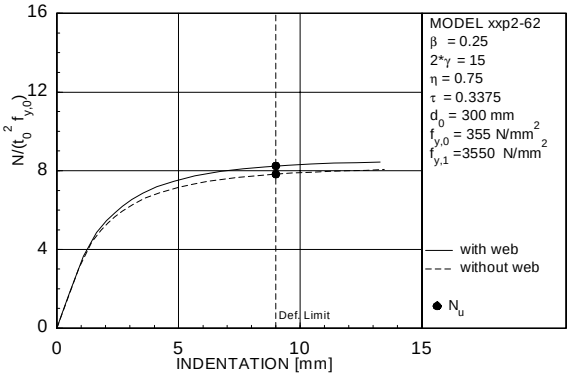

Figure 6.49 Load-displacement curves for model XXP2-62

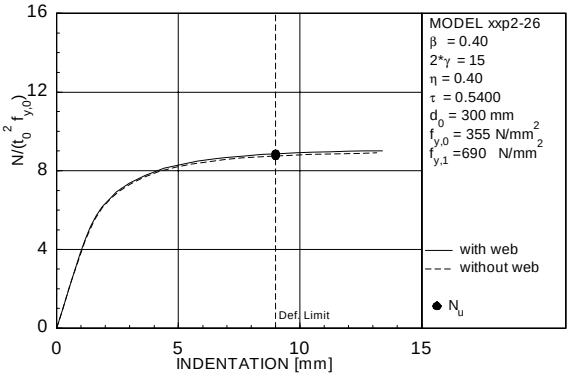

Figure 6.50 Load-displacement curves for model XXP2-26

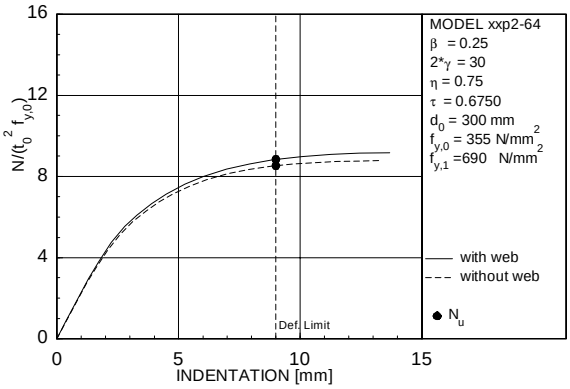

Figure 6.51 Load-displacement curves for model XXP2-64

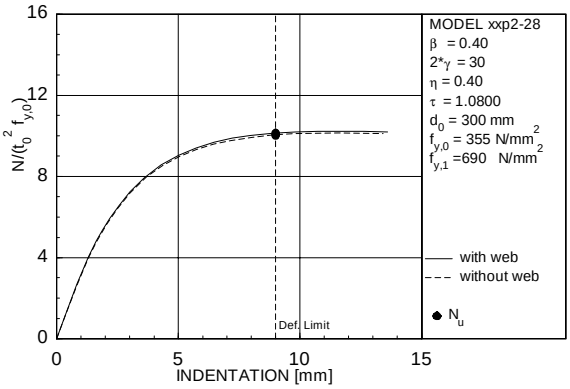

Figure 6.52 Load-displacement curves for model XXP2-28

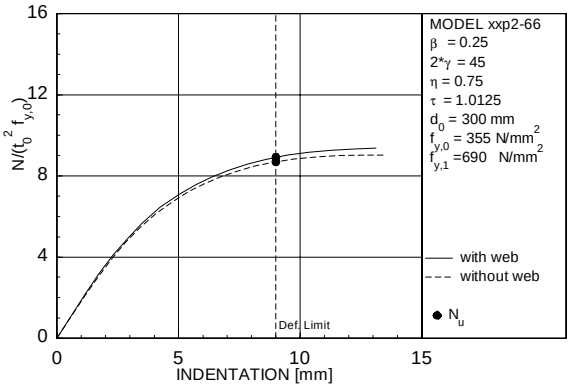

Figure 6.53 Load-displacement curves for model XXP2-66

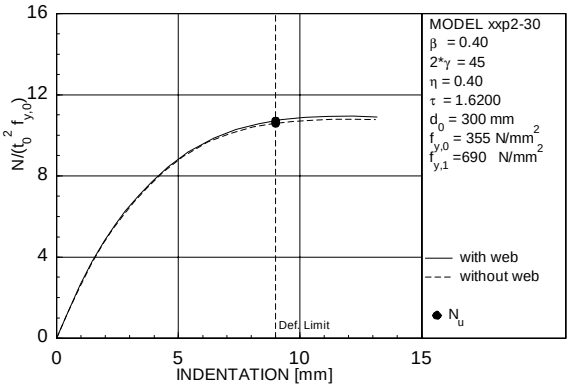

Figure 6.54 Load-displacement curves for model XXP2-30

Note: The figures are organised on this and next pages: from top to bottom an increasing 2γ, from left to right an increasing η and β.

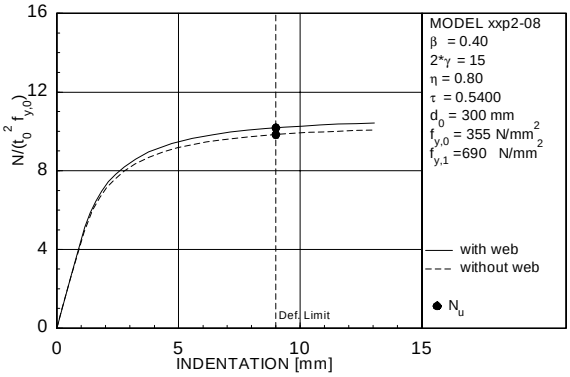

Figure 6.55 Load-displacement curves for model XXP2-08

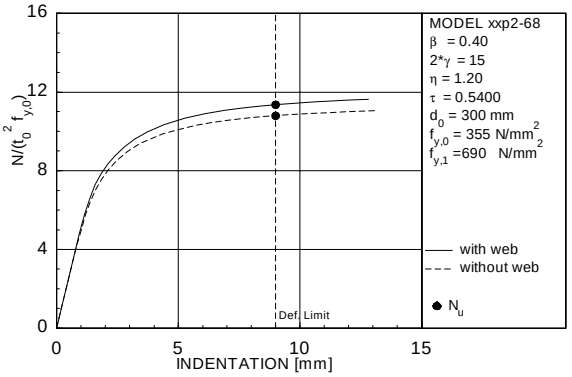

Figure 6.56 Load-displacement curves for model XXP2-68

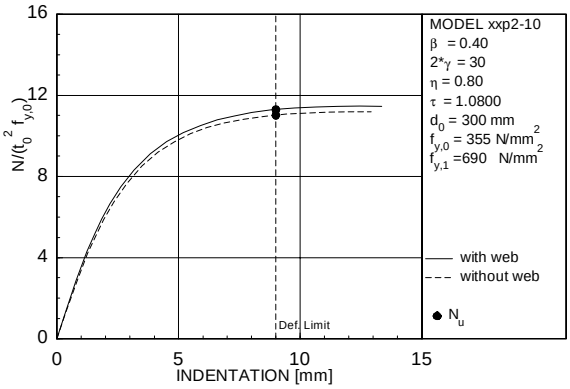

Figure 6.57 Load-displacement curves for model XXP2-10

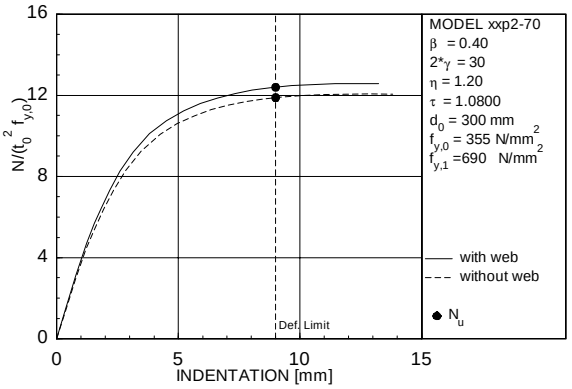

Figure 6.58 Load-displacement curves for model XXP2-70

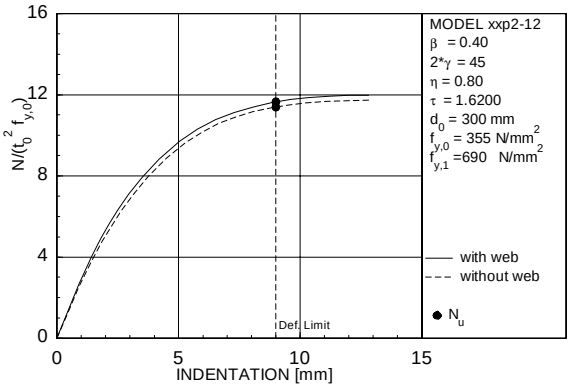

Figure 6.59 Load-displacement curves for model XXP2-12

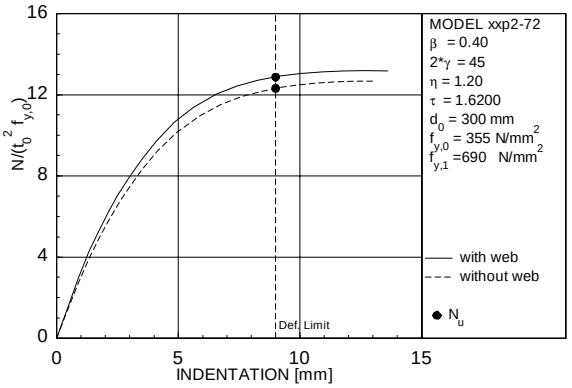

Figure 6.60 Load-displacement curves for model XXP2-72

Note: The figures are organised on this and next pages: from top to bottom an increasing 2γ, from left to right an increasing η and β.

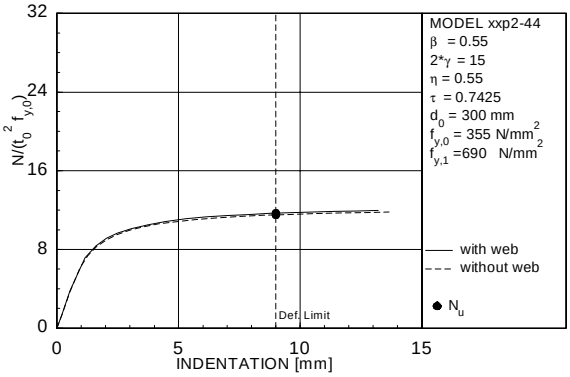

Figure 6.61 Load-displacement curves for model XXP2-44

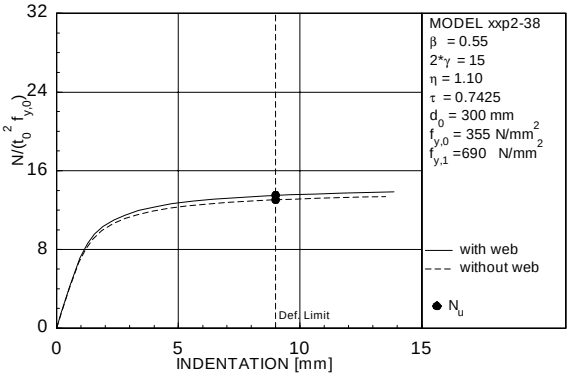

Figure 6.62 Load-displacement curves for model XXP2-38

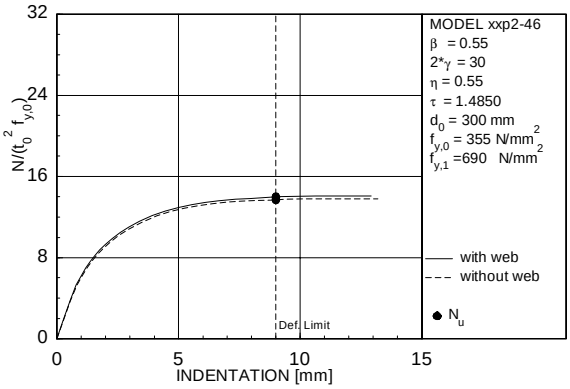

Figure 6.63 Load-displacement curves for model XXP2-46

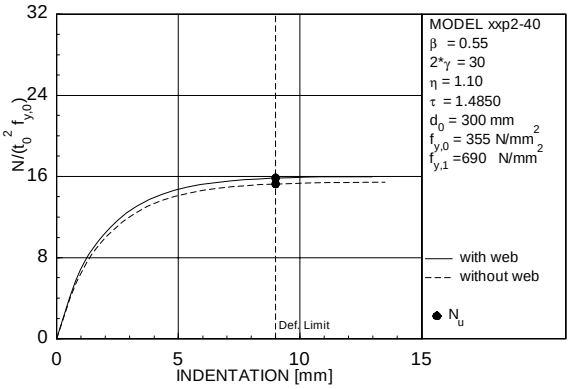

Figure 6.64 Load-displacement curves for model XXP2-40

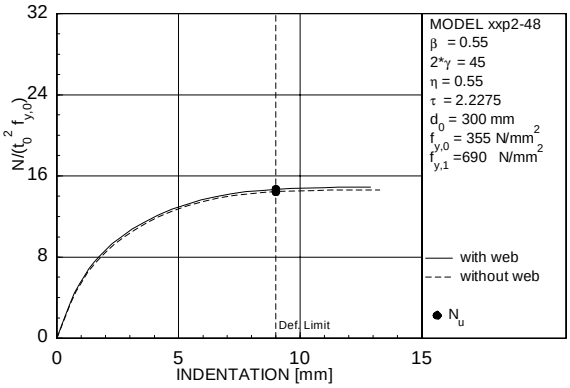

Figure 6.65 Load-displacement curves for model XXP2-48

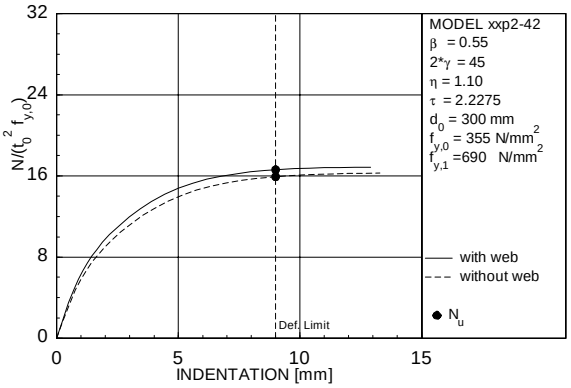

Figure 6.66 Load-displacement curves for model XXP2-42

Note: The figures are organised on this and next pages: from top to bottom an increasing 2γ, from left to right an increasing η and β.

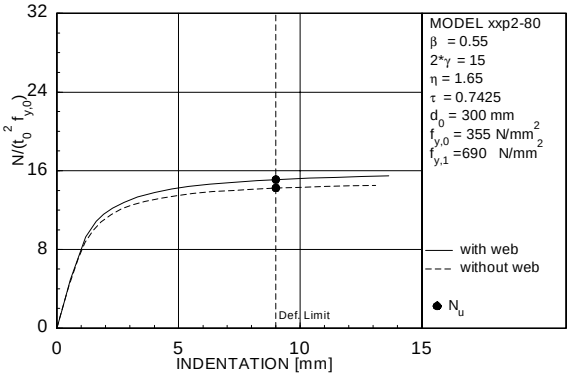

Figure 6.67 Load-displacement curves for model XXP2-80

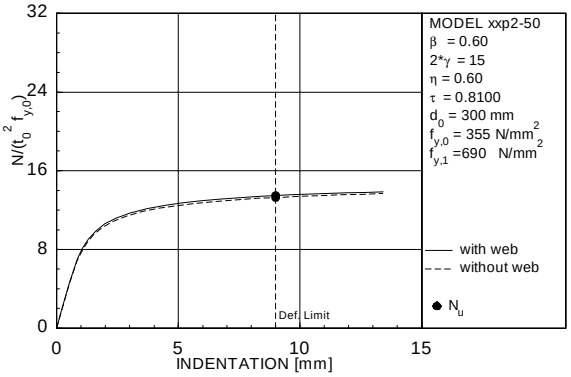

Figure 6.68 Load-displacement curves for model XXP2-50

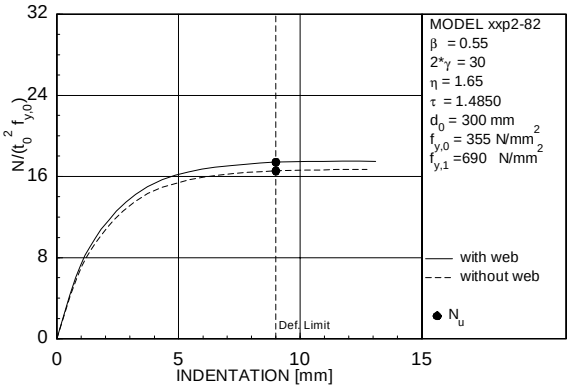

Figure 6.69 Load-displacement curves for model XXP2-82

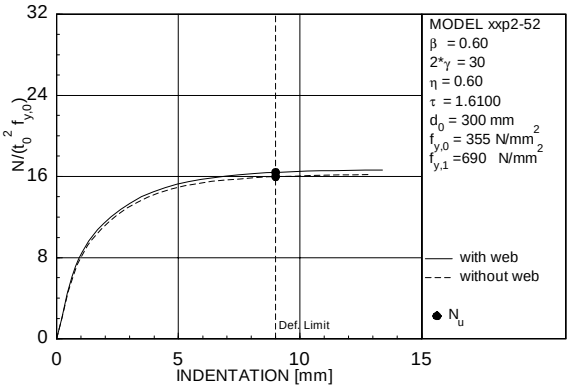

Figure 6.70 Load-displacement curves for model XXP2-52

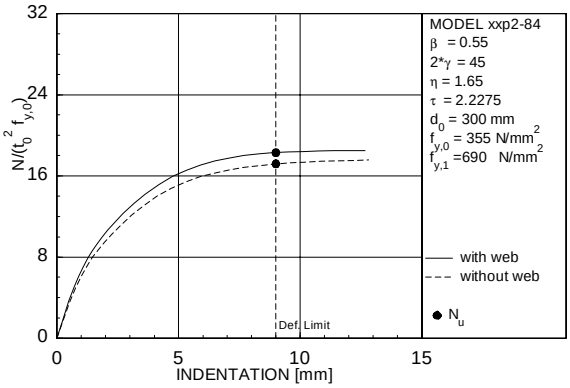

Figure 6.71 Load-displacement curves for model XXP2-84

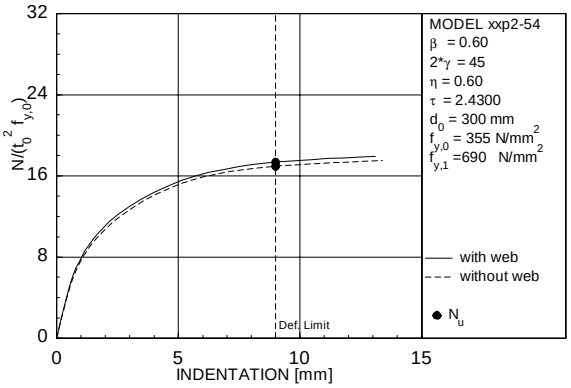

Figure 6.72 Load-displacement curves for model XXP2-54

Note: The figures are organised on this and next pages: from top to bottom an increasing 2γ, from left to right an increasing η and β.

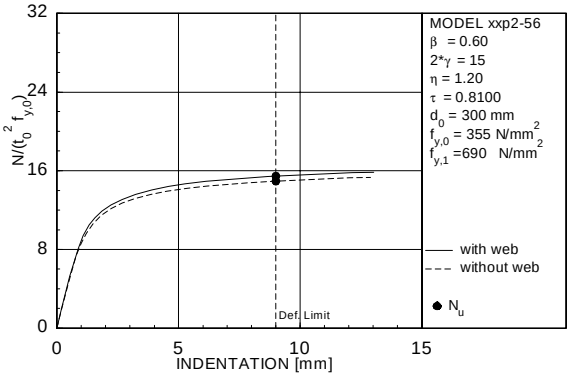

Figure 6.73 Load-displacement curves for model XXP2-56

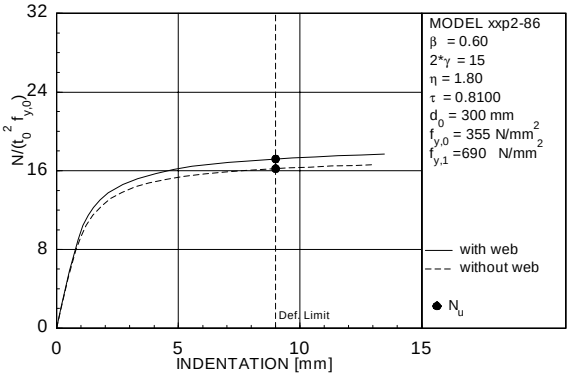

Figure 6.74 Load-displacement curves for model XXP2-86

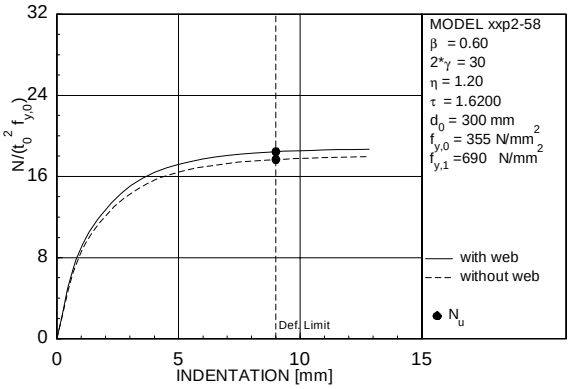

Figure 6.75 Load-displacement curves for model XXP2-58

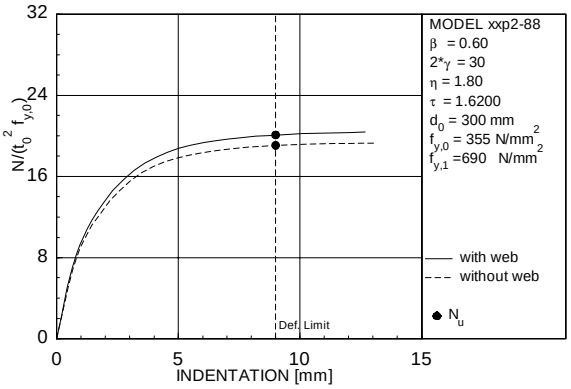

Figure 6.76 Load-displacement curves for model XXP2-88

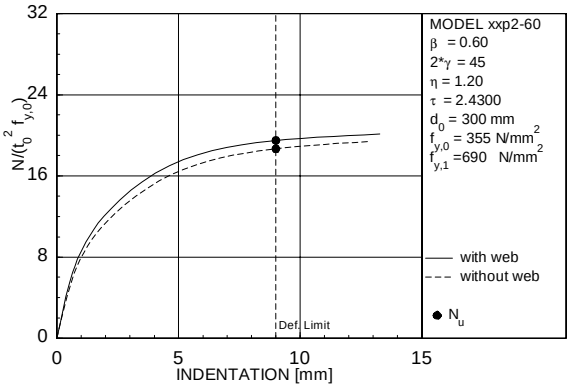

Figure 6.77 Load-displacement curves for model XXP2-60

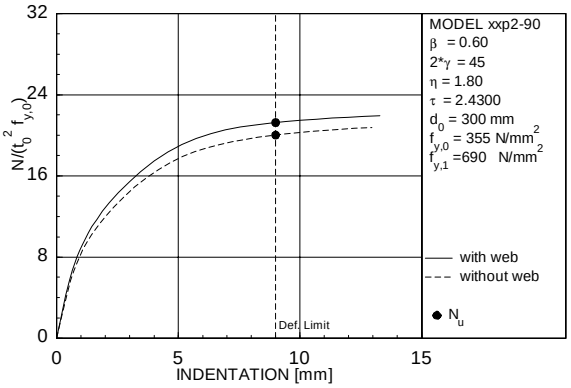

Figure 6.78 Load-displacement curves for model XXP2-90

Note: The figures are organised on this and next pages: from top to bottom an increasing 2γ, from left to right an increasing η and β.

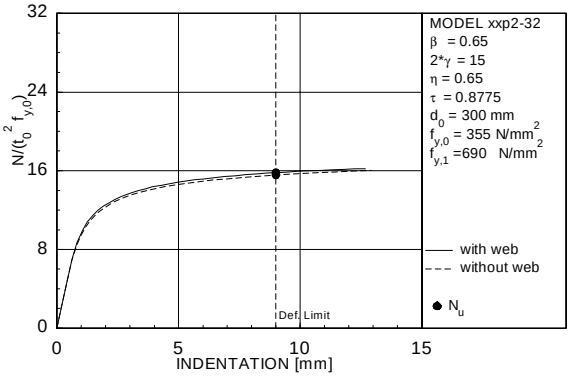

Figure 6.79 Load-displacement curves for model XXP2-32

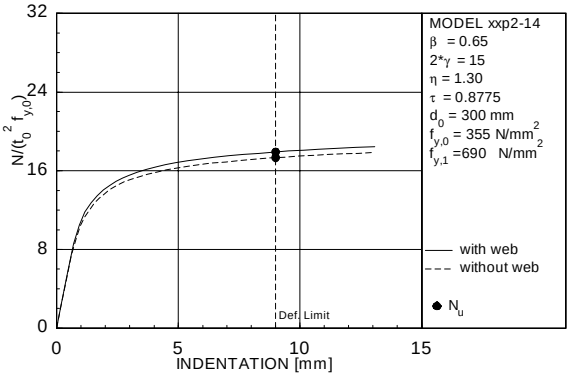

Figure 6.80 Load-displacement curves for model XXP2-14

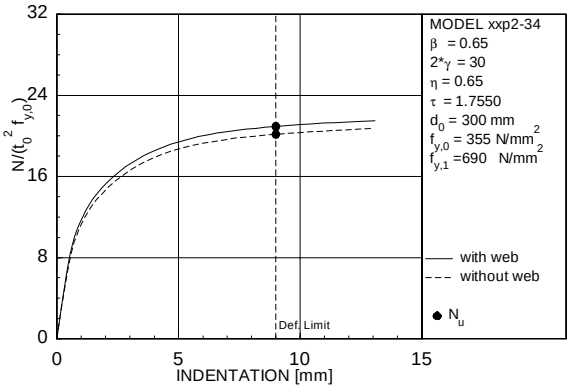

Figure 6.81 Load-displacement curves for model XXP2-34

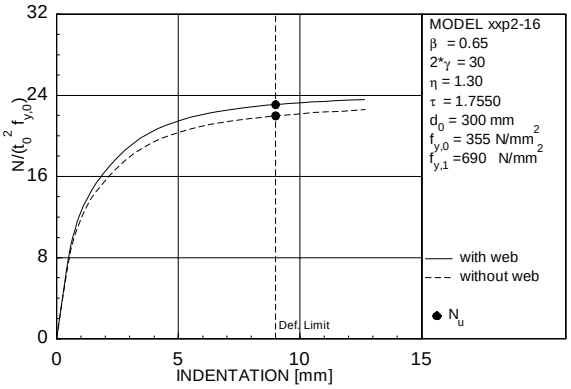

Figure 6.82 Load-displacement curves for model XXP2-16

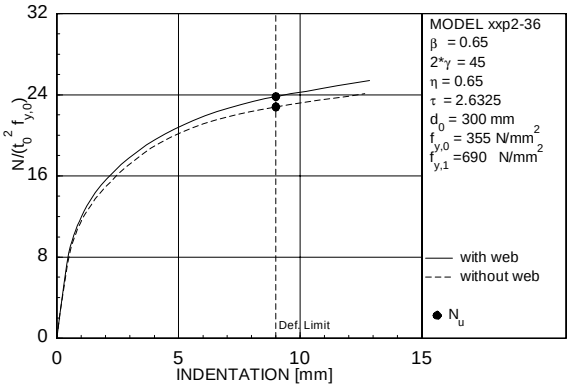

Figure 6.83 Load-displacement curves for model XXP2-36

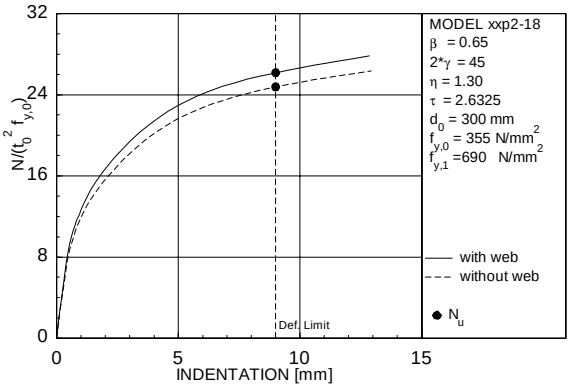

Figure 6.84 Load-displacement curves for model XXP2-18

Note: The figures are organised on this and next pages: from top to bottom an increasing 2γ, from left to right an increasing η and β.

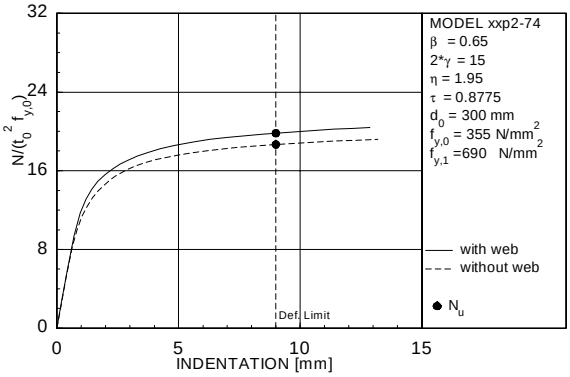

Figure 6.85 Load-displacement curves for model XXP2-74

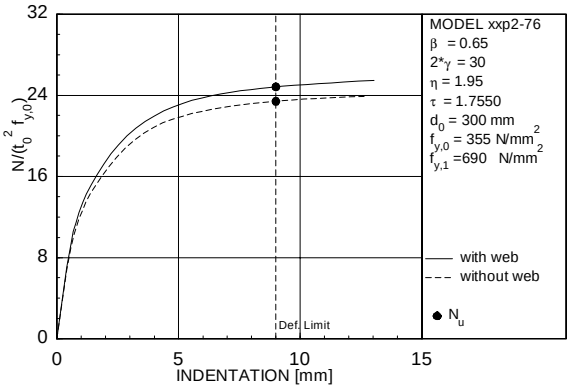

Figure 6.86 Load-displacement curves for model XXP2-76

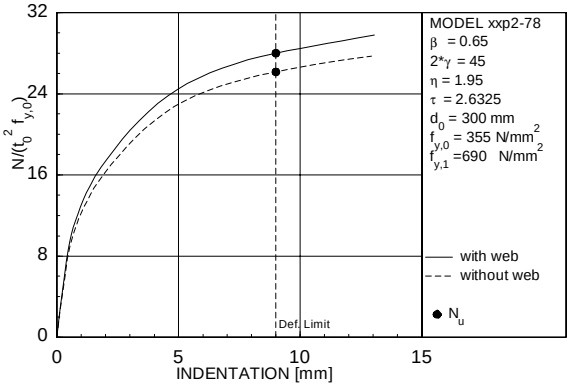

Figure 6.87 Load-displacement curves for model XXP2-78

Table 6.9 Results of the finite element analyses on multiplanar I-beam to CHS column connections under axial loading

name	β	2γ	η	τ	$N_u/(t_0^2 f_{y,0})$ For load ratio J =				
					-1.0	-0.5	0.0	+0.5	+1.0
xxp2-02	0.25	15	0.50	0.3375	4.48	5.69	7.49	8.84	9.38
xxp2-04	0.25	30	0.50	0.6750	5.06	6.38	8.22	9.53	9.68
xxp2-06	0.25	45	0.50	1.0125	5.26	6.58	8.39	9.91	10.42
xxp2-08	0.40	15	0.80	0.5400	5.69	7.26	9.69	12.53	14.29
xxp2-10	0.40	30	0.80	1.0800	6.69	8.49	11.29	14.58	16.40
xxp2-12	0.40	45	0.80	1.6200	6.95	8.78	11.64	15.17	17.58
xxp2-14	0.65	15	1.30	0.8775	10.62	13.49	17.91	23.99	29.64
xxp2-16	0.65	30	1.30	1.7550	14.16	17.68	23.07	31.01	45.45
xxp2-18	0.65	45	1.30	2.6325	16.34	20.22	26.17	34.94	57.51
xxp2-20	0.25	15	0.25	0.3375	4.12	5.18	6.48	7.24	7.51
xxp2-22	0.25	30	0.25	0.6750	4.81	6.02	7.25	7.98	8.01
xxp2-24	0.25	45	0.25	1.0125	5.06	6.30	7.66	8.54	8.81
xxp2-26	0.40	15	0.40	0.5400	5.02	6.38	8.42	10.41	11.45
xxp2-28	0.40	30	0.40	1.0800	6.00	7.62	10.13	12.74	13.74
xxp2-30	0.40	45	0.40	1.6200	6.35	8.04	10.71	13.62	15.01
xxp2-32	0.65	15	0.65	0.8775	9.41	11.93	15.80	20.81	25.23
xxp2-34	0.65	30	0.65	1.7550	12.83	16.01	20.92	28.09	41.81
xxp2-36	0.65	45	0.65	2.6325	14.89	0.00	23.81	0.00	53.87
xxp2-38	0.55	15	1.10	0.7425	7.97	10.12	13.49	18.17	22.72
xxp2-40	0.55	30	1.10	1.4850	9.51	11.97	15.85	21.61	28.01
xxp2-42	0.55	45	1.10	2.2275	10.02	12.55	16.61	23.03	30.69
xxp2-44	0.55	15	0.55	0.7425	6.90	8.75	11.68	15.53	18.94
xxp2-46	0.55	30	0.55	1.4850	8.36	10.52	13.97	19.20	24.67
xxp2-48	0.55	45	0.55	2.2275	8.84	11.07	14.68	20.52	27.31
xxp2-50	0.60	15	0.60	0.8100	7.95	10.08	13.41	17.83	22.27
xxp2-52	0.60	30	0.60	1.6100	9.93	12.43	16.40	22.44	31.63
xxp2-54	0.60	45	0.60	2.4300	10.68	13.26	17.34	24.02	36.21
xxp2-56	0.60	15	1.20	0.8100	9.10	11.55	15.37	20.70	26.34
xxp2-58	0.60	30	1.20	1.6200	11.19	14.01	18.44	25.09	35.13
xxp2-60	0.60	45	1.20	2.4300	11.99	14.91	19.49	26.84	39.69
xxp2-62	0.25	15	0.75	0.3375	4.83	6.16	8.24	10.20	11.09
xxp2-64	0.25	30	0.75	0.6750	5.34	6.76	8.84	10.73	11.13
xxp2-66	0.25	45	0.75	1.0125	5.51	6.92	8.91	10.95	11.80
xxp2-68	0.40	15	1.20	0.5400	6.32	8.08	10.85	14.42	16.99
xxp2-70	0.40	30	1.20	1.0800	7.38	9.35	12.39	16.24	18.69
xxp2-72	0.40	45	1.20	1.6200	7.71	9.73	12.87	16.84	20.05
xxp2-74	0.65	15	1.95	0.8775	11.60	14.81	19.81	26.91	34.03
xxp2-76	0.65	30	1.95	1.7550	15.22	19.02	24.83	33.55	49.09
xxp2-78	0.65	45	1.95	2.6325	17.50	21.67	27.99	37.36	60.83
xxp2-80	0.55	15	1.65	0.7425	8.83	11.25	15.09	20.62	26.43
xxp2-82	0.55	30	1.65	1.4850	10.46	13.17	17.40	23.78	31.11
xxp2-84	0.55	45	1.65	2.2275	11.04	13.84	18.29	25.15	33.54
xxp2-86	0.60	15	1.80	0.8100	10.02	12.78	17.11	23.38	30.39
xxp2-88	0.60	30	1.80	1.6200	12.20	15.29	20.09	27.44	38.49
xxp2-90	0.60	45	1.80	2.4300	13.08	16.29	21.26	29.12	42.76

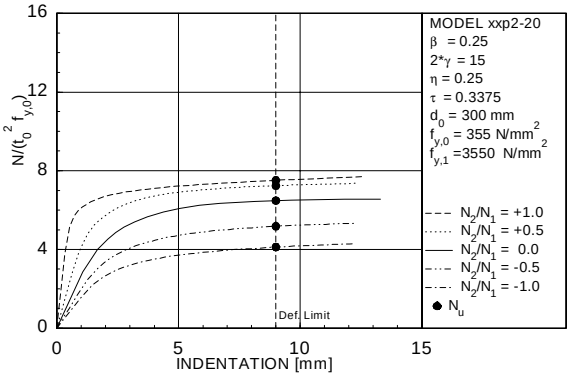

Figure 6.88 Load-displacement curves for model XXP2-20

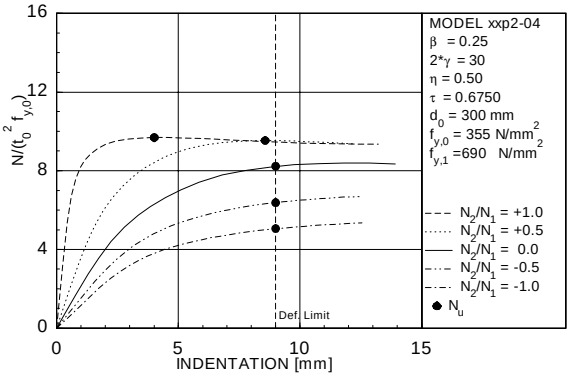

Figure 6.89 Load-displacement curves for model XXP2-02

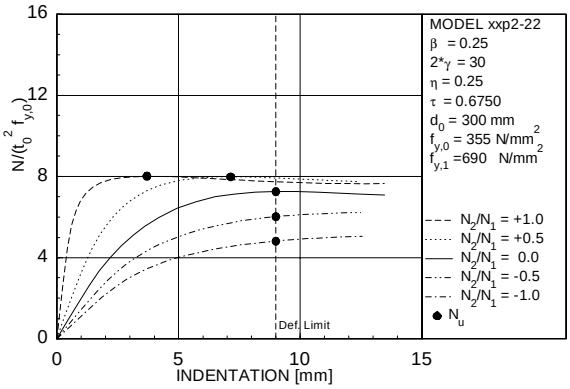

Figure 6.90 Load-displacement curves for model XXP2-22

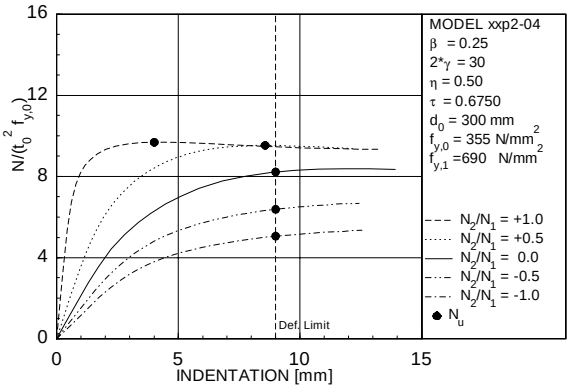

Figure 6.91 Load-displacement curves for model XXP2-04

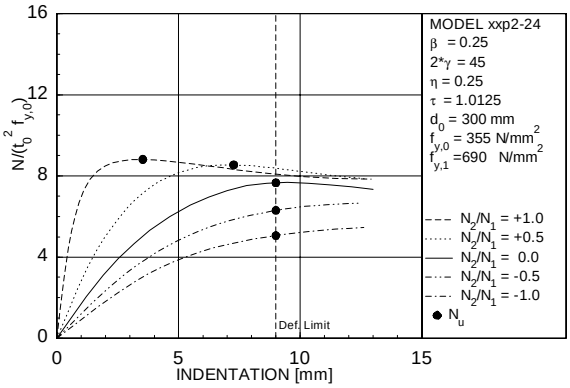

Figure 6.92 Load-displacement curves for model XXP2-24

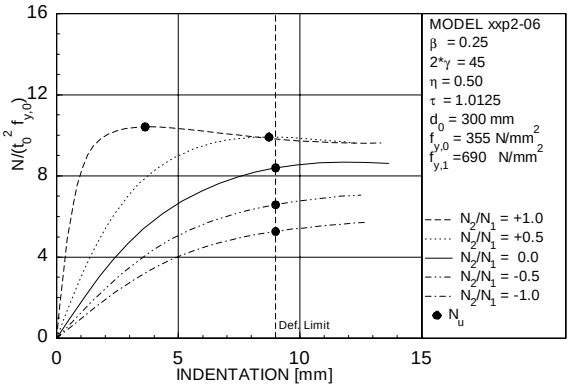

Figure 6.93 Load-displacement curves for model XXP2-06

Note: The figures are organised on this and next pages: from top to bottom an increasing 2γ, from left to right an increasing η and β.

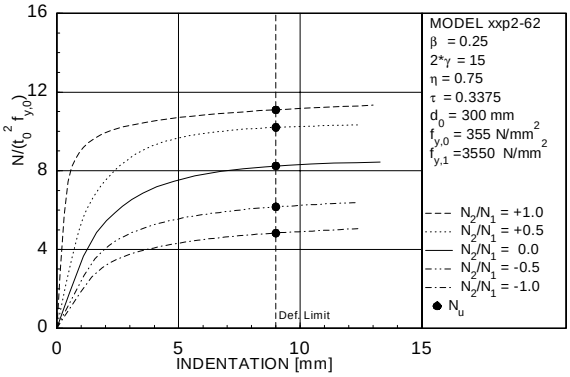

Figure 6.94 Load-displacement curves for model XXP2-62

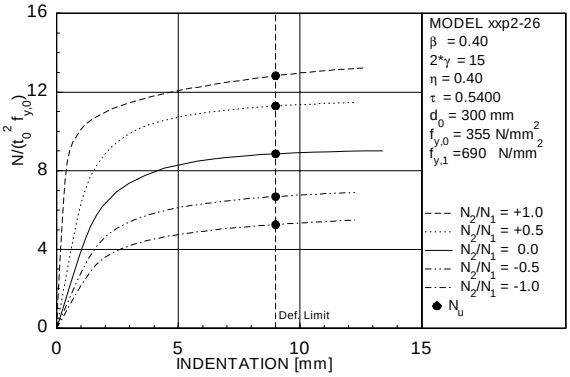

Figure 6.95 Load-displacement curves for model XXP2-26

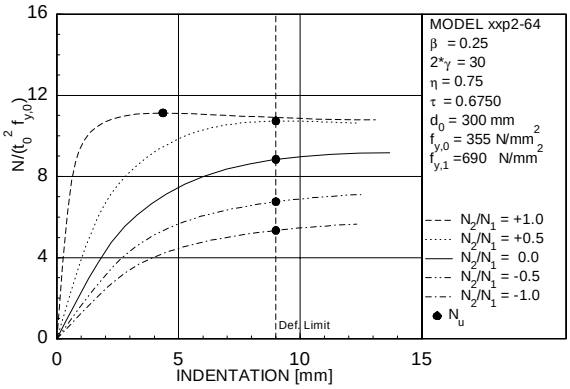

Figure 6.96 Load-displacement curves for model XXP2-64

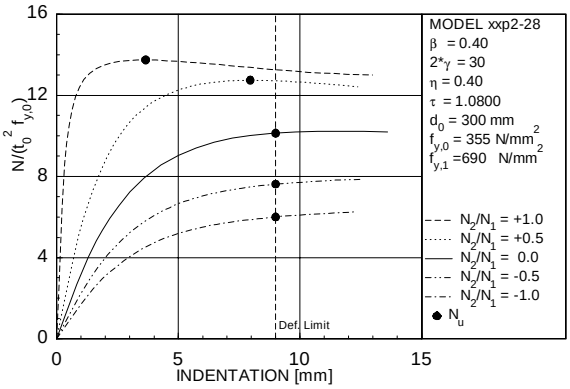

Figure 6.97 Load-displacement curves for model XXP2-28

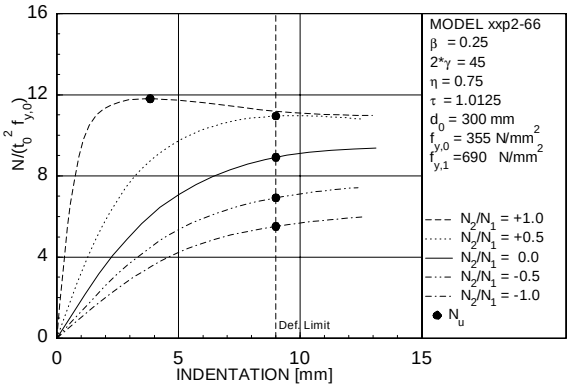

Figure 6.98 Load-displacement curves for model XXP2-66

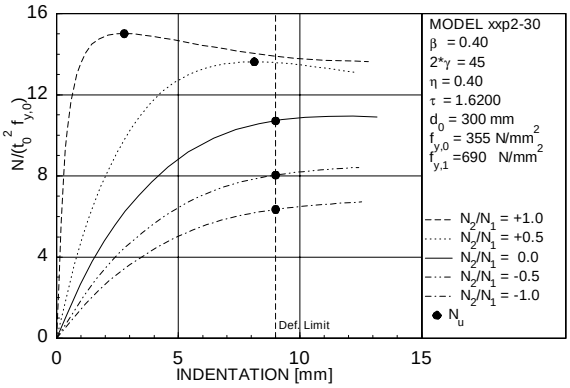

Figure 6.99 Load-displacement curves for model XXP2-30

Note: The figures are organised on this and next pages: from top to bottom an increasing 2γ, from left to right an increasing η and β.

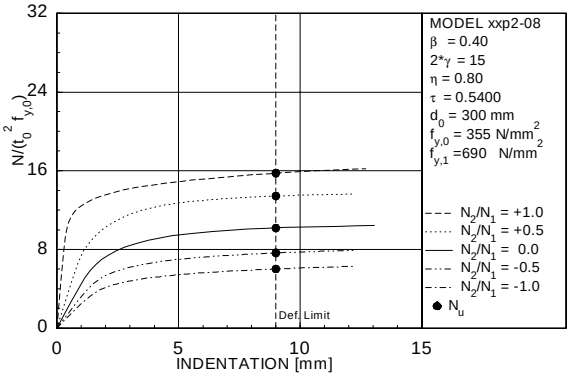

Figure 6.100 Load-displacement curves for model XXP2-08

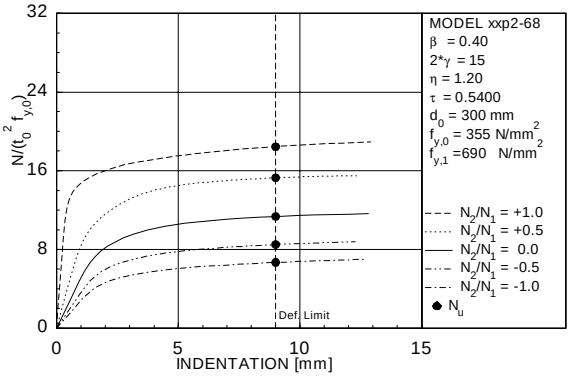

Figure 6.101 Load-displacement curves for model XXP2-68

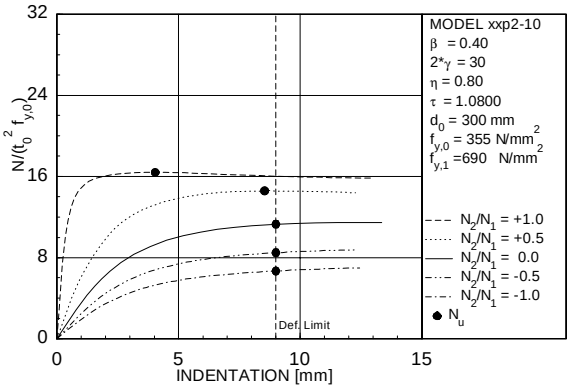

Figure 6.102 Load-displacement curves for model XXP2-10

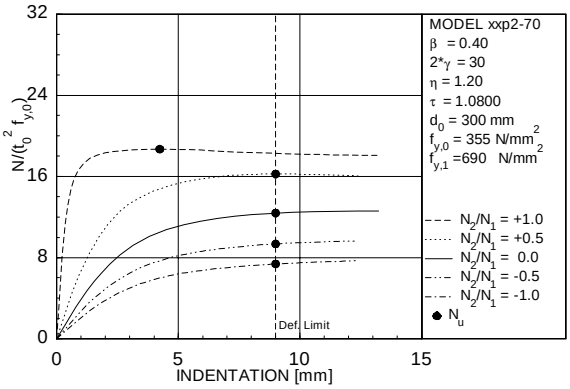

Figure 6.103 Load-displacement curves for model XXP2-70

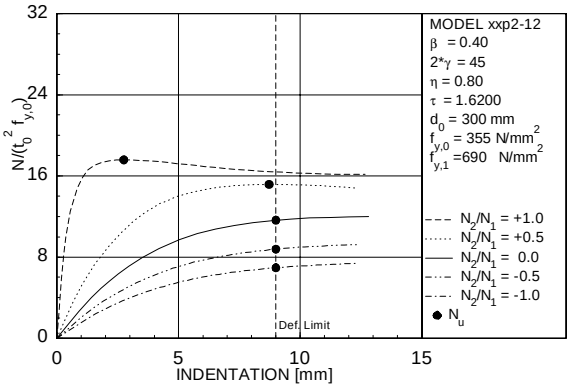

Figure 6.104 Load-displacement curves for model XXP2-12

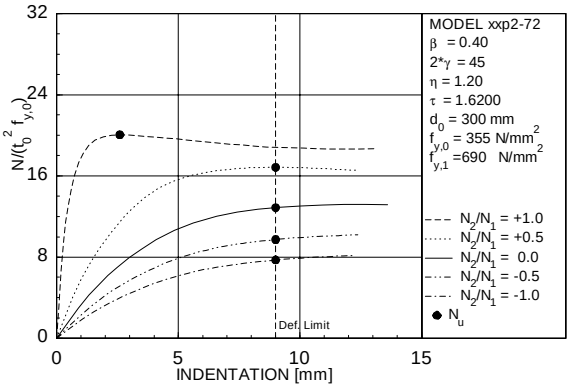

Figure 6.105 Load-displacement curves for model XXP2-72

Note: The figures are organised on this and next pages: from top to bottom an increasing 2γ, from left to right an increasing η and β.

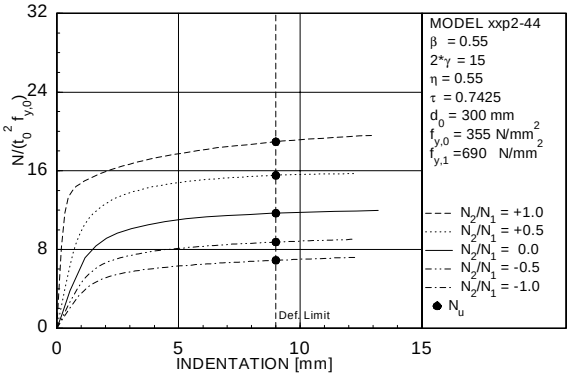

Figure 6.106 Load-displacement curves for model XXP2-44

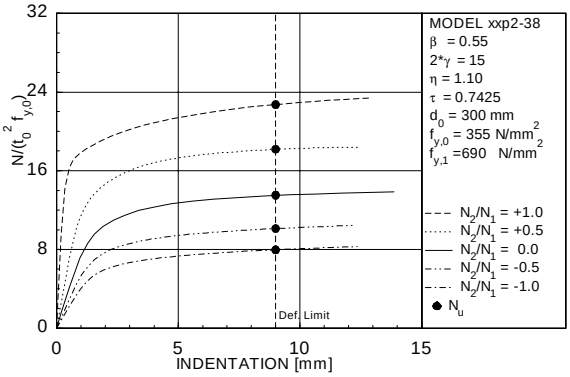

Figure 6.107 Load-displacement curves for model XXP2-38

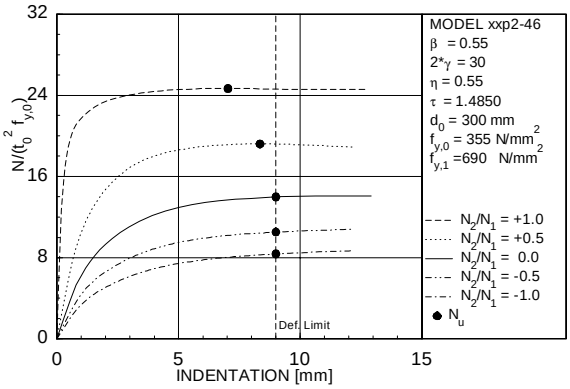

Figure 6.108 Load-displacement curves for model XXP2-46

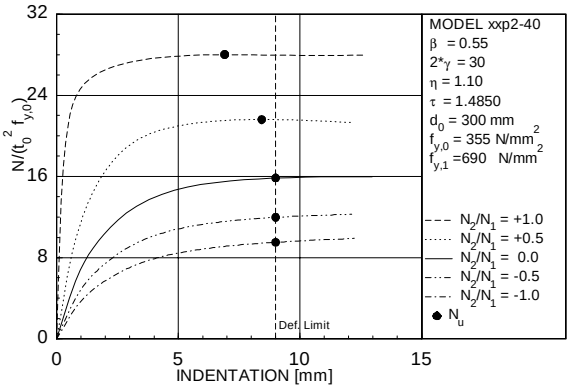

Figure 6.109 Load-displacement curves for model XXP2-40

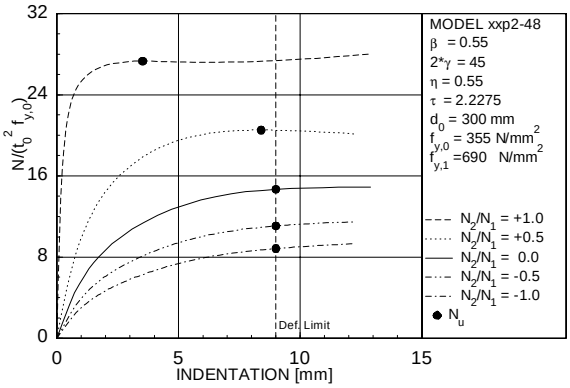

Figure 6.110 Load-displacement curves for model XXP2-48

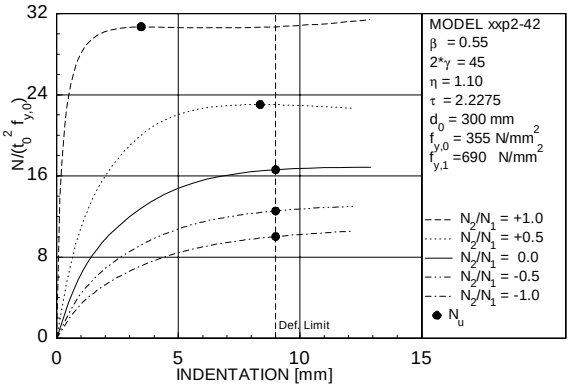

Figure 6.111 Load-displacement curves for model XXP2-42

Note: The figures are organised on this and next pages: from top to bottom an increasing 2γ, from left to right an increasing η and β.

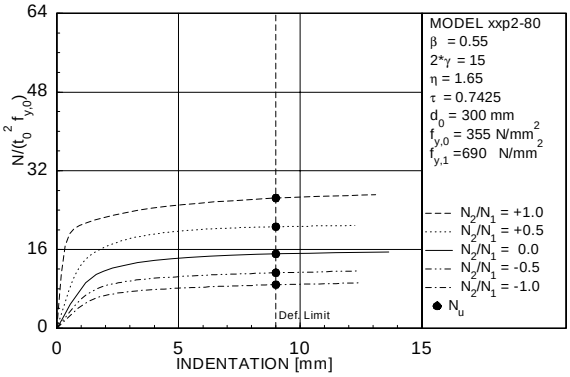

Figure 6.112 Load-displacement curves for model XXP2-80

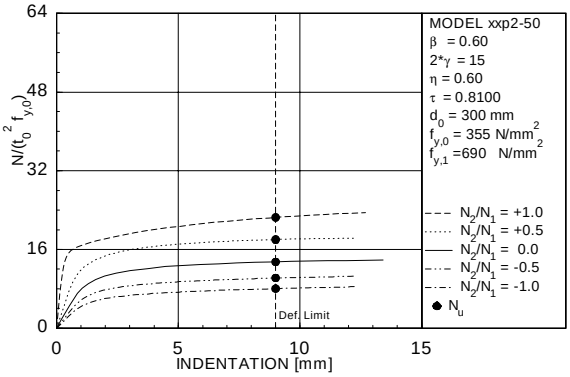

Figure 6.113 Load-displacement curves for model XXP2-50

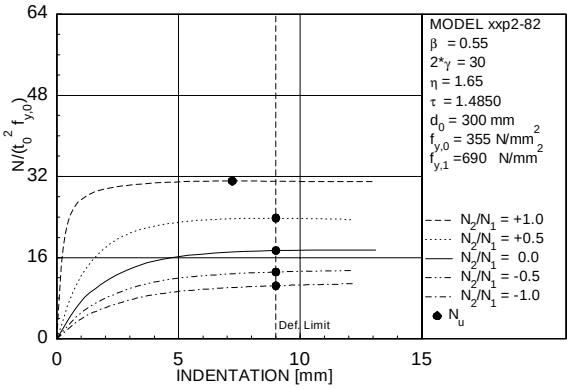

Figure 6.114 Load-displacement curves for model XXP2-82

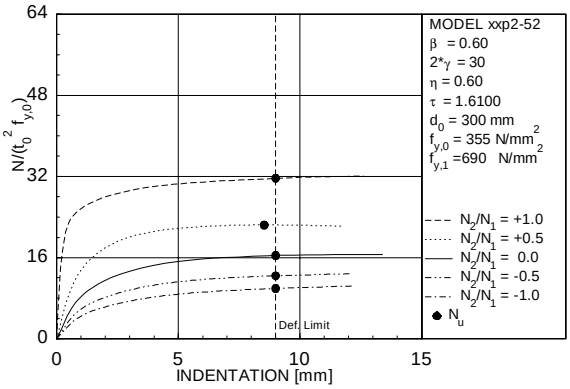

Figure 6.115 Load-displacement curves for model XXP2-52

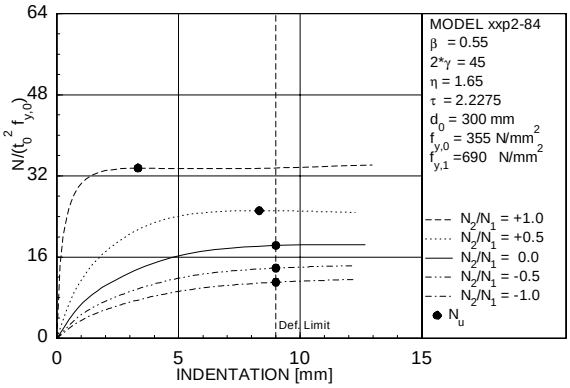

Figure 6.116 Load-displacement curves for model XXP2-84

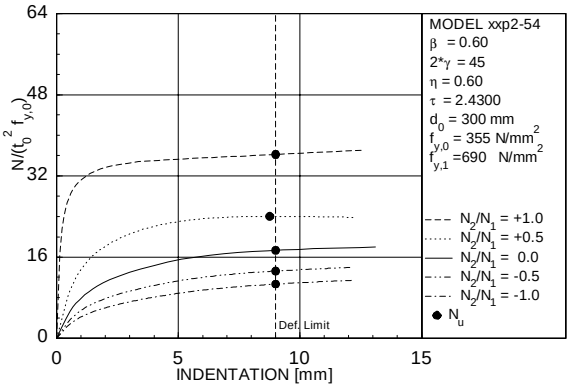

Figure 6.117 Load-displacement curves for model XXP2-54

Note: The figures are organised on this and next pages: from top to bottom an increasing 2γ, from left to right an increasing η and β.

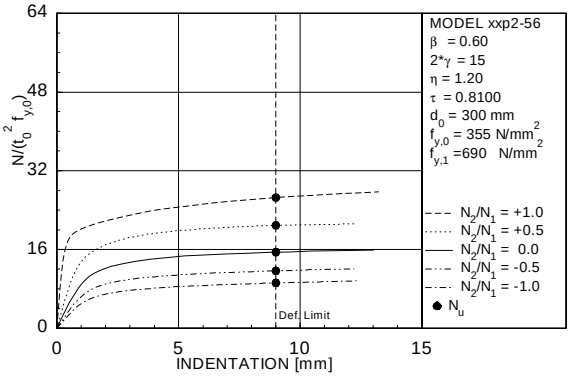

Figure 6.118 Load-displacement curves for model XXP2-56

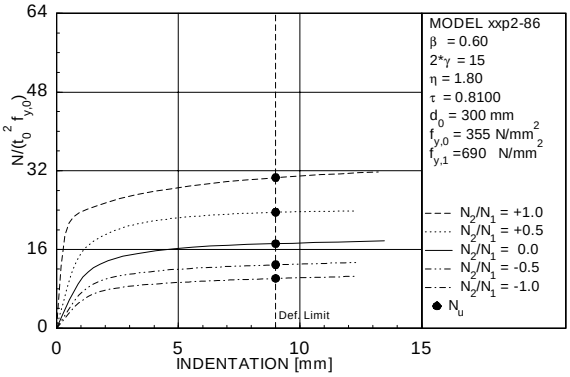

Figure 6.119 Load-displacement curves for model XXP2-86

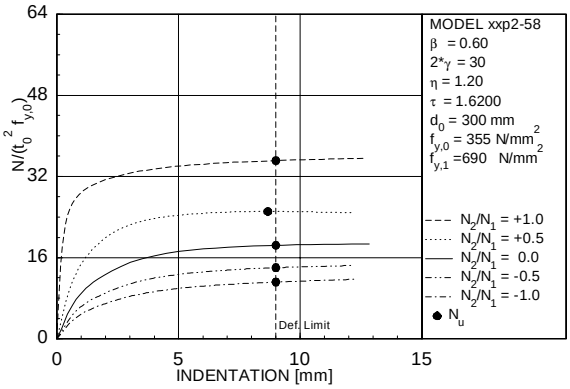

Figure 6.120 Load-displacement curves for model XXP2-58

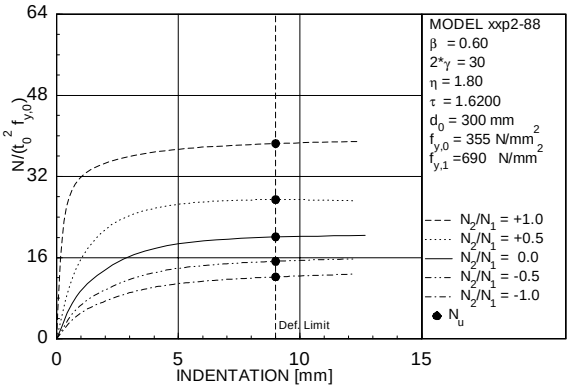

Figure 6.121 Load-displacement curves for model XXP2-88

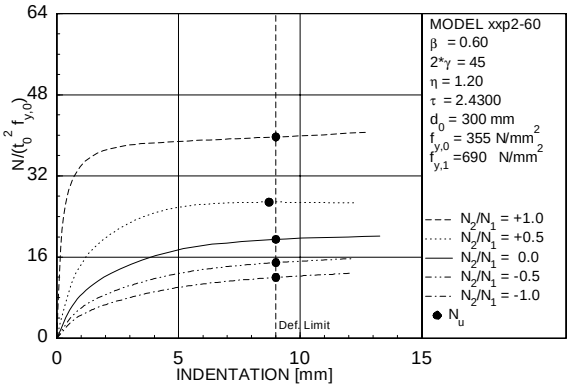

Figure 6.122 Load-displacement curves for model XXP2-60

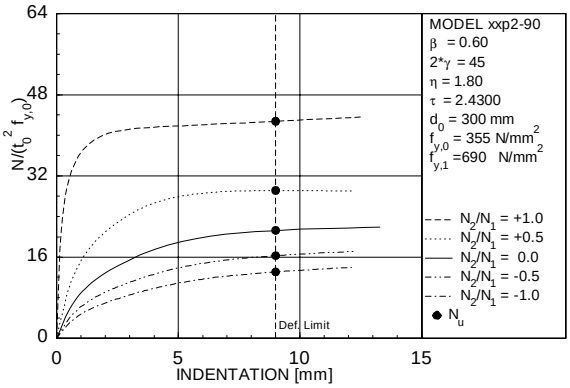

Figure 6.123 Load-displacement curves for model XXP2-90

Note: The figures are organised on this and next pages: from top to bottom an increasing 2γ, from left to right an increasing η and β.

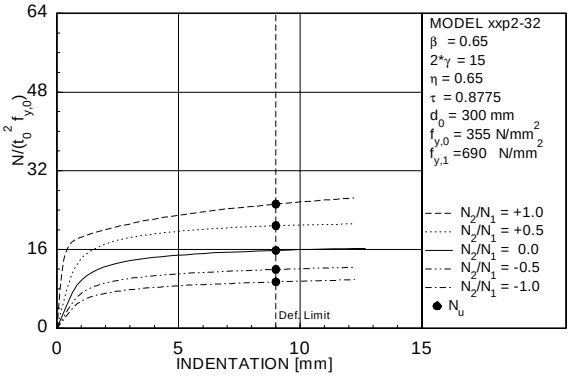

Figure 6.124 Load-displacement curves for model XXP2-32

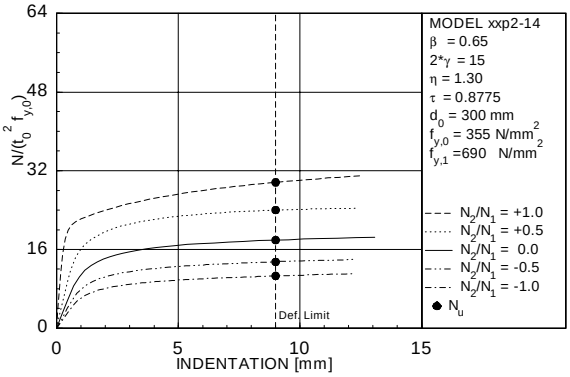

Figure 6.125 Load-displacement curves for model XXP2-14

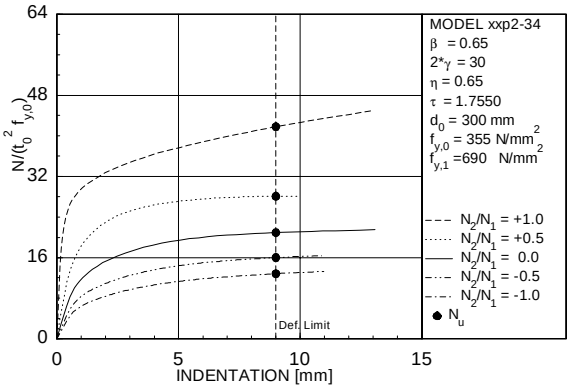

Figure 6.126 Load-displacement curves for model XXP2-34

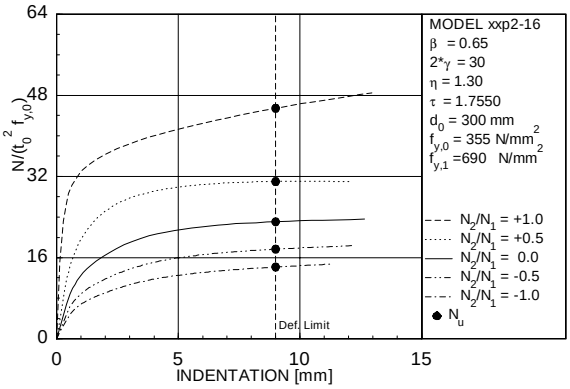

Figure 6.127 Load-displacement curves for model XXP2-16

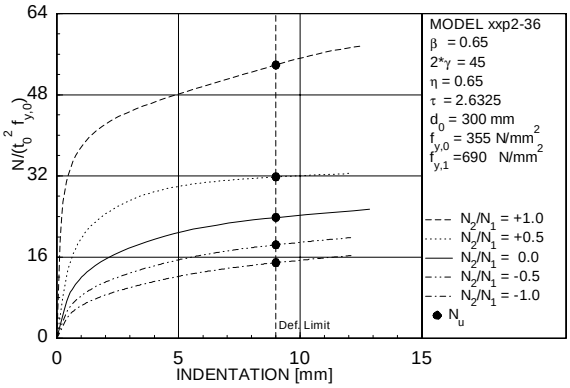

Figure 6.128 Load-displacement curves for model XXP2-36

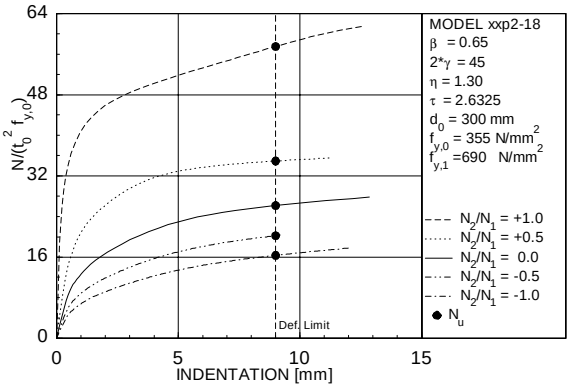

Figure 6.129 Load-displacement curves for model XXP2-18

Note: The figures are organised on this and next pages: from top to bottom an increasing 2γ, from left to right an increasing η and β.

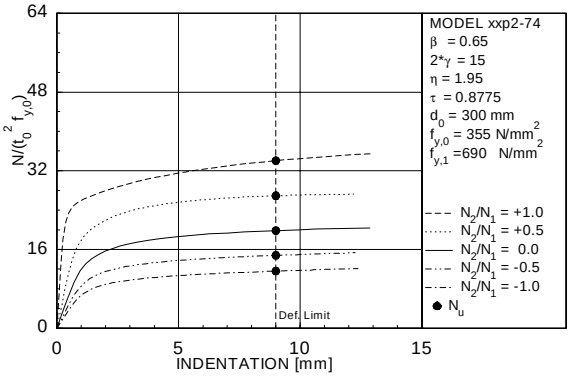

Figure 6.130 Load-displacement curves for model XXP2-74

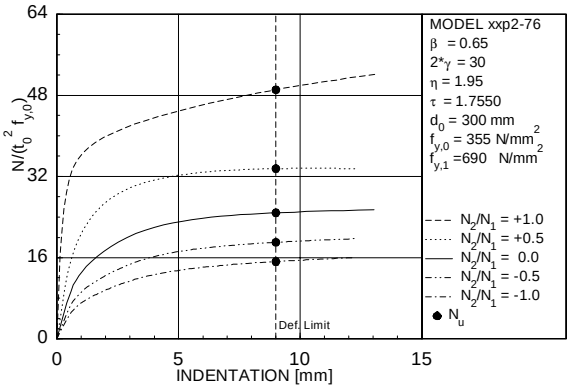

Figure 6.131 Load-displacement curves for model XXP2-76

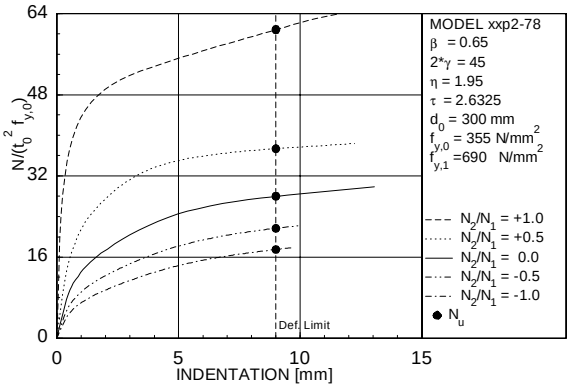

Figure 6.132 Load-displacement curves for model XXP2-78

6.3 I-beam to CHS column connections under in-plane bending

6.3.1 Research programme

For the parametric study on I-beam to CHS column connections loaded with in-plane bending moments, 24 uniplanar and also 24 multiplanar connections were analysed with four different β ratios, for each β ratio two η ratios, three 2γ ratios and two τ ratios. The geometrical parameters of the models are listed in Tables 6.10 and 6.11 and also shown in Figure 6.133. The column length is taken as six times the column diameter d_0 plus the I-beam height. The I-beam length is five times the I-beam height. These lengths are sufficient to minimize boundary and load introduction effects. The flange thickness is taken as 6% or 9% of the flange width; the web thickness is taken as 60% of the flange thickness (see also section 6.2). The combination of the parameters gives 48 finite element models. From these models 24 are selected for analyses, as shown in Tables 6.10 and 6.11.
The multiplanar models were loaded with five different load cases, namely M_2/M_1 = -1.0, -0.5, 0.0, +0.5 and +1.0. For the finite element analyses, displacement control is used for M_2/M_1 = 0.0 and +1.0, and load control for the other load cases. Displacement control reduces the computer time needed for the analyses. However, to preserve a fixed ratio between the bending moments on the in-plane and on the out-of-plane beams, only load control can be used.

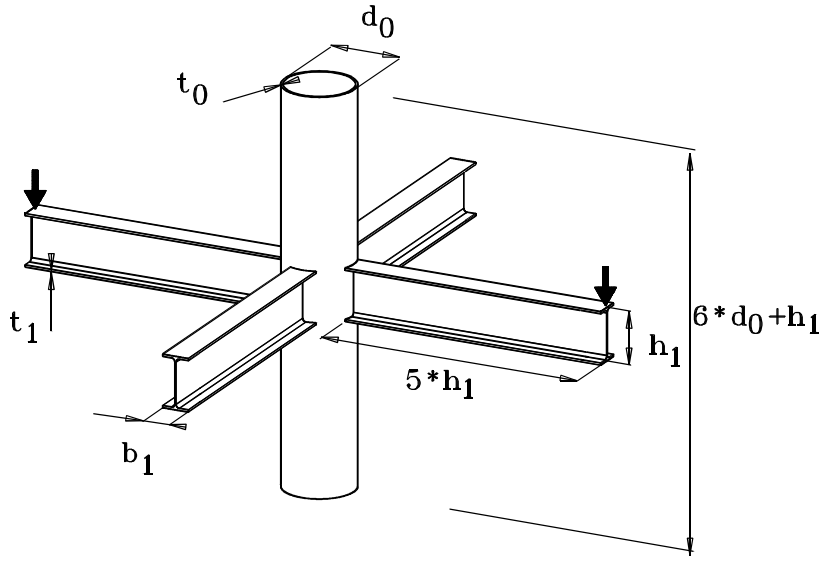

Figure 6.133 Main dimensions FE model for I-beam to CHS column connections loaded with in-plane bending moments

Table 6.10 Overview of the research programme on uniplanar and multiplanar XXP4 connections

		2γ					
		15		30		45	
β	η	b_1/t_1		b_1/t_1		b_1/t_1	
		16.67	11.11	16.67	11.11	16.67	11.11
0.25	0.25		xxp4-20		xxp4-22		xxp44-45
	0.50		xxp4-02		xxp4-04		xxp44-06
0.40	0.40	xxp4-25	xxp4-26		xxp4-28		
	0.80	xxp4-07	xxp4-08	xxp4-09	xxp4-10	xxp44-11	
0.55	0.55		xxp4-44		xxp4-46		xxp44-48
	1.10		xxp4-38		xxp4-40		xxp44-42
0.65	0.65		xxp4-32		xxp4-34		xxp44-36
	1.30		xxp4-14				

Table 6.11 Overview research programme uniplanar and multiplanar I-beam to CHS column connections loaded with in-plane bending moments

model	β	2γ	η	τ	$f_{y,1}^{*}$ [MPa]
xup4/xxp4-02	0.25	15	0.50	0.3375	3550
xup4/xxp4-04	0.25	30	0.50	0.6750	690
xup4/xxp4-06	0.25	45	0.50	1.0125	355
xup4/xxp4-07	0.40	15	0.80	0.3600	3550
xup4/xxp4-08	0.40	15	0.80	0.5400	3550
xup4/xxp4-09	0.40	30	0.80	0.7200	355
xup4/xxp4-10	0.40	30	0.80	1.0800	355
xup4/xxp4-11	0.40	45	0.80	1.0800	355
xup4/xxp4-14	0.65	15	1.30	0.8775	690
xup4/xxp4-20	0.25	15	0.25	0.3375	3550
xup4/xxp4-22	0.25	30	0.25	0.6750	690
xup4/xxp4-24	0.25	45	0.25	1.0125	355
xup4/xxp4-25	0.40	15	0.40	0.3600	3550
xup4/xxp4-26	0.40	15	0.40	0.5400	3550
xup4/xxp4-28	0.40	30	0.40	1.0800	355
xup4/xxp4-32	0.65	15	0.65	0.8775	690
xup4/xxp4-34	0.65	30	0.65	1.7550	355
xup4/xxp4-36	0.65	45	0.65	2.6325	355
xup4/xxp4-38	0.55	15	1.10	0.7425	690
xup4/xxp4-40	0.55	30	1.10	1.4850	355
xup4/xxp4-42	0.55	45	1.10	2.2275	355
xup4/xxp4-44	0.55	15	0.55	0.7425	690
xup4/xxp4-46	0.55	30	0.55	1.4850	355
xup4/xxp4-48	0.55	45	0.55	2.2275	355

Note:

*: In cases where the I-beam flange failure would be critical, a higher steel grade for the flanges was used, to avoid local buckling in the flanges under compression. The flanges have a steel grade with $f_{y,1}$=690 N/mm^2 or an artificial elasto-plastic steel grade with $f_{y,1}$=3550 N/mm^2. The column diameter d_0 for all models is 300 mm and the steel grade for the columns is S355 ($f_{y,0}$ = 355 N/mm^2).

6.3.2 Uniplanar connections

Table 6.12 shows the main results of the finite element analyses for the uniplanar I-beam to CHS column connections loaded with in-plane bending moments. Figure 6.134 shows a typical deformed finite element mesh for this connection type. The moment-rotation curves are shown in Figures 6.136 to 6.159.
In most cases the moment rotation curves show no obvious peak. In such cases, the connection strength is taken at a deformation (rotation) limit equal to $0.06/\eta$ [13].

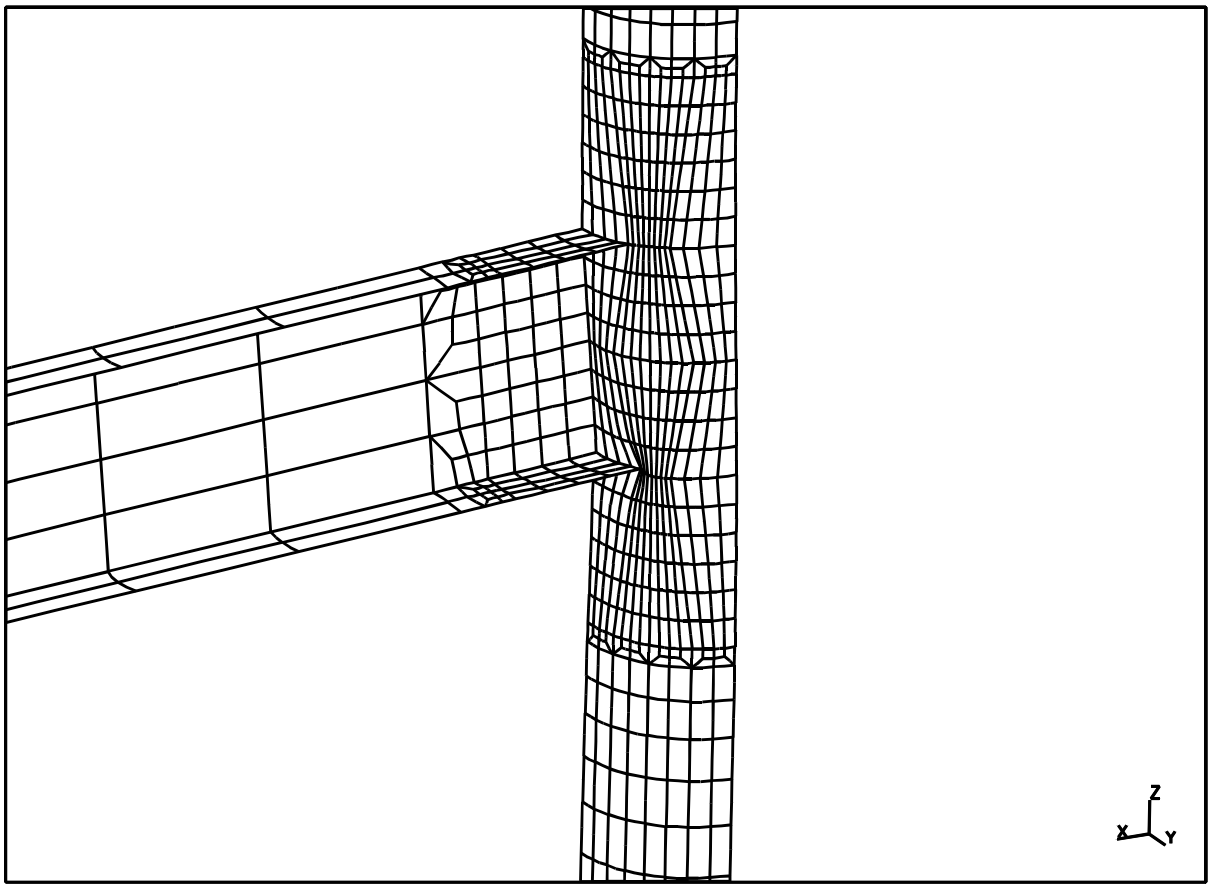

Figure 6.134 Deformed finite element mesh of model XXP4-342U

Based upon the finite element analyses results, the following observations can be made:

β Influence

The non-dimensional strength increases with an increasing β ratio.

2γ Influence

The non-dimensional strength of the connections is increasing for larger 2γ ratios. This effect becomes stronger for larger β ratios.

η ratio

The η-ratio has a small influence on the non-dimensional strength. Only for large β ratios in combination with small 2γ ratios a larger η ratio influence is found than that which is directly taken into account by h_m.

Failure modes

For all connections the chord face plastification failure mode was observed.
The finite element models could not include the punching shear failure mode, due to the absence in the finite element program of a reliable crack model.

Table 6.12 Results finite element analyses uniplanar I-beam to CHS column connections loaded with in-plane bending moments

model	β	2γ	η	τ	$M_u/(t_0^2 f_{y,0} h_m)$
xup4-02	0.25	15	0.50	0.3375	4.31
xup4-04	0.25	30	0.50	0.6750	4.98
xup4-06	0.25	45	0.50	1.0125	5.32
xup4-07	0.40	15	0.80	0.3600	5.20
xup4-08	0.40	15	0.80	0.5400	5.30
xup4-09	0.40	30	0.80	0.7200	6.14
xup4-10	0.40	30	0.80	1.0800	6.36
xup4-11	0.40	45	0.80	1.0800	7.35
xup4-14	0.65	15	1.30	0.8775	7.02
xup4-20	0.25	15	0.25	0.3375	4.41
xup4-22	0.25	30	0.25	0.6750	5.76
xup4-24	0.25	45	0.25	1.0125	6.15
xup4-25	0.40	15	0.40	0.3600	5.46
xup4-26	0.40	15	0.40	0.5400	5.62
xup4-28	0.40	30	0.40	1.0800	6.61
xup4-32	0.65	15	0.65	0.8775	8.23
xup4-34	0.65	30	0.65	1.7550	10.75
xup4-36	0.65	45	0.65	2.6325	12.98
xup4-38	0.55	15	1.10	0.7425	6.11
xup4-40	0.55	30	1.10	1.4850	8.11
xup4-42	0.55	45	1.10	2.2275	9.35
xup4-44	0.55	15	0.55	0.7425	7.53
xup4-46	0.55	30	0.55	1.4850	8.89
xup4-48	0.55	45	0.55	2.2275	10.96

6.3.3 Multiplanar connections

Table 6.13 shows the main results of the finite element analyses for the multiplanar I-beam to CHS column connections loaded with in-plane bending moments. Figure 6.135 shows an example of the finite element meshes used for this type of connections.

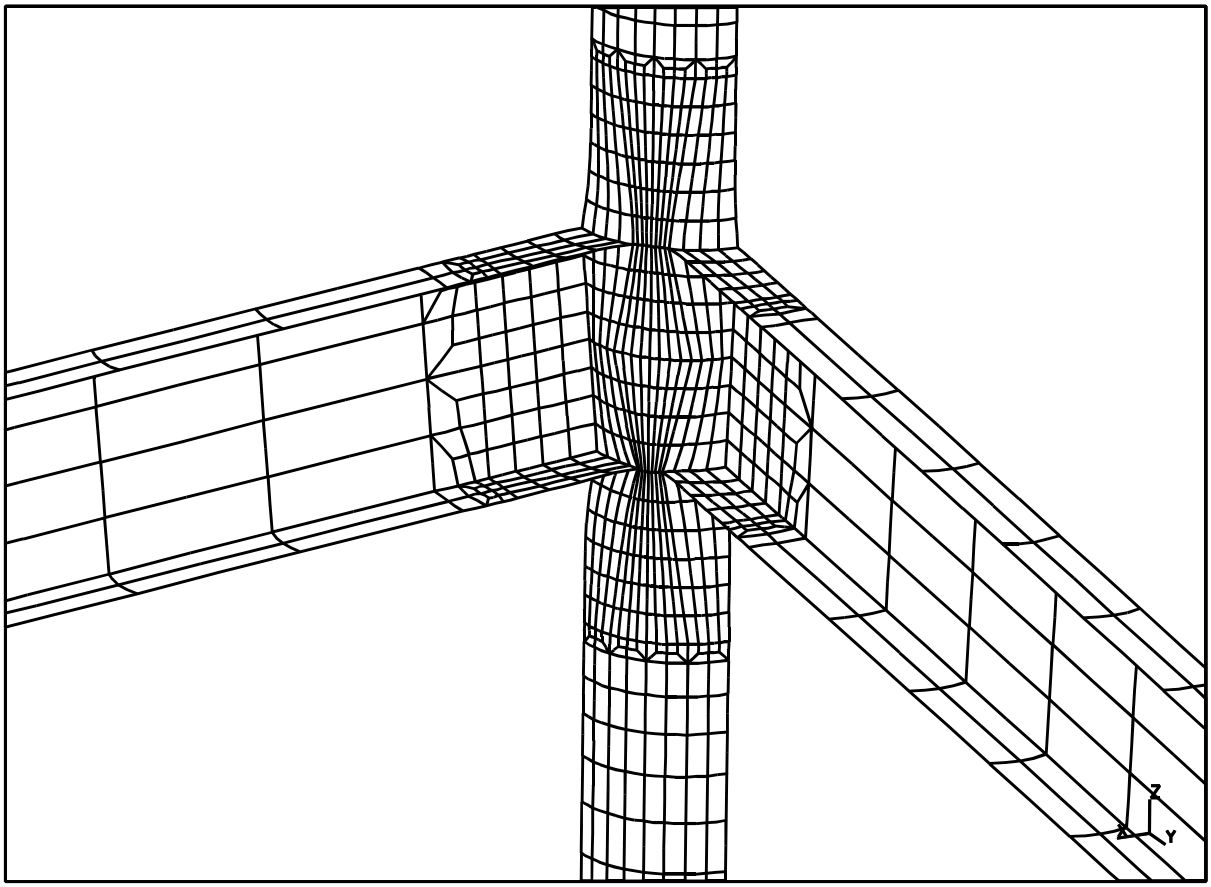

Figure 6.135 Deformed finite element mesh of model XXP4-38 for load ratio +1.0

From the finite element analyses, the following observations can be made:

β Influence

The non-dimensional strength of the connections increases for larger β ratios.

2γ Influence

The non-dimensional strength of the connections is increasing for larger 2γ ratios. This effect becomes stronger for larger β ratios.

η ratio

The η ratio has a small influence on the non-dimensional strength. Only for large β ratios in combination with small 2γ ratios a larger η ratio influence is found.

Failure modes

For all connections the chord face plastification failure mode is observed.
The finite element models could not include the punching shear failure mode, due to the absence in the finite element program of a reliable crack model. For design, the punching shear failure criterion should also be checked [11].

These findings are similar to those of the uniplanar connections

Multiplanar loading effects

In general, negative load ratios reduce the connection strength, while positive load ratios increase the connection strength. However, the decrease in connection strength by negative load ratios is more than the increase in connection strength by positive load ratios. In fact, in several cases the increase in connection strength by positive load ratios can be neglected.
The maximum strength is generally found for a load ratio M_2/M_1 equal to +0.5.

Table 6.13 Results of the finite element analyses on multiplanar I-beam to CHS column connections loaded with in-plane bending moments

name	β	2γ	η	τ	$M_u/(t_0^2*h_m*f_{y,0})$ For J =				
					-1.0	-0.5	0.0	+0.5	+1.0
xxp4-02	0.25	15	0.50	0.3375	4.26	4.90	5.31	5.41	5.33
xxp4-04	0.25	30	0.50	0.6750	5.69	6.31	6.50	6.57	6.19
xxp4-06	0.25	45	0.50	1.0125	6.53	6.67	6.69	6.69	6.50
xxp4-07	0.40	15	0.80	0.3600	4.65	5.80	7.01	7.70	7.79
xxp4-08	0.40	15	0.80	0.5400	4.71	5.88	7.12	7.83	7.94
xxp4-09	0.40	30	0.80	0.7200	6.49	7.67	8.34	8.63	8.14
xxp4-10	0.40	30	0.80	1.0800	6.66	7.89	8.66	9.00	8.49
xxp4-11	0.40	45	0.80	1.0800	8.31	9.51	9.92	10.10	9.48
xxp4-14	0.65	15	1.30	0.8775	5.66	8.04	10.47	12.78	13.50
xxp4-20	0.25	15	0.25	0.3375	4.37	4.76	4.87	4.88	4.91
xxp4-22	0.25	30	0.25	0.6750	5.81	6.10	6.13	6.15	6.10
xxp4-24	0.25	45	0.25	1.0125	6.90	6.96	6.97	6.96	6.85
xxp4-25	0.40	15	0.40	0.3600	5.31	6.26	6.96	7.15	7.03
xxp4-26	0.40	15	0.40	0.5400	5.07	5.87	7.08	6.47	7.13
xxp4-28	0.40	30	0.40	1.0800	7.32	8.33	8.87	9.04	8.39
xxp4-32	0.65	15	0.65	0.8775	6.97	-	10.65	-	11.51
xxp4-34	0.65	30	0.65	1.7550	10.23	12.69	15.28	17.58	18.93
xxp4-36	0.65	45	0.65	2.6325	13.43	16.63	19.69	22.80	25.64
xxp4-38	0.55	15	1.10	0.7425	5.20	6.63	8.45	10.02	10.57
xxp4-40	0.55	30	1.10	1.4850	7.63	9.63	11.75	13.43	13.69
xxp4-42	0.55	45	1.10	2.2275	9.60	12.23	14.50	16.14	15.92
xxp4-44	0.55	15	0.55	0.7425	5.97	7.32	8.67	9.35	9.29
xxp4-46	0.55	30	0.55	1.4850	8.67	10.52	12.17	13.23	12.76
xxp4-48	0.55	45	0.55	2.2275	11.06	13.41	15.23	15.97	14.95

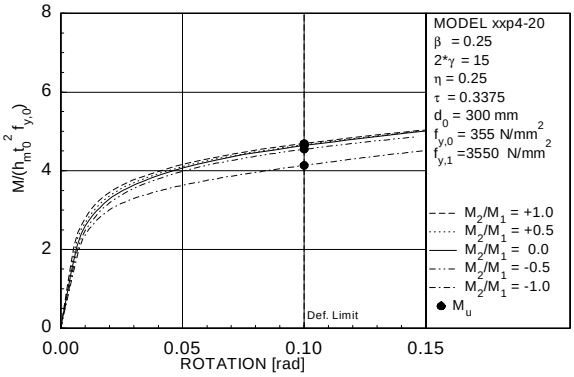

Figure 6.136 Load-displacement curves for model XXP4-20

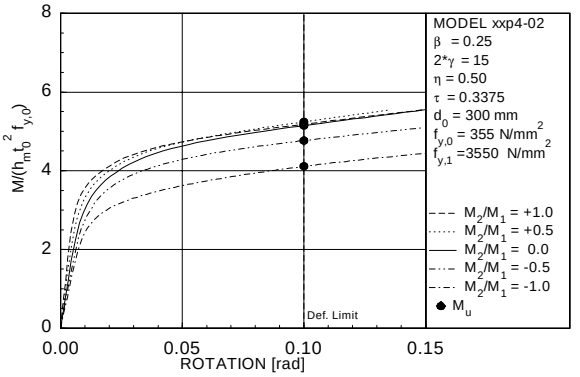

Figure 6.137 Load-displacement curves for model XXP4-02

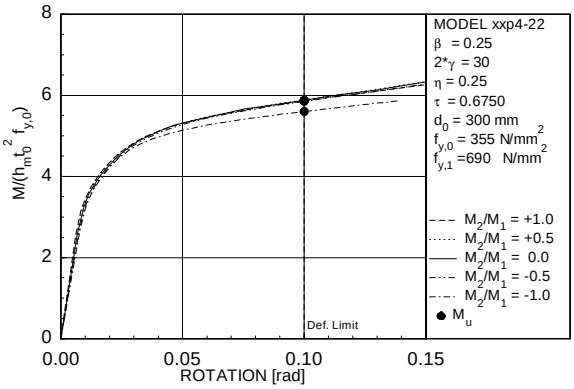

Figure 6.138 Load-displacement curves for model XXP4-22

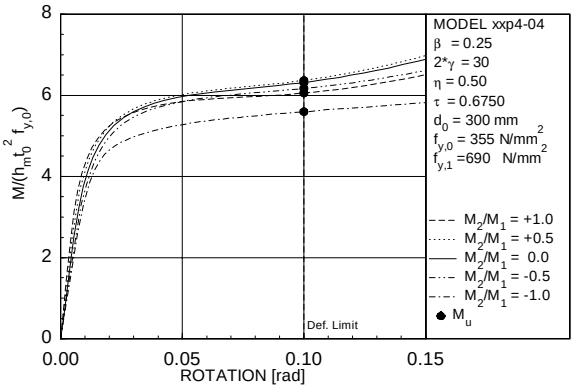

Figure 6.139 Load-displacement curves for model XXP4-04

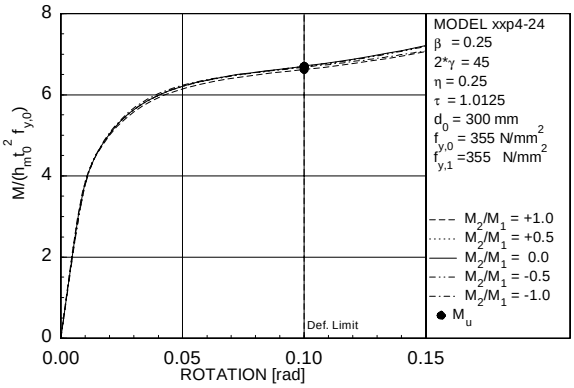

Figure 6.140 Load-displacement curves for model XXP4-24

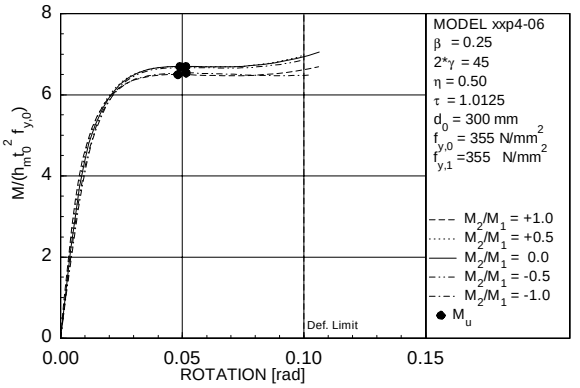

Figure 6.141 Load-displacement curves for model XXP4-06

Note: The figures are organised on this and next pages: from top to bottom an increasing 2γ, from left to right an increasing η and β.

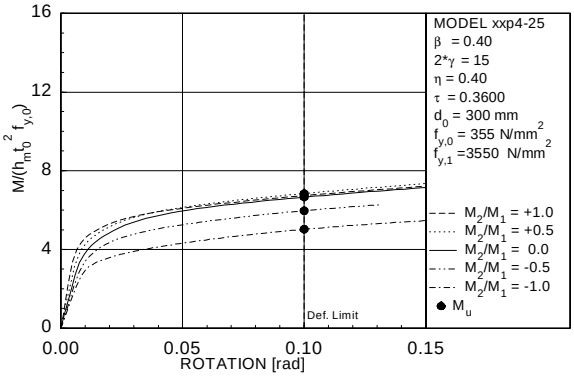

Figure 6.142 Load-displacement curves for model XXP4-25

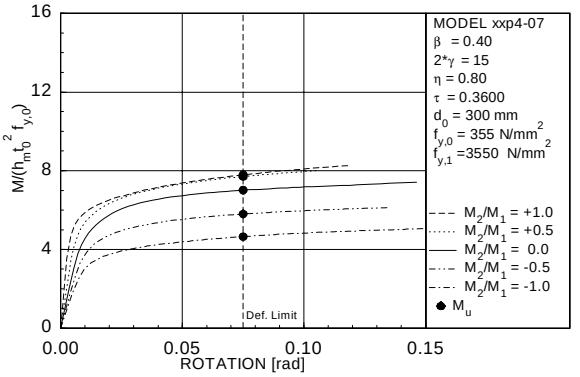

Figure 6.143 Load-displacement curves for model XXP4-07

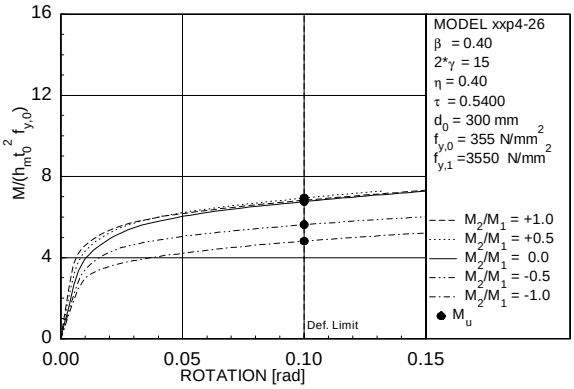

Figure 6.144 Load-displacement curves for model XXP4-26

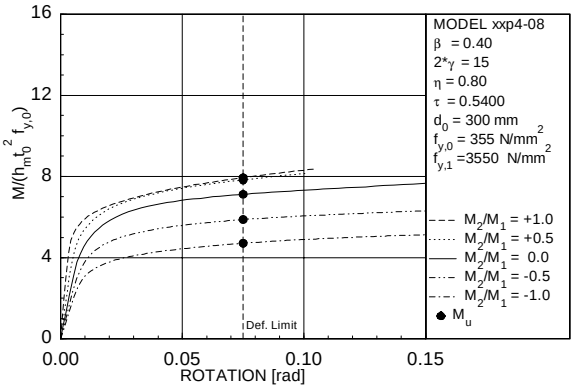

Figure 6.145 Load-displacement curves for model XXP4-08

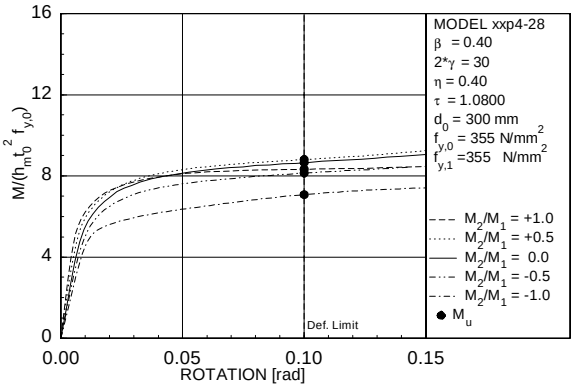

Figure 6.146 Load-displacement curves for model XXP4-28

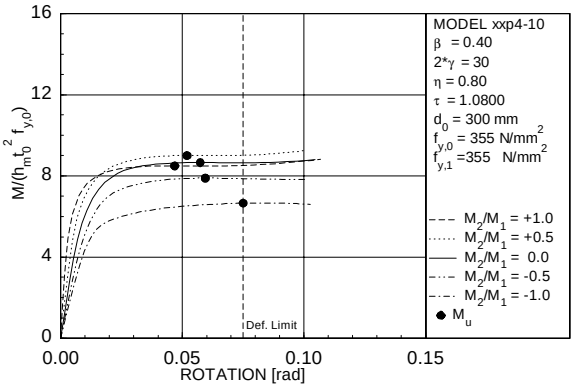

Figure 6.147 Load-displacement curves for model XXP4-10

Note: The figures are organised on this and next pages: from top to bottom an increasing 2γ, from left to right an increasing η and β.

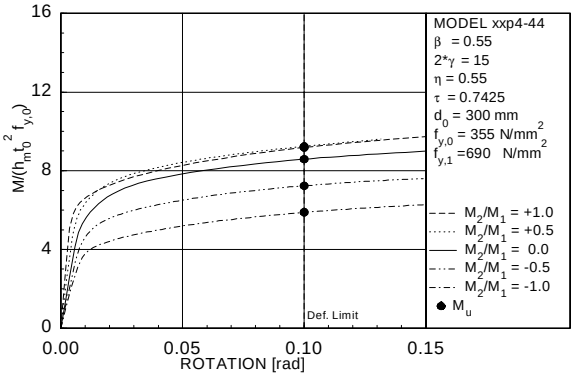

Figure 6.148 Load-displacement curves for model XXP4-44

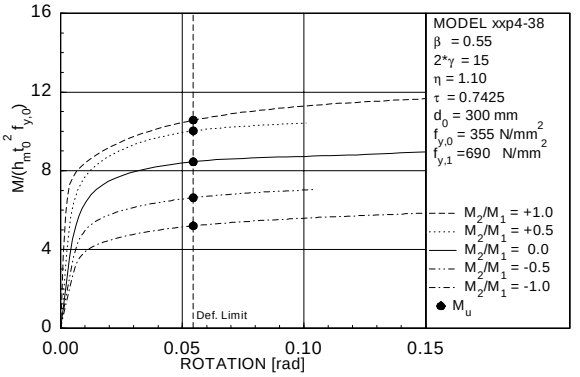

Figure 6.149 Load-displacement curves for model XXP4-38

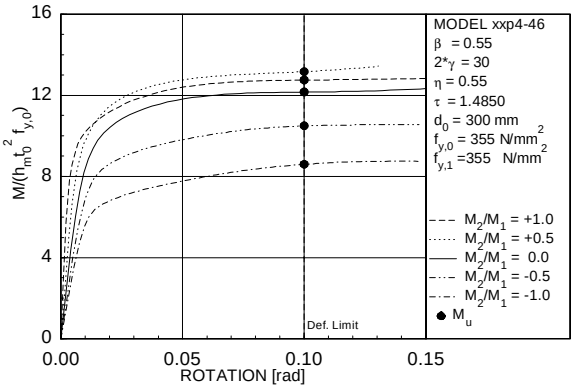

Figure 6.150 Load-displacement curves for model XXP4-46

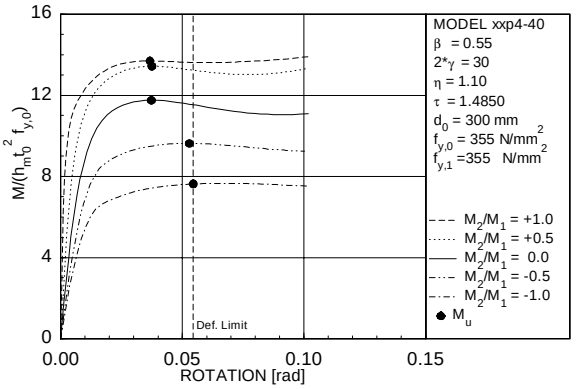

Figure 6.151 Load-displacement curves for model XXP4-40

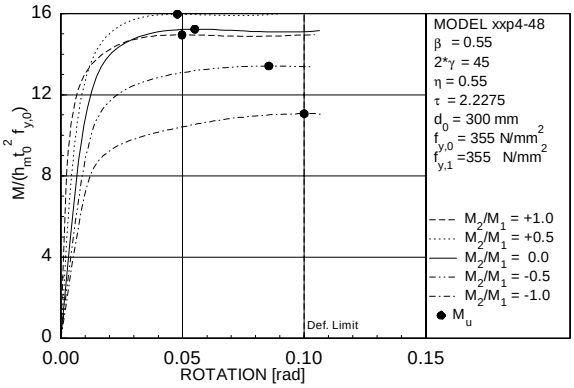

Figure 6.152 Load-displacement curves for model XXP4-48

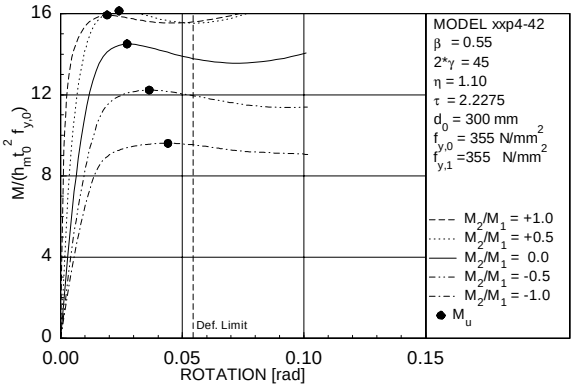

Figure 6.153 Load-displacement curves for model XXP4-42

Note: The figures are organised on this and next pages: from top to bottom an increasing 2γ, from left to right an increasing η and β.

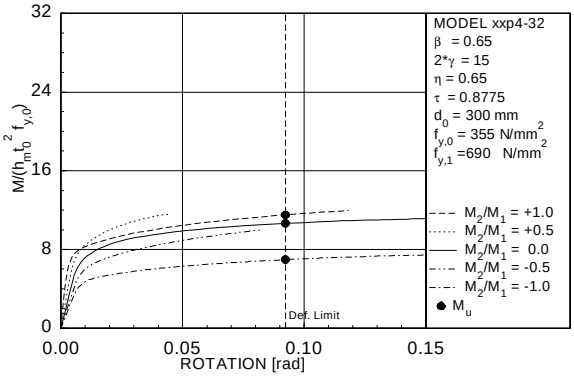

Figure 6.154 Load-displacement curves for model XXP4-32

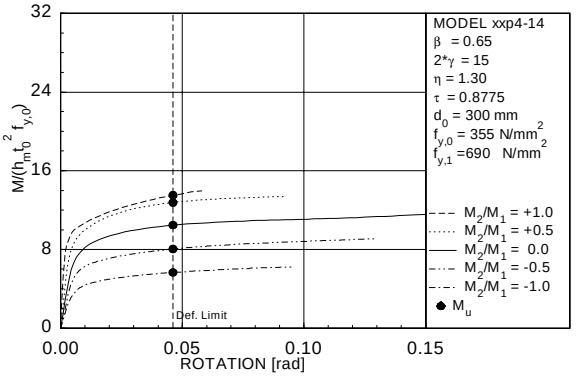

Figure 6.155 Load-displacement curves for model XXP4-14

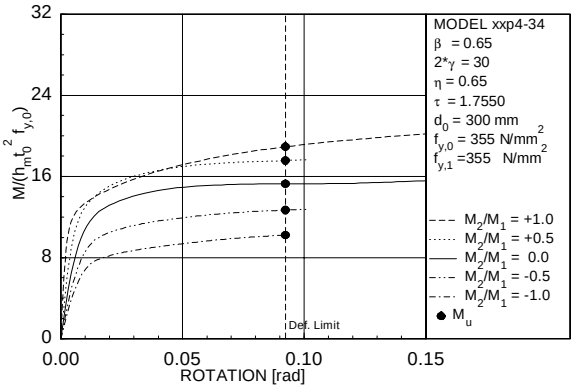

Figure 6.156 Load-displacement curves for model XXP4-34

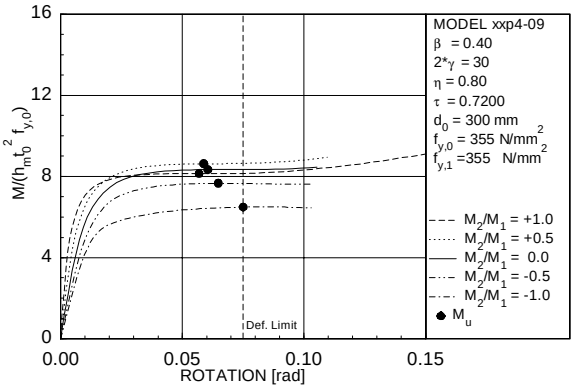

Figure 6.157 Load-displacement curves for model XXP4-09

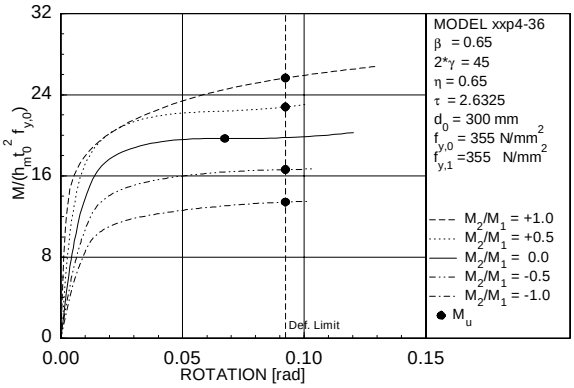

Figure 6.158 Load-displacement curves for model XXP4-36

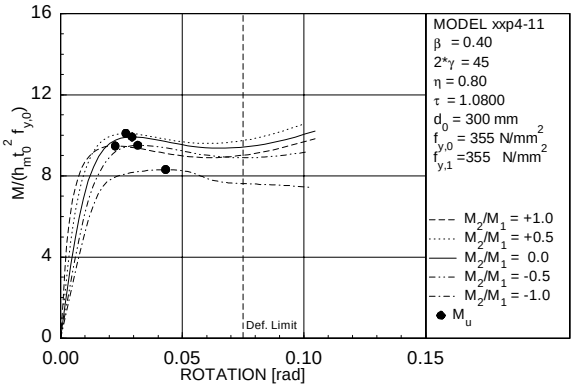

Figure 6.159 Load-displacement curves for model XXP4-11

Note: The figures are organised on this and previous pages: from top to bottom an increasing 2γ, from left to right an increasing η and β (except Fig. 6.157 and 6.159)..

6.3.4 Influence of pre-stress of the column

The influence of a compression pre-stress of the column is only analysed for the uniplanar XUP4 connections as listed in Tables 6.10 and 6.11. Three different load cases are analysed, namely 0.40, 0.60 and 0.80 times the squash load of the column. The results of the finite element analyses are listed in Table 6.14. As shown in Figures 6.160 to 6.183, the pre-stress has a significant influence on the connection strength. The influence of the pre-stress ratio is larger for larger 2γ-ratios. Connections with a pre-stress of 0.80 times the squash load and a 2γ-ratio equal to 45 fail by buckling of the column. This type of failure mode can be seen in Figures 6.177 and 6.180; these two connections show complete failure at a rotation of approximately 0.09 rad.

Table 6.14 Results finite element analyses uniplanar I-beam to CHS column connections loaded with in-plane bending moments and a pre-stress on the column.

name	β	2γ	η	τ	d_0	$M_u/(t_0 2 f_{y,0} h_m)$ For pre-stress n=			
						0.0	0.4	0.6	0.8
xup4-02	0.25	15	0.50	0.3375	300	5.14	4.89	4.40	3.54
xup4-04	0.25	30	0.50	0.6750	300	6.31	5.80	5.17	3.97
xup4-06	0.25	45	0.50	1.0125	300	6.69	6.04	5.46	4.40
xup4-07	0.40	15	0.80	0.3600	300	6.99	6.23	5.41	4.26
xup4-08	0.40	15	0.80	0.5400	300	7.08	6.32	5.51	4.37
xup4-09	0.40	30	0.80	0.7200	300	8.29	7.45	6.44	4.79
xup4-10	0.40	30	0.80	1.0800	300	8.60	7.72	6.67	5.00
xup4-11	0.40	45	0.80	1.0800	300	9.86	8.76	7.71	5.42
xup4-14	0.65	15	1.30	0.8775	300	9.38	8.36	7.32	5.29
xup4-20	0.25	15	0.25	0.3375	300	4.64	4.59	4.34	3.31
xup4-22	0.25	30	0.25	0.6750	300	5.88	5.60	5.25	3.65
xup4-24	0.25	45	0.25	1.0125	300	6.70	6.07	5.46	3.95
xup4-25	0.40	15	0.40	0.3600	300	6.65	6.20	5.53	4.11
xup4-26	0.40	15	0.40	0.5400	300	6.76	6.33	5.67	4.62
xup4-28	0.40	30	0.40	1.0800	300	8.62	7.82	6.88	5.30
xup4-32	0.65	15	0.65	0.8775	300	10.08	9.65	8.48	6.95
xup4-34	0.65	30	0.65	1.7550	300	14.69	12.91	11.15	8.58
xup4-36	0.65	45	0.65	2.6325	300	18.86	16.44	13.64	9.39
xup4-38	0.55	15	1.10	0.7425	300	8.26	7.30	6.32	5.01
xup4-40	0.55	30	1.10	1.4850	300	11.75	10.09	8.11	6.17
xup4-42	0.55	45	1.10	2.2275	300	14.42	12.21	9.35	6.56
xup4-44	0.55	15	0.55	0.7425	300	8.52	7.64	6.70	5.44
xup4-46	0.55	30	0.55	1.4850	300	11.99	10.61	9.21	7.17
xup4-48	0.55	45	0.55	2.2275	300	14.83	13.40	11.49	8.24

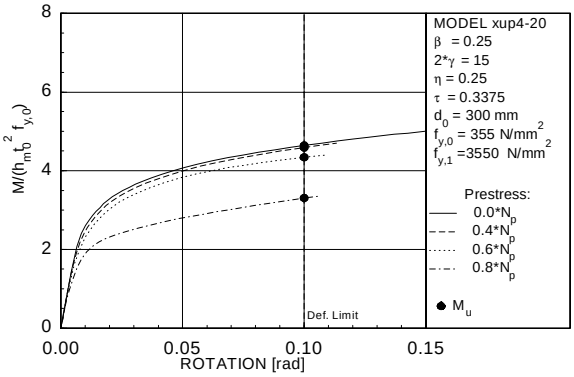

Figure 6.160 Load-displacement curves for model XUP4-20

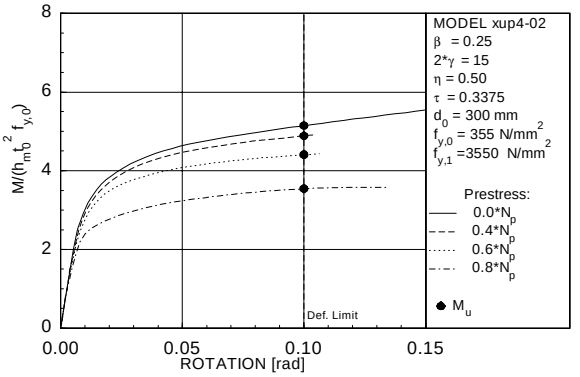

Figure 6.161 Load-displacement curves for model XUP4-02

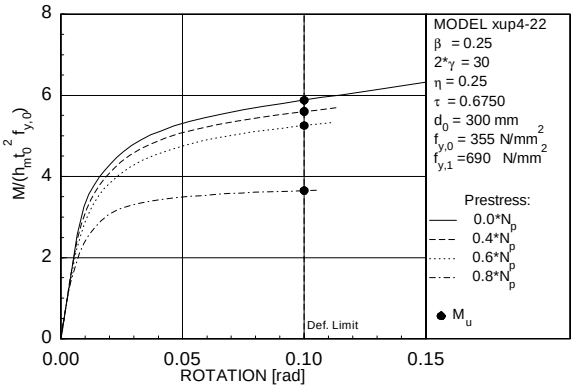

Figure 6.162 Load-displacement curves for model XUP4-22

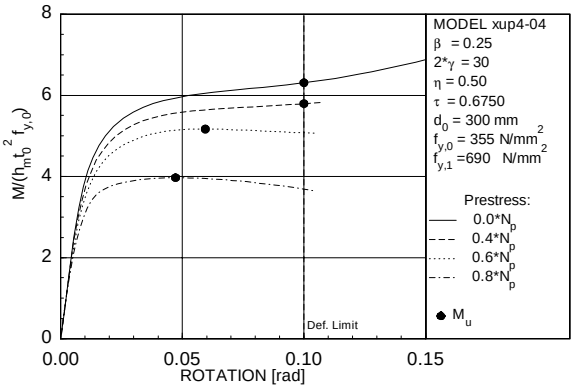

Figure 6.163 Load-displacement curves for model XUP4-04

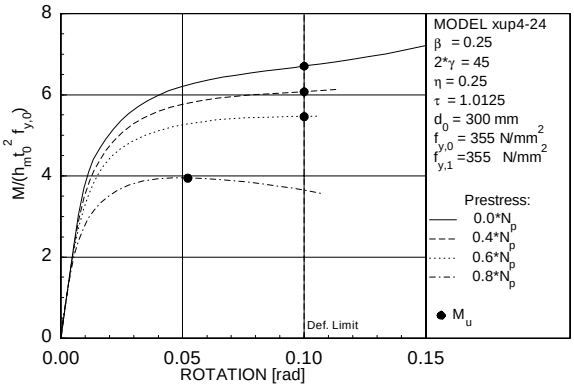

Figure 6.164 Load-displacement curves for model XUP4-24

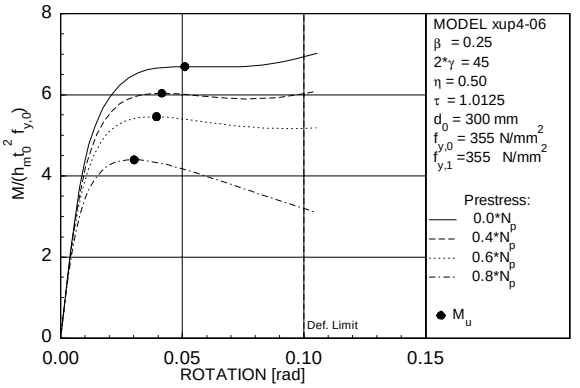

Figure 6.165 Load-displacement curves for model XUP4-06

Note: The figures are organised on this and next pages: from top to bottom an increasing 2γ, from left to right an increasing η and β.

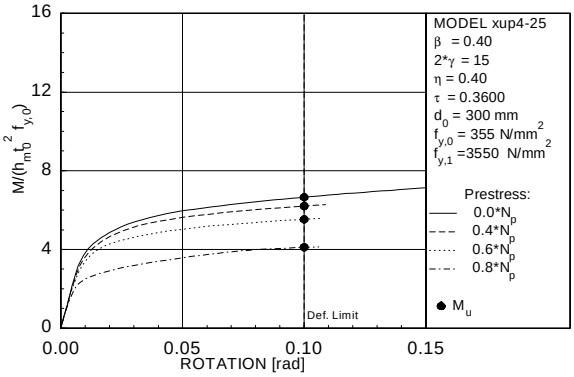

Figure 6.166 Load-displacement curves for model XUP4-25

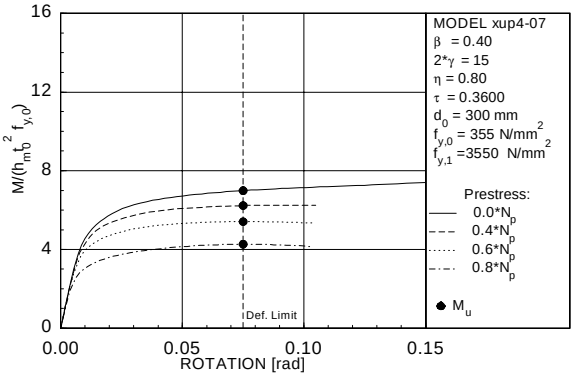

Figure 6.167 Load-displacement curves for model XUP4-07

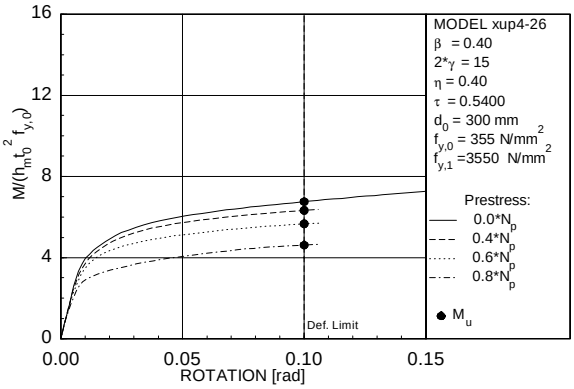

Figure 6.168 Load-displacement curves for model XUP4-26

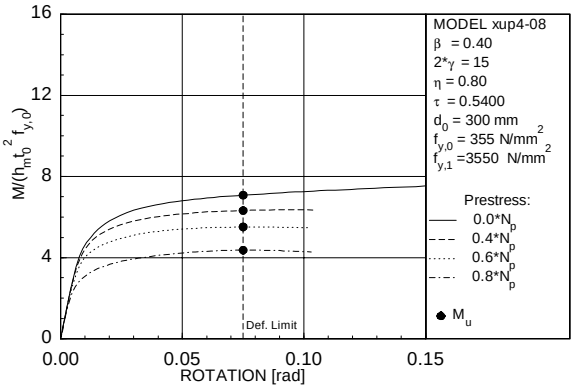

Figure 6.169 Load-displacement curves for model XUP4-08

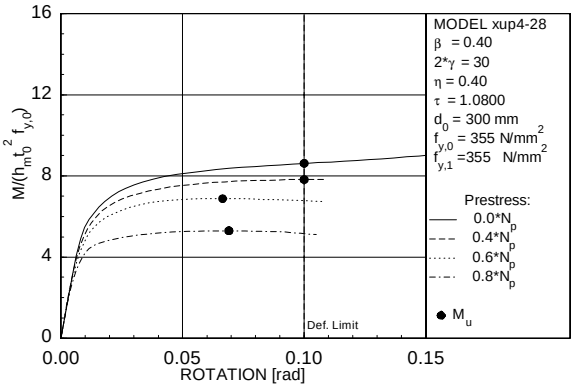

Figure 6.170 Load-displacement curves for model XUP4-28

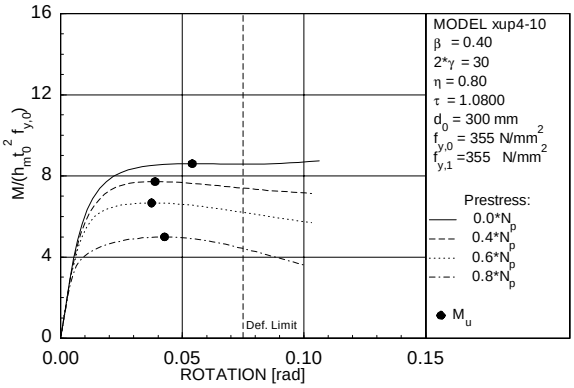

Figure 6.171 Load-displacement curves for model XUP4-10

Note: The figures are organised on this and next pages: from top to bottom an increasing 2γ, from left to right an increasing η and β.

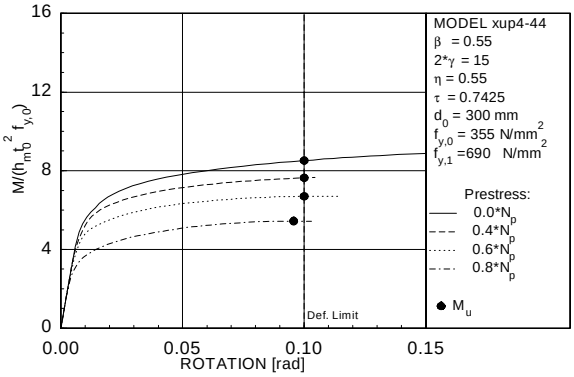

Figure 6.172 Load-displacement curves for model XUP4-44

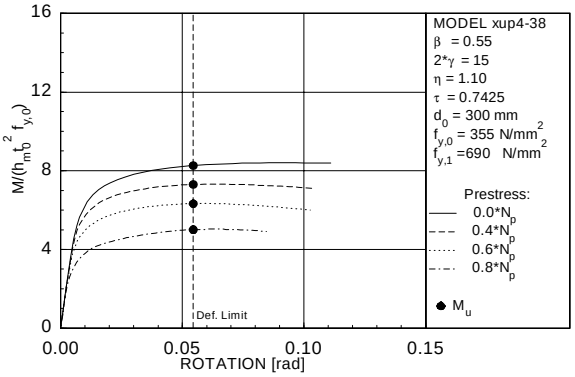

Figure 6.173 Load-displacement curves for model XUP4-38

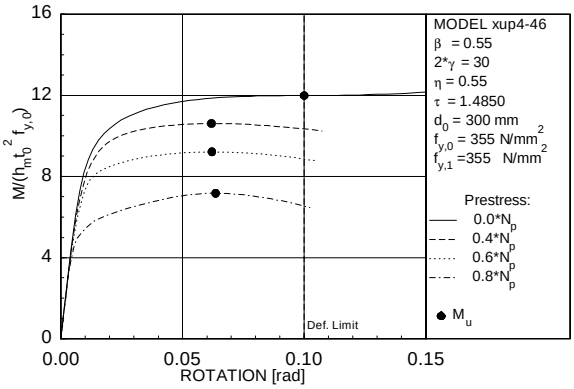

Figure 6.174 Load-displacement curves for model XUP4-46

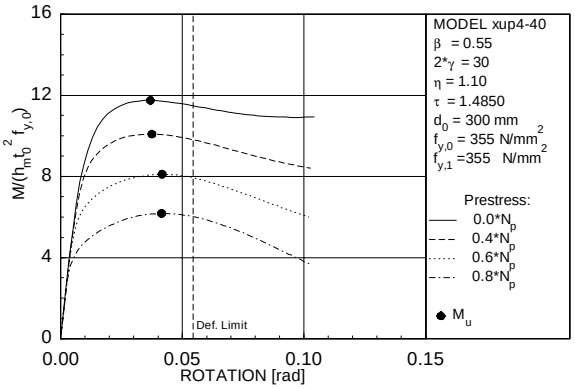

Figure 6.175 Load-displacement curves for model XUP4-40

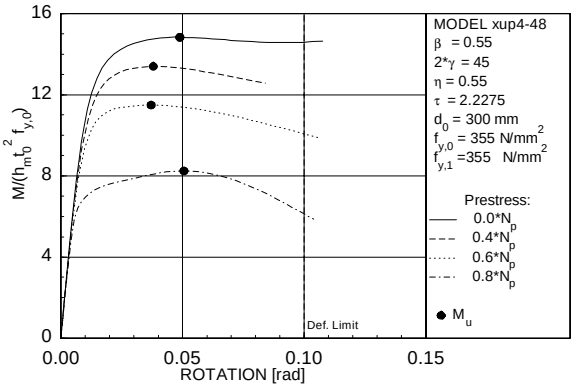

Figure 6.176 Load-displacement curves for model XUP4-48

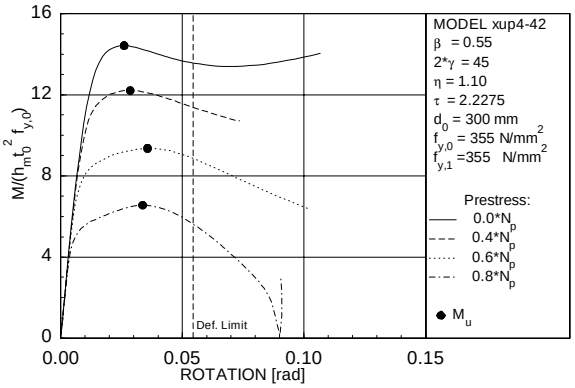

Figure 6.177 Load-displacement curves for model XUP4-42

Note: The figures are organised on this and next pages: from top to bottom an increasing 2γ, from left to right an increasing η and β.

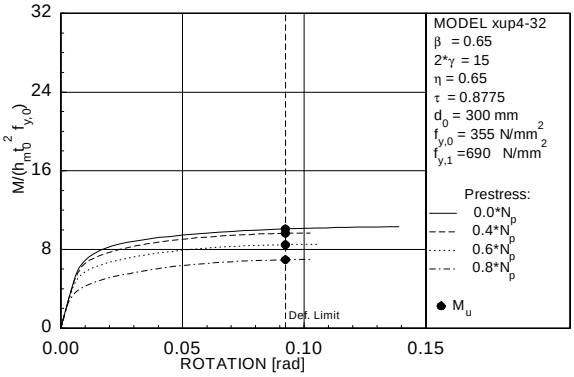

Figure 6.178 Load-displacement curves for model XUP4-32

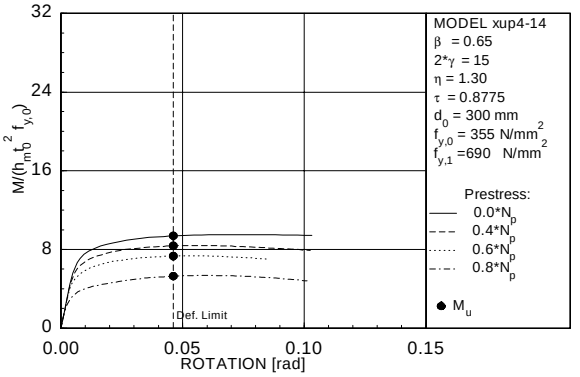

Figure 6.179 Load-displacement curves for model XUP4-14

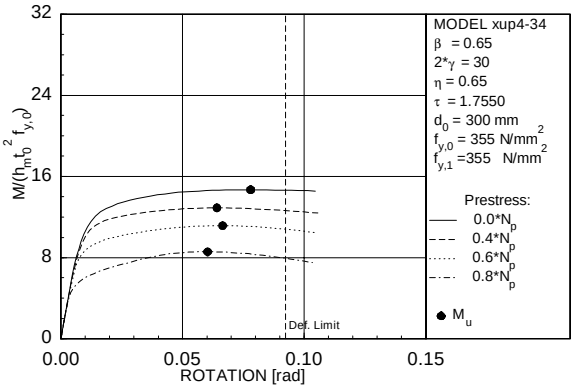

Figure 6.180 Load-displacement curves for model XUP4-34

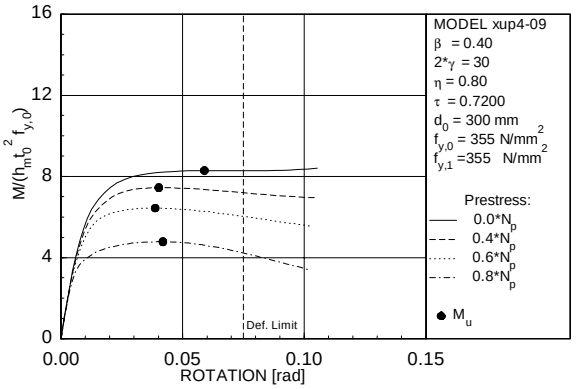

Figure 6.181 Load-displacement curves for model XUP4-09

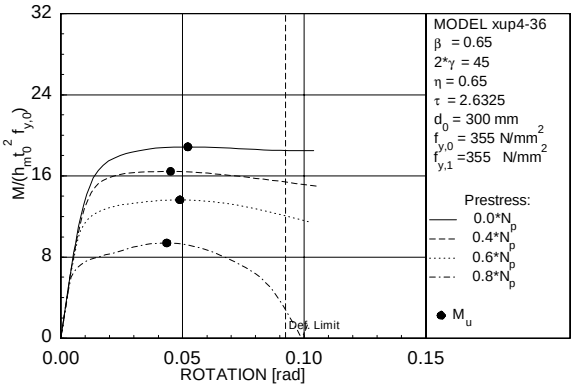

Figure 6.182 Load-displacement curves for model XUP4-36

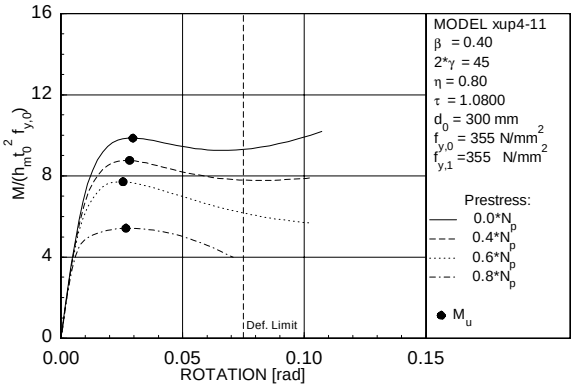

Figure 6.183 Load-displacement curves for model XUP4-11

Note: The figures are organised on this and previous pages: from top to bottom an increasing 2γ, from left to right an increasing η and β (except Fig. 6.181 and 6.183).

7 THE RING MODEL

7.1 Introduction

Analytical yield line models for connections between tubular columns and plates or I-beams cannot easily be made. A more simple model, also based on plasticity theory, has been derived for connections between tubular members by Togo [49], Mäkeläinen [57], Paul [15] and others. In the literature, this model is known as "ring model". The connection is represented by a two dimensional model in the shape of a ring. The connection characteristics in axial direction of the column are not included in the model, but are defined by a function representing the effective length of the ring. This effective length (B_e) cannot theoretically be derived, but must be empirically determined, using experimental or finite element analyses results. The 2-dimensional model, where the behaviour in axial direction is not defined, implies that the beam or brace, e.g. I-beam, plate or tubular member, has no influence on the definition of the model, but only on the effective length of the ring.

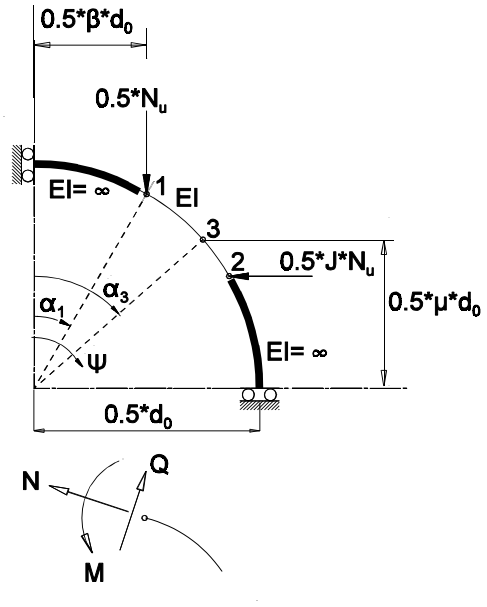

Figure 7.1 Ring model

The ring model can only be used for axially loaded connections. However, in-plane bending can be simulated by using two ring models at a distance equal to the mid-planes of the I-beam flanges (h_m).

In this chapter, the general solution of the ring model is derived for the multiplanar connection loaded with multiplanar axial loading. With this general solution, the equations for more simple cases, like uniplanar loaded connections and uniplanar connections can be obtained.

In the ring model as derived here, normal forces, shear forces and bending moments are included. The ring models as derived by others included only bending moments (e.g. Togo [49]) or gave only a simplified solution (e.g. Paul [15]).

7.2 Derivation ring model

The assumed force ($N_\psi$and Q_ψ) and moment (M_ψ) distribution in the ring can be given as a function of the angle ψ (see Figure 7.1):

$$M_\psi = M_1 - \frac{1}{2}d_0\frac{1}{2}N_u(\sin\psi - \sin\alpha_1) + \frac{1}{2}d_0\frac{1}{2}JN_u(\cos\alpha_1 - \cos\psi) \tag{7.1}$$

where M_1 is the moment in the ring at location 1 as shown in Figure 7.1.

$$N_\psi = -\frac{1}{2}N_u(\sin\psi + J\cos\psi) \tag{7.2}$$

$$Q_\psi = -\frac{1}{2}N_u(\cos\psi - J\sin\psi) \tag{7.3}$$

The approximated interaction formula between the axial force, the shear force and the bending moment for a rectangular cross-section according to the theory of plasticity is shown in Eq. 7.4.

$$\frac{M}{M_p} + \left(\frac{N}{N_p}\right)^2 + \left(\frac{Q}{Q_p}\right)^2 = 1 \tag{7.4}$$

With Eq. 7.1 to 7.4 the following set of equations can be derived for the plastic hinges, which are located at the angles α_1 and α_3 (see Figure 7.1):

$$M(\alpha_1) = M_1 \tag{7.5}$$

$$-M(\alpha_3) = M_1 - \frac{1}{4}\,N_u\,d_0\,(\sin(\alpha_3) - \sin(\alpha_1) + J(\cos(\alpha_3) - \cos(\alpha_1))) \tag{7.6}$$

$$N(\alpha_1) = -\frac{1}{2}\,N_u\,\left(\sin(\alpha_1) + J(\cos(\alpha_1)\right) \tag{7.7}$$

$$N(\alpha_3) = -\frac{1}{2}\,N_u\,\left(\sin(\alpha_3) + J(\cos(\alpha_3)\right) \tag{7.8}$$

$$Q(\alpha_1) = -\frac{1}{2}\,N_u\,\left(\cos(\alpha_1) - J(\sin(\alpha_1)\right) \tag{7.9}$$

$$Q(\alpha_3) = -\frac{1}{2}\,N_u\,\left(\cos(\alpha_3) - J(\sin(\alpha_3)\right) \tag{7.10}$$

$$\frac{M(\alpha_1)}{M_p} + \left(\frac{N(\alpha_1)}{N_p}\right)^2 + \left(\frac{Q(\alpha_1)}{Q_p}\right)^2 = 1 \tag{7.11}$$

$$\frac{M(\alpha_3)}{M_p} + \left(\frac{N(\alpha_3)}{N_p}\right)^2 + \left(\frac{Q(\alpha_3)}{Q_p}\right)^2 = 1 \qquad (7.12)$$

Eq. 7.5 to 7.10 can be substituted into Eq. 7.11 and 7.12, after which the set of equations 7.11 and 7.12 can be solved for N_u as dependent variable. With substitution of Eq. 7.13 to 7.18,

$$N_p = t_0 \; f_{y,0} \; B_e \qquad (7.13)$$

where B_e is the effective length of the ring.

$$Q_p = \frac{t_0 \; f_{y,0} \; B_e}{\sqrt{3}} \qquad (7.14)$$

$$M_p = \frac{1}{4} \; t_0^2 \; f_{y,0} \; B_e \qquad (7.15)$$

$$\frac{d_0}{t_0} = 2 \; \gamma \qquad (7.16)$$

$$\alpha_1 = \arcsin(\beta) \qquad (7.17)$$

$$\alpha_3 = \arccos(\mu) \qquad (7.18)$$

the following general solution for the ring model is obtained:

$$\frac{N_u d_0}{t_0^2 f_{y,0} B_e} = \frac{4}{x + \sqrt{x^2 + \frac{y}{2 \cdot \gamma^2}}} \qquad (7.19)$$

with

$$x = \sqrt{1-\mu^2} - \beta + J(\mu - \sqrt{1-\beta^2}) \qquad (7.20)$$

and

$$y = (1+3J^2)(\beta^2+1-\mu^2) + (3+J^2)(1-\beta^2+\mu^2) - 4J(\beta\sqrt{1-\beta^2} + \mu\sqrt{1-\mu^2}) \qquad (7.21)$$

In Eq. 7.19, the location of plastic hinge 3 is still an independent variable.
The minimum solution for Eq. 7.19 with substituting Eq. 7.20 and 7.21 can be obtained by setting $\frac{\delta N_u}{\delta \mu} = 0$, which results in:

For $J \geq \frac{\beta}{\sqrt{1-\beta^2}}$: $\mu = \frac{J}{\sqrt{1+J^2}}$.

For $J \leq \frac{\beta}{\sqrt{1-\beta^2}}$: $\mu = \beta$, because μ cannot be smaller than β, or in other words, the

plastic hinges must be between the two flanges or plates. For this solution, the ring model has only two plastic hinges at locations 1 and 2 in Figure 7.1.

Figures 7.2 to 7.4 show for three 2γ values and for β = 25, 40 and 65 the non-dimensional strength vs. the load ratio and also the location of plastic hinge 3.

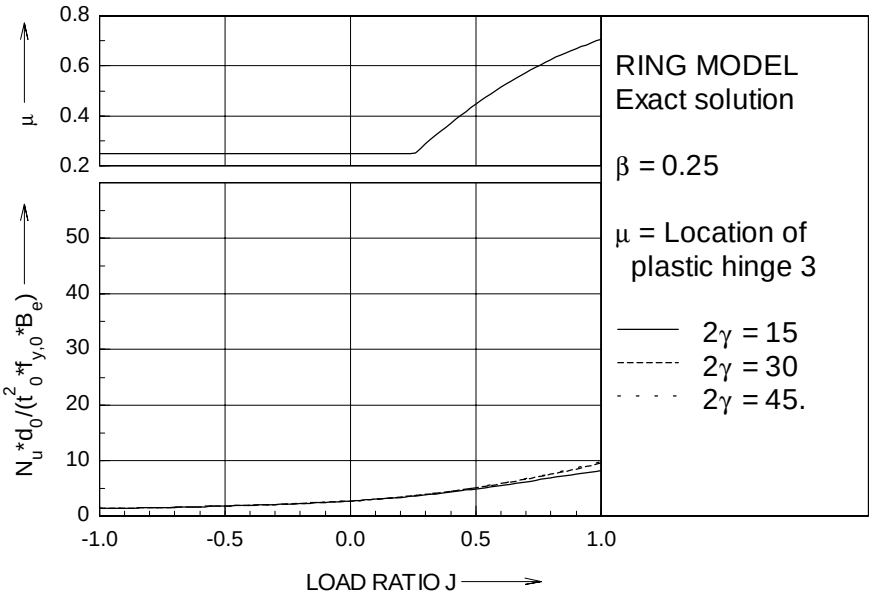

Figure 7.2 Ring model for β = 0.25, multiplanar loading influence

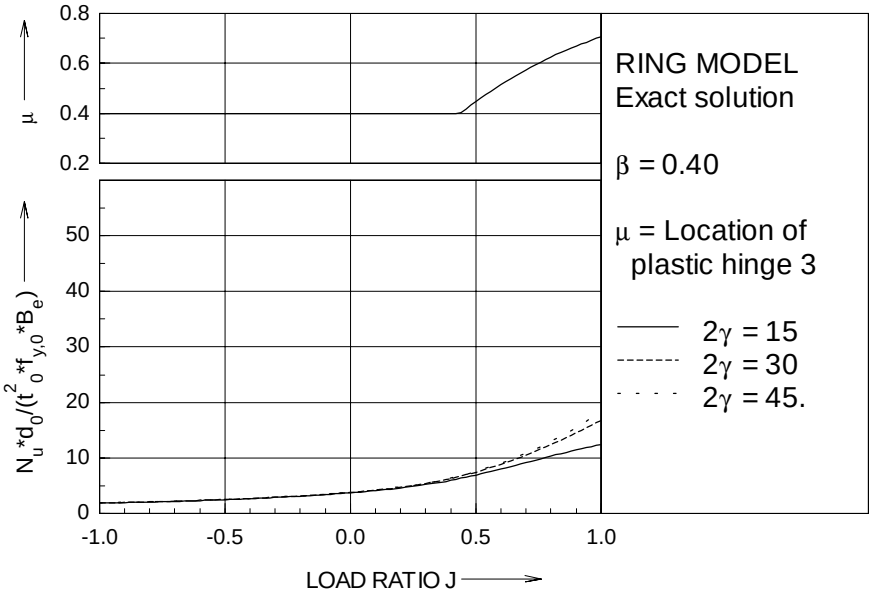

Figure 7.3 Ring model for β = 0.40, multiplanar loading influence

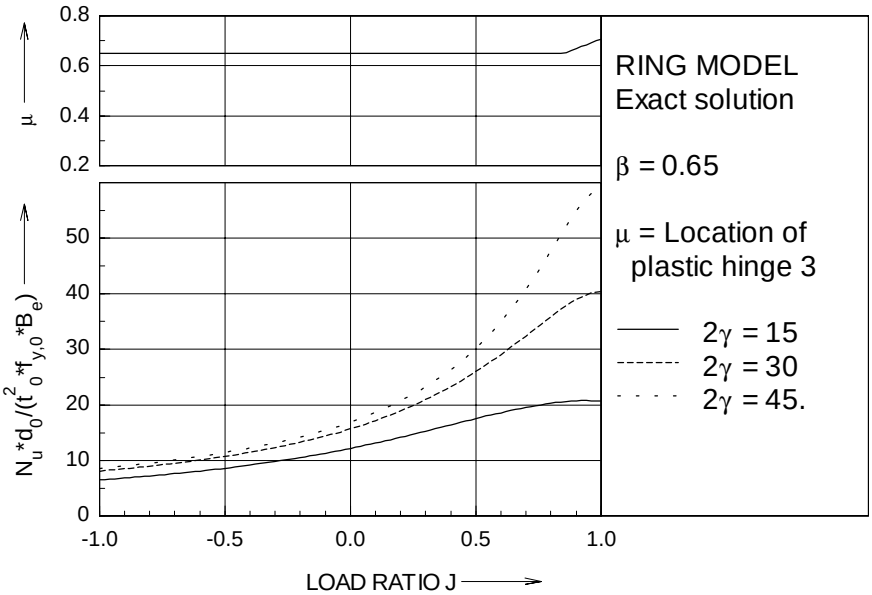

Figure 7.4 Ring model for β = 0.65, multiplanar loading influence

7.3 Solution ring model for uniplanar connections

The equation for uniplanar connections can be obtained by substituting J = 0 and μ = 0 in Eq. 7.19 to 7.21. For the uniplanar connections there are only two plastic hinges, namely at location 1 and at $\alpha_3 = \pi/2$. Plastic hinge 2 is absent.

Thus,

$$\frac{N_u d_0}{t_0^2 f_{y,0} B_e} = \frac{4}{1-\beta+\sqrt{(1-\beta)^2 + \frac{2(2-\beta^2)}{2\cdot\gamma^2}}} \qquad (7.22)$$

Note that for β=1 the non-dimensional strength is equal to 4γ.
Figure 7.5 shows β vs. the non-dimensional strength for three 2γ values. Since the plastic hinge is in a fixed position, the location is not shown in the figure.

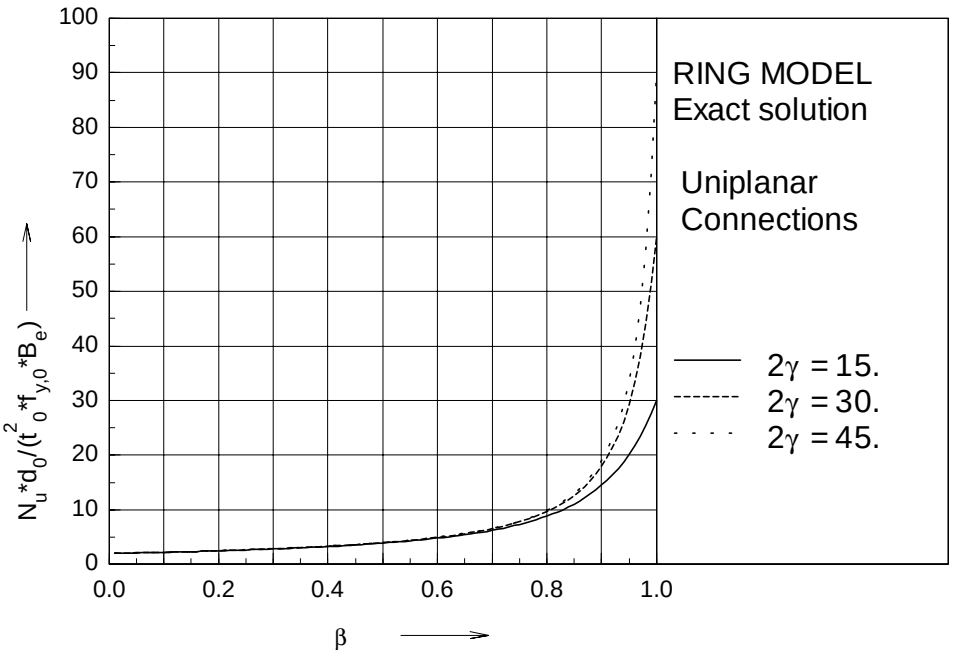

Figure 7.5 Ring model for the uniplanar connections

7.4 Solution ring model for uniplanar loaded multiplanar connections (load ratio J=0)

For the uniplanar loaded multiplanar connections, there are only plastic hinges at location 1 and at location 2. Actually, plastic hinge 3 is also located at location 2 in Figure 7.1. The equation for the uniplanar loaded multiplanar connections can be obtained by substituting J = 0 and $\mu = \beta$ in Eq. 7.19 to 7.21.

Thus,

$$\frac{N_u d_0}{t_0^2 f_{y,0} B_e} = \frac{4}{\sqrt{1-\beta^2} - \beta + \sqrt{\left(\sqrt{1-\beta^2} - \beta\right)^2 + \frac{4}{2\cdot\gamma^2}}} \tag{7.23}$$

Note that for $\beta = \frac{1}{2}\sqrt{2}$ the non-dimensional strength N^* is equal to $2\gamma\cdot\sqrt{2}$.
Figure 7.6 shows β vs. the non-dimensional strength for three 2γ values. Since the plastic hinge is in a fixed position, the location is not shown in the figure.

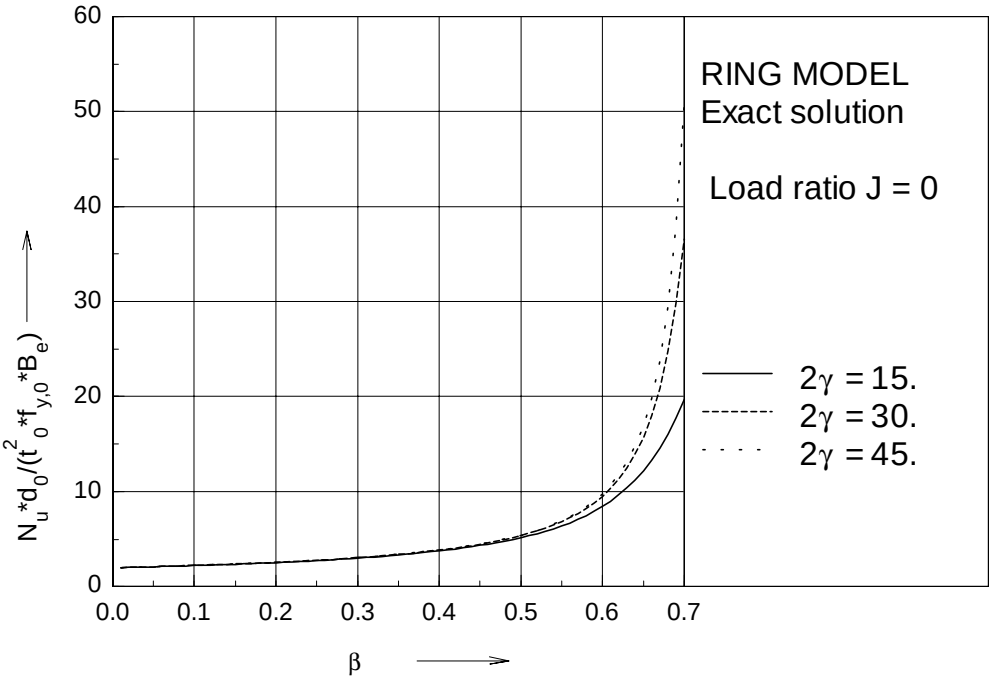

Figure 7.6 Ring model for load ratio J = 0

7.5 Solution ring model for multiplanar connections with load case J = 1

For the multiplanar connections, with load case J = 1, there are three plastic hinges, namely at location 1,2 and 3. Due to the symmetry of the load case, plastic hinge 3 is located at $\mu = ½\sqrt{2}$. The equation for the uniplanar loaded multiplanar connections can be obtained by substituting J = 1 and $\mu = ½\sqrt{2}$ in Eq. 7.19 to 7.21.

Thus,

$$\frac{N_u d_0}{t_0^2 f_{y,0} B_e} = \frac{4}{-\beta+\sqrt{2}-\sqrt{1-\beta^2} + \sqrt{(-\beta+\sqrt{2}-\sqrt{1-\beta^2})^2 + \frac{3-2\beta\sqrt{1-\beta^2}}{\gamma^2}}} \qquad (7.24)$$

See also Figure 7.7. Note that for $\beta=½\sqrt{2}$ the non-dimensional strength is equal to $2\gamma\cdot\sqrt{2}$.

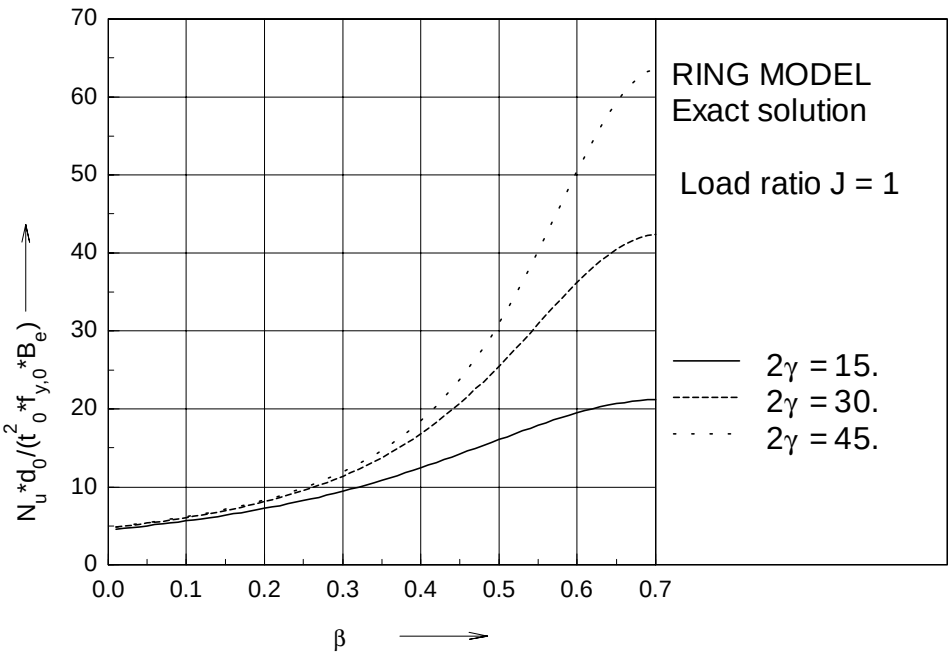

Figure 7.7 Ring model for load ratio J = 1

7.6 Solution ring model for multiplanar connections for $\beta=\frac{1}{2}\sqrt{2}$

It is remarkable that for $\beta=\frac{1}{2}\sqrt{2}$ the non-dimensional is the same for both J=0 and J=1, as shown in Figure 7.8. However, if $\beta=\frac{1}{2}\sqrt{2}$ and $\mu=\frac{1}{2}\sqrt{2}$ is substituted in Eq. 7.19 to 7.21 the equation, showing the non-dimensional strength as function of J for $\beta=\frac{1}{2}\sqrt{2}$, is obtained:

$$\frac{N_u d_0}{t_0^2 f_{y,0} B_e} = \frac{4\gamma}{\sqrt{2(J^2 - J + 1)}} \tag{7.25}$$

It is clear that J=0 and J=1 give the same non-dimensional strength. The maximum non-dimensional strength is obtained for J=½ and is equal to $4\gamma\cdot\sqrt{2/3}$.

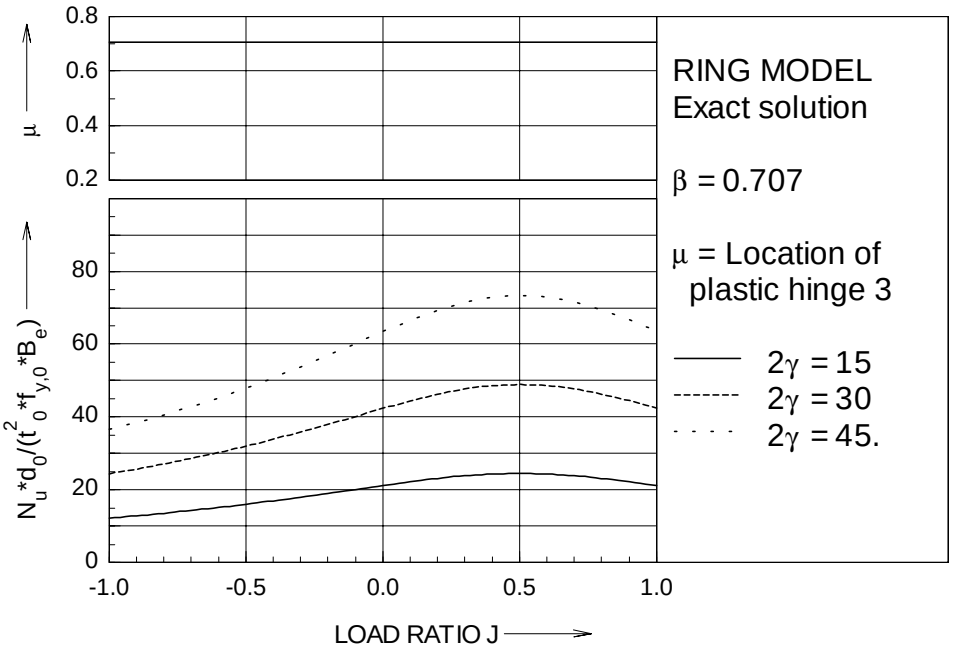

Figure 7.8 Ring model for $\beta=\frac{1}{2}\sqrt{2}$

7.7 Conclusions

Using the ring model approach, analytical models can be obtained for plate or I-beam to CHS column connections. The derived formulae for the uniplanar connections and uniplanar loaded multiplanar connections are relatively simple, and can be used as a basis for the derivation of design formulae for the connection strength of such connections. However, the analytical equations for multiplanar loaded connections are more complicated, especially since a set of equations is necessary to describe the connection strength for the whole range of possible β-ratios and load ratios.

From the solutions of the ring model the following observations can be made:

An increase of the β-ratio results in an increase in the non-dimensional strength of the ring model.

For the uniplanar ring model and the uniplanar loaded multiplanar ring model, an influence of the 2γ-ratio on the non-dimensional strength occurs only for larger β-ratios.

Negative load ratios give a decrease in connection strength, while positive load ratios give an increase in connection strength. This influence becomes stronger for larger β-ratios and larger 2γ-ratios.

For negative load ratios in combination with smaller β-ratios, there is no influence of the 2γ-ratio on the non-dimensional strength of the ring model. For positive load ratios in combination with larger β-ratios, there is a significant influence of the 2γ-ratio on the non-dimensional strength of the ring model. In such cases, larger 2γ-ratios increase the non-dimensional strength.

8 DETERMINATION OF STRENGTH FORMULAE

8.1 General

The strength of connections with tubular columns is usually given by non-dimensional strength formulae. The non-dimensional strength is defined as $\frac{N_u}{t_0^2\ f_{y,0}}$ for axial loading and as $\frac{M_u}{t_0^2\ f_{y,0}\ h_m}$ for in-plane bending. In the strength formulae, non-dimensional geometrical parameters are used, describing the geometry. These parameters are the flange or plate to column diameter ratio β, the column diameter to column wall thickness ratio 2γ. The load ratio J is the ratio between the load on the out-of-plane and in-plane plates or beams.

For these non-dimensional strength formulae the assumption has been made that scale effects can be neglected. This assumption is not entirely correct, since weld dimensions do not scale linearly with the actual dimensions of the connection for all possible sizes of the connections. For example, when the absolute dimensions of a connection are small, minimum weld sizes have to be taken into account ([2], [7]). In such cases, the strength formulae as derived here are conservative.

The strength formulae as derived here are partly theoretical and partly empirical. The theoretical part is described in chapter 7. As stated in chapter 7, the effective length of the ring model has to be determined empirically. The effective length of the ring model is dependent on the β-ratio and the 2γ-ratio. For the function for the effective length of the ring model several functions have been analysed. The best results were obtained with:

$$B_e = R_1 * \gamma^{(R_2 \cdot \beta - R_3 \cdot \beta^2)} \qquad (8.1)$$

R_1 to R_3 are regression constants.

It was found, that the γ ratio influence in the non-dimensional ring model formulae is too strong for large β ratios in comparison with the finite element results. The term with $1/\gamma^2$ in the ring model formulae defines the non-dimensional strength for β=1.0 for the uniplanar connections (Eq. 7.22) and for $\beta = ½\cdot\sqrt{2}$. for the multiplanar connections (Eq. 7.23). Therefore, in the regression analyses the $1/\gamma^2$ term is replaced by $1/\gamma^{R4}$ to reduce the γ ratio influence, thus introducing the extra regression constant R_4.

Although the load ratio is incorporated in the ring model formulae, the strength formulae as derived here are based upon the uniplanar loaded ring model formulae, thus with J = 0. The reason is that the load ratio influence cannot be described with one single formula for the range of J from -1.0 to +1.0. Also, using the exact ring model formulation of the multiplanar load behaviour would lead to complicated strength formulae. Since the aim of this research is to give the basics for design formulae, too complicated formulae are undesirable. The influence of the load ratio on the connection strength is mainly dependent on an interaction relation between the β-ratio and the load ratio J. This influence can be described by the following general function:

$$\frac{N(\beta,J)}{N(J=0)} \text{ or } \frac{M(\beta,J)}{M(J=0)} = 1 + J(R_5\cdot\beta + R_6\cdot\beta^2) + J^2(R_7\cdot\beta + R_8\cdot\beta^2) \qquad (8.2)$$

The regression constants R_1,....,R_8 are to be determined using regression analyses. Since the equations to be used for the regression analyses cannot be rewritten in linear terms in such way that R_1,..,R_8 are independent parameters, regression analyses with non-linear solving techniques must be used.
The nonlinear regression analyses are carried out with the computer program NONLIN, specially developed by the author for this PhD study. The part of the program that solves sets of non-linear equations is based on a modified Levenberg-Marquant algorithm. The subroutines of the solver of the program are developed at the Argonne National Laboratory, USA, in the framework of the MINPACK project.

8.2 Method used for regression analyses

The least-squares estimations of the regression constants are chosen so as to minimize the sum of squares of deviations of finite element results from corresponding points of the regression model. Letting Y_i denotes the finite element results and letting $\hat{Y}_i$ denotes the responds of the regression model, the minimum sum of squares SSE can be written as

$$SSE = \sum_{i=1}^{n} (Y_i - \hat{Y}_i)^2 \qquad (8.3)$$

This is the common method for least-square estimations. The disadvantage of this method is that the absolute errors for small and large values of $\hat{Y}_i$ are approximately the same. As a result, the relative errors for small values of $\hat{Y}_i$ can be much larger than for large values of $\hat{Y}_i$. For the connections investigated here, it would mean that for the smaller β-ratios and larger 2γ-ratios, the relative errors would be consequently larger than for the larger β-ratios and

smaller 2γ-ratios. To avoid this, an alternate method is used for the least square estimations:

$$SSE = \sum_{i=1}^{n} (1 - \frac{\hat{Y}_i}{Y_i})^2 \qquad (8.4)$$

Using this method, the weight of the data points in the least square estimations is inversely proportional with the value of the data points.

There are several options to perform the least square estimations. The regression constants R_1 to R_8 can be determined with a complete regression model or by using partial models. These partial models together describe the connection behaviour. For example, one part of the model describes the behaviour of a uniplanar loaded connection, the second part of the model describes the multiplanar behaviour of the model. The first method will give better correlation between the finite element results and the regression model, the second method might give a better insight in the structural behaviour by examining the different influences separately.

In the tables of the results, four statistical indicators are listed:

r^2 - the coefficient of correlation
COV - the coefficient of variation
F - the F-statistic, to test the significancy of the regression model.
DOF - the number of degrees of freedom of the model.

8.3 Plate to CHS column connections under axial loading

8.3.1 Uniplanar connections

The regression model for the uniplanar plate to CHS column connections under axial loading is based upon the ring model (Eq. 7.22) as described in Chapter 7.3 and the effective length of the ring (Eq. 8.1) is given by Eq. 8.5:

$$\frac{N_u}{t_0^2 \, f_{y,0}} = \frac{R_1 * \gamma \;\; R_2 \cdot \beta - R_3 \cdot \beta^2}{1 - \beta + \sqrt{(1-\beta)^2 \; + \; \frac{2(2-\beta^2)}{2 \cdot \gamma^{R_4}}}} \tag{8.5}$$

Table 8.1 Results of the regression analyses for uniplanar plate to CHS column connections loaded with axial loading

R_1	R_2	R_3	R_4	r^2	COV	F	DOF
4.26	1.24	1.35	1.66	0.99	0.03	342	16

As shown in Table 8.1 and Figure 8.1, there is a good correlation found between the finite element results and the regression model.

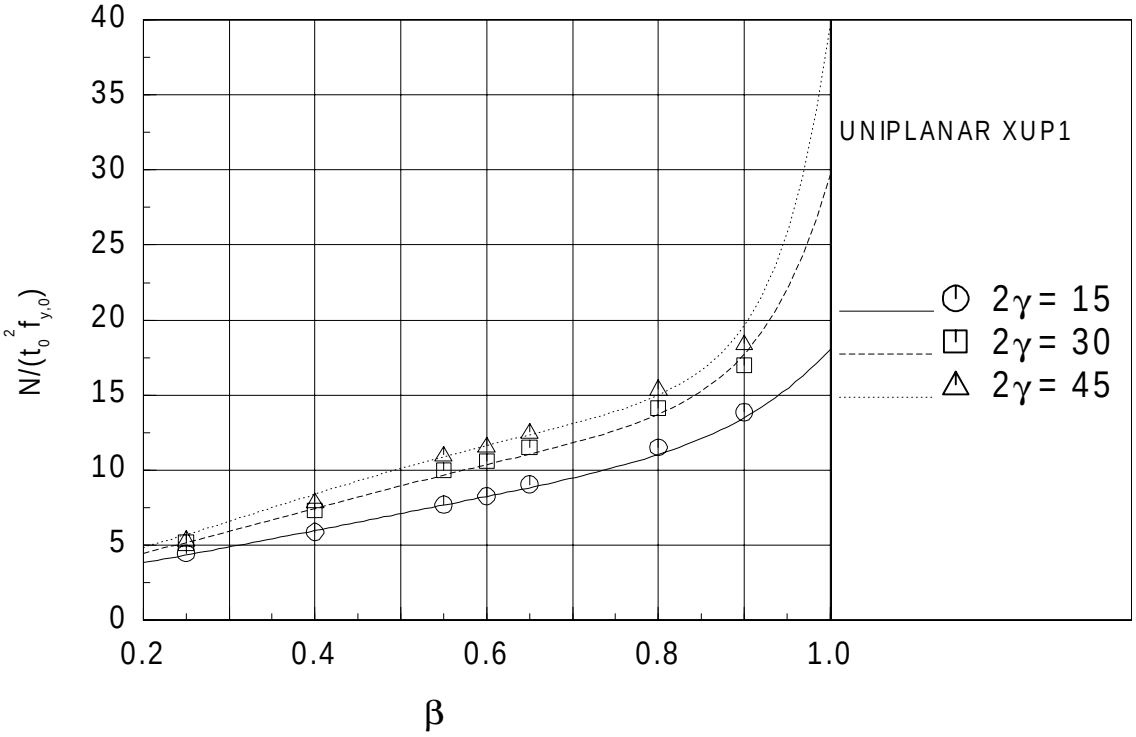

Figure 8.1 Results regression analysis uniplanar plate to CHS column connections under axial loading

8.3.2 Multiplanar connections

The regression model for the uniplanar loaded multiplanar plate to CHS column connections under axial loading is based upon the ring model (Eq. 7.23) as described in chapter 7.4 and the effective length of the ring (Eq. 8.1) is given by Eq. 8.6:

$$\frac{N_u}{t_0^2 f_{y,0}} = \frac{R_1 * \gamma^{\,R_2 \cdot \beta - R_3 \cdot \beta^2}}{\sqrt{1-\beta^2} - \beta + \sqrt{\left(\sqrt{1-\beta^2} - \beta\right)^2 + \frac{4}{2 \cdot \gamma^{R_4}}}} \tag{8.6}$$

Table 8.2 Results of the regression analyses for multiplanar plate to CHS column connections under axial loading with load ratio J=0

R_1	R_2	R_3	R_4	r^2	COV	F	DOF
6.06	0.69	1.01	0.97	0.99	0.03	339	9

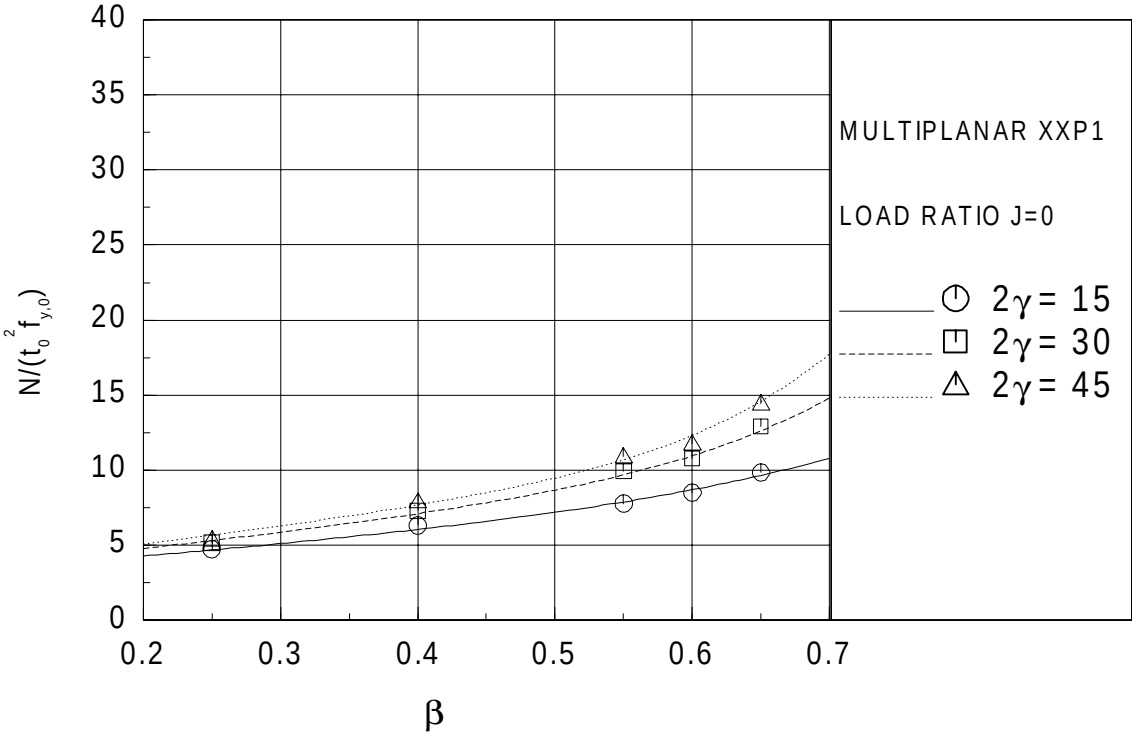

Figure 8.2 Axially loaded multiplanar plate to CHS column connections with load ratio J = 0

As shown in Table 8.2 and Figure 8.2, there is a good correlation found between the finite element results and the regression model.

The multiplanar loading effects are described by Eq. 8.7:

$$\frac{N_u}{N(J=0)} = 1 + J(R_5 \cdot \beta + R_6 \cdot \beta^2) + J^2(R_7 \cdot \beta + R_8 \cdot \beta^2) \qquad (8.7)$$

The regression analyses is performed by first dividing the finite element results of the plate to CHS column connections under multiplanar axial loading by the results of the finite element results of the corresponding uniplanar loaded multiplanar models.

Table 8.3 Results of the regression analyses for multiplanar axial loading

R_5	R_6	R_7	R_8	r^2	COV	F	DOF
0.465	0.433	-0.642	1.28	0.94	0.046	262	70

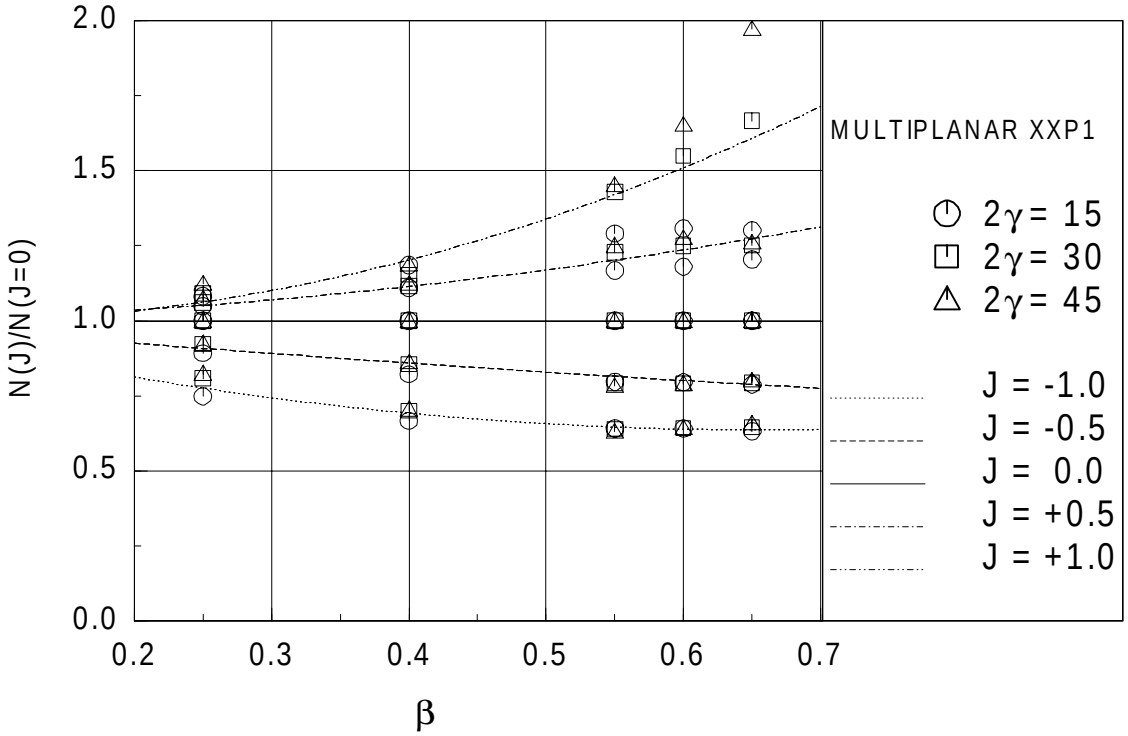

Figure 8.3 Multiplanar axially loaded plate to CHS column connections, multiplanar loading influence

As shown in Table 8.3 and Figure 8.3, the multiplanar load formula shows a good agreement with the experimental results. For load ratios not equal to 1, there is only a small interaction between the load ratio J and the β-ratio. However, for load ratio J = 1, there is also a 2γ-ratio influence which is not covered by the formula. This behaviour is also found for the analytical ring model as show in Figure 7.6. For the ring model it was derived that for $J \geq \frac{\beta}{\sqrt{1-\beta^2}}$ there is a 2γ-ratio influence.

8.4 Plate to CHS column connections under axial loading, interaction effects

8.4.1 Multiplanar connections, no web influence included

If the contribution in strength of the I-beam web is neglected, an I-beam under compression can be seen as two plates welded to the CHS column at two levels. The aim is to determine the interaction between the plates at the two levels. The distance of the two levels is the distance of the two mid-planes of the I-section beams. If the distance of the two planes is infinite, than the connection strength is exactly two times the strength of a comparable connection with plates in one plane. If this distance is very small, than the connection strength will be approximately equal to one time the strength of a comparable connection with plates in one plane.

One of the most simple possible interaction formulae, which fulfils this constraint is:

$$\frac{N_{u,\ 2\ planes}}{N_{u,\ 1\ plane}} = 2 - \frac{R_1}{1 + R_2 \cdot \eta} \tag{8.8}$$

In this simple interaction formula, the only geometrical parameter is the beam height to column diameter ratio η.
The regression analyses is performed by first dividing the finite element results of the I-beam to CHS column connections by the results of the corresponding plate to CHS column connections.

Table 8.4 Results of the regression analyses for interaction effects, simple model

R_1	R_2	r^2	COV	F	DOF
0.8695	1.308	0.684	0.053	45	42

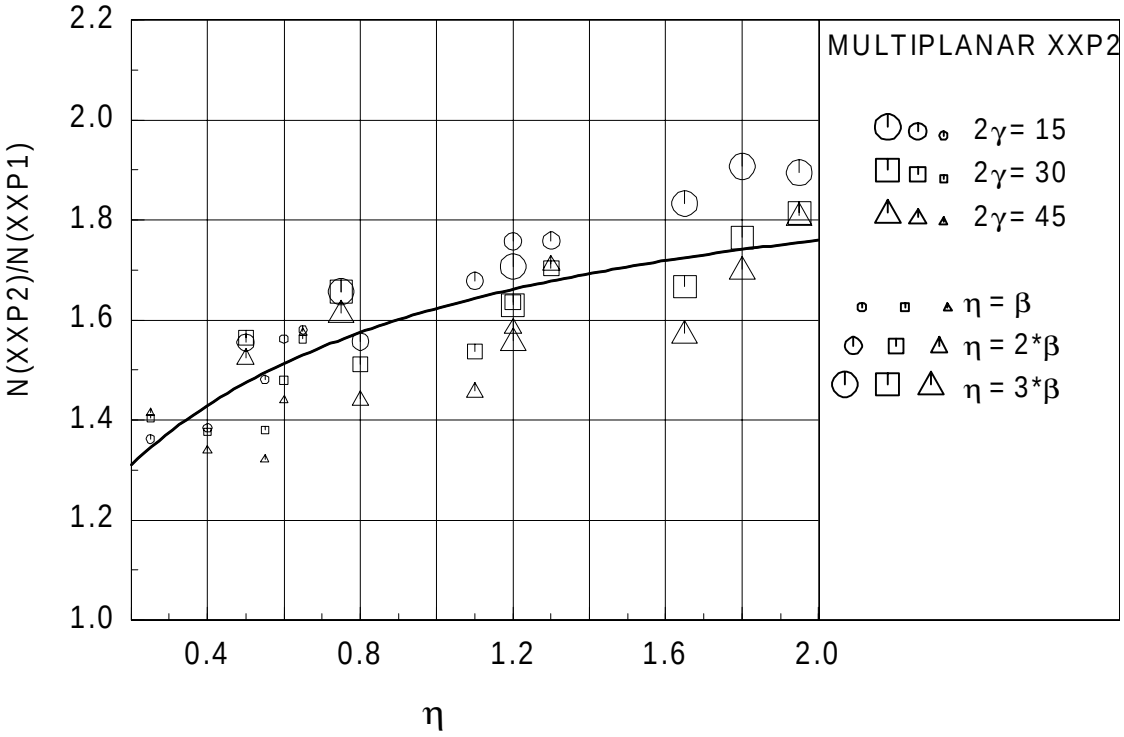

Figure 8.4 Interaction effects of plates to CHS column connections loaded with axial loading, according to Eq. 8.8

As shown in Table 8.4 and Figure 8.4, the correlation between the regression model and the finite element model is poor. It is clear, that only one geometrical parameter, namely the beam height to column diameter ratio η is not sufficient, since there is a significant interaction between the η-ratio, the β-ratio and the 2γ-ratio.

Eq. 8.9 gives the interaction formula for this three geometrical parameters.

$$\frac{N_{u,\ 2\ planes}}{N_{u,\ 1\ plane}} = 2 - \frac{1}{1 + \frac{R_1 \cdot \eta}{(2\gamma)^{R_2}} * (1 + R_3 \cdot \beta + R_4 \cdot \beta^2)} \tag{8.9}$$

The results of the regression analysis with this enhanced model are given in Table 8.5 and Figure 8.5. The correlation between the regression model and the finite element results is much better than the correlation of the simple model.

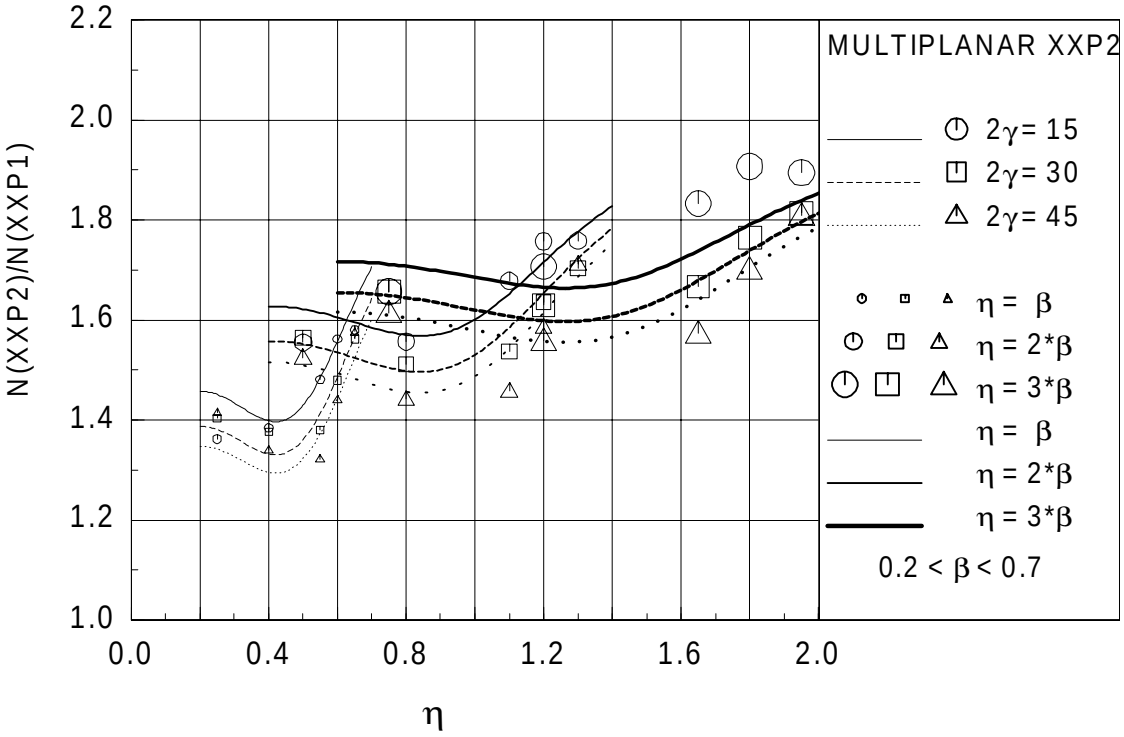

Figure 8.5 Interaction effects of plate to CHS column connections loaded with axial loading, according to Eq. 8.9

Table 8.5 Results of the regression analyses for interaction effects, enhanced model

R_1	R_2	R_3	R_4	r^2	COV	F	DOF
30.08	0.416	-3.61	3.83	0.91	0.027	107	40

8.5 I-beam to CHS column connections under axial loading

8.5.1 Influence of the web on the connection strength

In the previous paragraph, the relation between the distance of two plates and the connection strength is formulated. In this paragraph, the influence of the web of an I-section beam on the connection strength is studied. In Table 6.7, the strengths of the connections with and without the web are compared with each other. This table shows that the web gives an increase in connection strength up to 7%. The increase of the connection strength is proportional with the η-ratio. Therefore, a simple regression model has been made as shown in Eq 8.10.

$$\frac{N_u(\text{with web})}{N_u(\text{without web})} = 1 + R_1 \cdot \eta \qquad (8.10)$$

The results of the regression analysis are shown in Table 8.6 and Figure 8.6. The correlation between the regression model and the finite element results is reasonable, but the absolute errors are small.

Table 8.6 Results of the regression analyses, influence presence of the web

R_1	r^2	COV	F	DOF
0.0352	0.83	0.008	208	43

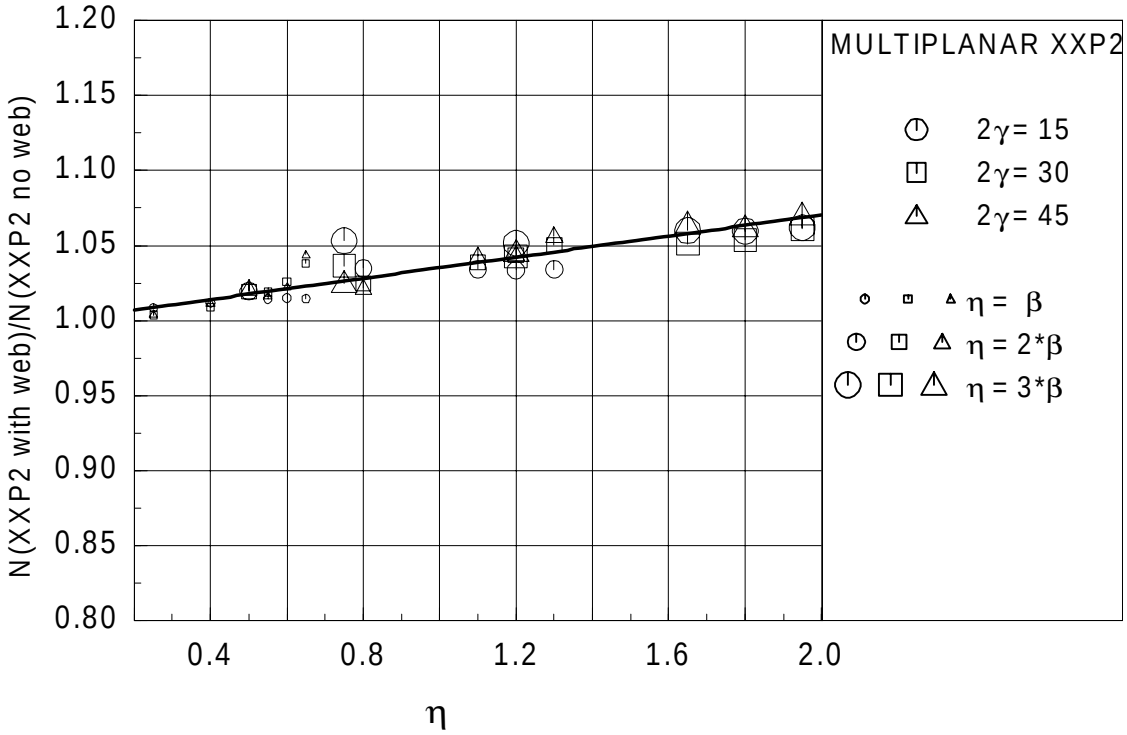

Figure 8.6 Results regression analysis, influence of the presence of the web on the connections strength (Eq. 8.10)

Combining Eq. 8.9 and Eq. 8.10 gives

$$\frac{N_{u,\ 2\ planes}}{N_{u,\ 1\ plane}} = \left(2 - \frac{1}{1 + \dfrac{R_1 \cdot \eta}{(2\gamma)^{R_2}}(1 + R_3 \cdot \beta + R_4 \cdot \beta^2)} \right) \left(1 + R_5 \cdot \eta\right) \qquad (8.11)$$

The statistical parameters are shown in Table 8.7. For the determination of these parameters the regression constants from Table 8.5 and 8.6 are used. There is a good agreement between the finite element results and the regression model.

Table 8.7 Results of the regression analysis for interaction effects, enhanced model

R_1	R_2	R_3	R_4	R_5	r^2	COV	F	DOF
30.08	0.416	-3.61	3.83	0.0352	0.94	0.028	114	39

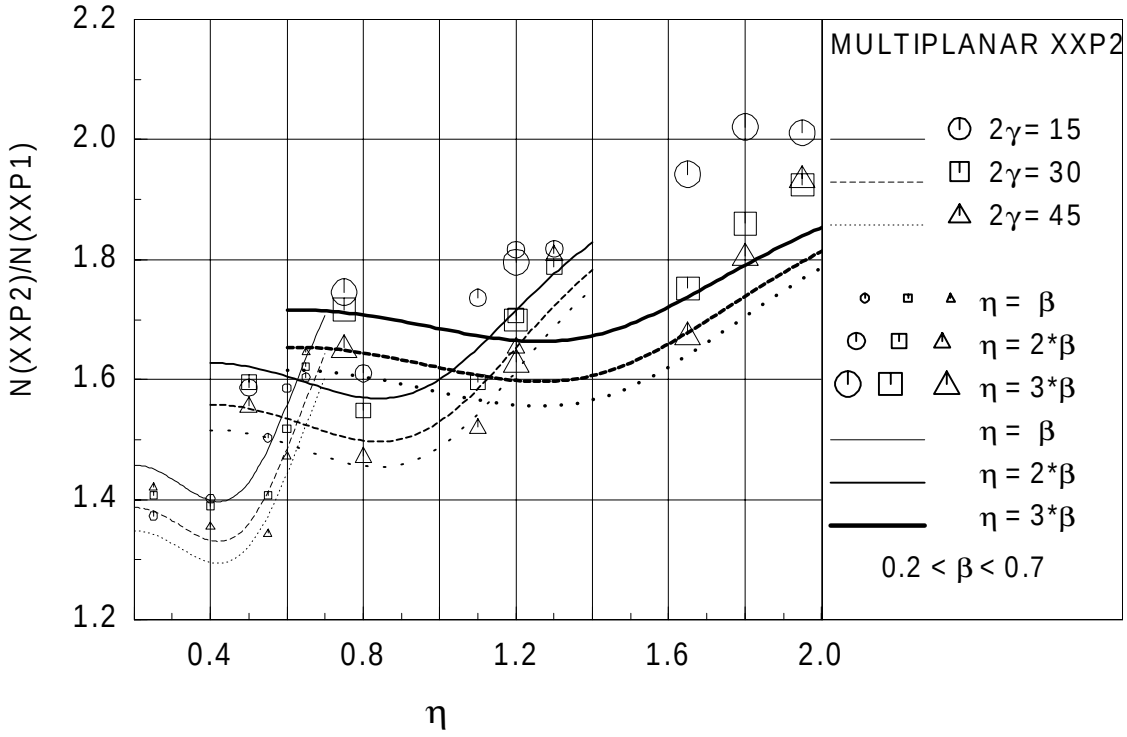

Figure 8.7 Results regression analysis for the interaction effects of I-beam to CHS column connections loaded with axial loading, enhanced model with web influence included (Eq. 8.11)

8.5.2 Multiplanar loading effect

To investigate the influence of the multiplanar axial loading on the connection strength, the data points for all connections are divided by the corresponding data points for load ratio J = 0. From the data points it can be observed that there is no interaction between the load ratio J and the beam height to column diameter ratio η. For load ratios not equal to 1, there is only a small interaction between the load ratio J and the β-ratio. However, for load ratio J = 1, there is also a 2γ-ratio influence. This behaviour is also found for the theoretical ring model as shown in Figure 7.6. For the ring model it was derived that for $J \geq \frac{\beta}{\sqrt{1-\beta^2}}$ there is a 2γ-ratio influence.

For the data points as used in the parametric study, the critical values for J are as follows:

β= 0.25: J>0.26

β= 0.40: J>0.44

β= 0.55: J>0.66

β= 0.60: J>0.75

β= 0.65: J>0.86

However, this 2γ-ratio influence is small for $\beta<0.5$.

Due to the complicated structure of Eq. 7.19, it is not possible give an analytical formula for the multiplanar loading effect.

Therefore, the following model is used for the regression analysis:

$$\frac{N_u(J)}{N_u(J=0)} = 1 + \left(J(R_1\cdot\beta + R_2\cdot\beta^2)+J^2\beta^2\right)\left(1 + \mathrm{INT}(0.5J+0.5)(R_4+R_5\cdot\beta\cdot(2\gamma)^{R_6}\right) \qquad (8.12)$$

Note:

INT = Intrinsic function, which converts it's argument to an integer by truncating.

The regression formula looks complicated, but this was done to be able to perform the regression analyses for all data points in one run. In fact, the formula can be divided in two parts:

$$\frac{N_u(J)}{N_u(J=0)} = 1 + \left(J(R_1\cdot\beta + R_2\cdot\beta^2)+J^2\cdot\beta^2\right) * f(\beta,2\gamma,J) \qquad (8.13)$$

with

$$f(\beta,2\gamma,J) = 1 \quad \text{for } J \neq 1 \qquad (8.14)$$

and

$$f(\beta,2\gamma,J) = R_4 + R_5\cdot\beta(2\gamma)^{R_6} \quad \text{for } J = 1 \qquad (8.15)$$

The results of the regression analysis is shown in Table 8.8 and Figures 8.8 to 8.10. It is not possible to show all data in one figure, therefore three figures are used, namely one for each 2γ-ratio. To distinguish the η-ratios, different symbol sizes are used. Since there is only a small η-ratio influence, most of the data points with the same β-ratio overlap with each other. From Table 8.8 can be concluded that there is a good agreement between the regression model and the finite element results.

Table 8.8 Results of the regression analysis for multiplanar loading influence

R_1	R_2	R_3	R_4	R_5	R_6	r^2	COV	F	DOF
1.906	-1.486	0.586	-0.788	0.337	0.429	0.99	0.036	3212	218

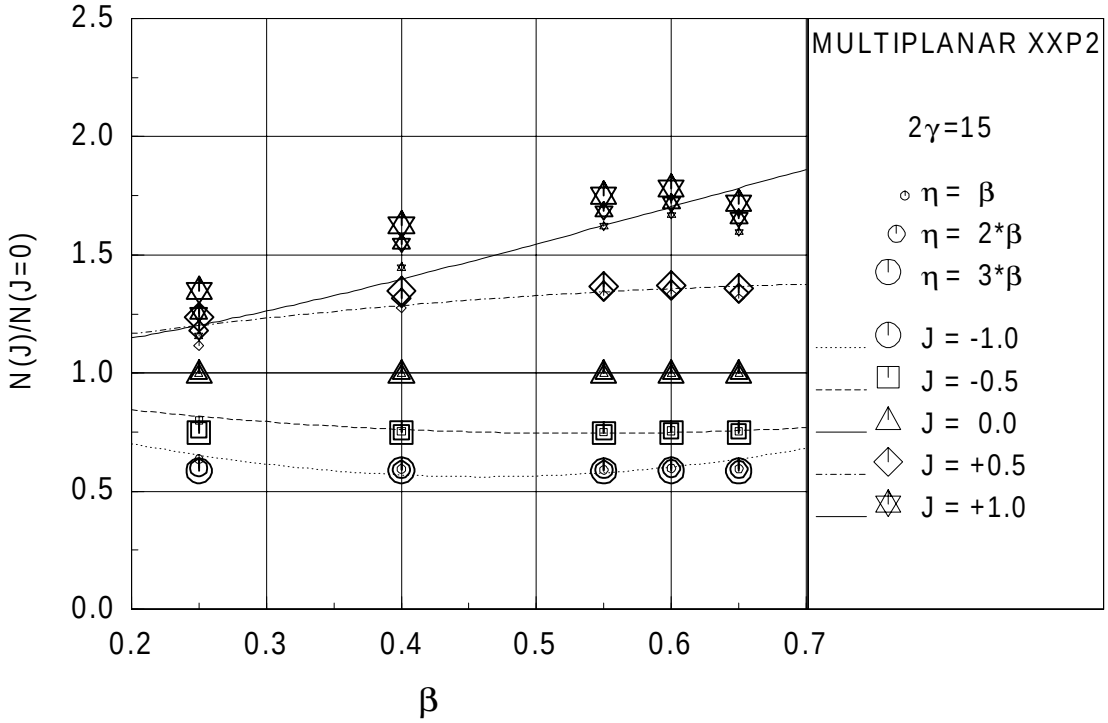

Figure 8.8 Results regression analysis for the multiplanar loading effects for $2\gamma=15$ (Eq. 8.12)

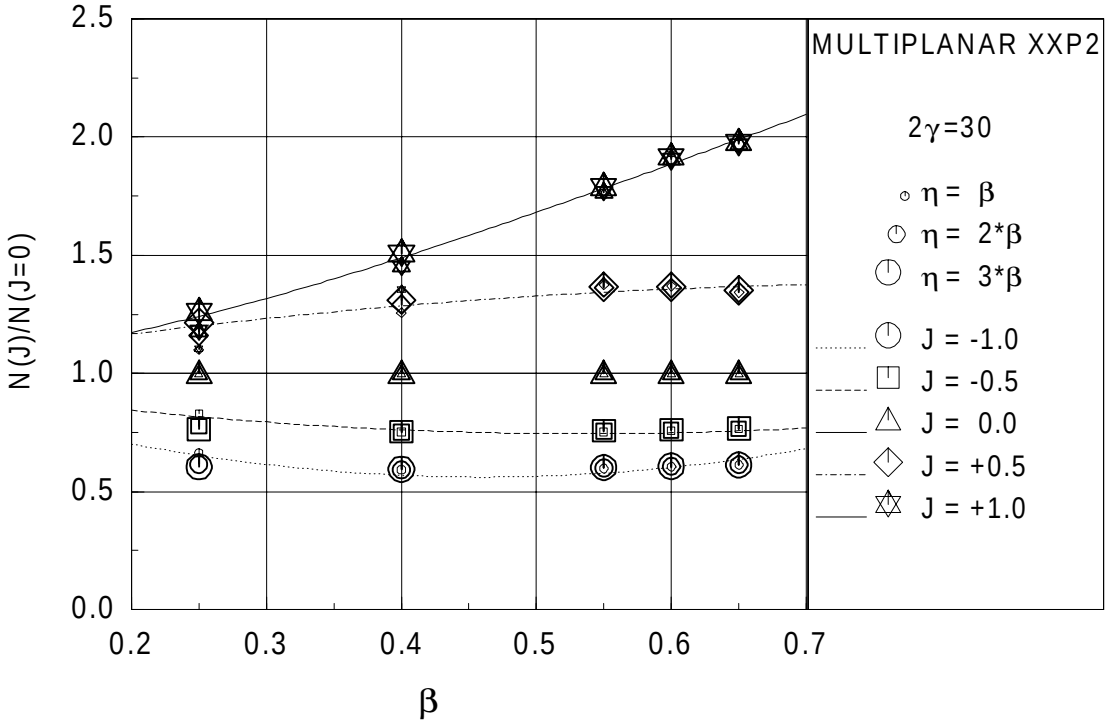

Figure 8.9 Results regression analysis for the multiplanar loading effects for 2γ=30 (Eq. 8.12)

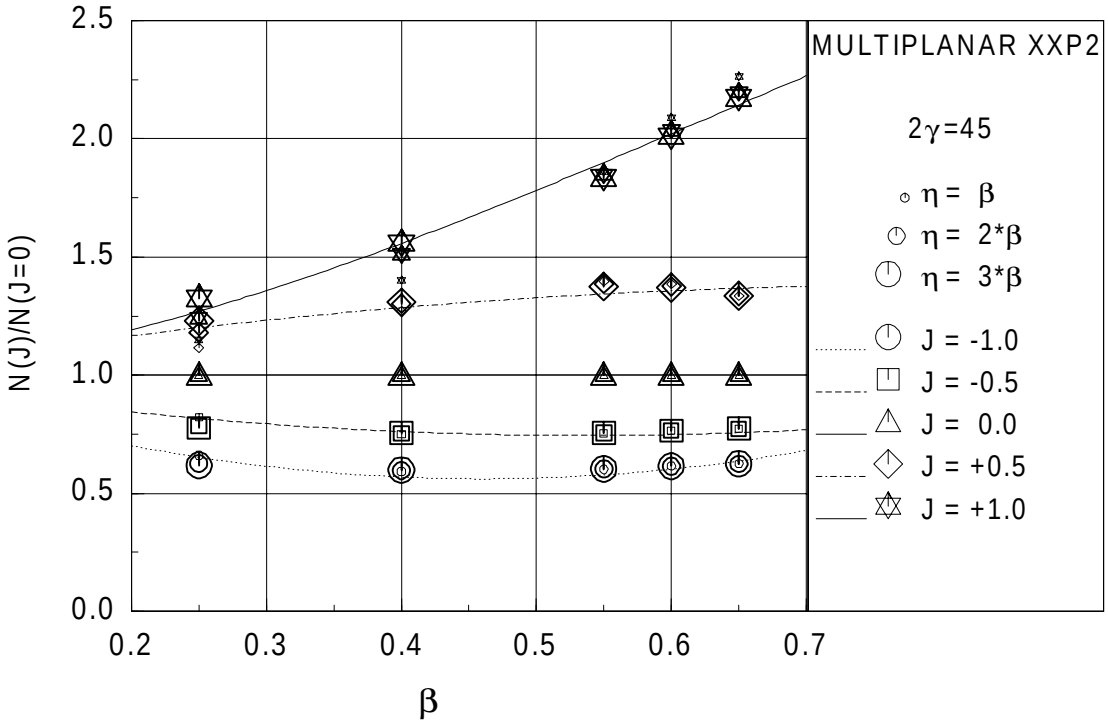

Figure 8.10 Results regression analysis for the multiplanar loading effects for 2γ=45 (Eq. 8.12)

8.6 I-beam to CHS column connections under in-plane bending

8.6.1 Uniplanar connections

The regression model for the uniplanar I-beam to CHS column connections under in-plane bending moments is based upon the ring model as described in chapter 7.3 (Eq. 7.22) and the effective length of the ring as given by Eq. 8.1, resulting in:

$$\frac{M_u}{t_0^2\ f_{y,0}\ h_m} = \frac{R_1 \cdot \gamma^{\ R_2 \cdot \beta - R_3 \cdot \beta^2}}{1-\beta+\sqrt{(1-\beta)^2 + \frac{2(2-\beta^2)}{2 \cdot \gamma^{R_4}}}} \tag{8.16}$$

Table 8.9 Results of the regression analyses for in-plane bending

R_1	R_2	R_3	R_4	r^2	COV	F	DOF
4.90	1.23	1.13	1.0	0.98	0.045	233	19

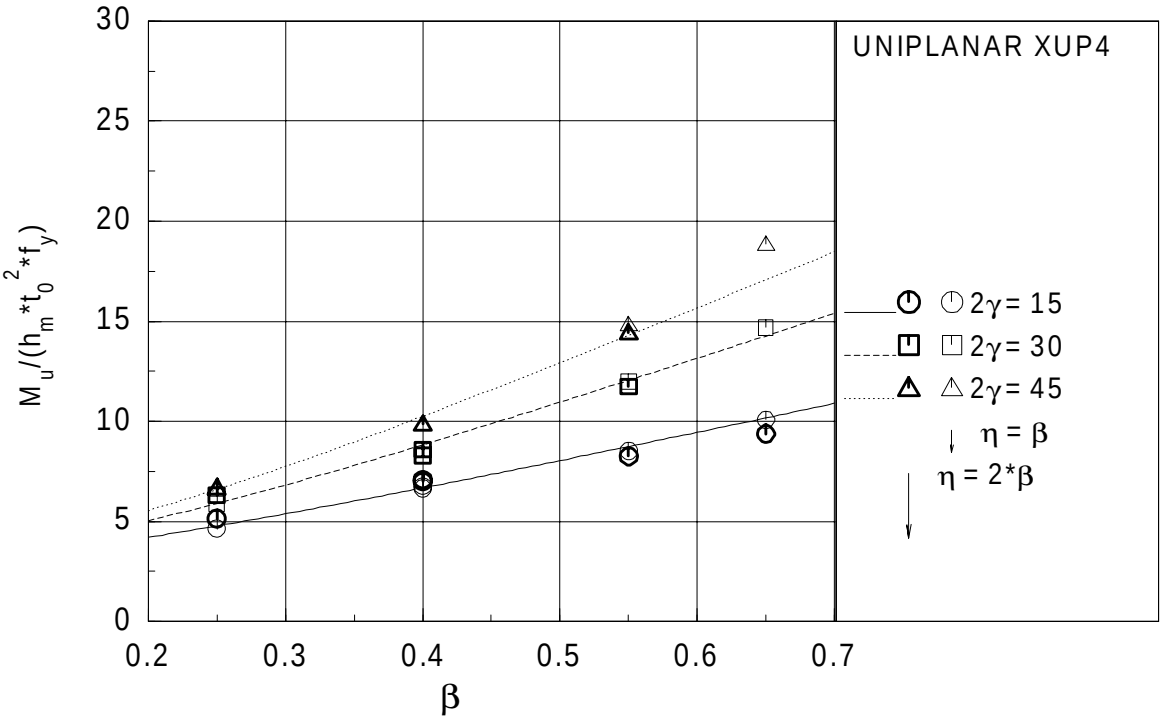

Figure 8.11 Results regression analysis for uniplanar I-beam to CHS column connections loaded with in-plane bending moments (Eq. 8.16)

8.6.2 Multiplanar connections

The regression model for the uniplanar loaded multiplanar I-beam to CHS column connections under in-plane bending moments is based upon the ring model as described in chapter 7.4 (Eq. 7.23) and the effective length of the ring as given by Eq. 8.1:

$$\frac{M_u}{t_0^2\ f_{y,0}\ h_m} = \frac{R_1 \cdot \gamma^{\ R_2 \cdot \beta - R_3 \cdot \beta^2}}{\sqrt{1-\beta^2} - \beta + \sqrt{\left(\sqrt{1-\beta^2} - \beta\right)^2 + \frac{4}{2 \cdot \gamma^{R_4}}}} \tag{8.17}$$

Table 8.10 Results of the regression analyses for in-plane bending with load ratio J=0

R_1	R_2	R_3	R_4	r^2	COV	F	DOF
4.89	1.33	1.66	1.0	0.99	0.035	581	19

As shown in Table 8.10 and Figure 8.12, a good agreement is achieved between the finite element results and the regression model.

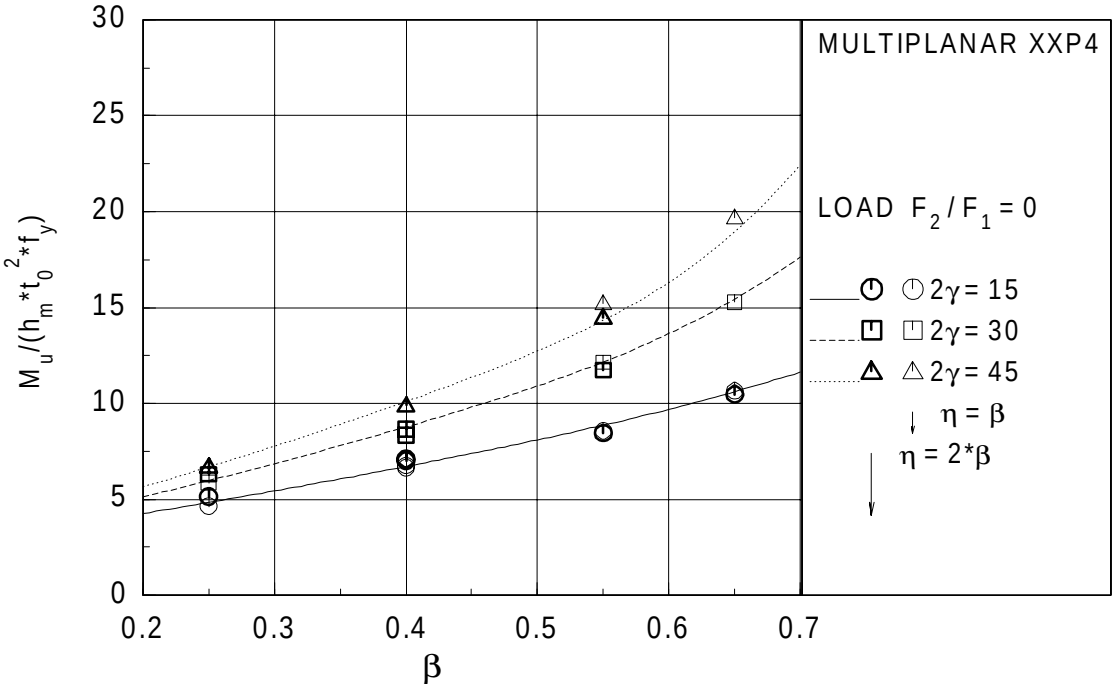

Figure 8.12 Results regression analysis for multiplanar I-beam to CHS column connections loaded with in-plane bending moments for load ratio J = 0 (Eq. 8.17)

The multiplanar loading effect is empirically determined and described by Eq. 8.18:

$$\frac{M_u}{M(J=0)} = 1 + J(1 + \beta + R_6 \cdot \beta^2 - (2\gamma)^{R_7}) + J^2(R_8 \cdot \beta + R_9 \cdot \beta^2) \qquad (8.18)$$

From the data can be concluded, that there is a significant interaction between the 2γ-ratio and the load ratio, therefore this influence is also included in the regression model. This interaction between the load ratio and the 2γ-ratio can also be theoretically be explained from the ring model, see e.g. Eq. 7.25. The results of the regression analyses are shown in Table 8.11 and Figures 8.13 to 8.15.

Table 8.11 Results of the regression analyses for in-plane bending, multiplanar loading effects

R_6	R_7	R_8	R_9	r^2	COV	F	DOF
-0.372	0.0567	-0.430	0.456	0.912	0.045	299	114

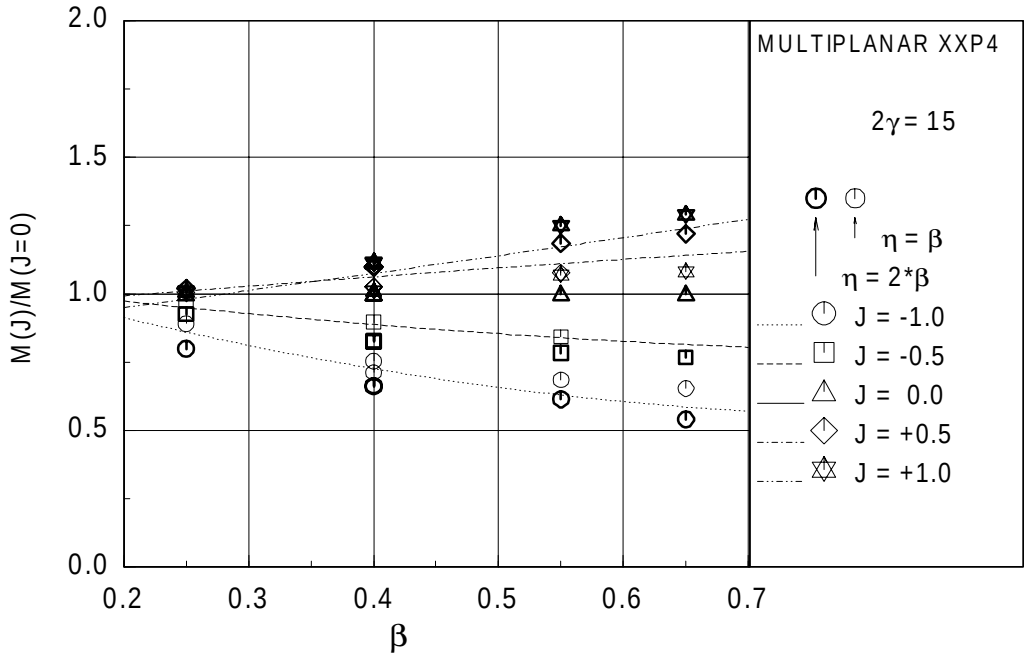

Figure 8.13 Results regression analysis for multiplanar I-beam to CHS column connections loaded with in-plane bending moments for 2γ=15, multiplanar loading effects (Eq. 8.18)

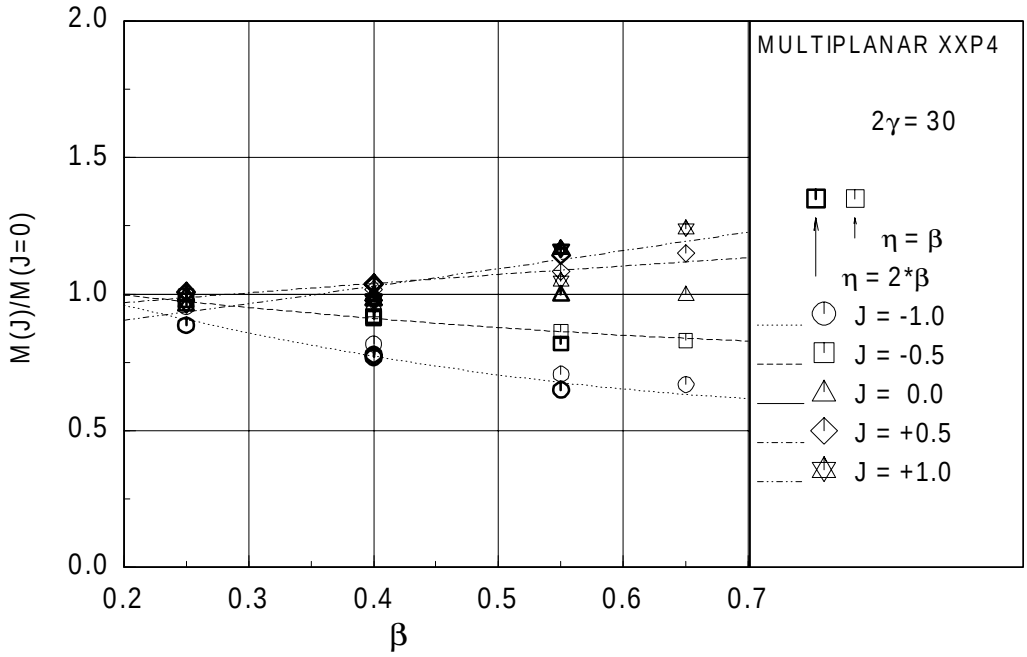

Figure 8.14 Results regression analysis for multiplanar I-beam to CHS column connections loaded with in-plane bending moments for 2γ=30, multiplanar loading effects (Eq. 8.18)

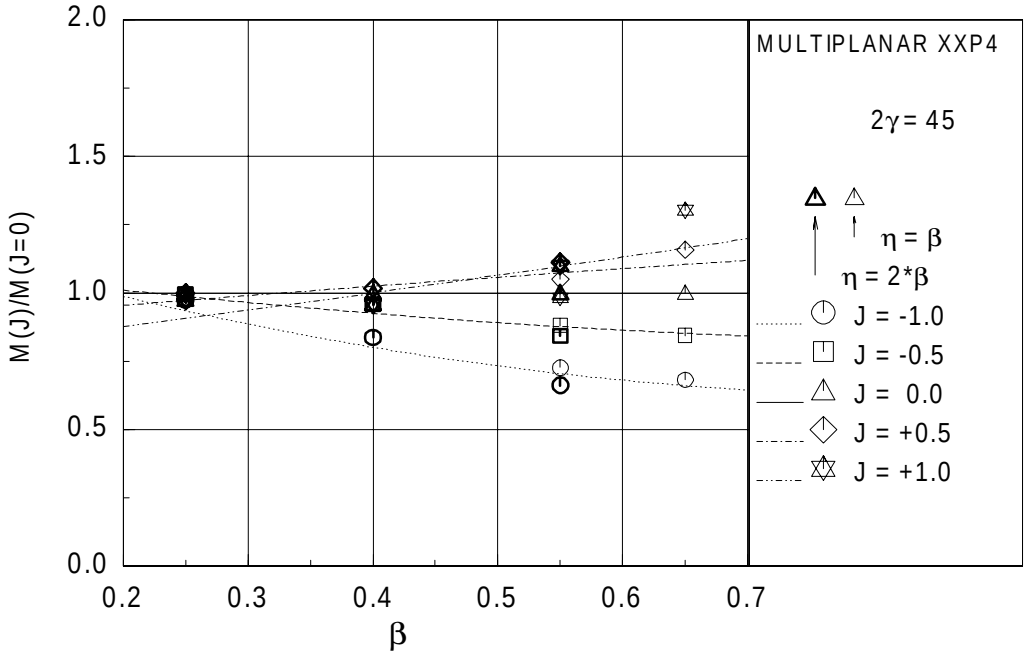

Figure 8.15 Results regression analysis for multiplanar I-beam to CHS column connections loaded with in-plane bending moments for 2γ=45, multiplanar loading effects (Eq. 8.18)

8.6.3 Influence of pre-stress on the column on the connection strength

The influence of a pre-stress on the column is only determined for the uniplanar I-beam to CHS column connections. The pre-stress function, which describes the influence of the pre-stress on the column on the connection strength cannot be determined theoretically for the investigated connections. It is clear, that if the pre-stress on the column is equal to the yield strength, there is almost no bearing capacity left, since the column fails due to the pre-stress. To be able to determine the influence of the pre-stress, all data points are divided by the correspondent data point without pre-stress.

The pre-stress function is empirically determined and given in the following formula:

$$f(n) = 1 - n^2(\beta - \beta^2) * (2\gamma)^{R_1} \tag{8.19}$$

where n is the ratio between the axial load on the column and the squash load of the column.

The results of the regression analysis are shown in Table 8.12 and Figures 8.16 to 8.21. There is a good agreement between the finite element results and the regression model, despite the fact that the regression formula has only one regression constant.
There is almost no interaction between the pre-stress and the η-ratio, therefore the data points with the same β-ratio, 2γ-ratio, τ-ratio and the ratio of the pre-stress, but a different η-ratio overlap completely in the figures. The largest influence on the pre-stress is found for β=0.50. The reduction in connection strength is larger for larger 2γ-ratios, which could be expected, because the stability of the column wall becomes smaller if the wall thickness of the column decreases.

Table 8.12 Results of the regression analyses for pre-stress effects

R_1	r^2	COV	F	DOF
0.303	0.96	0.045	2245	94

Equation 8.19 can also be based upon the total axial load in the column:

$$f(n') = 1 - (n')^2(\beta - \beta^2) * (2\gamma)^{R_1} \qquad (8.20)$$

were n' is the ratio between the total axial load in the column and the squash load of the column.

Using this equation, the regression results thus obtained are shown in Table 8.13.

Table 8.13 Results of the regression analyses for pre-stress effects, based upon the total axial load in the column

R_1	r^2	COV	F	DOF
0.277	0.96	0.046	2010	94

If the results of Tables 8.12 and 8.13 are compared, it can be concluded that there is only a minor difference in the results. Since the results of these regression models are almost the same, the results of Eq. 8.20 are not shown graphically.

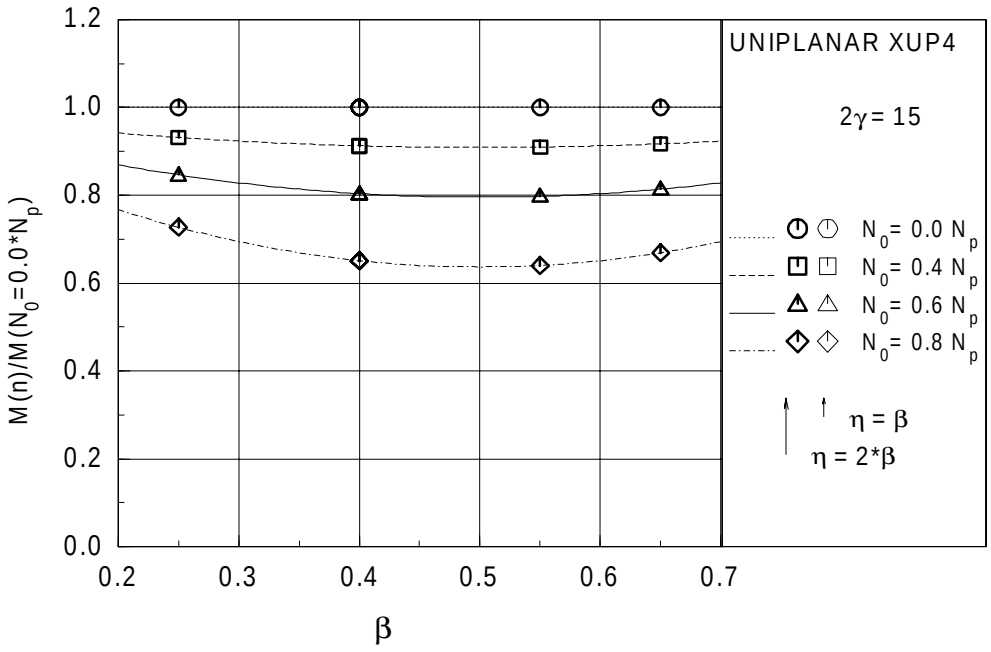

Figure 8.16 Results regression analysis, influence pre-stress on the connection strength for 2γ=15 (Eq. 8.19)

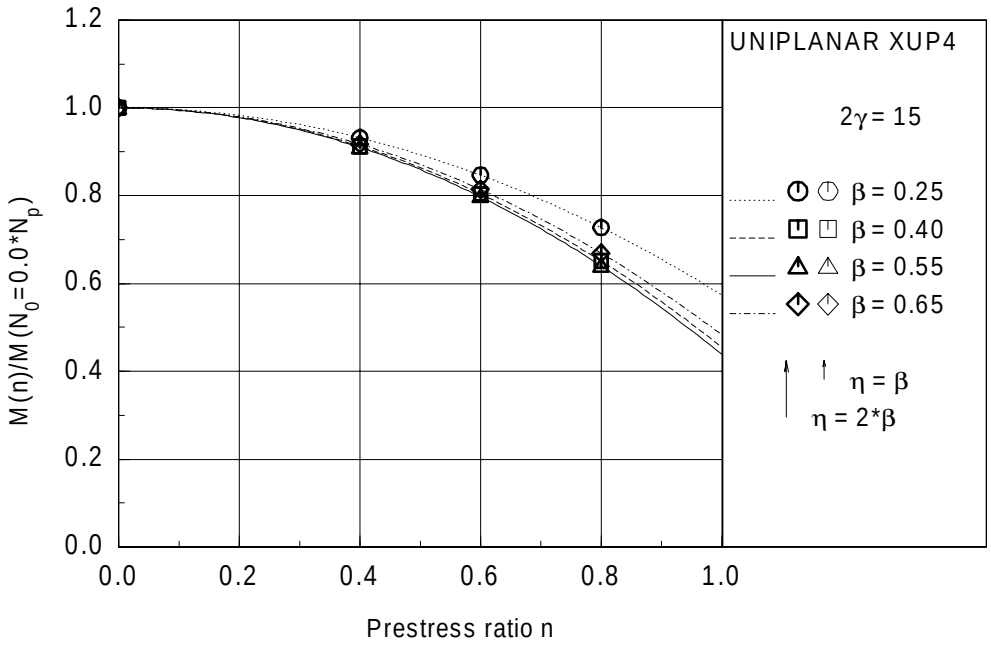

Figure 8.17 Results regression analysis, influence pre-stress on the connection strength for 2γ=15 (Eq. 8.19)

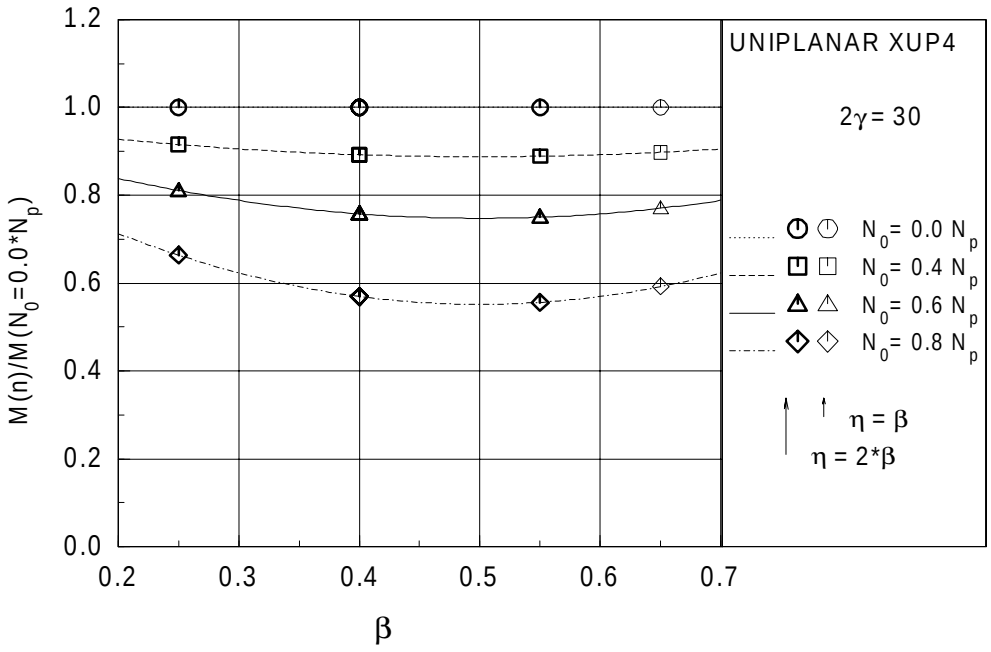

Figure 8.18 Results regression analysis, influence pre-stress on the connection strength for 2γ=30 (Eq. 8.19)

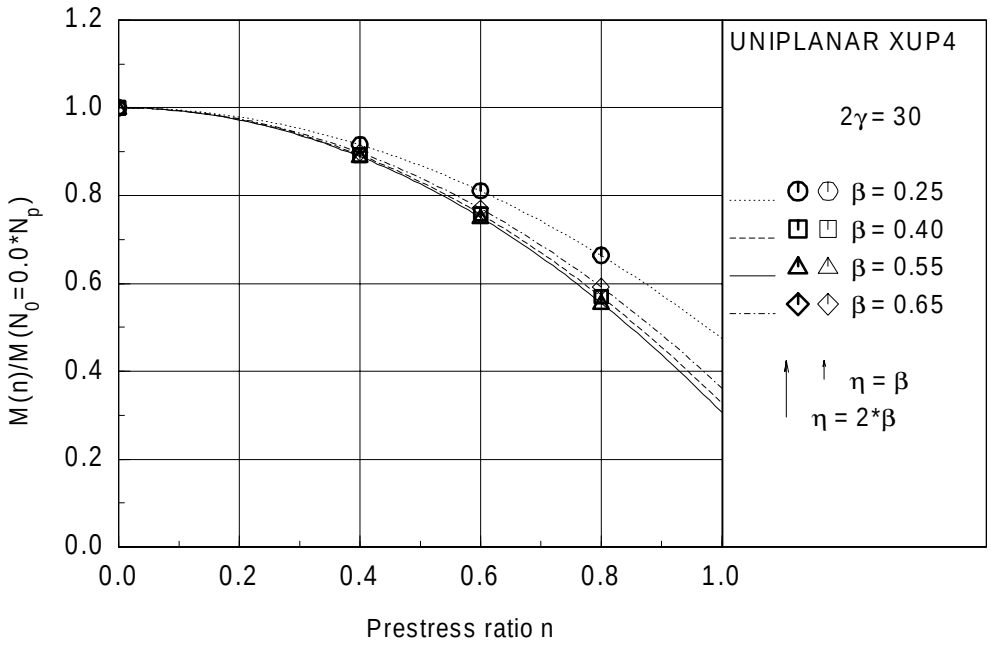

Figure 8.19 Results regression analysis, influence pre-stress on the connection strength for 2γ=30 (Eq. 8.19)

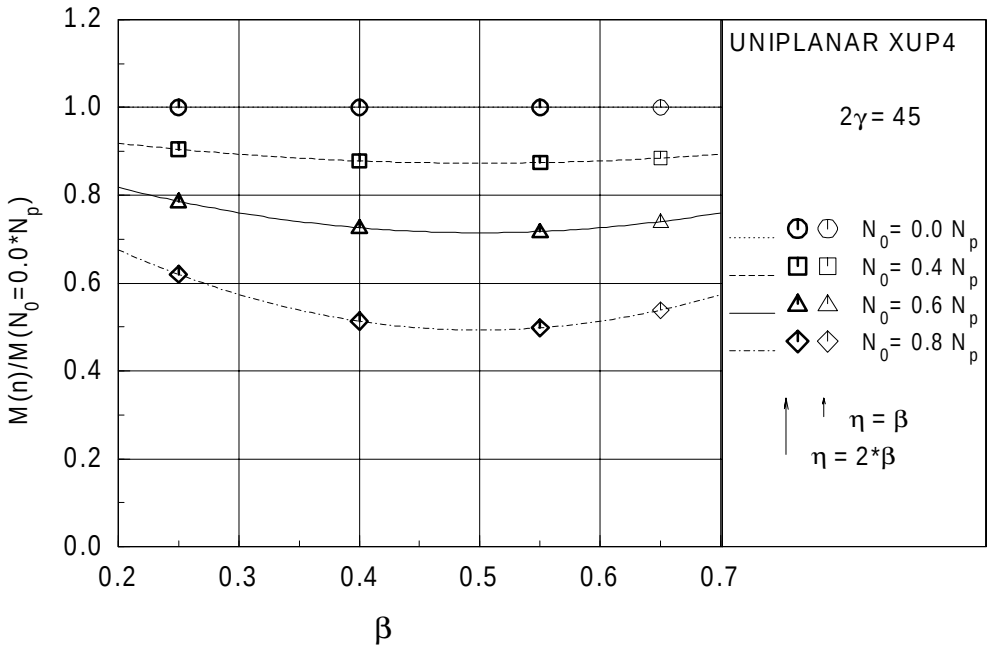

Figure 8.20 Results regression analysis, influence pre-stress on the connection strength for 2γ=45 (Eq. 8.19)

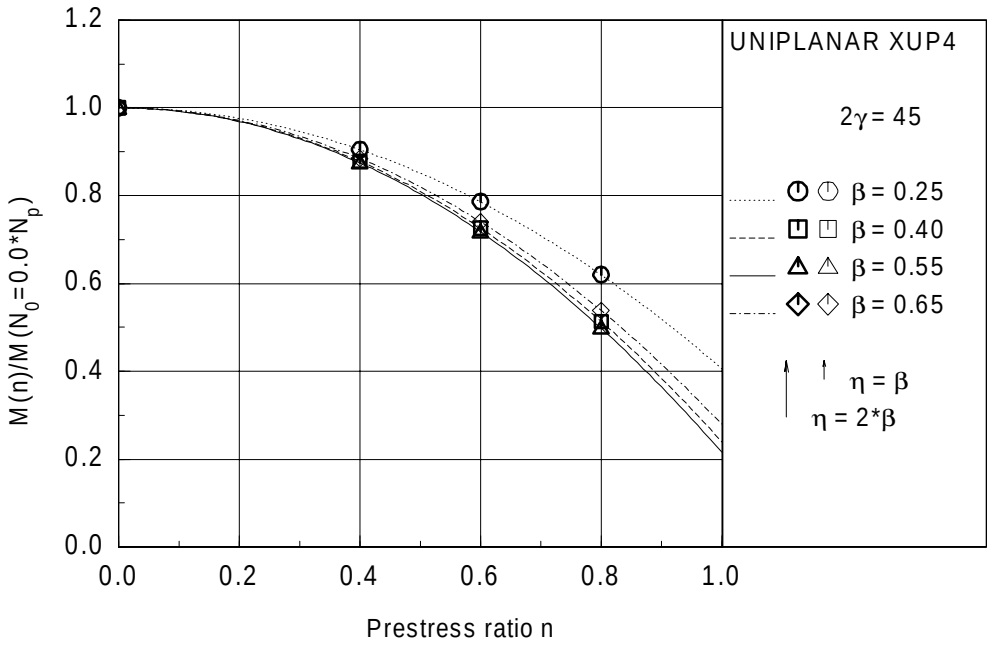

Figure 8.21 Results regression analysis, influence pre-stress on the connection strength for 2γ=45 (Eq. 8.19)

9 COMPARISON WITH EXISTING EVIDENCE

9.1 General

Little experimental evidence is available for the comparison with the obtained strength formulae.
A limited number of experimental tests on uniplanar plate to CHS column connections under axial loading and uniplanar I-beam to CHS column connections under axial loading or in-plane bending were carried out in Japan. All these test results can be found in Chapter 2. All existing design formulae for this type of connections are based upon these experiments. The most recent design formulae are given in the CIDECT design guide [11] and the AIJ design recommendations [1].

9.2 Plate to CHS column connections under axial loading

The basic formula for uniplanar plate to circular column connections under axial loading can be found in the CIDECT design guide [11] (Eq.2.8).

The CIDECT [11] formula is:

$$\frac{N_{R.d}}{t_0^2 \, f_{y,0}} = \frac{5}{1-0.81\beta} \qquad (9.1)$$

This formula is based upon Togo's (simple) ring model. The formulae proposed by Wardenier [19] (Eq. 2.7) is the same except for rounding off the figures. The formula proposed by Makino [45] (Eq. 2.6) is also the same, but gives the (mean) ultimate strength and not the design strength. In the formula given in the AIJ recommendations [1] (Eq. 2.5), the influence of the column diameter to wall thickness ratio is added to the strength formula. The formula of the AIJ recommendation gives the allowable and maximum strength, according to the Japanese design code. All these formulae are based upon a limited amount of test data.
Van den Broek [12] has been carried out a limited parameter investigation including 4 finite element analyses on uniplanar plate to CHS column connections loaded with axial compression load (see section 2.3). All design and strength formulae and test and numerical data for plate to CHS column connections loaded with axial loading are compared in Figures 9.1 and 9.2 with Eq. 8.5 as derived in Chapter 8.
As can be concluded from Figures 9.1 and 9.2, the experimental data points are higher than the derived strength formula (marked as de Winkel). The test specimens of these tests have fillet welds, which cause usually somewhat higher strengths than comparable specimens with butt welds, especially because the specimens were relatively small in size and therefore the

weld sizes were relatively large.

The formulae proposed by Wardenier and given by the CIDECT design guide are close to the formulae (for $2\gamma=30$) as derived in Chapter 8. However, the formulae by Wardenier and CIDECT lack the 2γ-ratio influence.

In Figure 9.3, Eq. 8.5 is compared with the finite element results of Van der Broek (see Table 2.2).

These finite element results give approximately 2-10% lower values than Eq. 8.5.

The finite element results of Van der Broek on multiplanar axially loaded multiplanar plate to CHS column connections are compared with the combined Eq. 8.6 and 8.7 in Figure 9.4.

Also this finite element results are somewhat lower than the results of Eq. 8.6 and 8.7.

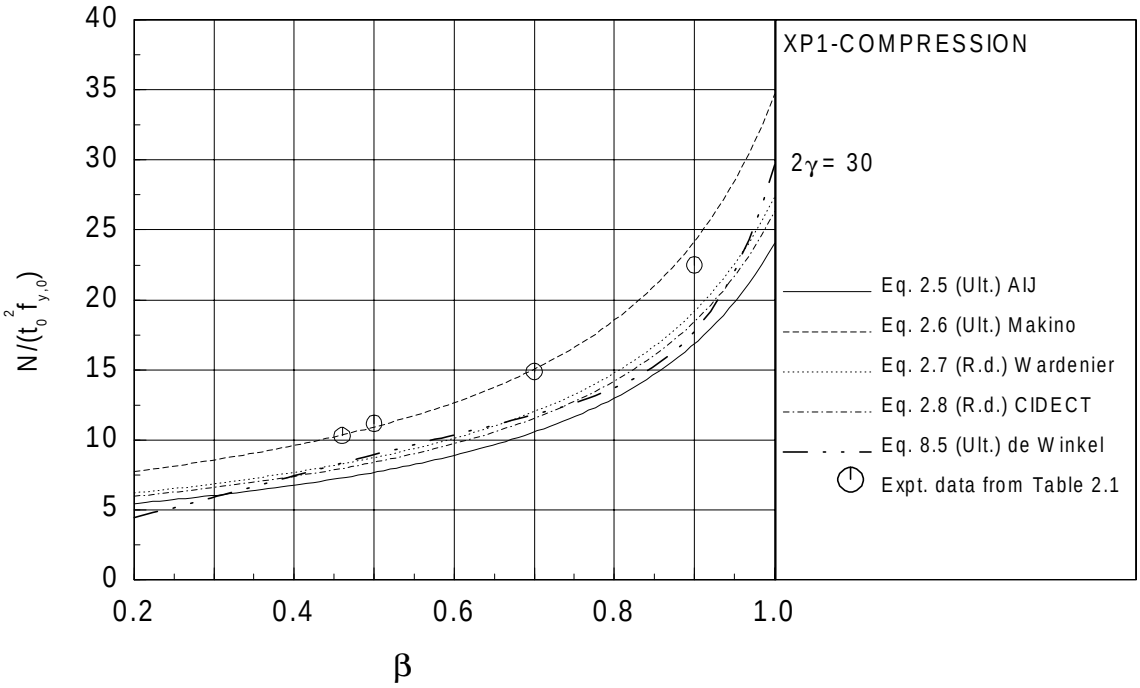

Figure 9.1 Comparison strength formulae with test and finite element results for Uniplanar Plate to CHS column connections loaded with axial loading

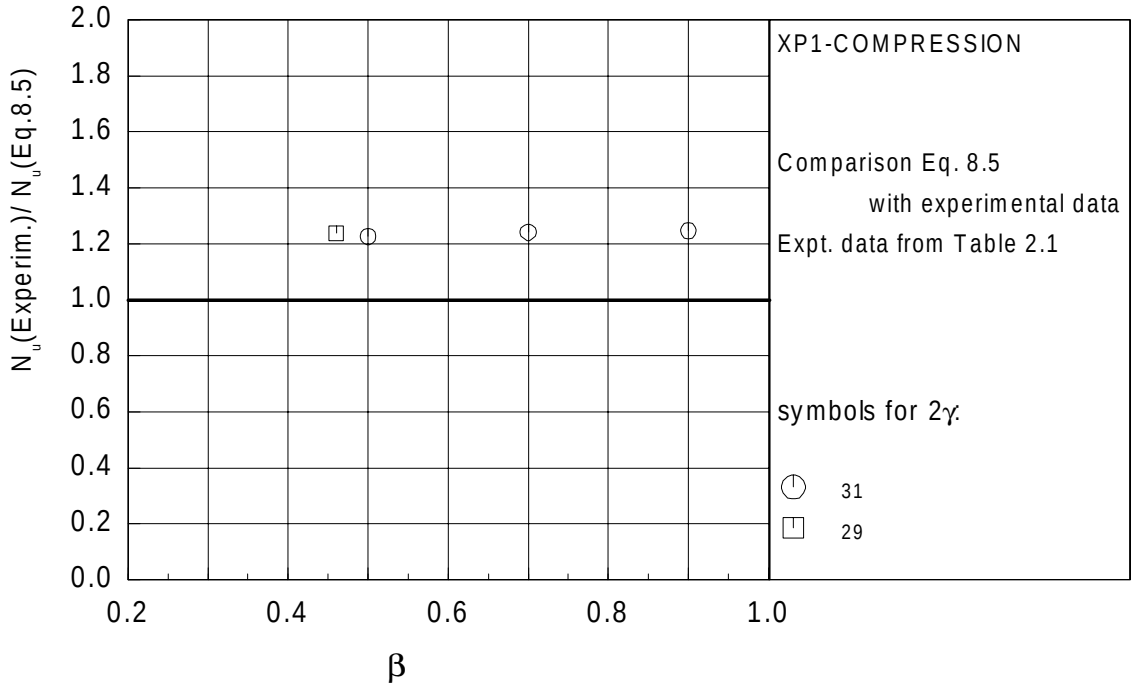

Figure 9.2 Comparison strength formula Eq. 8.5 with test results for Uniplanar plate to CHS column connections under axial loading

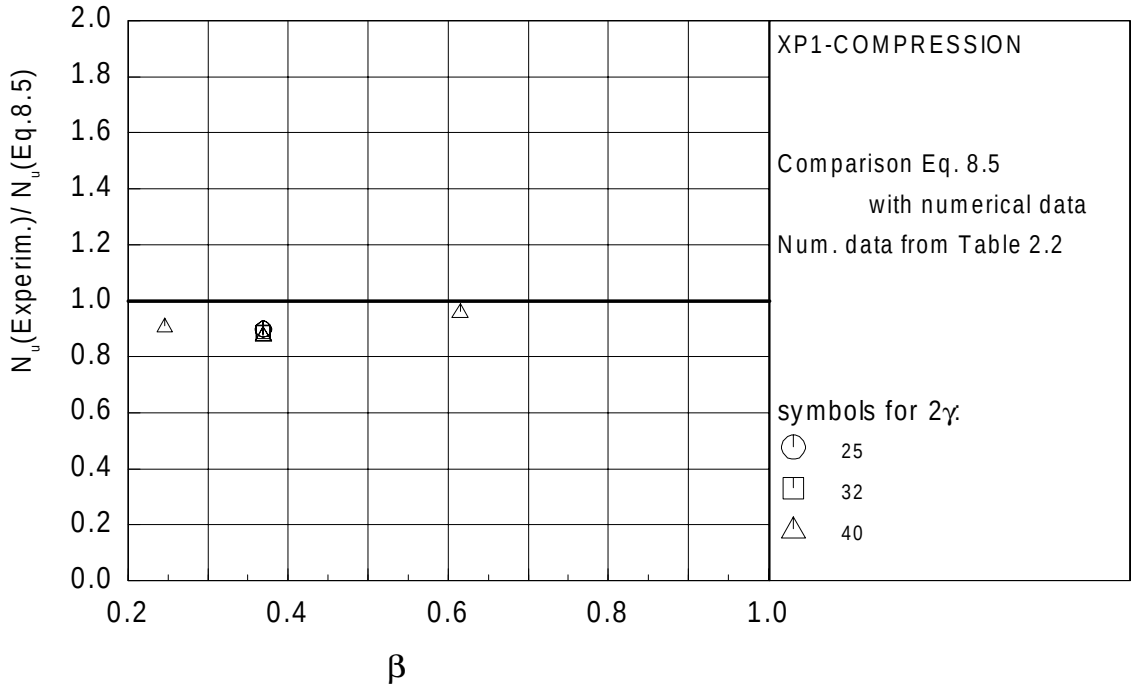

Figure 9.3 Comparison of the strength formula Eq. 8.5 with existing numerical results (see Table 2.2) for Uniplanar plate to CHS column connections under axial loading

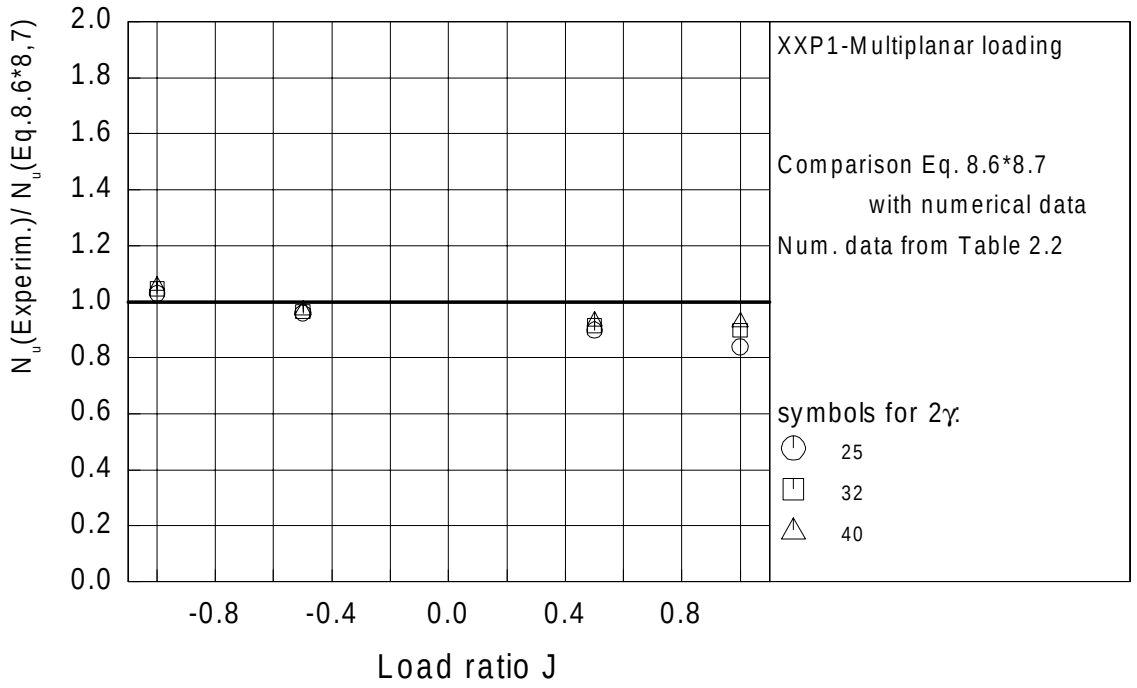

Figure 9.4 Comparison of the combined strength formula Eq. 8.6 and 8.7 with the existing numerical results (see Table 2.2) for Multiplanar plate to CHS column connections under axial loading

9.3 Uniplanar I-beam to CHS column connections under axial compression load

For axially loaded I-beam to CHS column connections, only 6 Japanese experimental test results are available for comparison with the strength formulae derived in Chapter 8. The strength formula for this connection type and loading can be obtained from Chapter 8 by combining the strength formulae of the separate influences. The influences are the flange (Eq. 8.5), the distance between the two flanges (Eq. 8.8) and the presents of the web (Eq. 8.10). The total connection strength is obtained by the product of these three equations.
In Figure 9.5, the comparison is made between the combined strength formulae with the experimental data. As can be concluded, there is a good agreement between the experimental data and the combined strength formulae. Note that only a small range of β-ratio's is covered by the tests.

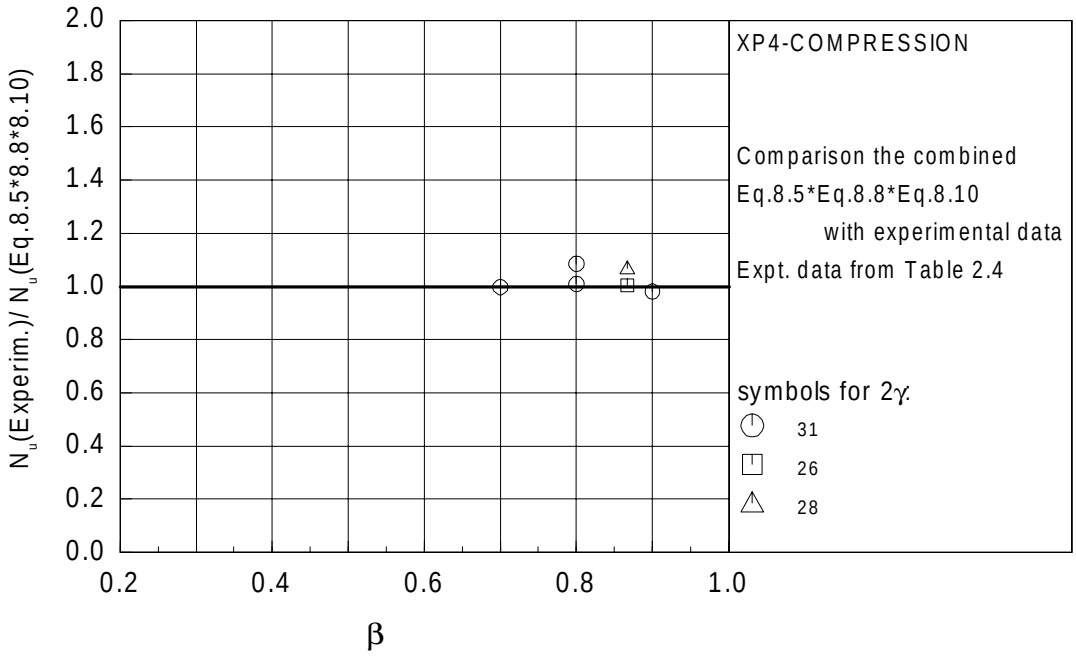

Figure 9.5 Comparison combined strength formula Eq. 8.5, Eq.8.8 and Eq. 8.10. with test results for Uniplanar I-beam to CHS column connections loaded under axial compression loading

9.4 Uniplanar I-beam to CHS column connections under in-plane bending

A simple formula for the connection strength for I-beam to CHS column connections under compression loading is given by the CIDECT design guide [11] (Eq.2.39):

$$\frac{M_{R.d}}{t_0^2 \, f_{y,0} \, h_1} = \frac{5}{1 - 0.81\beta} \qquad (9.2)$$

As can be seen, no 2γ influence is included in this formula. This formula is equal to Eq. 9.1, except that the beam height is added in the formula.

No experimental tests were carried out on uniplanar connections in the framework of this research there are. However, in Japan 5 experimental tests were done by Togo and published by Washio [52], 2 tests by Makino et al [46] and 2 additional tests were obtained from the database collected by Kamba [35] (see Table 2.4). Note that all test specimens have relatively thin walled column sections and there is only a small range of β-values covered by the tests. As shown in Figures 9.6 and 9.7, the experimental tests are in reasonable agreement with the derived strength formula. In Figure 9.6, the curves are shown according to the available design and strength formulae, listed in Section 2.6.3.
The formula (Eq. 8.16) from Chapter 8 is shown for $2\gamma=30$, $2\gamma=40$ and $2\gamma=50$; the formula from the AIJ recommendations (Eq. 2.39) is only shown for $2\gamma=30$.
One test with $\beta=0.832$ gives a much lower strength than could be expected.
The CIDECT Design Guide strength formula is conservative for all tests.
In Figure 9.7, a comparison is made between Eq. 8.16 and the experimental data from Table 2.4. Although there is some scatter of the experimental data, there is a reasonable agreement between the experiments and Eq. 8.16, except for the test result for $\beta = 0.832$.

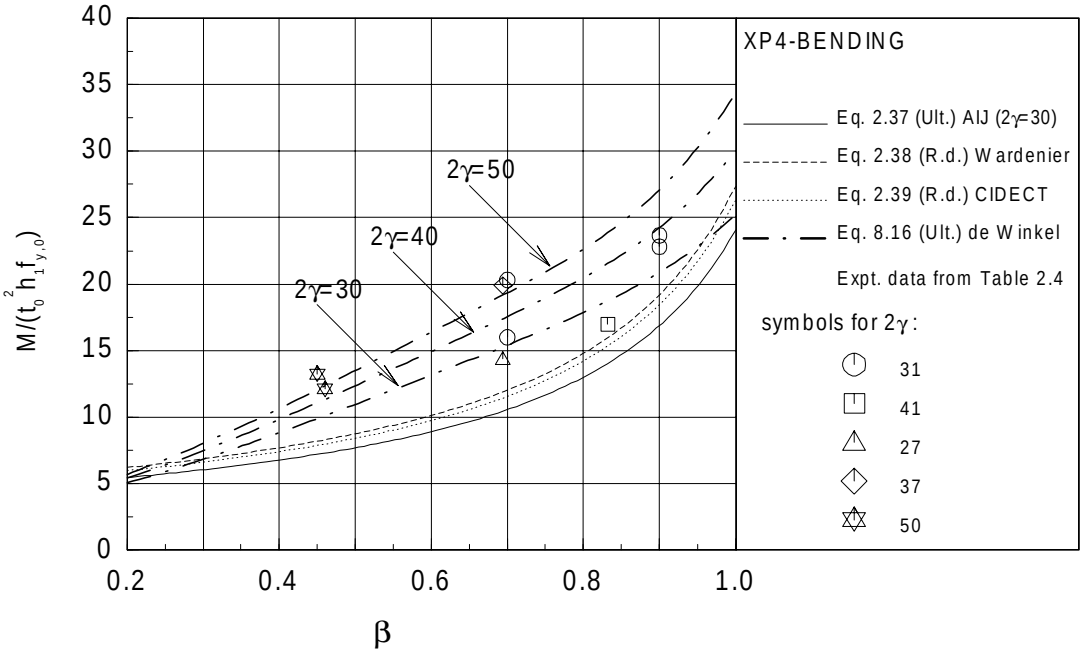

Figure 9.6 Comparison of the strength formulae with existing test results for Uniplanar I-beam to CHS column connections loaded with in-plane bending moments

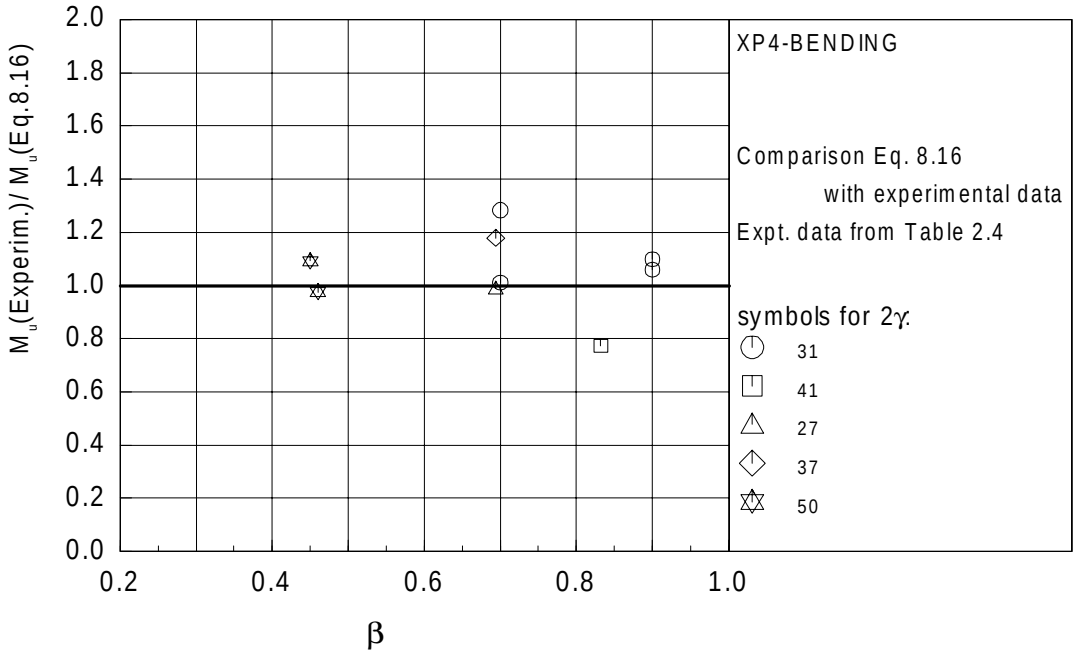

Figure 9.7 Comparison of the strength formula Eq. 8.16 with existing test results for Uniplanar I-beam to CHS column connections loaded with in-plane bending moments

10 SUMMARY AND CONCLUSIONS

10.1 Introduction

This research provides information on the static behaviour of plate to CHS column connections and I-beam to CHS column connections. Also, the static behaviour of bolted I-beam to CHS column connections in combination with a composite floor has been investigated and reported.

The deliverables of this research are:

- The finite element models of the investigated connections, calibrated with experimental tests.
- The static behaviour of the investigated connections in the form of load-displacement and moment-rotation curves for a wide range of geometrical parameters and load cases based upon finite element results.
- The failure modes of the investigated connections (except cracking, which is not covered in the finite element models).
- An analytical description of connection behaviour based upon the ring model
- Formulae, which can predict the strength of the investigated connections for a wide range of parameters, that can form the bases for future design codes, like EUROCODE 3.

10.2 General conclusions

The experimental tests have provided sufficient information for the calibration of the finite element models. This information consisted of failure modes, load-deformation curves, visual observations and additional displacement and strain measurements. With the accurately measured dimensions and material properties of the test specimens, a good agreement could be established between the measured data and the finite element results.
The calibration study has shown that the finite elements models, using thick shell elements with eight nodes and taking into account the stress-strain curves including strain hardening, can simulate the experiments accurately. Also, the behaviour of the bolted connections in combination with the composite steel floor could be simulated using thick shell elements. In these models the composite floor was simulated with layered composite elements with smeared concrete cracking and reinforcement bar yielding. The bolted connections were modelled using gap elements in combination with spring elements, in order to be able to simulate slipping of the bolts.

Based upon the analytical ring model strength formulae have been set up. These strength formulae were calibrated with the finite element results using non-linear regression analyses. Generally, a good agreement could be found between the strength formulae and finite element results.

10.3 Conclusions on the welded plate and I-beam to CHS column connections

In the experiments, all welded connections without a concrete filled column show a ductile behaviour. All these connections failed due to column plastification. Only minor cracks were observed in the column wall near the edges of the tension loaded plates or flanges. The specimens with a concrete filled column loaded in tension failed by punching shear; the cracks grow in the column wall at the edges of the plates or flanges in axial direction of the tubes.
The specimens with a concrete filled column loaded in compression failed by local plastic buckling of the plates under compression. No local deformation of the column wall was observed.
The influence of the plate width to column diameter ratio β, the column diameter to column wall thickness ratio 2γ and the load ratio J on the strength capacity was for all connections found to be in agreement with that found in the analytical ring model:

larger β: larger non-dimensional strength
larger 2γ: larger non-dimensional strength, this effect becomes stronger for larger β-ratios and also for positive load ratios
J>0 : larger non-dimensional strength
J<0: smaller non-dimensional strength

In addition, from the finite element results the following could be concluded:

A larger beam height to column diameter ratio η gives an significant increase of the non-dimensional strength $\frac{N_u}{f_{y,0} \cdot t_0^2}$ in case of axial loading, but only a small increase of the non-dimensional strength $\frac{M_u}{f_{y,0} \cdot t_0^2 \cdot h_m}$ in case of in-plane bending. No significant interaction was found between the η-ratio and the load ratio J.

For the axially loaded connections, the web of the I-beams gives only a small increase in connection strength, due to some local stiffening of the column wall.

A pre-loading on the column reduces the strength of I-beam to CHS column connections loaded by in-plane bending moments.

The results obtained are summarised in Tables 10.1 to 10.4.

Table 10.1 Main results and conclusions for axially loaded plate to CHS column connections

<table>
<tr><td colspan="3">AXIALLY LOADED PLATE TO CHS COLUMN CONNECTIONS</td></tr>
<tr>
<td> 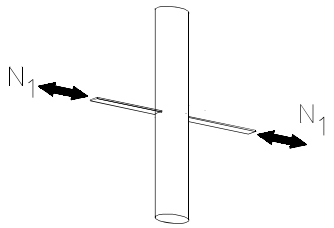
</td>
<td> 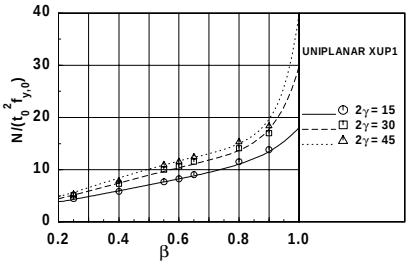
</td>
<td>Failure modes:
N in compression:
Chord face yielding
N in tension:
Chord face yielding + cracking after large deformation</td>
</tr>
<tr>
<td> 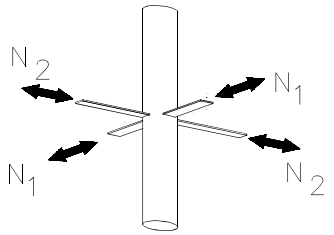

without concrete filled column
Load ratio J=N_2/N_1</td>
<td> 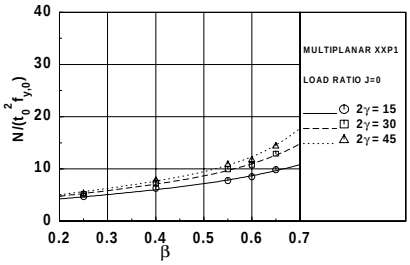

 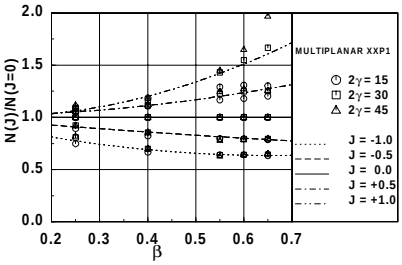
</td>
<td>Conclusions:
A positive load ratio (J=+1) increases the connection strength slightly.
A negative load ratio (J=-1) decreases the connection strength significantly.</td>
</tr>
<tr>
<td> 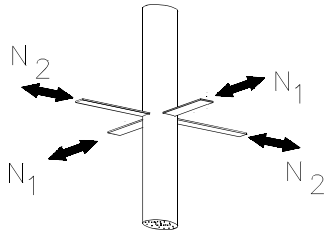

with concrete filled column</td>
<td> 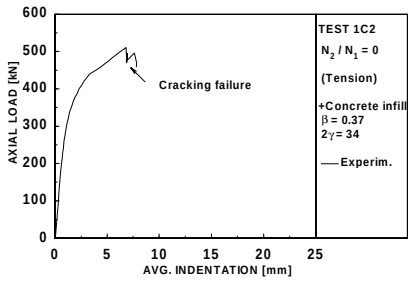
</td>
<td>Failure modes:
N in compression:
Plate yielding and local buckling of plate
N in tension:
Chord face yielding + cracking after large deformation</td>
</tr>
</table>

Table 10.2 Main results and conclusions for axially loaded I-beam to CHS column connections

<table>
<tr><td colspan="3">AXIALLY LOADED I-BEAM TO CHS COLUMN CONNECTIONS</td></tr>
<tr>
<td> 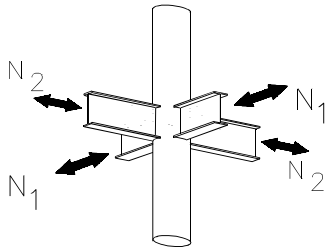

With web</td>
<td> 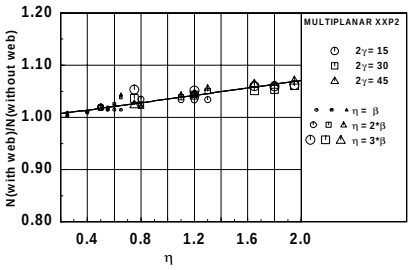
</td>
<td>Failure modes:
N in compression:
Chord face yielding
N in tension:
Chord face yielding + cracking after large deformation</td>
</tr>
<tr>
<td> 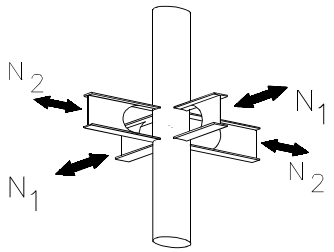

Without web</td>
<td> 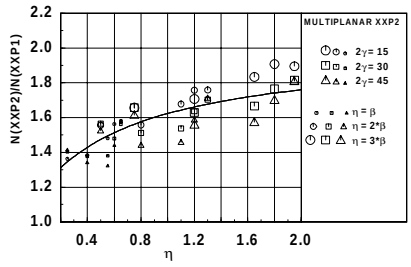

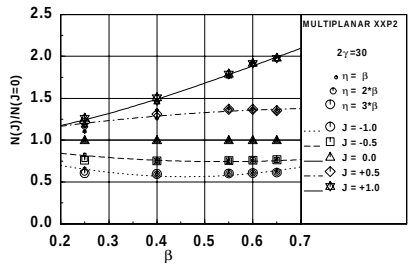
</td>
<td>Conclusions:
A positive load ratio (J=+1) increases the connection strength slightly.
A negative load ratio (J=-1) decreases the connection strength significantly.</td>
</tr>
<tr>
<td> 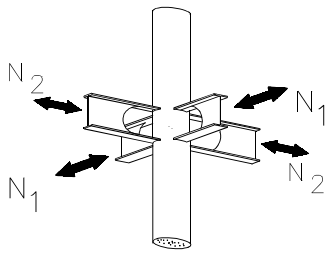

with concrete filled column</td>
<td> 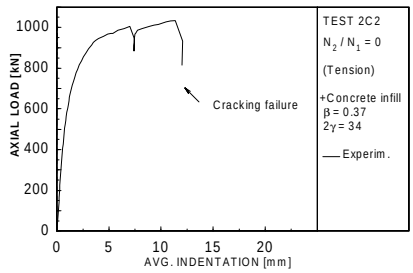
</td>
<td>Failure modes:
N in compression:
Plate yielding and local buckling of plate
N in tension:
Chord face yielding + cracking after large deformation</td>
</tr>
</table>

Table 10.3 Main results and conclusions for I-beam to CHS column connections loaded with in-plane bending moments

<table>
<tr><td colspan="3">I-BEAM TO CHS COLUMN CONNECTIONS LOADED WITH IN-PLANE BENDING MOMENTS</td></tr>
<tr><td> 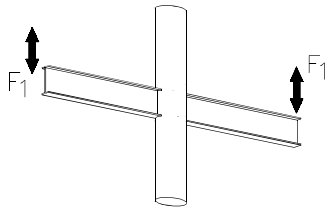

Uniplanar connection</td><td> 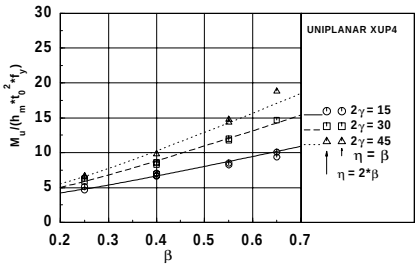
</td><td rowspan="2">Failure modes:
Chord face yielding

Conclusions:
Uniplanar and multiplanar connections have the same strength for small β-ratios.
For β>0.55 the strength of multiplanar connections is higher.
A positive load ratio (J=+1) increases the connection strength slightly.
A negative load ratio (J=-1) decreases the connection strength significantly. This effect becomes more significantly for larger 2γ ratios.</td></tr>
<tr><td> 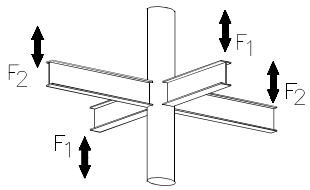

Multiplanar connection</td><td> 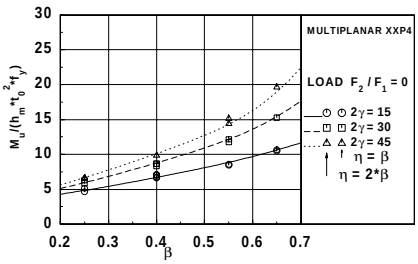

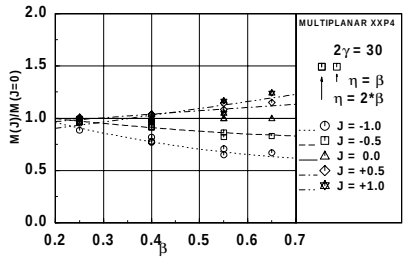
</td></tr>
<tr><td> 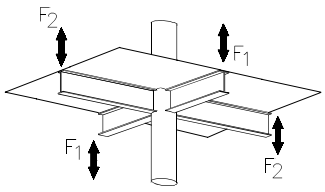

with steel floor</td><td> 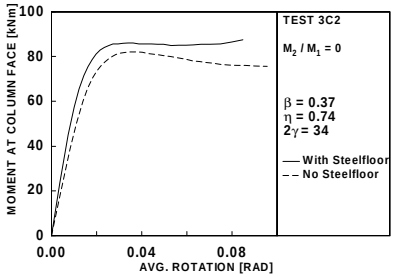
</td><td>Conclusions:
The presents of a steel floor increases the connection strength and stiffness slightly.</td></tr>
</table>

Table 10.4 Main results and conclusions for I-beam to CHS column connections loaded with in-plane bending moments and a pre-loading on the column

I-BEAM TO CHS COLUMN CONNECTIONS LOADED WITH IN-PLANE BENDING MOMENTS AND A PRE-LOADED COLUMN		
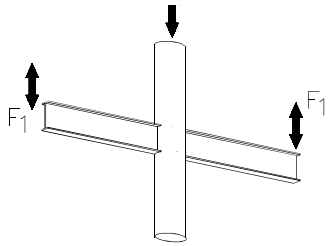 Uniplanar connection with pre-loaded column	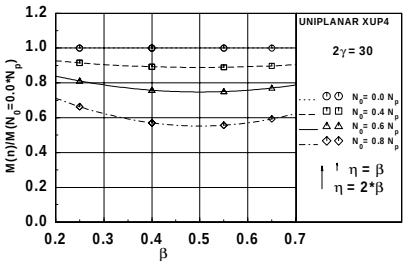 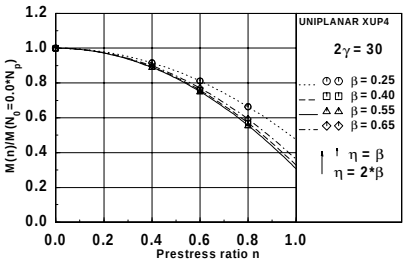	**Failure modes:** Chord face yielding Chord face buckling for large 2γ-ratio's in combination with a large pre-loading. **Conclusions:** Pre-loading of the column decreases the connection strength significantly. This effect agrees with that of tubular joints.

10.4 Conclusions on the bolted I-beam to CHS column connections with a composite concrete floor

All tested specimens with the composite floor failed by progressive failure of the reinforcement bars. The asymmetric failure of the composite floors caused a maximum load at testing, which was lower than the corresponding plastic capacity the reinforcement bars of the connection. Due to the high stiffness of the connection, the measured stiffness was significantly effected by the slip in the bolted connections between the lower flanges and the ring plates. This effect was investigated using the finite element model. The deformations of the tubular column and ring plates after testing were small. Since all rotation capacity of the connection has to be delivered by the concrete slab, this slab must be designed carefully. Ductile hot rolled reinforcement bars should be used in order to provide sufficient deformation capacity.

The multiplanar loading case reduced the connection strength with approximately 20-30%. The results of the tests and analyses on these connections are shown in Table 10.5.

Table 10.5 Main results and conclusions for bolted I-beam to CHS column connections with a composite concrete floor and loaded with in-plane bending moments

<table>
<tr><td colspan="3">BOLTED I-BEAM TO CHS COLUMN CONNECTIONS WITH A COMPOSITE CONCRETE FLOOR AND LOADED WITH IN-PLANE BENDING MOMENTS</td></tr>
<tr><td> 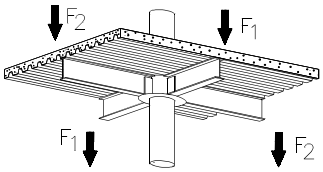

Without a concrete filled column</td><td> 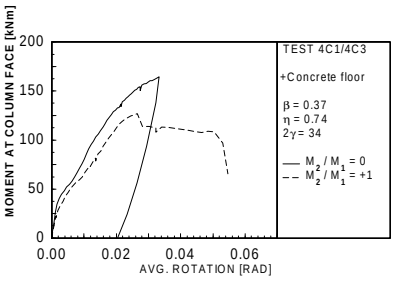
</td><td rowspan="2">Failure modes:
Progressive failure of the reinforcement bars

Conclusions:
Filling the column with concrete has no influence on the connection strength and stiffness.

The rotation capacity of the connections is limited due to the small deformation capacity of the reinforcement.

In the test, the slip of the bolted connections has a significant influence on the connection stiffness.

A load ratio of J=+1 gives a reduction of the connection strength with 20-30%, compared with the uniplanar loading condition (J=0).</td></tr>
<tr><td> 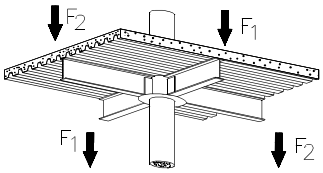

With a concrete filled column</td><td> 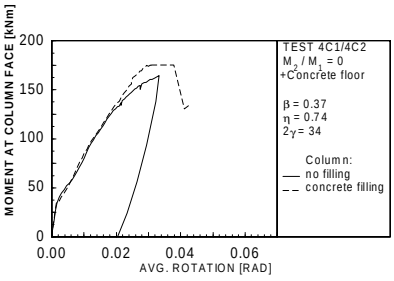

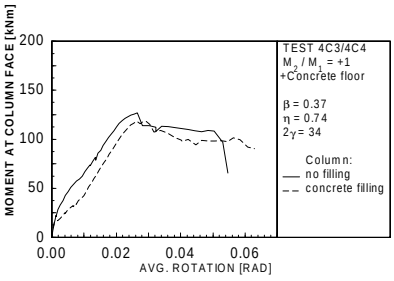
</td></tr>
</table>

10.5 Summary ultimate strength formulae

The strength formulae for the investigated connections as derived in Chapter 8 are summarized in Tables 10.6 to 10.9. The regression constants are included into the formulae.

Table 10.6 The ultimate strength formula for axially loaded plate to CHS column connections

AXIALLY LOADED PLATE TO CHS COLUMN CONNECTIONS	
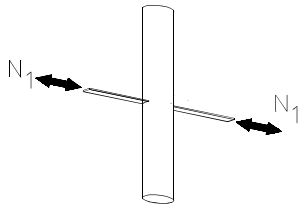	$\frac{N_u}{t_0^2 f_{y0}} = \frac{4.26\cdot\gamma\ (1.24\ \beta - 1.35\ \beta^2)}{1-\beta+\sqrt{(1-\beta)^2 + \frac{(2-\beta^2)}{\gamma^{1.66}}}}$ (8.5)
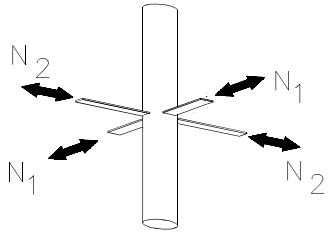 $J=N_2/N_1$	$\frac{N_u(J=0)}{t_0^2 f_{y0}} = \frac{6\cdot\gamma\ (0.7\cdot\beta - \beta^2)}{\sqrt{1-\beta^2} - \beta + \sqrt{\left(\sqrt{1-\beta^2} - \beta\right)^2 + \frac{2}{\gamma}}}$ (8.6) $\frac{N_u}{N(J=0)} = 1 + J\cdot(0.465\beta + 0.433\beta^2) + J^2\cdot(-0.642\beta + 1.28\beta^2)$ (8.7)
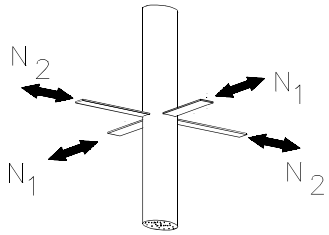 Concrete filled column	**N in compression:** Check plate on buckling according to design code **N in tension:** Check column on punching shear according to design code
ranges of validity	$0.2 \le \beta \le 1.0$ (for uniplanar connections) $0.2 \le \beta \le 0.7$ (for multiplanar connections) $15 \le 2\gamma \le 45$ $-1 \le J \le +1$

Table 10.7 The ultimate strength formula for axially loaded I-beam (or plates at two levels) to CHS column connections

I-BEAM (OR PLATES AT TWO LEVELS) TO CHS COLUMN CONNECTIONS	
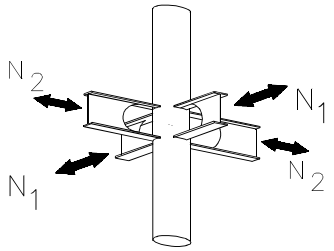	$\frac{N_{u,\ 2\ planes}}{N_{u,\ 1\ plane}} = 2 - \frac{1}{1 + 30\cdot\eta\cdot(1-3.61\beta + 3.83\beta^2)\cdot(2\gamma)^{-0.416}}$ (8.9) $\frac{N_u(\text{with web})}{N_u(\text{without web})} = 1 + 0.0352\cdot\eta$ (8.10)
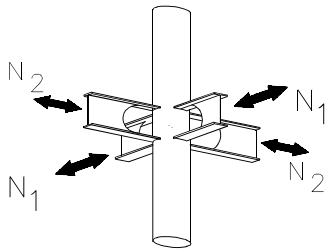 without concrete filled column $J=N_2/N_1$	$\frac{N_u(J)}{N_u(J=0)} = 1 + \left(J(1.9\beta - 1.486\beta^2) + J^2\beta^2\right) * f(\beta,2\gamma,J)$ (8.13) for $J \neq 1$: $f(\beta,2\gamma,J) = 1$ (8.14) for $J = 1$: $f(\beta,2\gamma,J) = -0.788 + 0.337\beta(2\gamma)^{0.429}$ (8.15) Note: as a simplified approach Eq. 8.14 may be used.
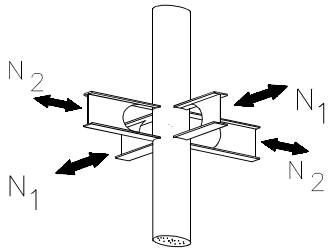 Concrete filled column	**N in compression:** Check plates/flanges on buckling **N in tension:** Check column on punching shear
ranges of validity	$0.2 \le \beta \le 0.7$ $\beta \le \eta \le 3*\beta$ $15 \le 2\gamma \le 45$ $-1 \le J \le +1$

Table 10.8 The ultimate strength formula for I-beam to CHS column connections loaded by in-plane bending moments

I-BEAM TO CHS COLUMN CONNECTIONS LOADED BY IN-PLANE BENDING MOMENTS	
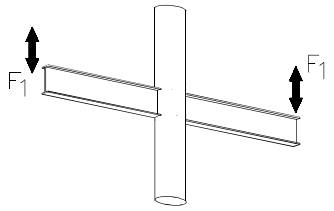	$\frac{M_u}{t_0^2\, f_{y,0}\, h_m} = \frac{4.9\cdot\gamma^{\,(1.23\,\beta-1.13\,\beta^2)}}{1-\beta+\sqrt{(1-\beta)^2+\frac{(2-\beta^2)}{\gamma}}}\cdot f(n)$ (8.16) where f(n) is Eq. 8.22
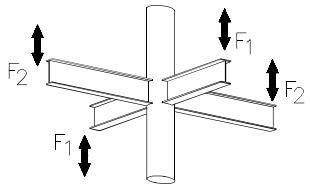	$\frac{M_u}{t_0^2\, f_{y,0}\, h_m} = \frac{4.89\cdot\gamma^{\,(1.33\,\beta-1.66\,\beta^2)}}{\sqrt{1-\beta^2}-\beta+\sqrt{\left(\sqrt{1-\beta^2}-\beta\right)^2+\frac{2}{\gamma}}}$ (8.19) $\frac{M_u}{M(J=0)} = 1+J(1+\beta-0.372\beta^2-(2\gamma)^{0.0567})+J^2(-0.43\beta+0.456\beta^2)$ (8.21)
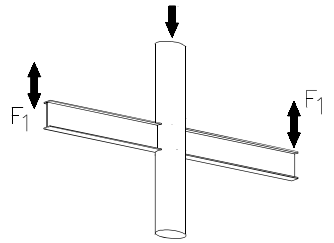 Pre-loading on column	$f(n) = 1-n^2(\beta-\beta^2)\cdot(2\gamma)^{0.3}$ (8.22) where $n=\frac{N_0}{A_0\cdot f_{y,0}}$
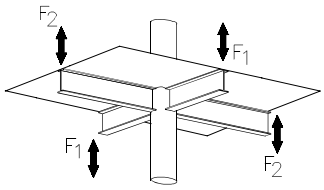	Connection strength according to Eq.8.19 and 8.21. The steel floor has no influence on the connection strength
ranges of validity	$0.2\le\beta\le1.0$ (for uniplanar connections) $0.2\le\beta\le0.7$ (for multiplanar connections) $\beta\le\eta\le2*\beta$ $15\le2\gamma\le45$ $-1\le J\le+1$ $0\le n\le0.8$

Table 10.9 The ultimate strength formula for bolted I-beam to CHS column connections with a composite concrete floor loaded by in-plane bending moments

BOLTED I-BEAM TO CHS COLUMN CONNECTIONS WITH A COMPOSITE CONCRETE FLOOR LOADED BY IN-PLANE BENDING MOMENTS	
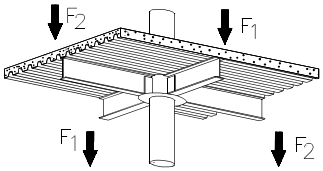 Without a concrete filled column	$M_u(J=0) = h_z \cdot \sum_{i=1}^{n} A_i \cdot f_{y,i} \cdot f(J)$ (5.1) where: h_z = distance between reinforcement bars and lower flange A_i = cross sectional area reinforcement bar i $f_{y,i}$ = yield stress reinforcement bar i n = number of reinforcement bars $M_u(J=1) = a \cdot M_u(J=0)$ $a \approx 0.7\text{-}0.8$ The following parts should be checked according to design codes: - bolted connections - shear studs
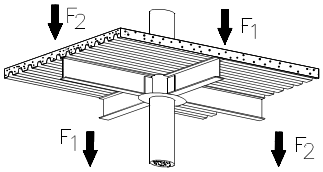 With a concrete filled column	Design as without a concrete filled column

10.6 Recommendations for further research work

Research on the following topics is recommended to extend the available evidence on statically loaded plate or I-beam to CHS column connections to establish future design recommendations on these connection types:

1. Current design evidence only covers either axial loading or in-plane bending moments. For frame analyses also the interaction between the various loadings is necessary. Therefore, additional numerical research is recommended to investigate the combined loading conditions.

2. For (semi-rigid) frame analyses, also the connection stiffness is needed. This connection stiffness is normally modelled with spring elements. The non-linear spring element properties can be obtained from load-deformation diagrams. In this research, the connection stiffness is made available through load-deformation curves. However, in this form these load-deformation curves are not directly usable for frame analyses, since they are only available for a limited number of geometrical parameters and load conditions. Load-deformation curves for arbitrary geometrical parameters can be obtained through interpolation using a computer programme and a database of the load-deformation curves obtained this research. A second method is using bilinear or multi-linear load-deformation curves where the branches are defined by parametric equations, based upon the finite element results.

3. The derived strength formulae might be too complicated to include in design codes. Simplification should be done in combination with strength formulae for other welded connections with tubular members, like tubular joints with CHS or RHS members and I-beam to RHS column connections. Since there are so many combinations in member type and loading conditions, some standardisation of the strength formulae in the design codes is recommended.

4. For the development of strength formulae for connections with concrete filled columns, crack modelling techniques for the finite element analyses are necessary to cover failure modes with cracking. Currently, these methods, like the Gurson damage model, are still experimental.

11 REFERENCES

This section gives the list of references as used in the thesis. In addition, some publications are given that can be used as background documentation.

The list of publications covers the following topics:

Literature A: Design codes and design guides
Literature B: Publications on plate and I-beam to CHS column connections based upon research in Delft
Literature C: Publications on plate and I-beam to CHS column connections based upon research in Japan
Literature D: Miscellaneous publications. These publications covers several topics, like the ring model and computer program manuals.

Literature A: Design codes and design guides

[1] AIJ (1990),
Recommendations for the design and fabrication of tubular structures in steel, Architectural Institute of Japan, Japan (in Japanese).

[2] AWS (1992),
Americal Welding Society, “Structural Welding Code -Steel”, AWS, Miami, USA.

[3] Brekelmans, ing. J.W.P.M. (1990),
"Staal-betonliggers, Praktijkvoorbeelden voor ontwerp en berekening," BI-89-143,vol. 6, p. 62, CUR, Rotterdam.

[4] CUR
“Staal-beton liggers - Praktijkvoorbeelden voor ontwerp en berekening” (Composite steel and concrete beams - examples of design and calculation in practice), CUR-Committee C 61/CS-Working Group 3, Jointly published by Staalbouwkundig Genootschap, Rotterdam, Centrum Staal Rotterdam and Civiel Technisch Centrum Uitvoering Research en Regelgeving, Gouda, ISBN 9037600263.

[5] ECCS (1988),
- Technical Committee 3 - Fire Safety of Steel Structures, Technical Note "Calculation of the fire resistance of centrally loaded composite steel-concrete columns exposed to the standard fire".

[6] EUROCODE 2, (1991)
ENV 1992-1: "Design of concrete structures - Part 1: General rules and rules for buildings". European Committee for Standardization (CEN).

[7] EUROCODE 3 (1992),
" Design of Steel Structures, Part 1: General Rules and Rules for Buildings.

[8] EUROCODE 3 (1989),
"Design of Steel Structures, Part 1: General Rules and Rules for Buildings, Chapter 3: Design Against Brittle Fracture, Background Documentation".

[9] EUROCODE 4 (1992),
ENV 1994-1-1: "Design of composite steel and concrete structures - Part 1-1: General rules and rules for buildings". European Committee for Standardization (CEN).

[10] EUROCODE 4 (1992),
CEN/TC 250/SC 4 N 39 prENV 1994-1-2 "Design of composite steel and concrete structures - Part 1.2: Structural fire design". Second draft 1992.

[11] Wardenier, J., Y. Kurobane, J.A. Packer, D. Dutta, N. Yeomans (1991),
"Design guide for circular hollow section (CHS) joints under predominantly static loading", ed. by Comité International pour le Développement et l'Etude de la Construction Tubulaire (CIDECT), Verlag TÜV Rheinland GmbH, Köln, Germany.

Literature B: Publications based upon Delft tests and research

[12] Broek, T.J. van der, R.S. Puthli, J. Wardenier (1990),
"The influence of multiplanar loading on the strength and stiffness of tubular joints", Final report, CIDECT report 5AR-90/10, Delft University of Technology, Delft, The Netherlands.

[13] Lu, L.H., G.D. de Winkel, J. Wardenier and Y. Yu (1994),
"Deformation Limit for the Ultimate Strength of Hollow Section Joins", Proceedings of The Sixth International Symposium on Tubular Structures, Melbourne, Australia..

[14]Lu, L.H. (1997),
"The Static Strength of I-beam to Rectangular Hollow Section Column Connections", Ph.D. Thesis, Delft University Press, Delft, The Netherlands.

[15] Paul, J.C. (1987),
"The Static Strength of Tubular Multiplanar Double T-Joints", Thesis report, RKER.88.076, KSEPL, Rijswijk, The Netherlands.

[16]Vegte G..J. (1995),
"The Static Strength of Uniplanar and Multiplanar Tubular T- and X-Joints", Ph.D. Thesis, Delft University Press, Delft, The Netherlands.

[17] Verheul, A, L.H. Lu, R.S. Puthli, J. Wardenier and G.D. de Winkel (1994),
"Semi-rigid connections between I-beams and Tubular Columns", ECSC project 7210-SA/611.

[18]Yu, Y. (1997),
"The Static Strength of Uniplanar and Multiplanar Connections in Rectangular Hollow Sections", Ph.D. Thesis, Delft University Press, Delft, The Netherlands.

[19] Wardenier, J. (1982),
Hollow Section Joints, Delft University Press, Delft, The Netherlands.

[20] Wardenier, J., G.D. de Winkel, L.H. Lu (1997),
"Semi-rigid I-Beam to Tubular Column Connections in Relation to Eurocode 3", Proceedings of the symposium on occasion of the retirement of Prof.dr. Y. Kurobane, Kumamoto University, Kumamoto, Japan..

[21] Winkel, G.D. de, H.D. Rink, J. Wardenier, R.S. Puthli (1993),
"The Behaviour and the Static Strength of Unstiffened I-Beam to Circular Column Connections Under Multiplanar In-Plane Bending Moments.", Proceedings ISOPE Third International Offshore and Polar Engineering Conference, Vol. IV, Singapore.

[22] Winkel, G.D. de, H.D. Rink, R.S. Puthl,i J. Wardenier (1993),
"The Behaviour and Static Strength of Plate to Circular Column Connections under Multiplanar Axial Loadings", Proceedings of the Fifth Int. Symposium Nottingham UK, Tubular Structures V, Nottingham, England.

[23] Winkel, G.D. de, H.D. Rink, J. Wardenier (1994),
"The Static Strength of Uniplanar and Multiplanar I-beam to Tubular Column Connections Loaded with In-Plane Bending Moments.", Proceedings ISOPE Fourth International Offshore and Polar Engineering Conference, Vol. IV, Osaka , Japan.

[24] Winkel, G.D. de, J. Wardenier (1994),

”Parametric study on the Static Behaviour of I-beam to Tubular Column Connections under In-plane Bending Moments”, Proceedings Sixth Int. Symp. Tubular Structures VI, Melbourne, Australia.

[25] Winkel, G.D. de, J. Wardenier (1995),
“Parametric Study on the Static Strength of Axially Loaded Multiplanar Plate to Circular Column Connections”, Proceedings ISOPE Fifth International Offshore and Polar Engineering Conference, Vol. IV., The Hague, The Netherlands.

[26] Winkel, G.D. de, J. Wardenier (1995),
“The Static Strength and Behaviour of Multiplanar I-Beam to Tubular Column Connections loaded with In-plane Bending Moments”, Proceedings of the Third International Workshop Connections in Steel Structures III., Trento, Italy.

[27] Winkel, G.D. de, J. Wardenier (1996),
“Parametric Study on the Static behaviour of Uniplanar I-beam-to-tubular Column Connections Loaded with In-plane Bending Moments Combined with Pre-stressed Columns., Proceedings of the Seventh Int. Symposium on Tubular Structures VII, Miskolc, Hungary.

Literature C: Publications based upon Japanese tests and research

[28] Akiyama, H.,
"Strength of joints in steel tubular structures,"Input to Monograph TC-43, Connections, Joint Committee and Tall Buildings.

[29] Akiyama, H. and T. Okumara (1976),
"Estimation of strength of tubular joints," Paper AIPC Conference, AIPC, Tokyo, Japan.

[30] Akiyama, N., M. Yajima, H. Akiyama, and A. Otaka (1974),
"Experimental study on strength of joints in steel structures," Journal of the JSSC, Vol. 10, No. 102, JSSC, Japan (in Japanese).

[31] JSSC,
"Experimental study on joints in tubular structures," JSSC, JSSC, Japan. (in Japanese).

[32] Kamba, T., H. Kanatani, K. Fujiwara, and M. Tabuchi (1981),

"Tests on the local failure of tubular column to H-beam connections in steel structures," Proceedings Conference on Joints in Structural Steelwork, Teeside, UK.

[33] Kamba, T., H. Kanatani, K. Fujiwara, and M. Tabuchi (1983),
"Empirical formulae for strength of steel tubular column to H-beam connections," Transactions of AIJ, Doc. 325, 67-73, AIJ, Japan (in Japanese).

[34] Kamba, T., H. Kanatani, K. Fujiwara, M. Tabuchi, T. Wakida, and T. Torigoe (1984),
"On the welded connections of the centrifugally cast steel tubular columns," Proceedings IIW Conference Welding of tubular structures, IIW, Boston, USA.

[35] Kamba, T. and M. Tabuchi (1995),
"Database for tubular column to beam connections in moment resisting frames", IIW doc. XV-893-95, Dep. of Architecture, Faculty of Engineering, Kobe University, Japan.

[36] Kanatani, H., M. Tabuchi, T. Kamba, J. Hsiaolien, and M. Ishikawa (1987),
"A study on concrete filled RHS column to H-beam connections fabricated with HT bolts in rigid frames, "Composite Construction in Steel and Concrete", vol. Proceedings of an Engineering Foundation Conference, ST Div. ASCE, p. 22, ASCE, Henniker, NH.

[37] Kanatani, H., T. Kamba, M. Aoki, and M. Tsuji (1977),
"Experimental study on tubular columns to H-beam connections," Abstracts of Ann. Conf. of AIJ, AIJ, Japan. (in Japanese).

[38] Kato, B. and H. Akiyama (1975),
"Strength of welded joints in steel structures," Report No. 1975-2, Lab. for steelstr., Dep. of Arch., University of Tokyo, Tokyo, Japan.

[39] Kurobane, Y. (1981),
"New developments and practices in tubular joint design," IIW Doc XV-488-81 and XIII-1004-81, IIW, Kumamoto, Japan.

[40] Kurobane, Y., M. Natarajan, and A.A. Toprac (1968),
Studies on Tubular Joints in Japan, Part II, Specifications on tubular steel structures and list of literature, Struct. Fat. Res. Lab, University of Texas, Texas, USA.

[41] Kurobane, Y., S. Hisamitsu, and S. Sukamoto (1967),

Tubular column to wide flange beam connections for multi-story buildings, Transcription. AIJ.

[42] Kurobane, Y., Y. Makino, and Y. Mitsui (1976),
"Ultimate strength formulae for simple tubular joints," IIW Doc XV-385-76, IIW.

[43] Kurobane, Y. and Y. Makino (1980),
"Re-analysis of ultimate strength data for truss connections in circular hollow sections," IIW Doc. XV-461-80, p. 40, Fac. of Engineering, Kumamoto University, Tokyo, Japan.

[44] Makino, Y.,
Stress analyses on tubular joints with gusset plates, Kumamoto University. (in Japanese).

[45] Makino, Y. and Y. Kurobane (1986),
"Recent research in Kumamoto University in tubular joint design," IIW Doc XV-615-86, XV-E- 86-108, p. 28, Fac. of Engineering, Kumamoto University, Tokyo, Japan.

[46] Makino, Y., Y. Kurobane, J.C. Paul, Y. Orita, K. and Hiraishi (1991),
Ultimate capacity of gusset plate-to-tube joints under axial and in-plane bending loads, Proc. Tubular Structures 4th International Symposium Delft 1991, Delft University Press, The Netherlands.

[47] Naka, T., B. Kato, H. Tada, and Y. Yamaraki (1960),
"Study on tubular structures, part 5," 27th Conference of AIJ, AIJ, Japan (in Japanese).

[48] Natarajan, M. and A.A. Toprac (1968),
Review of research reports, Part I: Studies on tubular joints in Japan, Struct. Fat. Res. Lab, University of Texas, Texas, USA.

[49] Togo, T. (1967),
"Experimental study on mechanical behaviour of tubular joints," Ph.D. Thesis, Osaka University, Osaka, Japan (in Japanese).

[50] Tanaka, H. (1973),
"Proposal of design formulae for required web thickness of beam to column connections," AIJ Doc. No. 207 and No. 185, Japan (in Japanese).

[51] Wakabayashi, M., R. Sasaki, and Y. Kijima (1971),
"Experimental study on the centrifugal casting steel tubular column to H-beam connections," Abstracts of the Annual Conf. of AIJ, AIJ, Japan (in Japanese).

[52] Washio, K., Y. Kurobane, T. Togo, Y. Mitsui, and N. Nagao (1971),
"Experimental study on ultimate strength of tubular joints with gusset plates.," Part 1 and 2, Summary papers, Annual Conference AIJ, Japan (in Japanese).

[53] Yura, J.A., N. Zettlemoyer, I.F. Edwards (1980),
"Ultimate Capacity Equations for Tubular Joints," OTC Proceedings, Vol 1, No 3690.

Literature D: Miscellaneous publications

[54] DIANA Manuals (1993),
Diana Analysis BV, Delft, The Netherlands.

[55] Graff, W.J., P.W. Marshall, and A.N. Minas (1981),
"Review of design considerations of tubular joints," Proceedings ASCE Conference 1981, ASCE, New York, USA.

[56] Korol, R.M., F.A. Mirza (1982),
Finite element Analysis of RHS T-Joints, ASCE, USA.

[57] Mäkeläinen, P.K., R.S. Puthli, F.S.K. Bijlaard (1988),
"Strength, Stiffness and Non-Linear Behaviour of Simple (Multi-Braced) Welded Tubular Joints." T.N.O. Report BI-87-72/63.6.1098.

[58] Malaska, M., E. Korhonen, A. Vuolio, W. Lu, J. Outinen, J. Myllymäki, Z. Ma (1998),
"Design of Steel-Concrete Composite Structures", Seminar on Steel Structures, Julkaisu Report 4, Espoo 1998, Helsinki University of Technology, Finland.

[59] MARC Manuals (1996),
Volumes A-E, Revision K.62, Marc Analysis Research Corporation, Palo Alto, USA.

[60] Marshall, P.W. and W.J. Graff (1976),

"Limit state design of tubular connections," Proceedings BOSS '76, BOSS, Trondheim, Norway.

[61] Roark, R.J. (1954),
Formulae for stress and strain, Mc Graw Hill, USA.

[62] Rodabough, E.C. (1978),
"Review of data relevant to the design of tubular joints for use in fixed offshore platforms," Report to WRC, Sub comm. on Tubular Structures of the Struct. Steel Comm., vol. (Also WRC bulletin 256, 1980).

CURRICULUM VITAE

Name	:	Gerben Dick de Winkel
Born	:	On March 18, 1960, in Loosdrecht, The Netherlands.
Sept. 1979 - June 1988	:	Graduate at the Faculty of Civil Engineering, Delft University of Technology. Thesis: “The design and analyses of an alternative design of the hub for the WPS30 wind turbine’.
June 1988 - current date	:	Research engineer (“Toegevoegd onderzoeker”) at the Stevin Laboratory S&H of the Subfaculty of Civil Engineering of Delft University of Technology.

Projects:

- STW project DCT.99.1904 “Beam to Column Connections”.
- ECSC project 7210-SA/611“Semi-Rigid Connections between I-beams and Tubular Columns”.
- CIDECT project 5AX “Semi-Rigid Connections between I-beams and CHS or RHS Columns”.
- Various projects on the optimisation of wind turbine rotor blades for Dutch blade fabricators.
- Focus4, the development of an integrated wind turbine design tool.
- Starion Project, the implementation of existing evidence on buckling of curved shells into currently used rotor blade design programs, with experimental verification.
- Wisper project, fatigue tests on GRP test coupons using the WISPER loading spectrum.

STELLINGEN

behorende bij het proefschrift

The Static Strength of I-beam to Circular Hollow Section Column Connections

G.D. de Winkel

Delft, december 1998

1. Numeriek onderzoek kan experimenteel onderzoek nooit geheel vervangen. Bij numerieke modellering ontbreekt immers het onvoorspelbare, dat alleen bij experimenteel onderzoek ontdekt kan worden.

2. Niet het verkrijgen van beproevingsgegevens, maar het bepalen van alle effecten, die deze resultaten beïnvloed hebben, vormt de feitelijke uitdaging van de onderzoeker.

3. Analytisch afgeleide formules zijn vanwege de complexiteit vaak moeilijk toepasbaar in de praktijk. Echter, vereenvoudiging moet niet ten koste gaan van het inzicht van de ontwerper in het fysisch gedrag.

4. De vaststelling van het vervormingscriterium voor buisverbindingen op 3% van de buisdiameter is niet het resultaat van exacte wetenschap, maar van pragmatisme.

5. Het gebruik van de dimensieloze sterkte $N_u/(t_0^2 * f_y)$ in grafieken met betrekking tot de sterkte van buisverbindingen levert voor verbindingen met een hogere 2γ-verhouding (en daarmee een kleinere buiswanddikte) een hogere dimensieloze sterkte op. Dit kan bij niet-specialisten tot verkeerde interpretaties leiden.

6. Bij colleges op het gebied van de Eindige Elementen Methode wordt geleerd om zoveel mogelijk gebruik te maken van symmetrievlakken. Toepassing van het geleerde kan er toe leiden dat asymmetrische bezwijkvormen niet door het model beschreven worden, waardoor de kritische sterkte niet gevonden wordt.

7. Het manipuleren van resultaten is met de Eindige Elementen Methode even eenvoudig als met de Statistiek.

8. Code-sharing door nationale normcommissies is van groter belang dan code-sharing door luchtvaartmaatschappijen.

9. De toenemende rekensnelheid van supercomputers verkort de onderzoeksduur niet, aangezien de onderzoeker zijn modellen zo zal verfijnen dat de rekentijd ongeveer constant blijft.

10. Reorganisaties zoals op de faculteit Civiele Techniek, waar vakgroepen gedegradeerd worden tot secties als onderdeel van nieuw opgerichte vakgroepen, waarna de vakgroepen weer opgeheven worden en de secties weer verzelfstandigd, brengen op de werkvloer nauwelijks veranderingen, maar geven wel een grote ballast voor bestuur en beheer.

11. Een vooruitstrevende universiteit als de Technische Universiteit Delft zou geen Basis Netwerk Voorziening moeten aanleggen aan het einde van de jaren negentig met actieve componenten met een capaciteit van de jaren tachtig.

12. De kwaliteit van programmatuur is omgekeerd evenredig met het aantal uitgebrachte update versies per jaar.

13. Gezien de hoeveelheid medische informatie en het aantal zelfhulpgroepen op het Internet, zou een internetaansluiting voor chronische patiënten moeten worden vergoed door de ziektekostenverzekering.

14. Het lage stropdasgehalte in de wereld van de windenergie wijst er op dat er nog steeds sprake is van een alternatieve energiebron.

1. Numerical research can never completely replace experimental research. By their very nature, numerical models lack unpredictable aspects, which can only be discovered by experimental research.

2. Not the generation of test data, but the determination of all effects influencing the test results is the real challenge facing the researcher.

3. Analytical formulae are often too complicated to use in practice. However, simplifying them should not reduce the designers' insight in the physical phenomena.

4. The choice of the deformation criterion for tubular joints, equal to 3% of the column diameter, is not the result of exact science, but of pragmatism.

5. The usage of the non-dimensional strength $N_u/(t_0^2 * f_y)$ in graphs presenting the strength of tubular joints results for connections with a higher 2γ-ratio (thus with a smaller column wall thickness) in a higher non-dimensional strength. This could result in non-specialists drawing the wrong conclusions.

6. At the lecture series on the Finite Element Method students learn to make use of planes of symmetry as much as possible. Application of this lesson can prohibit the occurrence of asymmetric deformation shapes in the model. Thus, the critical strength will not be found.

7. Manipulating the results obtained with the Finite Element Method is as easy as it is with Statistics.

8. Code-sharing by national code committees is of more importance than code-sharing by airline companies.

9. The increasing speed of supercomputers does not reduce the turnaround time, since researchers will refine their models in such a way that the CPU time is kept approximately constant.

10. Reorganisations at the Faculty of Civil Engineering, where departments were degraded to sections as part of new constituted departments, after which departments were abolished and sections turned into independent units once again, do hardly effect working practices, but give raise to a high work load on the management.

11. A progressive university like the Delft University of Technology should not build a network for office automatisation at the end of the nineties with active components with a capacity of the eighties.

12. The quality of software is inversely proportional to the number of updates and patches per annum.

13. Considering the amount of medical information and self-help groups on the Internet, the costs of an Internet connection should be paid by medical insurance for chronical patients.

14. The small number of ties worn by people in the world of wind energy indicates that it can still be considered an alternative source of energy.